UNIVERSITY OF BIRMINGHAM

Formulation and Development of Ceramic Mould Materials For Investment Casting

by

Luke Tarrant

A thesis submitted in partial fulfilment for the
degree of DOCTOR OF ENGINEERING

in the
College of Engineering and Physical Sciences
School of Chemical Engineering

June 2012

"I have only one regret, that I have not worked harder"

Sir Henry Royce

Abstract

The relationship between the formulation of ceramic mould materials for investment casting and their mechanical properties was investigated. A number of different ceramic materials were employed throughout the investigation including alumina, zirconia, mullite and colloidal silica. A number of techniques were employed to characterise the raw materials including laser diffraction, sieve analysis and zeta potential. Ceramic shell specimens were investigated by measuring mechanical strength using flexural and compressive testing with the former being conducted at both room and elevated temperatures. Samples were further investigated by thermal expansion measurement and archimedes porosity measurement.

It was determined that the incorporation of unstabilised zirconia as both a stucco and filler material was effective in terms of reducing the fired strength of investment casting ceramics. Structural observations of samples under SEM revealed that the weakened samples featured significant cracking in the fired condition due to the occurrence of the zirconia phase transition. Thermal expansion measurements confirmed both the presence of the phase transition and the extent of the disruption caused.

It was observed for slurries containing silica and alumina, that variation of the proportions of either had a significant effect on the properties of the final shell material. As before these observations were confirmed through measurements of mechanical strength and also by observing the structure of samples under SEM. It was also shown that the size of the ceramic particles within the slurry had a significant effect on the final properties of the ceramic body.

The incorporation of polyethylene particles as a pore forming agent was investigated and found to be highly effective in reducing the flexural strength of shell specimens. The effect on compressive strength was however, less significant. The strength was also found to be highly dependant on the level of polyethylene included in the formulation.

The results of this work provide a useful basis for determining the properties of the ceramic materials based on their formulations.

Acknowledgements

The author would like to acknowledge the support of the EPSRC and Rolls-Royce plc for funding this research project. Further thanks is due to the School of Chemical Engineering at the University of Birmingham, in particular to Dr. Richard Greenwood. Thanks are also due to the staff at Interdisciplinary Research Centre at the University of Birmingham with particular thanks due to Mr. Grant Holt without whom many of the shelling trials would not have been possible.

Special mentions are required for Professor Stuart Blackburn, Mr. Steve Irwin and Dr. Paul Withey whose direction and support contributed significantly to the achievements of this work.

My thanks also extend to the Rolls-Royce engineers at the Precision Casting Facility in Derby for their support, with a special mention due to Dr. Jeffrey Knight, Dr. Paul Wilson and Dr. Stuart Welch for many useful discussions.

I would also like to thank my parents Nick and Carole Tarrant for giving me the opportunities which led me here.

Finally I would like to thank my wife Victoria and my son Sebastian, without you both I couldn't have achieved any of this.

Contents

List of Figures

List of Tables

Abbreviations

IC	Investment Casting
LC	Large Chill
MOR	Modulus Of Rupture
PCF	Precision Casting Facility
PSD	Particle Size Distribution
RX	Recrystallisation
SB	Small-Bore
SCU	Supply Chain Unit
SEM	Scanning Electron Microscope
SHT'd	Solution Heat Treated
SX	Single Crystal
XRD	X-Ray Diffraction
XRF	X-Ray Fluorescence
PFA	Pore Forming Agent

For Victoria,

Without your love and support this would never have been possible.

Thank you

1

Introduction

1.1 Introduction

Rolls-Royce plc is a manufacturer of gas-turbine engines for the aerospace industry. This project was conducted in conjunction with the Rolls-Royce Turbines supply-chain-unit (SCU). This SCU is responsible for the manufacture of metal components within the hot-section (aft of the combustor) of the gas-turbine engine using the investment casting process. The majority of the practical work associated with this project was conducted in the laboratories of the Interdisciplinary Research Centre (IRC) at the University of Birmingham, production support was provided from Rolls-Royce by the Precision Casting Facility (PCF) in Derby, UK.

1.2 Project aims

This project was performed in order to develop a new ceramic shell mould material which was capable of facilitating the casting of complex geometry parts using modern casting techniques. Within Rolls-Royce, components are manufactured using two different casting technologies each of which has a subtly different process. Traditionally single-crystal (SX) casting at Rolls-Royce was performed using small diameter moulds (small bore) featuring up to 4 components per mould. Commercial pressures and advances in technology lead to the introduction of larger diameter moulds (large chill) featuring in excess of 18 components per mould. One of the aims of this project was the development of a ceramic mould material capable of producing gas-turbine blades using large-chill furnace technology. To enable this, a significant aim of this research project was the development of an investment casting shell material capable of facilitating the manufacture of single-crystal (SX) blades with reduced incidence of the casting defect known as recrystallisation (RX); this defect is discussed in greater detail in section 2.2.3.

1.3 Thesis outline

The purpose of this chapter is to provide sufficient background information to provide a context for the following chapters. The chapter immediately succeeding this one contains information gathered during an extensive search of both academic and patent literature. Due to a lack of information regarding the properties of the existing shell materials in use by Rolls-Royce it was also necessary to perform an amount of original research prior to the commencement of the main trial work. Results of this characterisation are presented in Chapter 2 alongside information gleaned from the literature. The characterisation techniques and materials utilised within the experimental work are presented in Chapter 3.

The majority of the practical work performed as part of this thesis is reported in Chapters 4 to 6; each Chapter follows a similar structure with the beginning of the chapter outlining the reasons for completing the experiments using the selected materials, followed by the presentation and discussion of practical results and observations. Where relevant, discussions include references to similar or contradictory observations within the literature. The experimental work reported in Chapter 7 was performed in order to clarify and understand unexpected observations made during the preceding three chapters, the structure however remained similar.

The final Chapter summarises and concludes observations made throughout preceding chapters. Finally, potential further development work following on from this thesis is discussed.

1.4 Business case

The business case for this project was predominantly based on scrap costs due to the occurrence of a casting defect known as recrystallisation (RX) wherein areas of a single crystal alloy components form secondary crystal grains; the mechanisms of RX formation are discussed in greater detail in section 2.2.3. Figures 1.1 and 1.2 show the scrap rates for each defect as a percentage of the total for the 2009 and 2010 respectively. It can be seen that across both years the defect accounts for 3 % of the total scrap for the Rolls-Royce Precision Casting Facility (PCF) in Derby. Whilst this rate may appear low relative to other defects presented in the chart, it is important to note that the defect is only detectable following the casting cycle during the final stages of the inspection process. Due to the value-added nature of the components the late detection makes the cost associated with the defect significantly greater than some other more frequently occurring but less costly defects including those associated with wax.

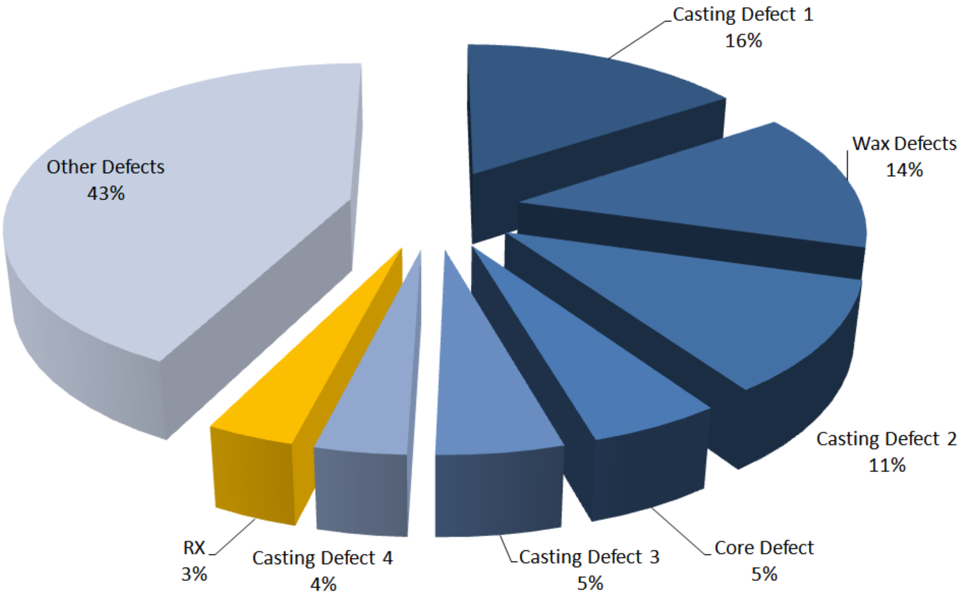

FIGURE 1.1: PCF scrap costs (percentage of total scrap cost) for the year 2009 - 2010. Recrystallisation data (RX) highlighted in yellow.

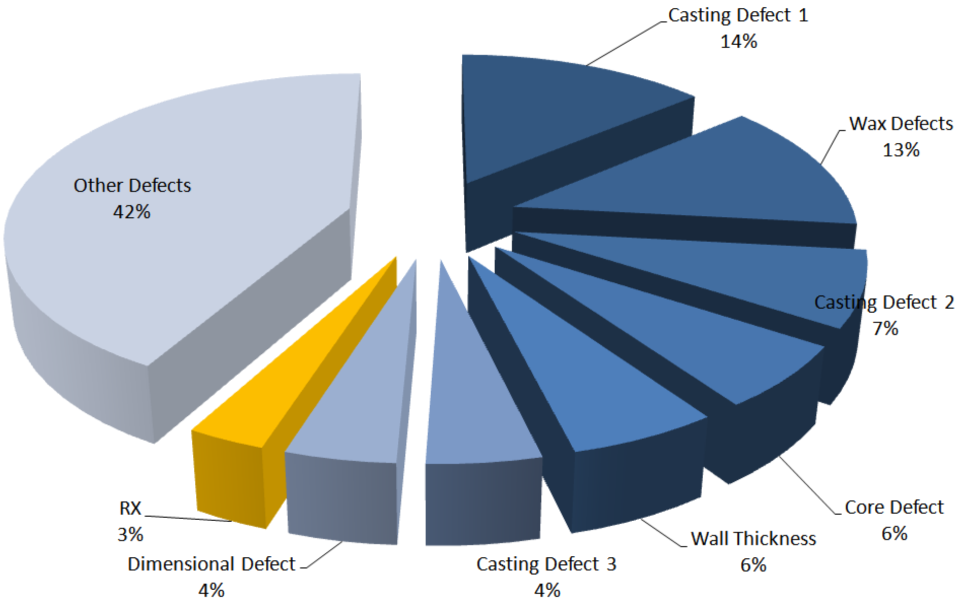

FIGURE 1.2: PCF scrap costs (percentage of total scrap cost) for the year 2010 - 2011. As before recrystallisation (RX) highlighted in yellow.

1.5 Material requirements

As an industrially viable solution the material would have to satisfy a number of requirements; these requirements were set-out by Rolls-Royce and were based on many years of commercial experience and process knowledge. The requirements stated that materials must be;

- Compatible with existing materials
- Manufacturable using existing process equipment
- Of similar casting performance to existing shell materials
- Dimensionally stable during the casting cycle
- Capable of sustained use at temperatures of 1540 °C
- Free from zirconium silicate (Zircon)
- Capable of manufacturing single-crystal blades on Large Chill furnaces
- Comparable to existing materials in terms of health and safety

Meeting these requirements would ensure that all materials would be capable of integration within Rolls-Royce factories worldwide. They would also ensure that through reducing the occurrence of RX no adverse effects on shell behaviour would be incurred. It was possible to investigate materials which did not fulfil one or more of these requirements however these would not be of commercial interest to Rolls-Royce.

2

Literature review and investigation of Rolls-Royce shell materials

The purpose of this chapter is to provide a review of the state of the art in terms of investment casting shell materials. The investment casting process is not well-documented within scientific journals, since the majority of research is conducted by industry the results are generally commercially sensitive and contain proprietary information. In some cases however, this leads to the publishing of patents within the field. These can provide a useful source of information about the processes used within industry and were, alongside research papers, searched extensively prior to and during the course of preparing this thesis. Since the aim of this work was the development of an industrially relevant material it was also useful to investigate patents in order to ensure that any trial formulations developed could be used without the risk of patent infringement.

Information gathered during the literature survey was complimented by original research characterising the mechanical and thermal properties of the shell materials currently in use by Rolls-Royce. These results are presented and discussed here as they provide a useful baseline for the behaviour of shell materials featuring different compositions; further to this, the shell behaviour was also related to casting observations gathered by Rolls-Royce.

2.1 The investment casting process

The earliest historical reference to the investment casting process dates back to 5000 BC in which principles of the technique were employed in order to manufacture metal tools [1], the technique was also employed by the Chinese to manufacture bronze statues [2]. The revival of the technique and its subsequent application to the aerospace industry did not come until the 20th century, specifically 1939 when the events of World War 2 created a great demand for high precision components for the arms and aerospace industries [3].

The investment casting process is represented schematically in Figure 2.1. The first step in the process is the production of a wax pattern; this is a replica of the component which will be cast and is produced by injection moulding the molten wax into a metal die. After removal from the die, patterns are cleaned and prepared for dipping. In order to produce the ceramic shell moulds which will be used for casting, wax patterns are dipped into ceramic slurries consisting of a colloidal binder, refractory filler powder and other additives. As the wax is dipped and removed from the slurry, a thin coat remains on its surface which is then coated with refractory particles, this process is known as stuccoing. The dipping and stuccoing procedure is repeated a number of times in order to build a shell with sufficient thickness that it is dimensionally stable during the rest of the casting process. Once the dipping process is complete the moulds are allowed to dry; the drying process is done in a temperature and humidity controlled environment and moulds are subjected to moving air. Following this the wax-filled shells are steam-autoclaved at 200 °C and 0.8-1 MPa [4] in order to melt the wax pattern leaving the shells ready to be fired and cast. Due to the nature of the application, turbine engine components must be manufactured to precise tolerances and high levels of material quality; currently the investment casting process is the method of choice within the industry for the manufacture of near-net shape components [5].

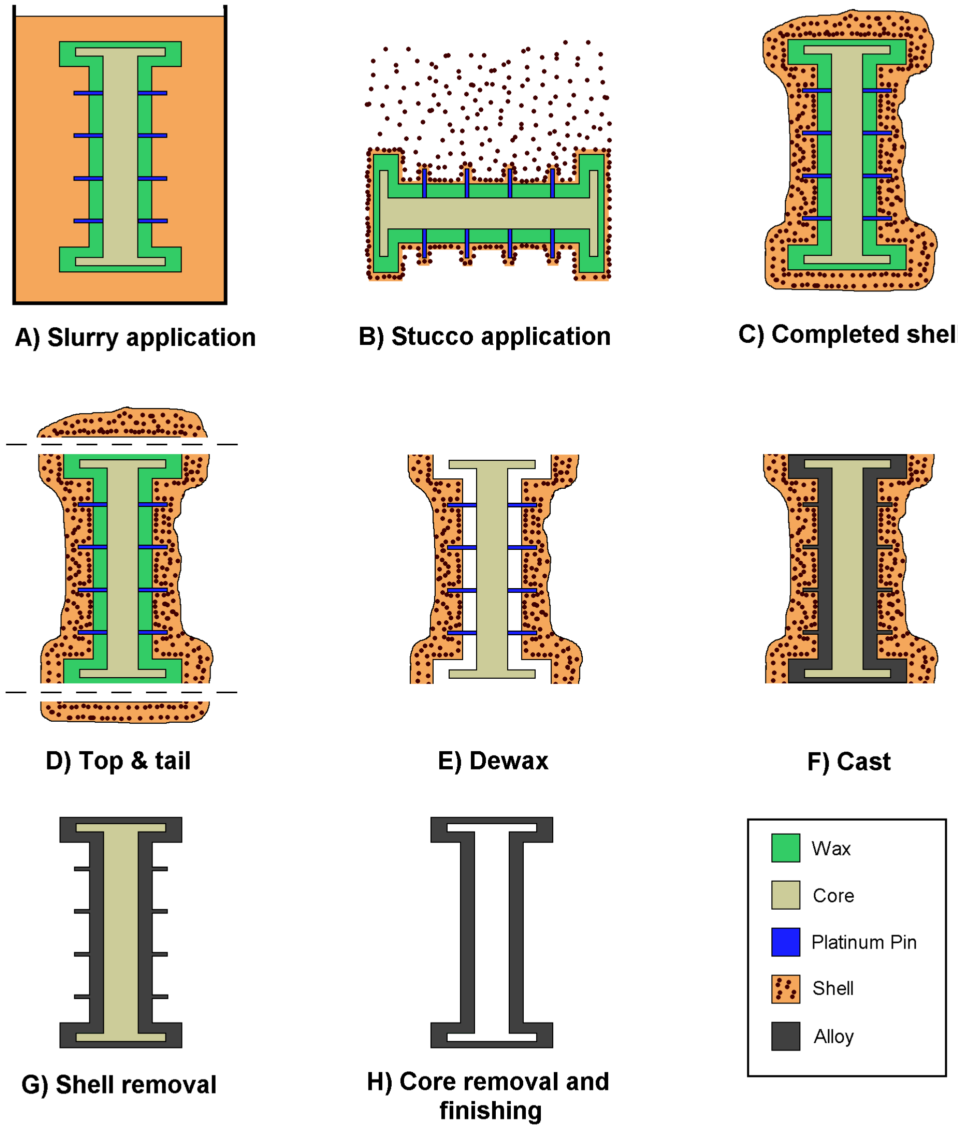

FIGURE 2.1: Schematic diagram showing the basic stages involved in the investment casting process

The main focus of this work is the ceramic material used to make the moulds. It is well known that a number of defects can arise due to the interaction between the mould material and the cast-article; the defects are discussed further in the following sections along with methods of altering the properties of the shell material to reduce their occurrence.

2.2 Superalloys

The motivation for Rolls-Royce to cast single-crystal (SX) blades using large-chill (LC) furnace technology is discussed in section 1.4. The following section contains background information regarding the casting of superalloys in general including different casting methods and their applications. One of the main aims of the project was the formulation of a shell material capable of reducing the level of a casting defect known as strain-induced recrystallisation (RX). The occurrence and formation mechanism of this defect is also discussed along with potential solutions.

2.2.1 Casting Techniques

Casting is the final step in the investment casting process in which molten alloy is poured into the ceramic shell mould to produce the cast article. One of three casting types can be used based on the required properties of the final component;

- Equiaxed
- Directional Solidification (DS)
- Single Crystal (SX)

The mechanical properties of the final components are partially determined by their crystal structures which are governed by the method of casting. Common to all casting types is the requirement that alloy pour occurs under high vacuum to reduce oxidation of the molten alloy; following this stage the casting procedure deviates somewhat according to the casting type.

Unlike SX and DS, equiaxed castings are only held under vacuum during the metal-pour phase, immediately afterwards the hot moulds are removed from the furnace and allowed to cool at room temperature and pressure. The radiative and convective heat losses from the mould create multi-directional temperature gradients within the cooling alloy which promote uniform three-dimensional crystal growth from the melt [6]. The resulting structure contains many small crystals with a correspondingly large number of grain boundaries between them; the structure is shown in Figure 2.2. Since the only part of the procedure carried out within the furnace is the metal pour, equiaxed casting is relatively inexpensive in terms of both cost and furnace-time offering high specific furnace output. However the mechanical properties and durability of equiaxed castings is relatively poor due to the number and orientation of grain boundaries present within structure. Intergranular bonding between crystals is weak compared to that within the crystals themselves and component failure often occurs at these sites; for this reason equiaxed castings are far less durable than SX or DS castings. This is unsurprising considering the nature of the loads placed on the castings; high rotational speed generates large axial stresses and grain boundaries perpendicular to these may act as nucleation sites for blade failure and grain boundary creep [6].

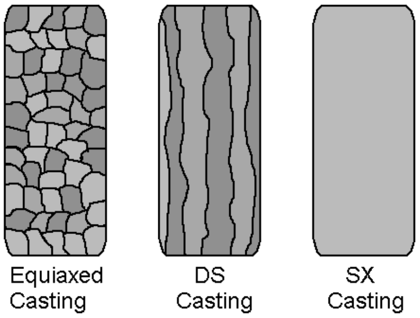

FIGURE 2.2: Schematic diagram showing the crystal structure of components using various casting techniques.

In order to increase the durability of turbine blades the number of grain boundaries perpendicular to the axial stress must be reduced, this can be achieved through growing crystals with a columnar structure extending the entire length of the component, parallel to the stress axis as shown in Figure 2.2. In order to produce this structure moulds are attached to water-cooled copper chill-plates and are withdrawn in a controlled manner from within the hot-zone of the furnace during cooling to generate temperature gradients within the component. The temperature gradient, in combination with the chill plate, encourages nucleation at the base of the component and also inhibits crystal growth elsewhere, in this way the parts are directionally solidified (DS). The columnar structure has far fewer grain boundaries perpendicular to the major axis and hence is much more resistant to grain boundary related failure. The disadvantage of the technique is that the furnaces required are more complex and expensive and since mould cooling is performed within the furnace itself the production of parts is slower. DS components are not immune to grain boundary effects and exhibit similar (although at greatly reduced rates) failure modes compared to equiaxed blades. Although the crystals within the columnar structure extend the entire length of the component the grain boundaries between them are not uniform, any part of the boundary perpendicular to the stress axis is susceptible to act as a nucleation site for blade failure.

Single crystal casting is similar to that of DS casting except the moulds do not fix directly onto the chill-plate, they instead connect to a small metal reservoir known as a starter [6]. The starter connects to the main casting via a grain-selector, a helical channel within the mould which serves to eliminate all crystal modes other than the most competitive. SX castings contain no grain boundaries and are therefore immune to grain boundary related failures, they exhibit the highest performance and durability of any casting type. The disadvantages of SX casting are the same as those of DS casting; additionally SX castings must be solution heat-treated in order to achieve optimum strength, it is also necessary to perform additional inspection operations in order to ensure that castings have the correct structure.

2.2.2 Component life

Casting components using the single crystal casting technique mentioned in the preceding section also has a benefit to the operational lifespan of the component. Elements such as Boron, Hafnium and Zirconium were typically included in Equiaxed and DS alloys in order to act as grain boundary strengthening agents [7]. The elimination of grain boundaries allowed the removal of these materials from the alloy, which in turn allowed more complete heat treatment regimes to be applied to the alloy. The result of this process improves the fatigue life of the cast components [8].

2.2.3 Recrystallisation

Strain induced recrystallisation (RX) is a casting defect which affects single crystal (SX) components; the problem manifests following solution heat treatment as the formation of secondary crystal growth regions within the component. This is undesirable since grain boundaries between crystals are known to reduce blade durability as mentioned in the preceding section.

Following the removal of the mould from the casting furnace the majority of the shell material cracks and detaches from the alloy due to the difference in thermal expansion coefficients between the two materials. However, in some areas of the mould, especially those areas with re-entrant features it is possible for the shell material to become constrained during cooling. The alloy contracts more rapidly than the shell material generating large stresses in these regions which are capable of inducing plastic strain within the alloy [9]. The plastic strain generated causes the crystal lattice in that area to enter a less energetically favourable state. During heat treatment the atoms within the lattice develop sufficient mobility to rearrange into a more favourable state; this manifests as RX within the component. One theory explaining the phenomenon is that during the firing process the ceramic shell moulds used to cast the components develop excessive strength due to sintering of the ceramic matrix; rather than failing due to the compressive stress they remain intact and induce strain in the component. Assuming thermal expansion coefficients for the ceramic shell material and the alloy are 5.4 x 10^{-6} K^{-1} and 1.4 x 10^{-5} K^{-1} it can be shown that the strain rate induced in the alloy could reach 6.7 x 10^{-6} S^{-1} depending on the geometry of the part [10].

Some preliminary casting trials were performed at the PCF using shrouded BR725 HP2 turbine blade waxes and the standard small bore SX (Std SX.) shell system. The trial involved varying the number of backup shell coats applied to the wax pattern in order to investigate the effect of shell strength on propensity to induce RX; the results of the trial are shown in Table 2.1. The dipping schedule listed in the table utilises the Rolls-Royce standard nomenclature for describing shell build, in this system the numbers represent the numbers of primary, primary +1, backup and seal coats respectively. It should be noted that the use of strength in this context does not relate to the material strength of the shell material, rather the ability of the mould material to resist an applied force without fracturing. Mechanical strengths of the shells were not characterised as part of the trial however it is clear that reduction in shell thickness gives a corresponding reduction in strength. The results indicate that reduced shell strength can also reduce the occurrence of RX, at least for the tested geometry.

Scrap costs due to RX at the Precision Casting Facility (PCF) in 2007 show that the parts featuring the highest levels of scrap due to RX all feature shrouded geometries. Inspection of Figure 2.3 shows that it is much more likely for blades with the shrouded design to constrain shell material than those without the shroud.

Table 2.1: RX incidence for different shell builds. Although castings made using 1–1–4–1 exhibited zero RX, 11 of 19 castings were insufficient to retain metal.

	Samples exhibiting Rx	
Dipping Schedule	Number	%
1–1–6–1	9 of 18	50
1–1–5–1	1 of 18	5.5
1–1–4–1	0 of 8	0

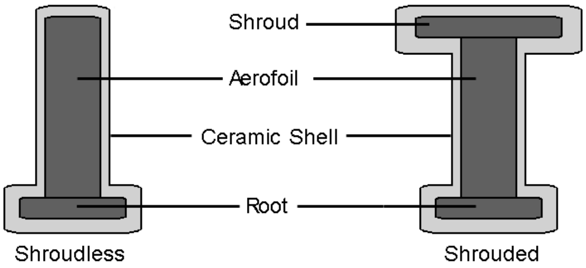

Figure 2.3: Schematic diagram showing the difference in geometry between shrouded and shroudless blade types.

In order to attempt to reduce RX it is necessary to generate a shell system which exhibits reduced strength or reduces the propensity to induce strain within the metal component by some other means.

2.3 Current Rolls-Royce shell materials

In order to formulate a shell system to augment current casting capability it was necessary to understand the performance of the incumbent shell materials. In this section the formulation and properties of the existing shell materials are discussed with reference to creating a baseline of properties to be used throughout the formulation of the Next Generation candidate systems.

A number of shell systems are in use across Rolls-Royce foundries worldwide however the two most relevant to this thesis are those used in the casting of single crystal (SX) components which will be referred to throughout as Hi-Shell and Std SX. Although the systems are both used for SX casting they are applied to different components and furnace types and as such exhibit different properties both thermal and mechanical. A trial shell material was also developed and used to manufacture a limited number of castings, the system consisted of the Std SX slurry paired with the mullite stucco from the Hi-shell system; the system was referred to as Hybrid. Much of the work presented here is either original research or based on historical RR data; due to the commercially sensitive nature of the formulations there are comparatively few references to the literature.

Table 2.2: Formulations for Rolls-Royce single crystal backup shell systems. Note that silica content reflects solid content only.

			Concentration	
Slurry	Material	Product	Wt %	mol %
Hi-shell	Silica	Wexcoat	9.0	40.8
	Nylon-fibre	Wexperm	0.6	
	Alumina	PFR15	20.7	59.2
	Mullite	Duramul 0.04	11.6	
	Mullite	Duramul 0.07	58.1	
Std SX	Silica	EHT	9.2	
	Zircon	CMMP Zircon	90.8	

The slurry materials used for primary (sometimes referred to as the facecoat as this is the material the alloy is in contact with) and primary +1 (the second coat applied) are detailed in Table 2.3. These materials were used throughout the development of all candidate and Rolls-Royce produced test specimens.

Table 2.3: Formulations for Rolls-Royce single crystal primary and primary +1 shell systems. Note that silica content reflects solid content only.

Slurry	Material	Product	Wt %
Primary	Silica	Morisol X30	18
	Zircon	CMMP Zircon	82
Primary +1	Silica	Ludox SK-CV	25
	Zircon	CMMP Zircon	75

2.3.1 Shell properties

One of the most widely used forms of testing for shell materials in the investment casting industry is flexural testing in 3-point bend also known as modulus of rupture (MOR). Due to sintering and other processes occurring during firing the structure of the shell material evolves during the casting cycle, it is therefore useful to characterise the shell in a number of conditions representative of the stages of the casting cycle. Figure 2.4 shows the results of flexural testing of the standard shell materials having been subjected to different thermal cycles. The firing processes are described in detail in section 3.1, however, for completeness they are mentioned here also. Samples having undergone the dewax process are referred to as being in the green state; those having subsequently undergone a firing cycle of 800 °C for a duration of 60 minutes are referred to as being in the pre-fired state. The final firing condition for samples tested at room temperature are those which having been through the pre-fire cycle are additionally fired to a temperature of 1550 °C for a duration of 30 minutes; samples in this condition are referred to as fired. The flexural strength of samples was also measured at 1540 °C in order to determine the performance of the mould material during the casting process. All techniques employed to characterise shell specimens are reported in detail in section 3.1.

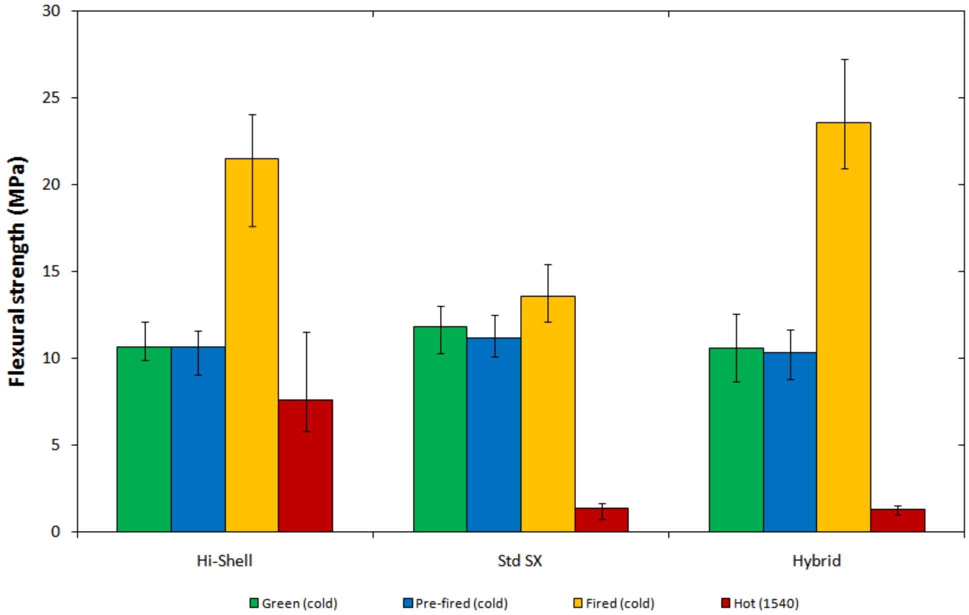

FIGURE 2.4: Flexural strength data showing the measured shell strengths across varying shell states; test results labelled green, pre-fired and fired all performed at room temperature. Results labelled 1540 were tested at a temperature of 1540 °C after a 20 minute soak time.

Inspection of the flexural results show that in the green and pre-fired states there was little difference between any of the shell materials with all samples exhibiting flexural strengths of approximately 11 MPa. In terms of compressive stress to failure, shown in Figure 2.5, Hi-shell samples exhibited reduced values compared to other systems; it is likely that this was due to the presence of pores within the structure due to the burnout of fibres during the pre-fire cycle. However in terms of the applied load required to induce failure, shown in Figure 2.6, both Hi-shell and the Hybrid system recorded higher values than the Std SX. This is linked to the greater shell thickness of Hi-shell samples compared to Std SX; average wall thickness' for specimens were 5.6 mm and 4.7 mm respectively.

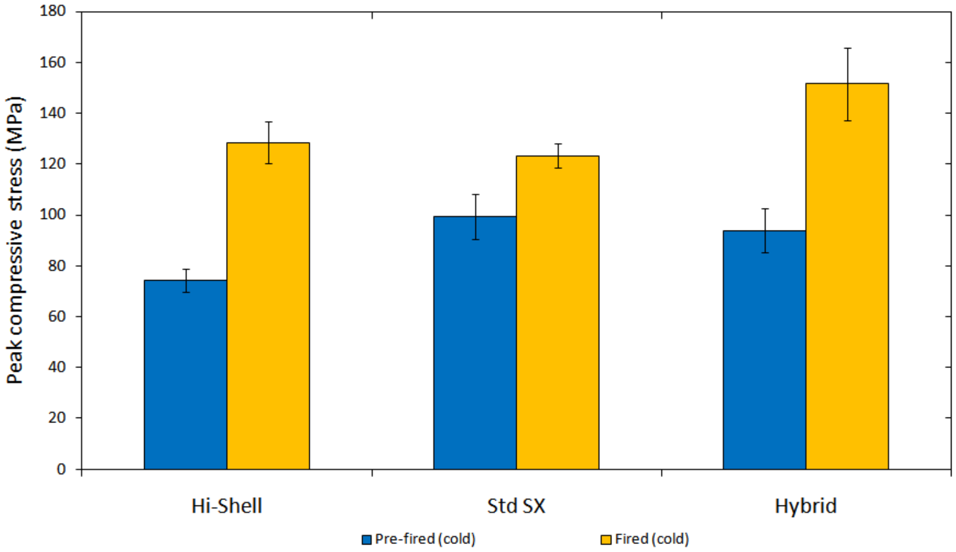

Figure 2.5: Data showing peak-stress values measured during compressive testing of pre-fired and fired shell specimens; all tests performed at room temperature.

Comparison of fired and high-temperature strengths for the Std SX. and Hi-shell materials presented in Figure 2.4 highlight the difference in their intended application. The Hi-Shell system was developed primarily to facilitate casting of large components with greater charge weight (volume of alloy) on large chill (LC) furnaces, such components require greater shell strength at high-temperature to maintain dimensional accuracy.

However these components are not generally subjected to heat-treatment and are therefore not at risk of developing RX. The Std SX system is used primarily to cast SX blades on small bore furnaces[1] which are subsequently heat treated and therefore susceptible to RX. During flexural testing Hi-shell and Std SX. specimens in the fired condition exhibited significantly different strengths of 21.5 MPa and 13.6 MPa respectively, during high-temperature testing the difference was further

---

[1] Several single crystal parts are also cast using the Std SX system on large chill furnaces

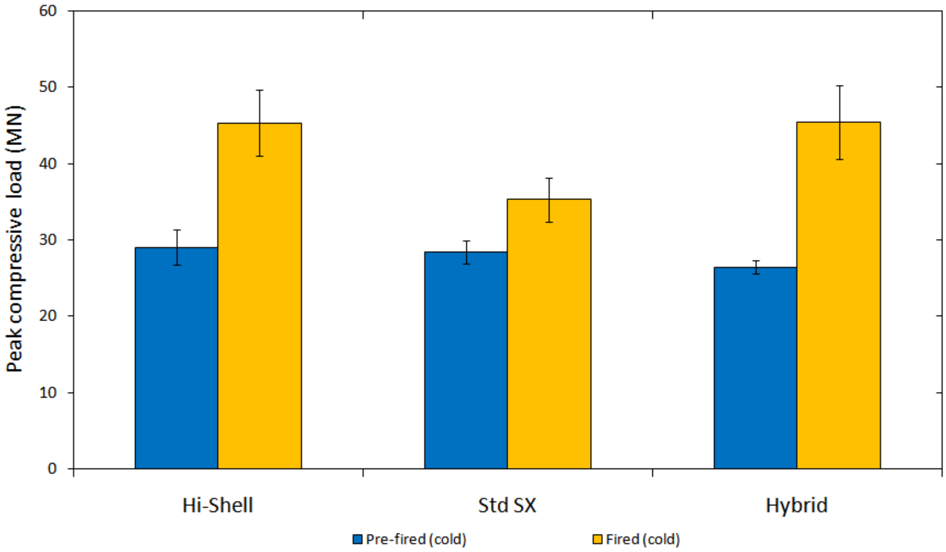

FIGURE 2.6: Data showing peak-loads measured during compressive testing of pre-fired and fired shell specimens; all tests performed at room temperature.

increased with recorded strengths of 7.6 MPa and 0.3 MPa respectively. This trend was continued in observations of high-temperature creep behaviour, the results of which are discussed in section 2.3.2.

Unfortunately due to the limitations of the testing equipment it was not possible to measure the compressive strength at high-temperature; fired strengths however were evaluated for all systems. The relative difference between the compressive strengths of the Std SX and Hi-shell specimens was not significant and lay within the spread of the data; the hybrid system however showed an increase of approximately 18 %. Once again comparison of the applied loads indicated that the load required to fracture Hi-shell samples was greater than for Std SX with the latter exhibiting a reduction of 22 %. As with pre-fired samples this was attributed to the increased shell thickness; it was, however, observed that the sample thickness‘ for Hybrid and Std. SX samples were similar indicating an increase in material strength of the former.

In order to further investigate the shell properties specimens were characterised using thermal expansion testing; the preparation and testing regime are discussed in Section 3.1. Thermal expansion measurements are summarised in Figure 2.7 and analysed in detail in Figures 2.8 to 2.10. Thermal expansion data were also

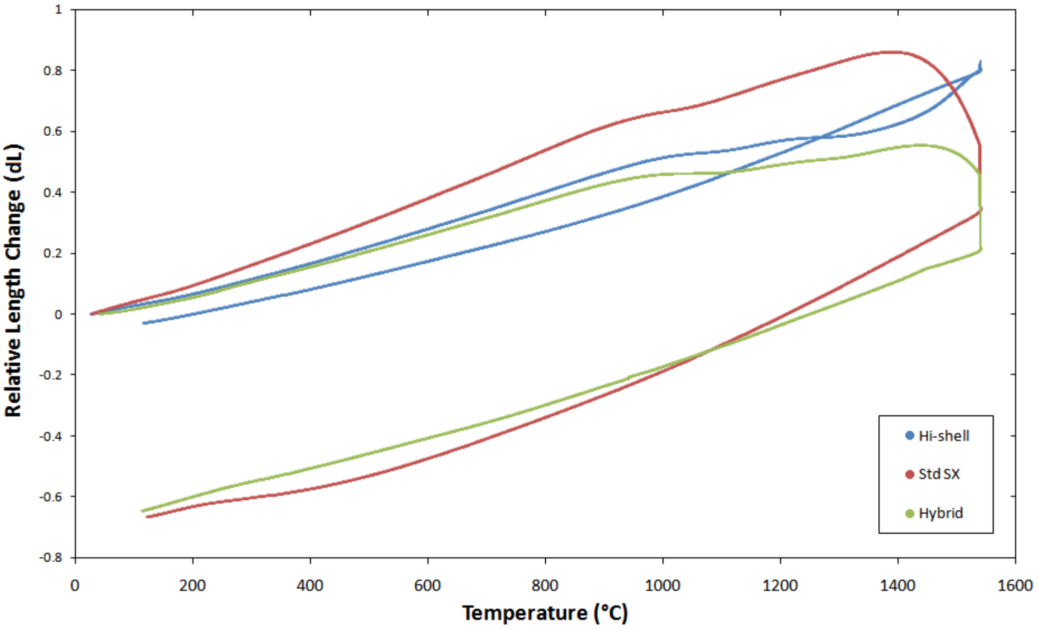

FIGURE 2.7: Data showing measured thermal expansion behaviour for PCF standard shells.

differentiated with respect to temperature in order to more clearly show sintering behaviour within the specimens. Throughout this thesis, thermal expansion measurements are presented in terms of relative length change, dL.

During sintering Std. SX and Hybrid systems exhibited similar behaviour due to both systems utilising the same zircon-based slurry matrix. However the difference in stucco between the systems (alumina for Std SX and mullite for the Hybrid) did lead to some differences in behaviour notably within the temperature ranges 900 - 1400 °C. It is well documented that the formation of mullite occurs within this temperature range in two stages, the first being the formation of pre-cursor mullite and the second being the conversion from the precursor material into stoichiometric mullite (mullite formation is discussed further in section 5.2). It was apparent from thermal expansion data that whilst both of the zircon-based systems exhibited similar behaviour during the first stage (between approximately 900 - 1200 °C) the alumina stuccoed Std SX material did not exhibit the second stage of mullite formation during the temperature range between approximately 1200 - 1400 °C. Both systems however experienced a large contraction at temperatures above 1400 °C; from inspection of the silica-alumina phase diagram (shown in Figure 2.27) it was apparent that this was due to the proximity of the melting temperature of silica at apprximately 1590 °C. This behaviour was consistent with observations

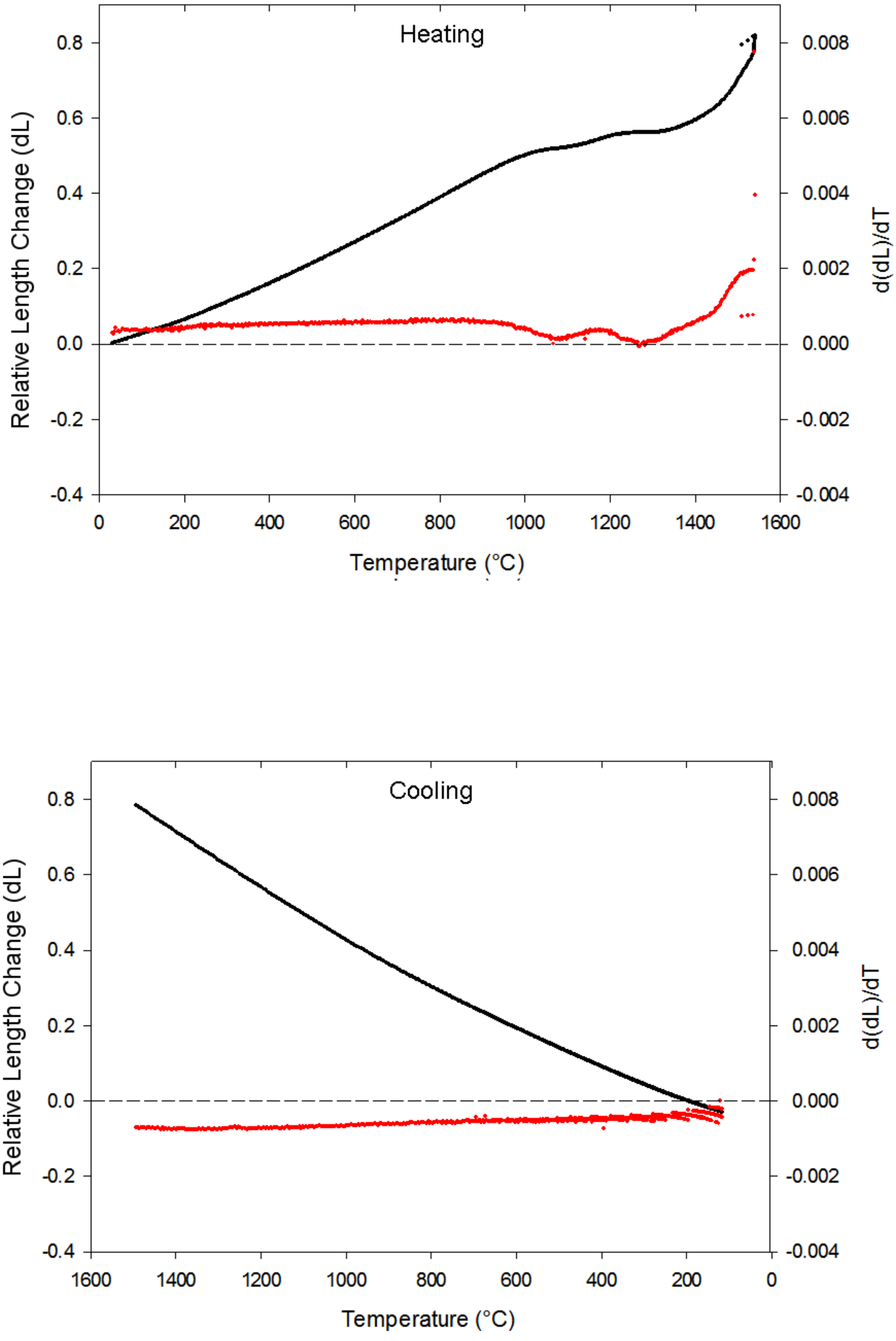

FIGURE 2.8: Thermal expansion data for Rolls-Royce Hi-shell system. Relative change in length is shown in black, rate of length change is shown in red.

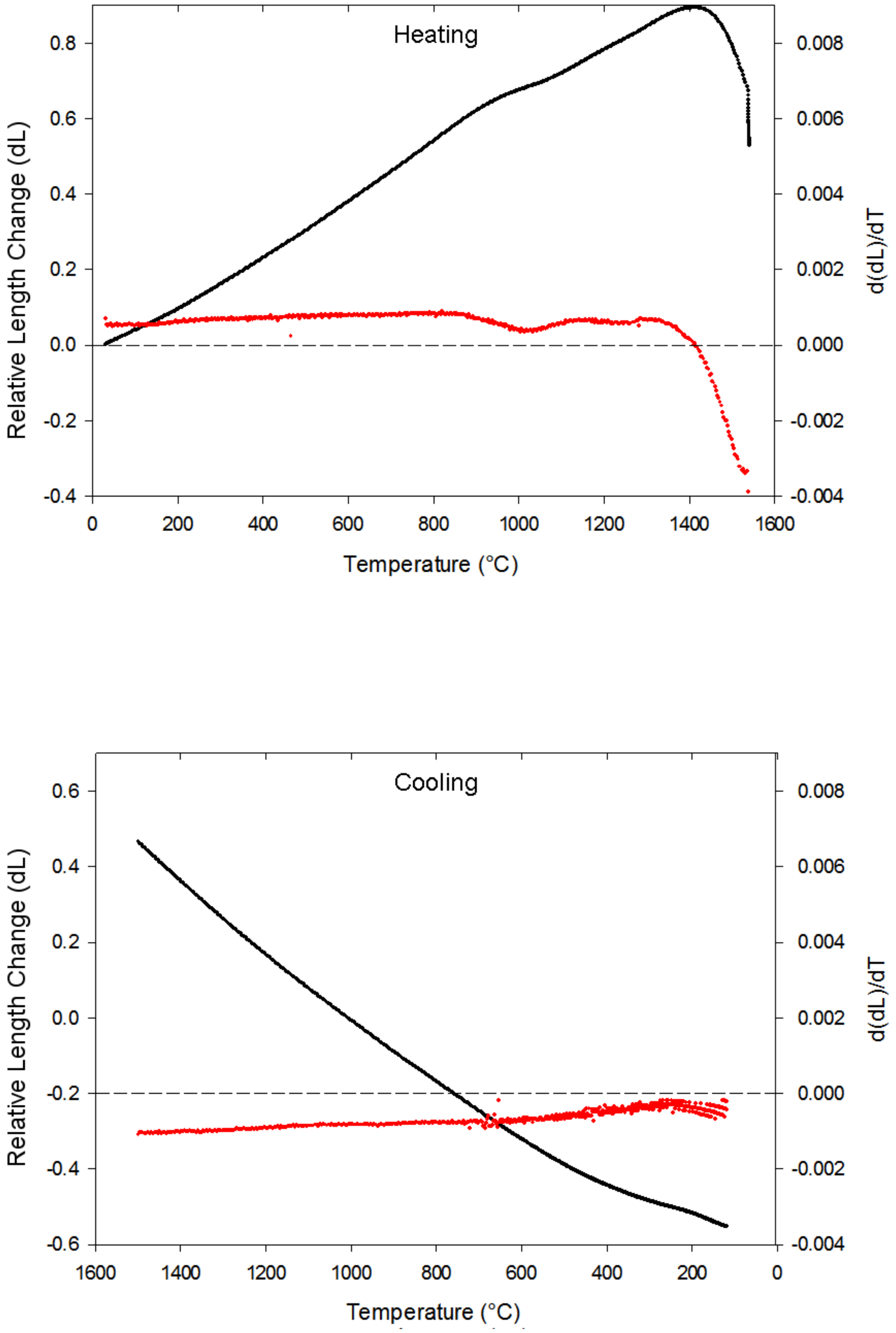

FIGURE 2.9: Thermal expansion data for Rolls-Royce Std SX system. Relative change in length is shown in black, rate of length change is shown in red.

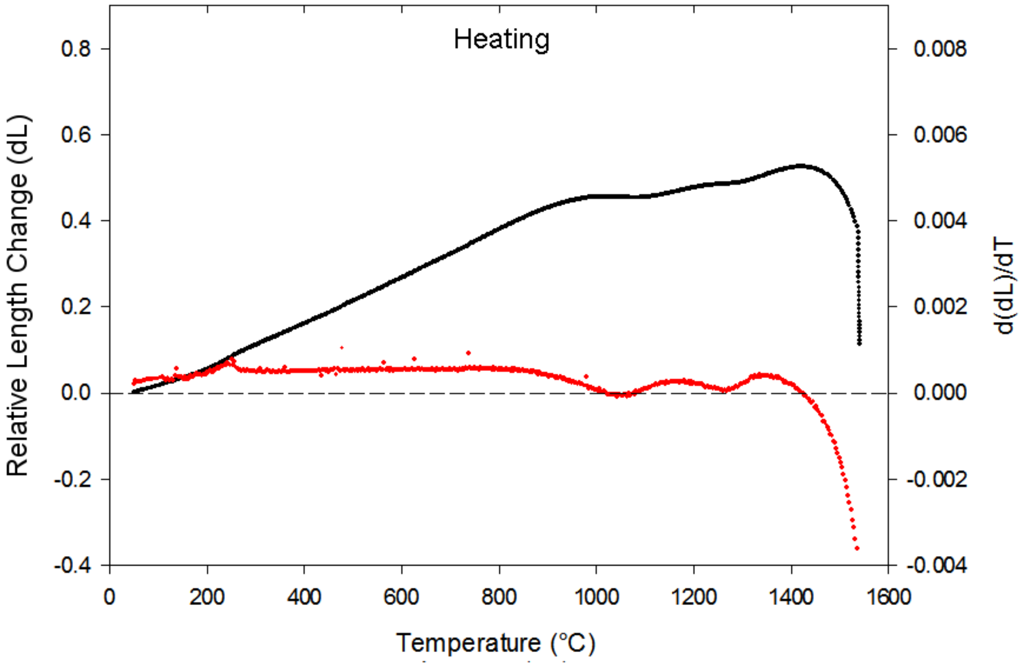

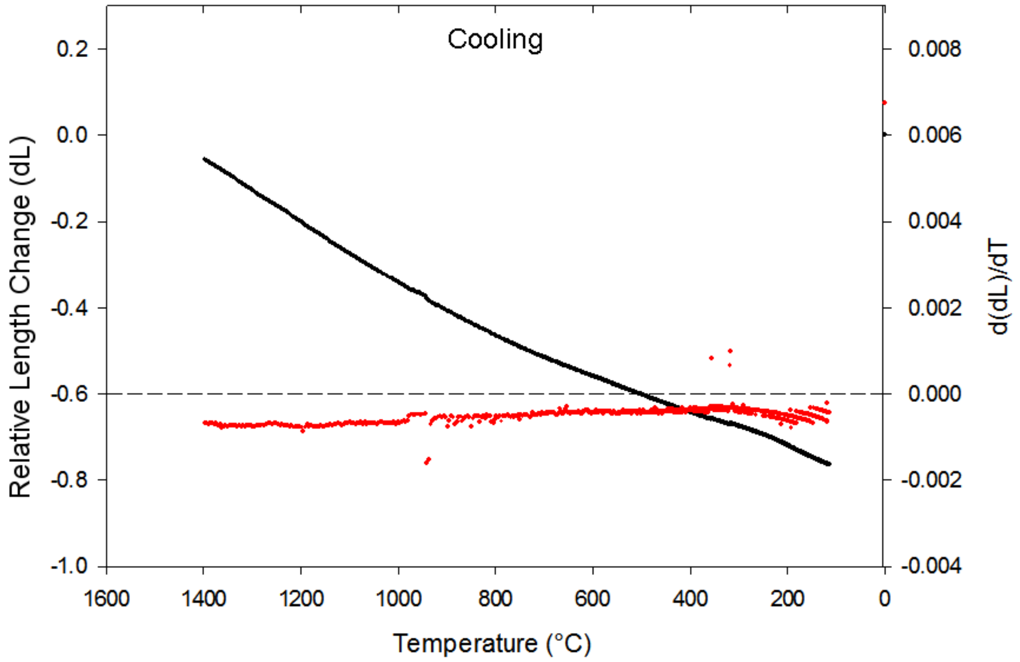

FIGURE 2.10: Thermal expansion data for Rolls-Royce Hybrid system. Relative change in length is shown in black, rate of length change is shown in red.

of high-temperature creep discussed in the following section. As expected due to the presence of fine alumina and silica the formation of mullite was observed to a greater extent in Hi-shell specimens; the reduced silica content remaining in the shell material as a result of mullite formation also led to greatly reduced contraction at high-temperatures. As for Std. SX and Hybrid materials, this behaviour was consistent with creep measurements reported below.

2.3.2 Creep deformation

It was mentioned in the preceding section that the Hi-shell system was developed for casting components with large charge weights.

From casting experience it is known that in order to maintain dimensional stability these moulds require greater high-temperature material-strength and resistance to creep in particular. Unlike the Std SX shell system which features a single grade zirconium silicate (zircon) filler material Hi-shell utilises a mixture of slurry components including reactive alumina, fused mullite and nylon fibres along with a colloidal silica binder. However, it is the inclusion of mullite and the in-situ mullitisation of silica and alumina during firing that gives Hi-shell its characteristic high-temperature strength and creep resistance. It is widely recognised in the literature that mullite exhibits good resistance to high temperature creep deformation [11] [12]. The reasons for this behaviour are reasoned to be partly due to the inter-meshing needle-like structure generated by mullite growth and also due to the high creep activation energy associated with the material [13]. This is evidenced in Table 2.4 which shows results taken from the 1972 paper by Penty illustrating the difference in creep deformation exhibited by samples manufactured in the same way using raw materials of comparable particle size. When tested at 1430℃ (15℃ hotter than the test temperature of alumina) the creep rate for mullite was 2 orders of magnitude lower than that of alumina.

Table 2.4: Measured elevated temperature creep values for alumina and mullite ceramics of similar particle size. Table adapted from [13]

Material	Temperature (℃)	Applied Stress (MPa)	Creep rate (s^{-1})
Alumina	1415	56.5	1.0 x 10^{-4}
Mullite	1430	56.5	3.2 x 10^{-6}

To provide further information on the capability of shell materials their creep rates were characterised at elevated temperature in three point bend as described in section 3.1.3. Table 2.5 shows the creep results for both Std SX and Hi-shell samples. It should be noted that when testing Std SX specimens their creep resistance was too low to enable the application of the 3.2 N load and the samples essentially crept under their own weight, in contrast the creep rate of the Hi-shell specimens was very low. The Hybrid shell material which consisted of the Std SX slurry stuccoed with the fused mullite stucco used in the Hi-shell material exhibited greatly reduced creep compared to the Std. SX but higher than the Hi-shell material. It is likely that the mullite stucco grains were better able to resist creep than were the alumina grains within the Std SX, the melting of the silica within the matrix however still induced a measurable increase in creep deformation.

Table 2.5: Measured elevated temperature creep values for Hi-shell and Std SX shell systems at 1540℃. Testing performed in 3-point bend using constant applied load of 3.2 N for 300 seconds.

Shell System	Temperature (℃)	Applied Load (N)	Creep rate (s^{-1})
Hi-Shell	1540	3.2	2.0 x 10^{-7}
Std SX	1540	N/A	1.9 x 10^{-4}
Hybrid	1540	3.2	1.8 x 10^{-6}

Creep testing is able to provide information on shell performance at casting temperatures however another useful metric is avaiable in the form of observation of the contraction of castings. Every casting is subjected to measurement by a Co-ordinate Measuring Machine (CMM) to assess its dimensional accuracy. For turbine blades a CMM is used primarily to determine the aerofoil shape and the overall length of the aerofoil section known as the annulus length. In shrouded blades the shell material between the root and tip of the blade is constrained, therefore as the blade cools it will subject the shell material to compressive forces (as mentioned in 2.2.3) whilst these can induce RX they can also give an empirical measurement of shell creep and sintering within the process. During a Rolls-Royce casting trial a number of BR725 high-pressure (HP) turbine blades were cast using three shell variants primarily to assess the occurrence of RX, however as part of the exercise the blades were subjected to a CMM process. Figure 2.11 shows the increased annulus contraction of both Std SX and the Hybrid shell material as compared to blades cast using Hi-shell.

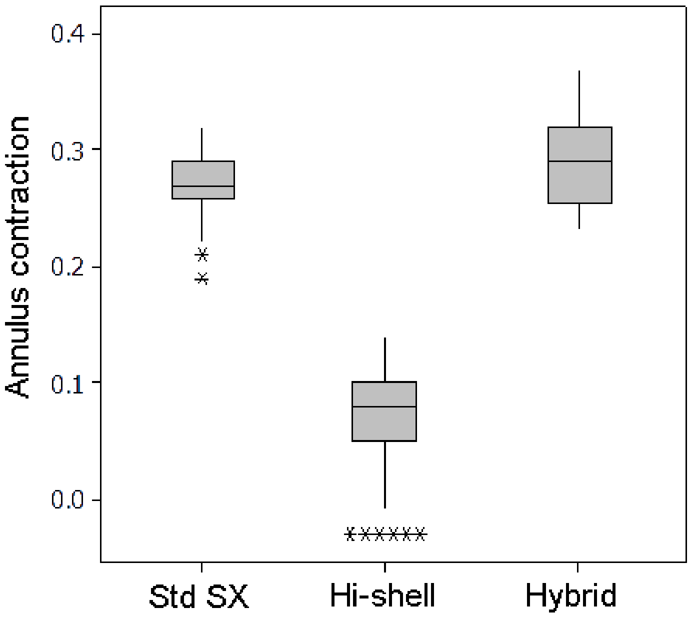

FIGURE 2.11: Dimensional data for annulus length of BR725 high-pressure turbine blade measured using CMM. Annulus contraction is measured relative to baseline data for blades cast using Hi-shell; a more positive result indicates greater annulus contraction with respect to Hi-shell.

Although both the Hi-shell and Hybrid shell materials exhibited reduced creep compared to that of the Std. SX material the overall contraction during thermal expansion was similar for both Std. SX and the Hybrid giving values of 0.6 %. It appears that annular contraction is more closely linked to thermal expansion measurements than to flexural creep testing. This is unsurprising as the compressive force during both thermal expansion and annular contraction is parallel to the laminar shell structure whereas during creep testing the load application is perpendicular.

2.3.3 RX performance of current shell systems

In order to formulate a new shell system capable of reducing the propensity to induce RX it was necessary to understand the RX behaviour of the current shell systems. In general the Std SX and Hi-shell systems are cast using different furnace types for manufacturing different components. However, in order to directly compare performance, trials were conducted using both the high-pressure turbine blades (HP1 & HP2) from the BR725 engine. As mentioned previously these blades are generally cast using Hi-shell but for the purposes of the trial a number of moulds of each were also cast using the Std SX shell on using large-chill furnaces. Figure 2.13 shows the scrap rates observed during the HP1 trial. Data presented for Hi-shell is recorded from a standard production run of 342 blades; Std SX data is taken from trial production run of 72 blades. Inspection of the data revealed that casting using the Std. SX material caused 16.2 % and 1.8 % reductions in RX and P-pin RX respectively compared to Hi-Shell and an increase in the observation of scrap due to High Angle Boundaries (HAB). The origins of HABs within SX components are not thoroughly understood, however it is believed that their occurrence is linked to the thermal conductivity of the shell material during the solidification of the alloy. If during solidification a stray grain forms within the alloy, the difference in angle between the orientation of the stray grain to that of the parent grain determines whether or not the defect is classified as a Low Angle Boundary (LAB) or as a HAB. The distinction between LABs and HABs is largely arbitrary and based on empirical evidence. Figure 2.12 shows the function of platinum pins (P-pins) within the shell. P-pin RX occurs at sites where platinum pins holding the ceramic core in position pass through the wax pattern and into the shell material, stress concentration at these sites leads to secondary grain growth; it is generally observed that stronger shell systems exhibit greater propensity to induce P-pin RX.

The apparent increase in HABs using Std. SX is likely to be an artefact of the scrap allocation procedure rather than a material related one. As components pass through the inspection process any non-conforming parts are scrapped, after this they do not undergo additional inspection operations; this is known as single-sentencing scrap. Inspection for HABs does not occur until after RX is detected at Grain Size Analysis (GSA) therefore any blades which fail for RX may also exhibit HABs. The reduction in RX for BR725 blades cast using Std SX led to more blades being inspected for HABs and hence more failures were detected. It is likely that if blades made in Hi-shell had been subjected to additional inspection operations after having been scrapped due to RX additional failure modes would have been detected [14].

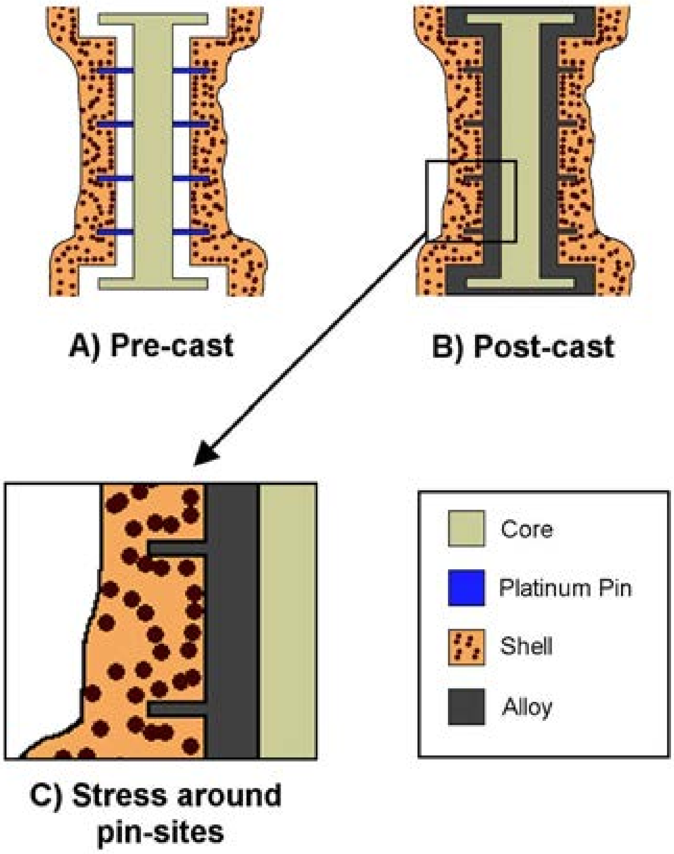

FIGURE 2.12: Schematic diagram showing the function of P-pin within the mould. Initially wax is injected around the core, platinum pins are then inserted through the wax such that they are in contact with the core.As the mould is dipped shell material builds up around them; following de-wax the P-pins provide support to the core during firing and casting.

2.3.4 Discussion of current shell systems

The overall understanding of the mechanisms which cause RX is incomplete however using a mixture of casting observations and shell properties, both thermal and mechanical, it is possible to form some conclusions about the shell properties related to the formation of RX. From the limited data available directly comparing the two shell systems, Hi-shell and Std SX, using the same parts and furnaces it is clear that the Std SX shell system produces lower levels of RX compared to Hi-shell. The difficulty in accurately quantifying this result comes from the fact that no single parameter characterises the RX performance of a given shell material. Linking the RX performance to the flexural strength data in Figure 2.4 suggests that a reduction in both fired and hot strengths causes a corresponding

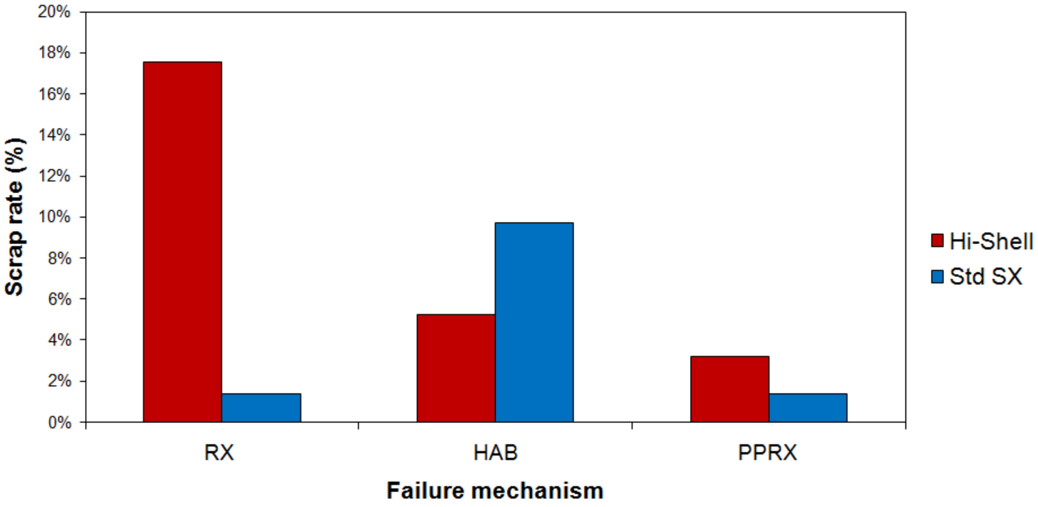

FIGURE 2.13: Scrap data for BR725 HP1 turbine blade cast on both Hi-shell and Std SX shell systems on large chill furnaces. Note the reduction in RX between shell systems. Increased incidence of high-angle-boundaries for Std SX is likely revealed by reduced scrap rate rather than an actual increase.

decrease in RX. Compressive shell strength data presented in Figure 2.5 shows a greater correlation between RX and peak load required to cause failure than peak stress; this suggests that in terms of material strength Std SX and Hi-shell are similar but due to differences in shell thickness, likely due to the fibre content within Hi-shell, the latter requires greater load to induce failure. This suggests that the compressive strength of the mould itself rather than the mould material is more closely related to the occurrence of RX. Along with measuring hot strength the shell materials were characterised in terms of thermal expansion and creep resistance, examination of Figure 2.7 shows that the overall contraction of the Std SX shell is much greater than that of Hi-shell, this is in agreement with the hot creep behaviour. These two observations suggest that a shell material which is more compliant in both axial compression and in tension should lead to better RX performance.

Casting observations made during trials at the PCF are shown in Tables 2.6 and 2.7 for BR725 HP1 and HP2 blades respectively. The occurrence of RX appears to be dependant on both the shell material used and also on the geometry of the components being cast. The longer annulus HP2 blade being more susceptible to RX than the shorter HP1 blade. It was also observed that the Hybrid shell material induced greater RX in the blades than did the Hi-shell material, although the mechanism responsible for this is not understood. The information presented

Table 2.6: Recrystallisation data for BR725 HP1 blades manufactured using Rolls-Royce Std SX, Hybrid and Hi-Shell mould materials. Hi-shell incidence is taken from observed background level at the PCF.

Shell material	RX occurence	No. Of blades
Std SX	0 %	0/54
Hybrid	0 %	0/54
Hi-Shell	10 %	background

Table 2.7: Recrystallisation data for BR725 HP2 blades manufactured using Rolls-Royce Std SX, Hybrid and Hi-Shell mould materials. Hi-shell incidence is taken from observed background level at the PCF.

Shell material	RX occurence	No. Of blades
Std SX	0 %	0/36
Hybrid	33 %	12/36
Hi-Shell	15 %	background

in this section forms the foundation and baseline on which the Next Generation shells will be built upon and measured against.

2.4 Thermal disruption

In order to develop ceramic shell materials which exhibit reduced strength compared to the standard Rolls-Royce shell materials a number of methods were employed; one of which was the inclusion of thermally disruptive materials within the shell. The term thermally disruptive in this context is defined as a material exhibiting unconventional thermal expansion behaviour during thermal cycling relevant to the casting cycle. Two materials exhibiting such behaviour are zirconium oxide and aluminium titanate. In its pure form (also referred to as unstabilised[2]) zirconium oxide or zirconia, exhibits a transformation of the crystal structure from monoclinic to tetragonal during firing, the structures of each polymorph are shown in Figure 2.14. Associated with the transition is a volumetric change, it was hoped that this change would induce sufficient damage within the shell material to reduce its strength; the transformation process discussed in detail in section 2.4.1. The

---

[2] The term unstabilised in this context refers to stability against changes in crystal structure and is achieved through doping the ceramic with other oxides such as yttria, magnesia and calcia.

thermal disruption associated with aluminium titanate, or tialite, is associated with the anisotropy of its thermal expansion, with different axes exhibiting significantly different behaviour, relative to other materials within the shell. The nature of the thermal disruption of these materials are discussed further in the following sections along with their usage in both the scientific literature and commercially within patent literature.

Since this thesis was conducted in conjunction with Rolls-Royce it is necessary to discuss the restrictions imposed by the industrial shell manufacturing process. The shell process itself is relatively flexible with it being possible to employ different slurry and stucco materials within each layer of the shell, however the logistics of doing this on an industrial scale must be considered. In production shell rooms moulds are dipped robotically to ensure accurate and repeatable coating for each layer. The number of materials which can be applied to a shell is limited by the number of slurry tanks and stucco towers present within the shell cell. Although this did not limit the scope of systems to be evaluated within the laboratory it had to be considered for industrially relevant systems. The interaction between different materials must also be taken into account when formulating new materials particularly those being introduced into Rolls-Royce factories.

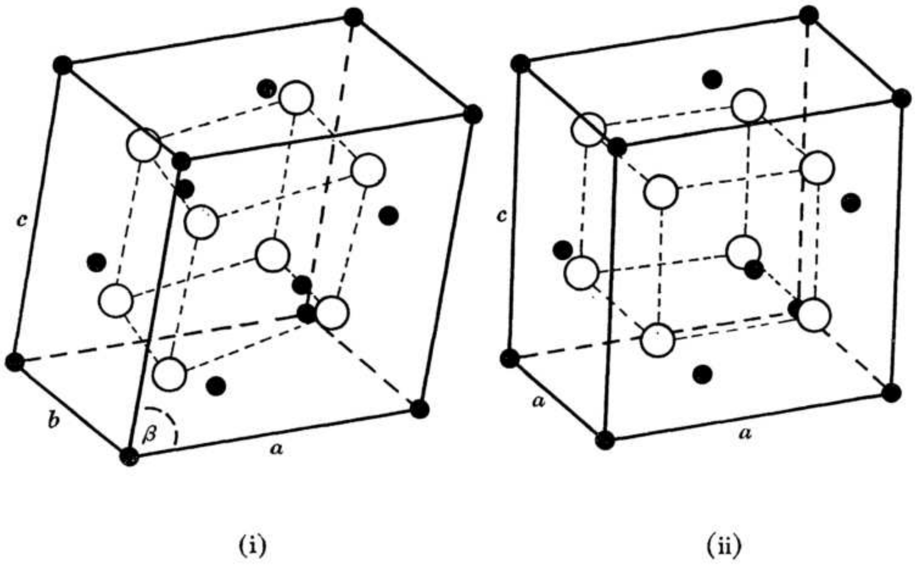

Figure 2.14: Schematic diagram illustrating the crystal structures of (i) Monoclinic and (ii) Tetragonal zirconia. Black and white circles represent zirconium and oxygen atoms respectively. Figure reproduced from Bailey [15].

2.4.1 Zirconia

Zirconia is a refractory metal oxide with three well-defined crystal structures, which occur depending on the temperature (and pressure) of the material, namely monoclinic, tetragonal and cubic. The existence of a fourth high-pressure orthorhombic form has also been reported but like the cubic structure its presence requires relatively extreme atmospheric conditions uncommon in the investment casting process and hence will not be discussed further [16]. The two phases occurring in the temperature range relevant to the investment casting process are the monoclinic and the tetragonal phase. At temperatures up to approximately 1170 °C pure zirconia exhibits a monoclinic crystal structure, above this temperature the structure undergoes transition to a tetragonal structure. The nature of the crystalline structures is such that the the unit cell in the monoclinic form has a larger volume than that of the tetragonal form, therefore upon transformation the cell experiences a reduction in volume of between 3-5 % [17]; the different crystal structures are illustrated in Figure 2.14.

The consideration of monoclinic zirconia as a potentially useful shell material is primarily based on its ability to induce disruption within the shell structure during thermal cycling; in this case the disruption is the result of a change in crystalline structure from monoclinic to tetragonal. It is generally accepted in the literature that the transition from monoclinic to tetragonal is not commutative with that from tetragonal to monoclinic in terms of either temperature or mechanism. In the interest of clarity the transitions from monoclinic to tetragonal and tetragonal to monoclinic will be referred to hereafter as the *forward* and *reverse* transitions respectively. Table 2.8 summarises the transition temperatures for both forward and reverse transitions as reported in the literature. Immediately obvious from inspection of the data is that the transformation occurs in both forward and reverse processes across a temperature range, also clear is that the temperature range for the transition depends on its direction. In order to explain this it is necessary to consider the processes occurring within the material during transformation. Through the use of high temperature X-ray diffraction (XRD) Patil *et al.* [18] were reportedly able to directly observe changes in crystal structure of monoclinic zirconia during thermal cycling.

As the material entered the transformation temperature range they observed the

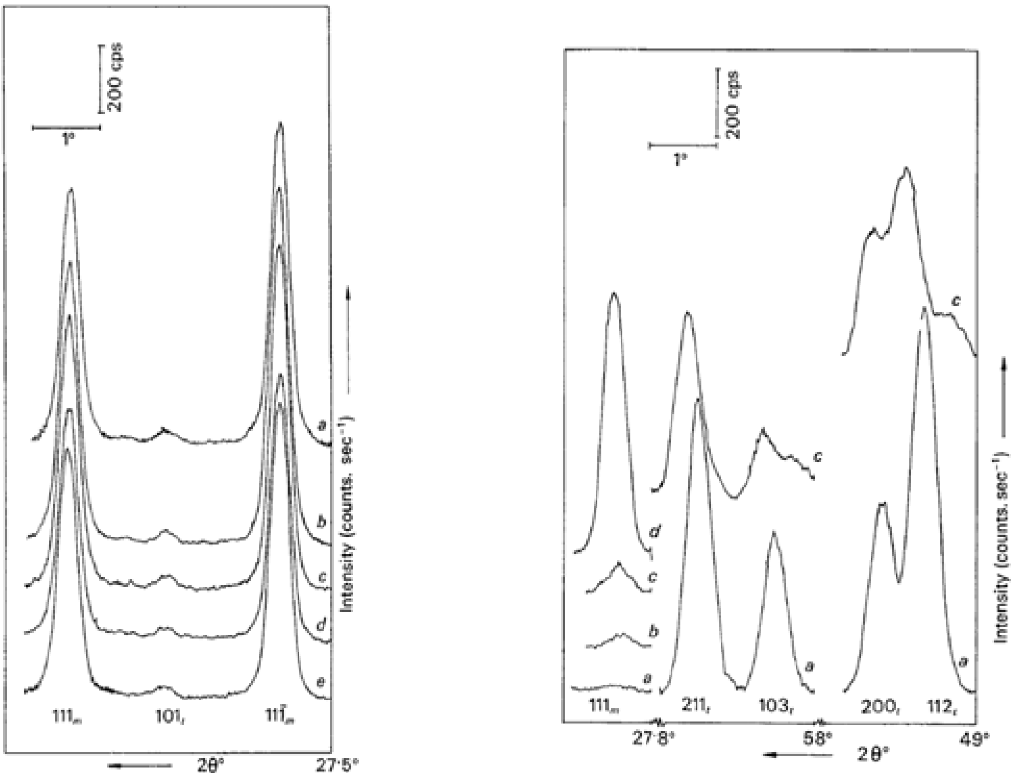

Figure 2.15: XRD spectra for zirconia showing the evolution of crystal planes within the material during the monoclinic to tetragonal phase transformation. Labels a to e correspond to spectra measured at decreasing temperature levels. Left is shown the emergence of the 101_t plane, right shows the rapid onset of the reverse transformation. Adapted from [18].

diffraction pattern begin to diverge from that exhibited at low temperature, specifically lines characteristic of the tetragonal phase begin to appear in the diffraction pattern. The first signal is the appearance of the 101_t plane[3] accompanied by a decrease in the intensity of 111_m and $11\bar{1}_m$ planes. During the transition this process occurs for all monoclinic planes as they are supplanted by their tetragonal counterparts. The 111_m and $11\bar{1}_m$ are mentioned specifically as they are the most persistent planes and their disappearance marks the end of the transition [18]; the evolution of the XRD spectrum is shown in Figure 2.15. The majority of sources report the onset of the reverse process at temperatures around 1000 - 1050 °C however some discrepancy was observed; the large range in transition temperatures presented in Table 2.8 can be explained by the persistence of the 101_t plane to as low temperatures as low as 680°C, [25].

---

[3] Subscripts m and t are used to denote planes from monoclinic and tetragonal crystals respectively.

Table 2.8: Survey of experimental results to determine monoclinic - tetragonal phase transformation temperature in both forward and reverse directions. Notice the considerable difference in temperature range for the different directions. Table adapted from [19]

Paper	Source	Transition Temperature (℃) forward	reverse	Technique
Patil (1970)	[18]	930 - 1220	1030 - 700	X-ray
Dietzel	[20]	950 - 1250	1250 - 740	X-ray
Curtis	[21]	1100 - 1250	N/A	DTA
Mumpton	[22]	1170 - 1240	1030 - 940	DTA
		1175 - 1220	1035 - 700	X-ray
Hinz	[23]	1150 - 1200	1000 - 700	X-ray
Baun	[24]	1000 - 1200	970 - 750	X-ray
Wolten	[25]	960 - 1120	920 - 680	X-ray
Fehrenbacher	[26]	1130 - 1200	1025 - 950	metallography
Vest	[27]	1170	1000	electrical resistance
Glushkova	[28]	1150 - 1250	1000	X-ray
Ruh	[29]	1050 - 1187	1050 - 880	X-ray
		1160 - 1215	1038 - 993	DTA
Patil (1969)	[30]	1100 - 1220	1030 - 700	X-ray
Maiti	[31]	1125 - 1190	870 - 790	DTA

The difference in transition temperatures and also the way in which the XRD spectra evolve with respect to temperature indicate a different mechanism is responsible for each process. It was proposed by Patil *et al.* that the forward transition is caused by local thermal excitation of the zirconium atoms within the structure in a process similar to nucleation. This process is observed to occur over a broad temperature range. The reverse transformation was proposed to be due to the instability of the tetragonal state as a whole; once the transition temperature is reached the whole of the state reverts back to the monoclinic form. A more complete treatment is given in [18].

Whilst the transformation process is in itself scientifically interesting, it is the accompanying volumetric changes which are relevant to its application as a mould material. As the crystal structure of zirconia changes so too does the volume it occupies; this is reported in a number of sources including the book by Stevens [17] and papers by Bailey [15] and Park *et al.* [32]. Stevens describes the volumetric contraction accompanying the forward process as exhibiting a 3-5 % reduction, with a corresponding expansion during the reverse process. Bailey describes the practical applications of unstabilised zirconia as being severely restricted by the phase transformation due to the often catastrophic cracking induced within samples during cycling through the transition temperature. The destructive effects of the transition were subsequently investigated in the paper by directly examining changes in the crystal structure of zirconia during heating in a Scanning Electron Microscope (SEM). In this experiment zirconium foils were oxidised at 800℃ to produce monoclinic zirconia using a furnace stage, further heating to induce the transition was performed directly using the electron beam. Inspection of the heat-treated material revealed twinning (a process by which two grains form along a common axis) within the crystal structure which had been absent in the virgin material. It was proposed that the twinning was evidence of a stress-relief mechanism within the structure necessitated by the volumetric expansion experienced during cooling. Twinning was only observed in areas where the crystals were constrained by either the sample mounting or the presence of other crystals; unconstrained areas exhibited no twinning. Interestingly, examination of the crystals in the tetragonal phase did not feature twinning either suggesting greater ductility within the material than in the monoclinic phase. This observation was confirmed by Hart *et al.* in their study into the super-plasticity of pure zirconia material [33].

2.4.2 Disruptive effects of the zirconia transformation

The properties of the phase transformation have been discussed above with reference to the effect on the crystal structure. To determine their ability to strategically weaken shell moulds it is necessary to understand the manifestation of the transition on the macro-scale. The paper by Park *et al.* examines the behaviour of mullite - zirconia laminar composites for high-temperature applications. Composite laminates were manufactured from combinations of mullite and monoclinic zirconia and also from mullite combined with yttria-stabilised zirconia [32]. SEM micrographs presented in Figure 2.16 show the difference in microcracking induced by monoclinic and tetragonal zirconias.

Note the difference in the propagation paths of the microcracks within the different samples; the monoclinic-mullite laminates exhibited severe cracking following thermal cycling due to the large expansion during the reverse transformation. By contrast cracks in the tetragonal-mullite sample were contained entirely within

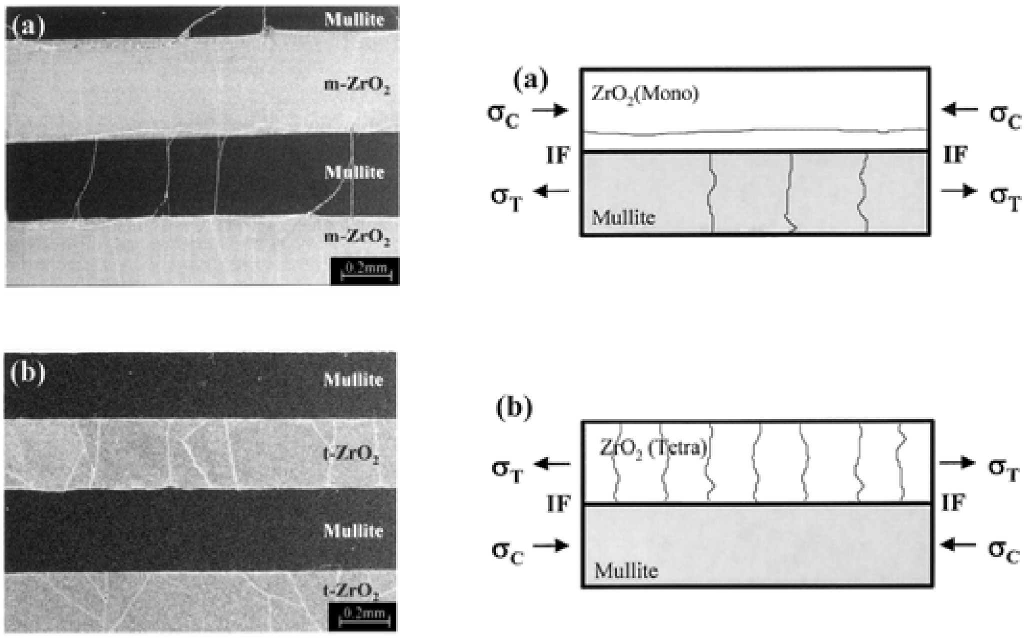

FIGURE 2.16: SEM micrographs of laminar composites of (a) mullite - monoclinic zirconia and (b) mullite - tetragonal zirconia. Note the propagation of microcracks into the mullite layer in the monoclinic composite. Figure reproduced from Park [32].

the zirconia layer itself and showed little propagation into the mullite layer. Figure 2.17 shows the condition of the laminates after 10 thermal cycles through the monoclinic-tetragonal transition temperature. It is clear that the phase transition in (a) is far more physically damaging than the effect of the differential thermal coefficients shown in (b). If the disruptive effect observed in these laminates can be reproduced in shell systems containing zirconia the weakening effect could contribute to the reduction of RX propensity.

2.4.3 Tialite

Tialite (also known as aluminium titanate) is a compound of titanium and aluminium and oxygen with the chemical formula Al_2TiO_5. It is a member of the psuedobrookite family of materials, most well known for exhibiting anisotropy in their thermal expansion coefficients [34]. Table 2.9 contains data regarding the thermal expansion coefficients of tialite and magnesium di-titanate along their relative axes [35].

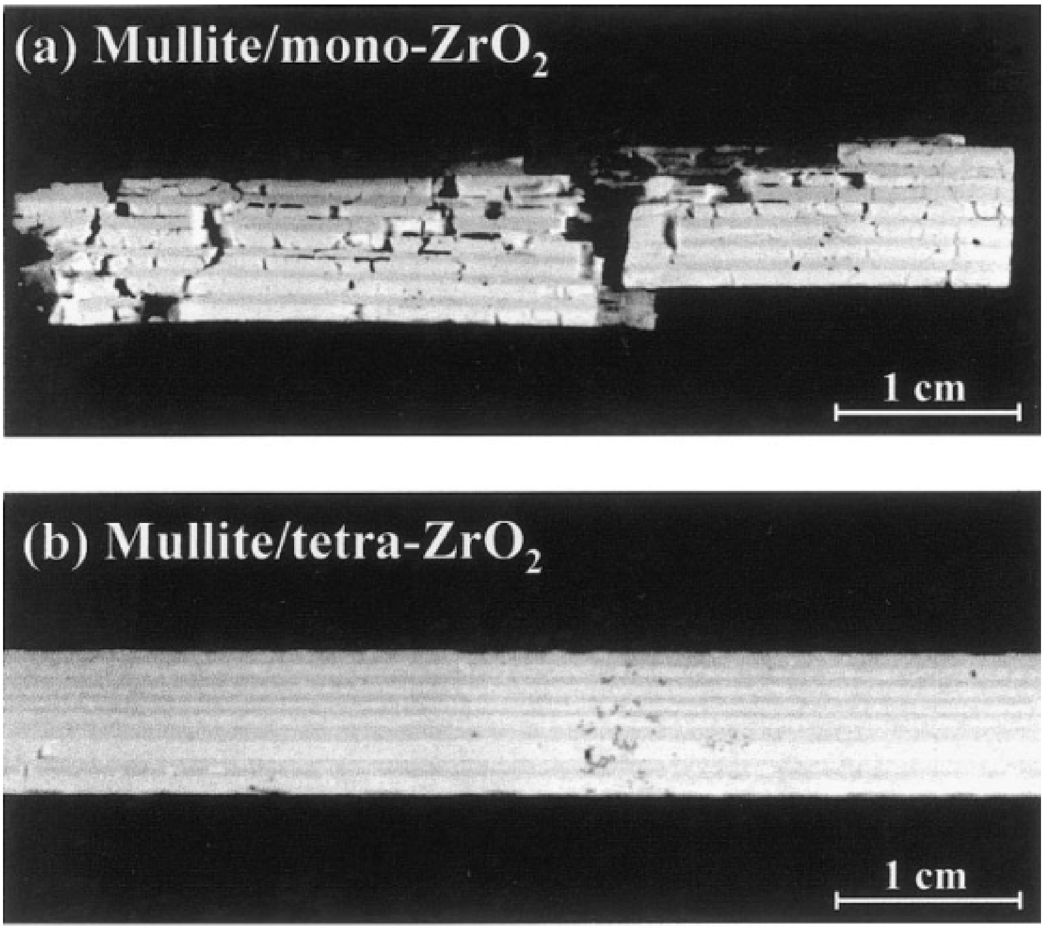

FIGURE 2.17: Photographs showing the condition of the both the (a) mullite - monoclinic zirconia and (b) mullite - tetragonal zirconia samples after 10 successive cycles through the transition temperature, note that the sample in (a) has failed completely. Figure reproduced from Park [32].

Unusually tialite exhibits a thermal contraction along one axis whilst simultaneously undergoing expansion in the other two, because of this tialite ceramics exhibit a critical grain size of 1-2 μm above which grain boundary microcracking occurs [34]. It was also observed that the grain size necessary to induce sufficient microcracking within a ceramic body to compromise its mechanical integrity the grain size must be 3-4 μm or greater. In general, tialite ceramics are of limited usefulness due to the above behaviour, however another issue to be considered is the possible dissociation of tialite into alumina and titania. At temperatures exceeding 1553℃ it is possible to form tialite via the forward mode of reaction 2.1, however below this temperature the reaction proceeds in the opposite direction. It is well known that in the temperature range 750 - 1280 ℃ the material is able to thermally decompose into its constituent oxides [39], however the results

Table 2.9: Thermal expansion coefficients of Tialite and Magnesium dititanate compared to more conventional materials exhibiting isotropic thermal expansions coefficients; Alumina, Mullite and Zircon.

Material	Thermal expansion coefficient (K^{1})			Temperature (°C)	Source
	a-axis	b-axis	c-axis		
Al_2TiO_5	$9.8x10^{-6}$	$20.8x10^{-6}$	$-1.4x10^{-6}$	1000	[35]
$MgTi_2O_5$	$8.1x10^{-6}$	$13.2x10^{-6}$	$2.3x10^{-6}$	1000	[35]
Al_2O_3	$9.6x10^{-6}$ (average)			1000	[36]
$3Al_2O_2.2SiO_2$	$4.9x10^{-6}$ (average)			1427	[37]
ZrO_2	$5.3x10^{-6}$ (average)			1000	[38]

of unpublished work at the University of Birmingham suggest that this may not be the case. In this work, ceramic shell materials were manufactured using a pan agglomerated titanita and alumina stucco, after firing to approximately 1400 °C samples were analysed using X-ray diffraction. The results showed that residual tialite was present within the ceramics [40]. Inclusion of other titanates including iron and magnesium can reduce the instance of both thermal decomposition and also microcracking; for the purposes of weakening shell materials reducing the instance of the latter is clearly undesirable.

$$Al_2O_3 + TiO_2 \rightarrow Al_2TiO_5 \tag{2.1}$$

Due to the potential destructive effects the inclusion of tialite within the shell as a weakening agent should be considered, however due to the temperatures involved in the casting process dissociation may reduce or remove the microcracking effect.

2.4.4 Patent analysis

Much of the work reported in this thesis is of a commercial nature and as such it is important that any processes developed can be used to produce saleable castings. In order to ensure that the candidate shell formulations were not in infringement of any existing patents and also to further determine the technologies in use within the industry a thorough patent search was conducted. There are few references to the use of materials exhibiting volumetric transformations within the investment casting industry the only instance being the 2000 patent by Springgate *et al.* [41]. The relevant claim in this patent refers to the use of a shell containing a material within the backup layers which is capable of undergoing a volumetric transformation during cool down. Elsewhere in the patent specific reference is made to the use of zirconia within the shell although clarification of its degree of stabilisation is omitted. This claim essentially precludes the use of zirconia for its intended use as a strength reduction agent within shell materials. However in order for a patent to be enforceable there must be no prior art available. In 1982 a paper was presented by Snow *et al.* at the European Investment Casting Federation conference referring to the use of fused silica as a high temperature shell material [42]. Within the paper the well-known phase transformation exhibited by one of the crystalline forms of silica, cristobalite, was referred to. It was proposed that at the transformation temperature of 220℃ the material undergoes a large volumetric transformation on cooling which causes shell removal to become much easier. The statement in the 1982 paper refers explicitly to the use of a material exhibiting a temperature induced volumetric phase transformation which is *exactly* what the patent by Springgate *et al.* is claiming as novel some 18 years later. Based on this information, systems using volumetric transformations to weaken shell materials are deemed as commercially viable by Rolls-Royce plc.

2.5 Fugitive materials

Porous ceramic materials are used in a number of applications including gas/liquid separators, molecular sieves, catalyst substrates and refractory materials [43], [44]. One technique used to fabricate porous ceramic materials is the inclusion of fugitive pore-forming agents (PFAs). The term fugitive refers the fact that they are present in the green ceramic but ‘flee’ as they burn out during firing. The size and shape of the pores generated by this process are dependent on the particle size and shape of the pore forming agent (PFA) included in the formulation. When selecting a suitable PFA there are a number of considerations including

- Burnout products
- Morphology
- Interaction with other materials

- Material cost
- Material availability

Porosity within ceramic components can affect the amount of deformation exhibited under the application of a compressive stress before fracture. As an axial compression is applied pores within the structure cause the load to be entirely supported by the interconnecting matrix. When the stress on the matrix becomes sufficiently large it will fracture and the pores will close up, in some cases this relieves the applied stress without causing the component to fail completely. In the case of investment casting shells it is proposed that this consolidation will accommodate some of the differential thermal expansion between the alloy and shell and therefore reduce the propensity to induce RX in areas of constrained shell material during cooling. It should be noted however that the Hi-shell system contains nylon fibres as a slurry constituent which are known to burn-out during the firing cycle and the occurrence of RX within the system is high. Failure modes due to the presence of pores are further discussed in section 6.3.

Materials suitable for use as PFAs can be classified in two groups, those which occur naturally such as starches and seeds and those which are produced synthetically such as polymers and resins [45]. Naturally occurring fugitives such as starches benefit from having simple and relatively clean pyrolysis products such that they neither deposit damaging residues onto equipment nor do they necessitate sophisticated, afterburner-type extraction systems [46] [47]. Since they are grown naturally starch and seed products are relatively cheap and security of supply is good with materials available from multiple sources. There are a number of downsides to the use of starch in particular for making ceramics, especially in the field of investment casting. The ceramic slurries used in investment casting are water based and can expect to have lifetimes of in excess of six months in some cases giving rise to the problem of starch swelling. In the work by Gregorova *et al.* linear swelling by a factor of 2 was exhibited by corn and wheat starches and swelling by a factor of 4 was observed in potato starch [48]. Unstable particle geometry could potentially lead to undesirable changes in rheology.

Another concern with the inclusion of polymeric materials, especially those which are organic in nature is the risk of bacterial growth within the slurry. This is a particular problem in terms of slurry-life as it can cause the pH and conductivity of the slurry to change and potentially destabilise the entire system; it is also difficult to correct often requiring the slurry to be completely discarded [49]. In order to avoid the above issues such materials are excluded from consideration and will not be discussed further.

Table 2.10: Pyrolysis temperatures and products for various fugitive materials pyrolysed in air.

	Pyrolisation	
Material	Temperature (℃)	Products
PE (Polyethylene)	600	Carbon dioxide Carbon Monoxide Water Aldehydes
PMMA (Polymethylmethacyrlate)	460	Hydrogen Carbon Dioxide Carbon Monoxide Ethene Methane
PVC (Polyvinyl chloride)	200	Hydrochloric Acid Aliphatic hydrocarbons Aromatic hydrocarbons
PVA (Polyvinyl acetate)	120	Water Acetic acid
PEG (Polyethylene glycol)	240	Short chain oligomers
PTFE (Polytetrafluoroethylene)	350	Carbonyl fluoride, Carbon tetrafluoride Hexafluoroethane Silicon tetrafluoride

As fugitive materials are fired they thermally decompose giving off so-called pyrolysis products; the products generated depend on the composition of the material. Examination of Table 2.10 reveals that the products generated from the burnout of synthetic materials are much more complex than just carbon dioxide and water expected from seeds and starches. The burn out products from polymethylmethacrylate (PMMA) [50], polyvinyl acetate (PVA) [51] polyethylene glycol (PEG) [51] and polyethylene (PE) [52] are all relatively clean and harmless, however polyvinyl chloride (PVC) [53] [54] and polytetrafluoroethylene (PTFE) release various harmful compounds. The aromatic hydrocarbons released by PVC create sooty black particulate deposits and the carbonyl fluoride generated by

PTFE is highly toxic [55]. These factors must be taken into account when developing new shell systems since deposits within furnaces are undesirable and could pose health and safety risks.

2.5.1 Patent Analysis

As is often the case with the investment casting industry the majority of research and development is not reported in the scientific literature or even within patent databases with proprietors preferring instead to rely on secrecy for protection of their intellectual property. An extensive patent search revealed three patents which were most relevant to the subject of shell systems featuring fugitive components. The first and most directly related to the preceding discussion is the 1994 Patent by Aimone *et al.* relating to the use of a compliant shell mould for the investment casting process [56]. The patent describes the use of a number of fugitive elements including graphite, ceramic beads and plastic or other vaporisable beads; the claim here would seem to encompass the use of any polymeric particulate material within an investment casting shell system. The nylon-fibres contained within the Hi-shell system are part of a commercially available binder system and must therefore be licensed for use. In terms of the application the document refers specifically to the use of these materials in order to generate a more crushable and compliant shell system which could reduce the instance of defects associated with excessive residual shell strength including recrystallisation (RX) for single crystal (SX) castings and hot tearing for equiaxed castings. The fact that the claim does not relate to any specific vaporisable material makes it more susceptible to be challenged by prior art, although it should be mentioned that no such evidence was found during the survey.

Similar patents by Watts and Yang *et al.* describe the use of fugitive elements in another way. Shells are made using conventional techniques but rather than using solid stucco particles use either agglomerates of smaller particles [57] or bundles of ceramic fibres [58] bound together with a fugitive material. Upon firing the binder is pyrolysed leaving porosity and loosely bound structures within the shell. It is proposed that this technique can be used to aid shell removal and also to reduce shell strength. This methodology is unlikely to be employed as part of the thesis and these patents are only mentioned for completeness. Materials protected by patents could still be evaluated during trials but were unlikely to be commercially viable.

2.6 Conventional Shell materials

In order to accurately formulate a new shell material suitable for large chill casting it was necessary to understand the shell materials used by other casting foundries performing similar work; one of the main competitors to Rolls-Royce in this field at the time of writing was Howmet. US patent number 4966225 describes a shell material based on alternate layers of zirconium silicate and alumina which is widely used to cast large chill moulds [59]. Although this patent may have precluded the use of the system from industrial usage a system based on the information in the patent was evaluated to understand the benefits of such a material.

Table 2.11: Stucco utilised on various shell coats for Howmet and Laminar shell materials.

	Stucco material				
System	Layer 1	Layer 2	Layer 3	Layer 4	Layer 5
Howmet	A	Z	A	Z	A
Laminar	A	A	A	A	A

Figure 2.18 shows the comparison between flexural strengths for the standard Rolls-Royce shell materials and a laminar hybrid using alternate layers of zircon and alumina shell. Unlike the shell mentioned in the Howmet patent, the candidate shell material used CerTab 28/48 mesh tabular alumina stucco on each backup layer. The difference in shell composition is illustrated in Table 2.11. Due to the poor mechanical properties in the green and pre-fired condition, and the fact that such a material was potentially protected by patent, the system was not pursued further.

2.7 Colloidal Silica Binders

In the period between the early 1960's and the mid 1990's the most commonly used binders in UK foundries were of the ethyl-silicate type. However the advent of the

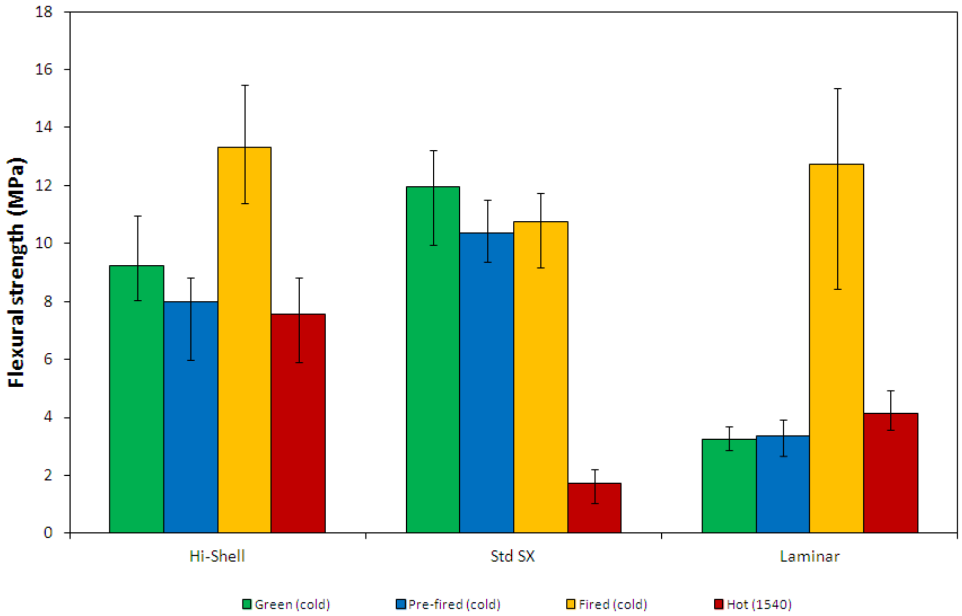

FIGURE 2.18: Flexural strength measurements for standard Rolls-Royce shell materials vs a laminar prototype shell material based on alternating layers of zircon and alumina.

Environmental Protection Act in 1990 and subsequent changes to UK regulations concerning the emissions of ammonia and other volatile compounds (on which such binders were dependant) would prohibit their use beyond April 1997[60]. In order to continue using the investment casting process a replacement binder was necessary, because of the need to provide silica within the shell the range of options was limited and the natural successor emerged in the form of silica sols otherwise referred to as colloidal silica.

Silica sols are dispersions of silica particles in an aqueous medium; within the investment casting industry the term silica sol is synonymous with colloidal silica and the terms are used interchangeably. In keeping with the standard definition of a colloid the particles within the dispersion should be sufficiently small that they do not settle under the influence of gravity but sufficiently large that they cannot be adequately classified as solutions [61].

2.7.1 Manufacturing Colloidal Silica

There are a plethora of manufacturing techniques available for the manufacture of aqueous colloidal silica including

- Ion exchange of sodium silicate
- Neutralising soluble silicates
- Electro-dialysis
- Peptisation of silica gel
- Hydrolysis of silicon compounds
- Dissolution of elemental silicon
- Dispersion of pyrogenic silica

The majority of commercially produced silica's are manufactured using a variation of the ion-exchange principal first patented by Bird in 1941 [62]. The technique relies upon removing the sodium content from sodium silicate resulting in the production of colloidal silica. As the name suggests sodium ions are exchanged for hydrogen ions via an ion-exchange process facilitated by a zeolite or a suitable ion-exchange resin in the hydrogen form (i.e. supplying hydrogen ions) as described by reaction 2.2

$$\mathrm{Na_2SiO_3(aq)} + 2\mathrm{H}^+ \xrightarrow{\textit{ion exchange}} \mathrm{H_2SiO_3(aq)} + 2\mathrm{Na}^+ \tag{2.2}$$

the resultant silicic acid is unstable and polymerises to form discrete, insoluble silica particles as per reaction 2.3.

$$\mathrm{H_2SiO_3(aq)} \rightarrow \mathrm{SiO_2} + \mathrm{H_2O} \tag{2.3}$$

The reactions detailed above will precipitate the silica from sodium silicate in a dilute form. In order to concentrate the material to a commercially useful grade it is heated in an evaporator to drive off water. To ensure that the newly formed colloidal silica does not aggregate it must be stabilised; techniques for performing this are detailed in the following section.

2.7.2 Sodium Stabilised Colloidal Silica

The majority of colloidal silica binders employed in the investment casting procedure are referred to as being sodium-stabilised. However the name is something of a misnomer as the stabilising species is actually the hydroxyl ion present in the alkali hydroxide; the sodium (or other alkali ions) are present only as a by-product.

At alkaline pH the acidic hydrogen ions present within the hydroxyl groups bound to the surface of the silica colloid are able to react with the hydroxyl ions present in the alkali-hydroxide to form water according to reaction 2.4.

$$[\mathrm{SiO_3}]\mathrm{OH} + \mathrm{NaOH} \rightarrow \mathrm{SiO_4^-} + \mathrm{Na^+} + \mathrm{H_2O} \tag{2.4}$$

The two by-products of this reaction are sodium ions and crucially free valences on the oxygen atoms; these charged sites provide the repulsive forces necessary to prevent particle attraction and therefore stabilise the colloid against aggregation. The sodium-stabilised surface is shown in Figure 2.19. In order for the colloid to remain stable it is important that these charged sites persist during the changing operating conditions which the colloid may experience. The two main threats to the stability of silica colloids stabilised in this way are variations in pH and the presence of salts.

Variations in pH can cause two complications for sodium-stabilised silica colloids, considering the stabilisation method discussed above it is clear that the presence of negative charge on the colloid ensures the repulsion of colloid particles. Excursions into the acidic pH range will cause the removal of the charged sites (through oxidation of $\mathrm{O^-}$ back to OH) and hence reduce stability to particle aggregation. The behaviour during excursions into the alkali pH range are more complicated, within the pH range between approximately 8.5 - 10.5 increasing pH gives rise to an increased number of negative sites which increase the particle repulsion due to increased surface charge and hence stability to aggregation. Above pH 10.5 the colloidal silica particles begin to dissolve reverting back to the precursor material, sodium silicate [63].

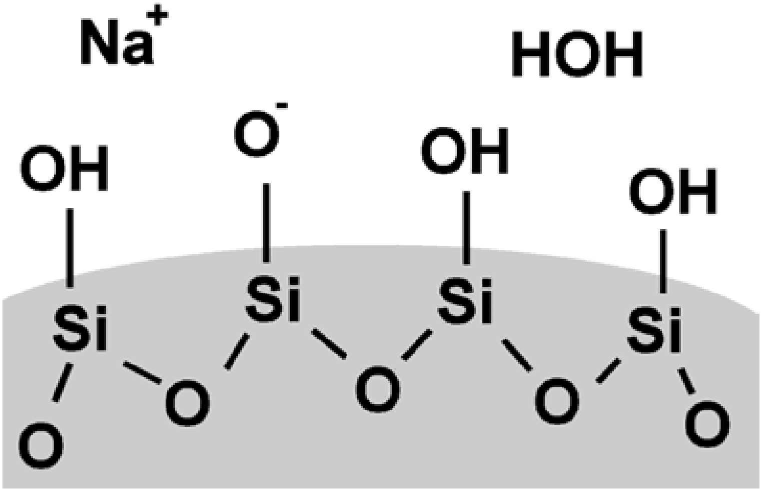

FIGURE 2.19: Schematic diagram of the surface of a sodium stabilised colloidal silica particle. Note the additional oxygen atom bound to each silicon atom exists in a plane perpendicular to the image.

2.7.3 Aluminium Modified Colloidal Silica

As mentioned in the previous section, sodium-stabilised binders are common in the investment casting industry, however there are alternate methods for stabilisation against aggregation. These are of particular interest to the investment casting industry as the presence of sodium can affect the refractory properties of certain ceramic materials, namely silica (see section 2.9.2). Eliminating (or greatly reducing) the sodium content can therefore be desirable in some applications.

As mentioned in the preceding section, sodium (or similar) is added as it enables the colloidal silica particles to develop surface charge which helps them repel one another reducing the chances of aggregation. In order to remove the sodium content some other mechanism must be employed to prevent aggregation. In the case of aluminium modified (AM) binders, the surface charge is provided by aluminium ions substituted into the lattice of the sodium particle as described in the patent by Alexander [64]. The substitution is possible since aluminium and silicon can both assume a coordination number of 4 toward oxygen and because the aluminate ion ($Al(OH)_4^-$) is geometrically similar to the silicate molecule [65]. Once the ion is present within the surface the extra valence possessed by the aluminate ion creates a site of permanent negative charge as shown in Figure 2.20. The permanently charged site negates the requirement of stabilisation by sodium hydroxide or similar and also makes the suspension much less sensitive to pH fluctuations.

Unfortunately mould materials made using these materials exhibit greatly reduced green and pre-fired strengths compared to sodium stabilised variants, although the reasons for this are not known [66]. Additionally aluminium modified binders are more costly than conventional sodium stabilised varieties [67].

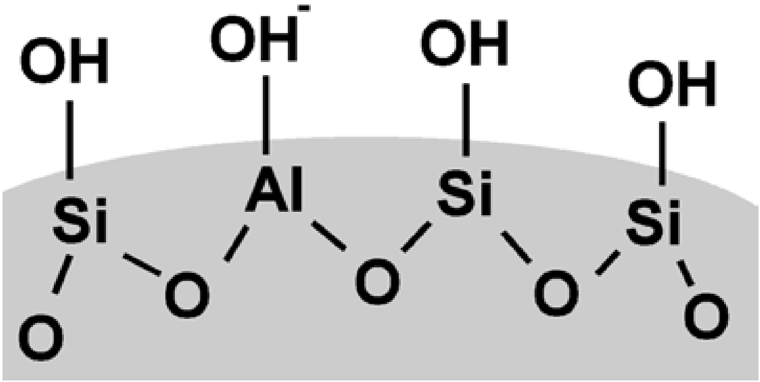

FIGURE 2.20: Schematic diagram of the surface of an aluminium modified colloidal silica particle. Note the additional oxygen atom bound to each silicon atom exists in a plane perpendicular to the image.

2.7.4 Colloidal Silica and DLVO theory

The DLVO theory was independently developed by Derjaguin and Landau (1941) and Verwey and Overbeek (1948) and draws its name from those researchers. It attempts to describe the stability of particles within colloidal systems by summing the attractive and repulsive forces due to van der Waals and charge repulsion into an electrical potential. By calculating the potential for a particle pair across all separation distances their stability to aggregation can be inferred [68]. It is not treated in depth here and the mathematics relating to the theory are omitted.

The theory predicts that stability against aggregation is controlled by the interaction potential which is a function of particle separation. Figure 2.21 shows two potential curves, curve A describes a system which is stable to particle collisions, the repulsive force due to the overlapping of electrical double layers exceeds the van der Waals attraction. Curve B shows a system which has become unstable due to increased electrolyte content. As the number of ions within the liquid phase is

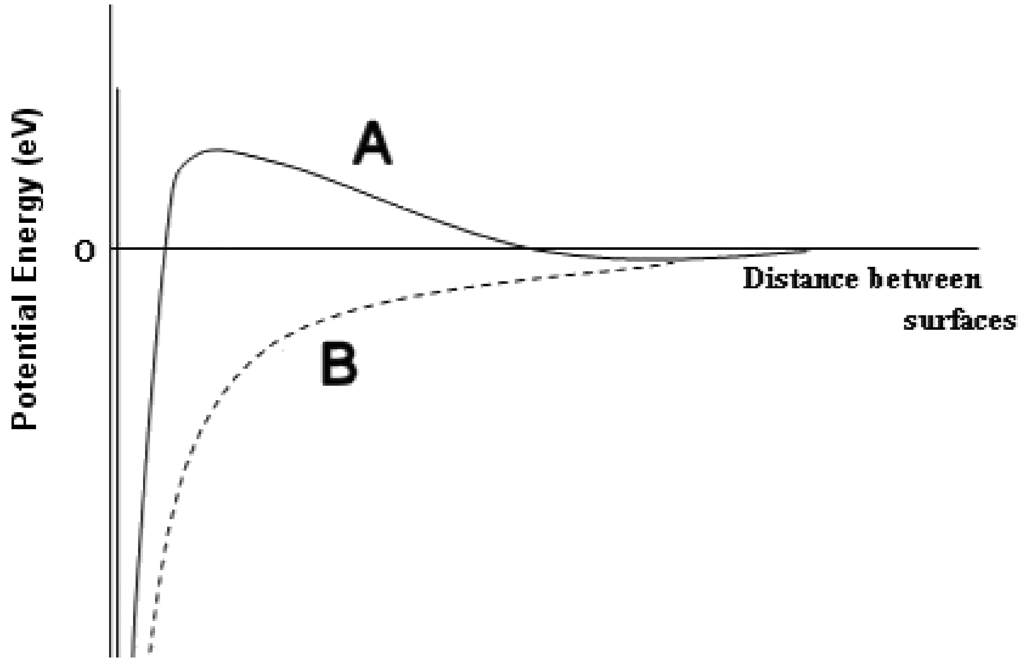

FIGURE 2.21: A shows the potential for a stable system. B shows the potential for a system which is unstable due to increased electrolyte content [69]

increased the thickness of the electrical double layer is reduced exponentially, once this occurs the van der Waals forces dominate and the system will flocculate [69].

Whilst the DLVO theory is useful it is unable to explain fully the behaviour of electrostatically stabilised colloidal silica systems. There are two areas in which predictions based on the theory directly contradict experimental observations. Inspection of Figure 2.22 shows the presence of two areas of stability in the aqueous colloidal silica system; information represented in the figure come from independently verified empirical data and can be considered irrefutable. The first region of stability is at pH 2 - 2.5, in this range the charge density on the silica surface is approximately zero due to a lack of hydroxyl ions present at acid pH. The repulsion due to the electrical double layer should therefore be absent, however evidence suggests that at these pH values colloidal silica can be at least metastable. The second trend which defies DLVO prediction is that of increasing stability with increasingly alkaline pH. The increasing concentration of hydroxyl ions in the liquid phase should reduce the thickness of the double layer and hence the stability, however colloidal silica is readily stabilised at pH 10. In its incumbent form the DLVO theory is incapable of explaining the stability of the water-silica system.

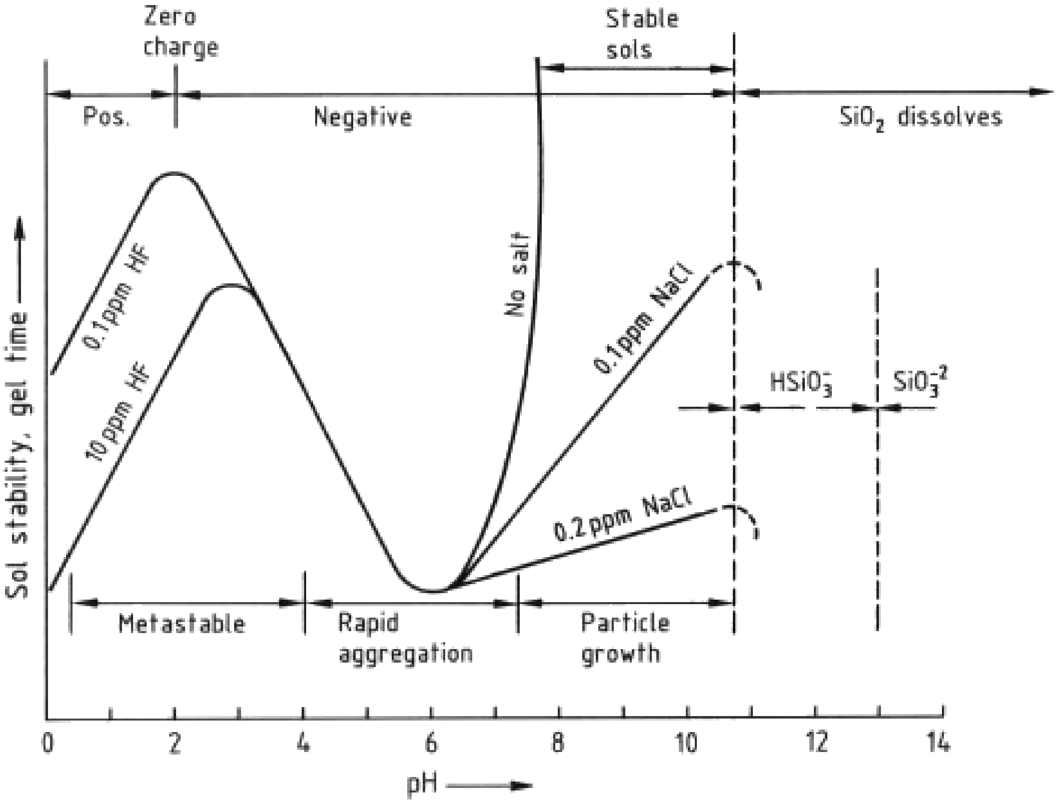

Figure 2.22: The effects of pH on the stability of aqueous colloidal silica [61]

2.8 Zeta Potential

As mentioned in the preceding section colloidal silica particles rely on surface charge to provide the repulsive force to prevent particles from colliding and aggregating under the influence of van der Waals forces, this is discussed in more depth in section 2.7. To characterise the stability of colloidal silica over a pH range it is necessary to measure the surface charge which is related to the zeta potential. This can be done using a number of techniques; the one to be discussed here is known as electroacoustics which was developed for characterisation of concentrated suspensions of particles; for this reason it is the most useful technique of its type for the materials featured in investment casting slurries.

The theoretical basis on which the technique relies was first proposed by Debye in 1933 [70]. It was proposed that sound waves passing through an ionic solution will cause ions within it to oscillate with different amplitudes depending on their masses, this oscillation will give rise to a measurable electrical potential which too will oscillate at the same frequency as the sound waves. It was also proposed that measuring the potential would provide information relating to the mass of the ions and the number of solvent molecules connected to them.

The modern technique is known as electroacoustics and can be used in two reciprocal processes. The first process uses the technique described above to generate a measurable electric potential on application sound waves. The second process uses an inverse methodology, instead of passing sound waves through a suspension an oscilating electric field is applied to it. This causes charged particles within the suspension to oscillate, depending on the mass and frictional coefficients of the suspended particles relative to the suspending medium the generated sound waves may exhibit a difference in phase angle relative to the applied potential. The motion of the vibrating particles can be considered as an acoustic dipole which creates a sound wave within the system, known as the electrokinetic sonic amplitude or ESA [71]. At the transducer the amplitude and phase difference are measured. At low frequencies the phase difference is zero, for increasingly higher frequencies the phase angle is expected to become greater, especially in the case of large particles which have greater inertia and frictional losses. The method by which the machine calculated the zeta potential from this measurement is mathematically complex and beyond the scope of this thesis, for the interested reader an excellent treatment is given by O'Brien [72].

Additional to the measured amplitude and phase angle of the sample the calculation also requires a number of other parameters concerning both the dispersed phase and the suspending medium, these include dielectric constant, density and the concentration of the dispersed phase. Along with measurement of the zeta-potential the machine also provides measurements of pH, temperature and the conductivity of the sample.

2.9 The silica - alumina system

Silica and alumina are important ceramic materials in the manufacture of investment casting shell systems both as materials in their own right and also in combination for the formation of mullite. The formation of mullite from these materials was mentioned for the Hi-shell system in section 2.3. It is discussed in greater depth in section 5.2 with regard to trial formulations based on various silica alumina contents; the desirable properties of mullite were discussed in section

2.3.2. In order to successfully utilise these materials it is necessary to understand their behaviour across the range of states relevant to shell manufacture.

The first part of this section is dedicated to discussion of the aqueous silica alumina system as a ceramic slurry. The second part relates to the ceramic materials subsequently generated from those systems.

2.9.1 Slurry stability of the silica - alumina system

The iso electric point (IEP) for pure silica occurs at pH values between 2-3, whereas the value for aqueous alumina is approximately pH 9, however the values are very dependant on surface chemistry and purity [61]. In isolation both materials can be processed simply by operating at pH values far from their IEP, in combination however the picture becomes more complex. When using systems which rely on surface charge to provide stabilisation against aggregation it is necessary to consider both the IEP and the polarity of the stabilising charge, this is especially pertinent to the silica - alumina system. Figure 2.23 shows zeta potential values for pure silica and alumina across a range of pH values, at alkaline pH the surface charge of both silica and alumina is negative, at highly acid pH particles share positive charge. The IEPs of each particle are widely different and hence there exists a wide pH range across which the species are stabilised by opposite surface charge leading to attraction by a process known as heterocoalulation.

Systems featuring particles stabilised by opposite surface charge risk instability problems due to interspecies attraction. The interaction between silica and alumina particles across a range of pH values was investigated using Atomic Force Microscopy (AFM) by Larson *et al.* [74]. Results in Figure 2.24 show the variation in attractive potential between a silica colloid and an alumina flat plate at different pH values. The IEP of the alumina flat-plate used in the experiment was determined using streaming potential, and occurred at pH 4.2 which is notably lower than that of pure alumina powder. The reasons for the discrepancy are unclear and the author dismisses the possibility of contamination, however the data remains useful; at pH values exceeding 4.2 the forces measured between the species are positive which implies repulsion. At pH values below the IEP the force is negative implying attraction. Occurring within an aqueous system this behaviour would lend itself to flocculation.

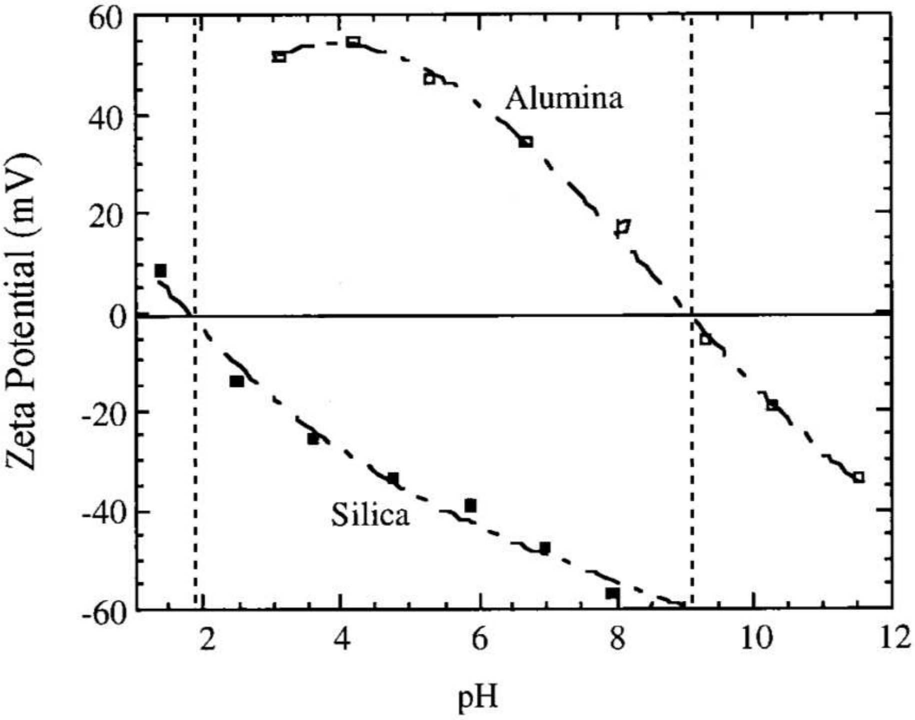

FIGURE 2.23: Zeta potentials for dilute systems of pure silica and alumina. IEP for silica shown at approximately pH 2, IEP for alumina at approximately pH 9. Figure adapted from [73].

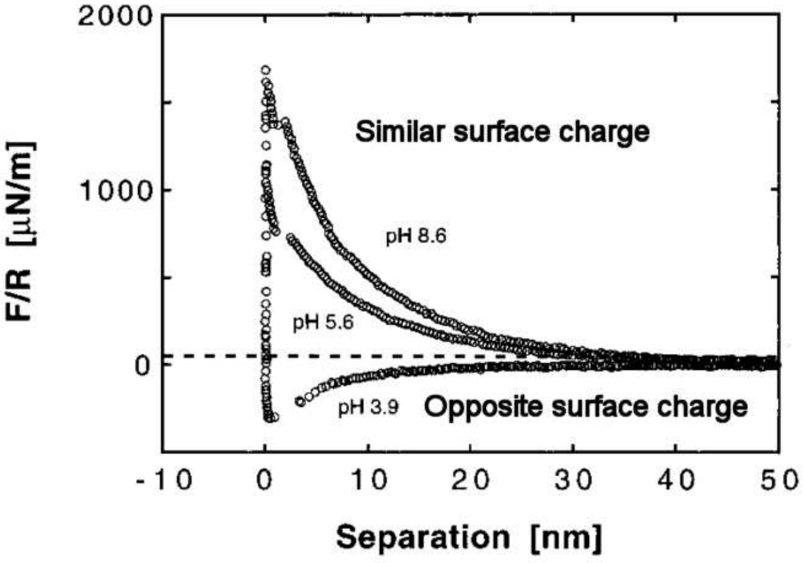

FIGURE 2.24: Force interaction between alumina and silica across a range of pH values measured using atomic force microscopy. Figure adapted from [74].

Further evidence of the potential for instability was observed using sedimentation of silica - alumina systems by Yates *et al.* [75]. Silica particles ranging in diameter from 4 to 285 nm were added to a stable aqueous suspension of 310 nm alumina particles; notable within the size range were 19 nm particles which have comparable size to those featured in the silica binders used for investment casting. In contrast to much of the work within the literature the purpose of this study was to investigate the optimum silica concentrations to *cause* aggregation within the system rather than inhibit it. The results of the sedimentation showed that the number of particles needed to induce aggregation reduces dramatically with increasing particle size; this is illustrated in Figure 2.25. Implicit within this observation is that the attraction between particles of similar size is greater than the case in which they have differing sizes. This is further illustrated in Figure 2.26 in which the effect of silica particle addition on the viscosity of an alumina suspension at pH 4.0 is shown [73]. At this pH alumina and silica particles have opposite surface charge and would be expected to aggregate; the shear thinning behaviour exhibited by the suspensions implies that this is the case. Except for very high shear rates, the 300 nm silica particles cause an increase in viscosity an order of magnitude higher than that of the smaller, 25 nm particles. This is consistent with the effect shown by Yates which was explained as being due to a combination of particle bridging due to van der Waals forces and neutralisation mechanisms consistent with the interaction between double layers permitted by their opposite charge.

When there exists a size difference between the species of particles in the silica alumina system it is possible for one species to completely adsorb to the surface of the other, when this occurs the surface chemisty of the coated particles will appear to the system as larger particles of the smaller species. One of the causes of this is the number of particle collisions which occur between particles of differing sizes. Bruinsma *et al.* [76] explain in detail the correlation between particle size and predicted rates of collision; through estimation of the Peclet number interaction rates between particles in a bi-modal system were evaluated. Collisions occurring at the fastest rate were those of large particles with small ones, with an average time between collisions of 20 μs. The second most readily occurring collisions were those between small particles on average occurring every 400 μs. Other collision types occurred much less frequently taking on average 4 orders of magnitude longer than those of the most prolific collisions. Assuming a similar relationship between collisions within the silica - alumina system it is natural to assume that in systems

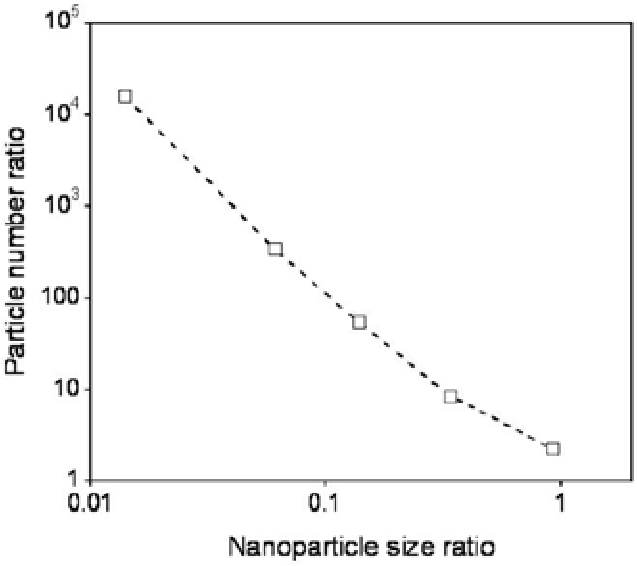

FIGURE 2.25: Relationship between optimum silica particle numbers required for aggregation and particle size relative to alumina. Figure adapted from [75].

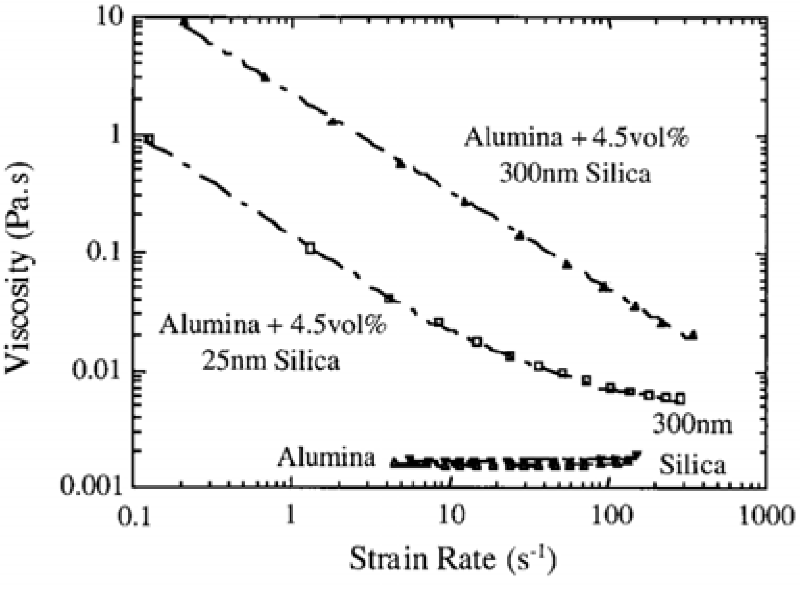

FIGURE 2.26: Effect of relative silica - alumina particle size on suspension viscosity; addition of 300 nm silica particles causes considerable increase in viscosity compared to similar addition of 25 nm particles. Results shown are measured at pH 4. Figure reproduced from [73].

where one species is much larger than the other some particle coating will occur. It is possible that the alumina particles within the silica alumina slurries will behave as larger silica particles due to coating, however, how this will affect slurry rheology is unclear.

Assuming that the relationship observed by Bruinsma *et al.* is correct, that the greatest collision rate occurs between large and smaller particles, appears to contradict observations made by Yates *et al.* who observed that flocculation occurred most rapidly for systems containing particles of approximately equal size. However it is not simply the number of collisions or interactions which affect particle stability but also the way in which those interactions affect the system. When silica and alumina particles are of similar size they are able to interact forming a continuous network which breaks down under the action of shear stress, however when there exists a size differential the smaller particles will coat the surface of the larger. In some cases this can alter the surface chemistry to mimic that of the smaller particle allowing the formation of a stable dispersion [73].

2.9.2 The solid silica alumina system

The effect of mullite formation within the silica alumina system is discussed in section 2.3.2 in relation to the creep properties of the Hi-shell system currently in use by Rolls-Royce. In order to achieve mullitisation within the shell it is necessary to include the correct ratio of silica and alumina; the phase diagram for the silica alumina system is presented in Figure 2.27. The highest temperature experienced by the mould is during casting at which point it will reach 1540 ℃, the portion of the phase diagram exceeding this temperature can therefore be disregarded. Referring to the mol % of silica within the system the diagram can be broken down into three sections: Above 42 mol % the system is predominantly mullite solid-solution containing small amounts of free-silica, below 38 mol % the system contains a small amount of free-alumina. For silica concentrations between 38 and 42 mol % the system forms mullite exclusively; this concentration is referred to hereafter as the stoichiometric ratio. Since silica, alumina and mullite all exhibit different thermal and mechanical behaviours it is possible to alter the properties of the ceramic by altering the silica alumina ratio. Hi-shell is formulated such that the silica alumina ratio is 40:60 in terms of mol % to maximise mullite formation within the shell; since the Hi-shell system exhibits many desirable characteristics one of the methodologies employed to reduce shell strength will be by varying the silica alumina ratio to attempt to reduce the excessive residual shell strength.

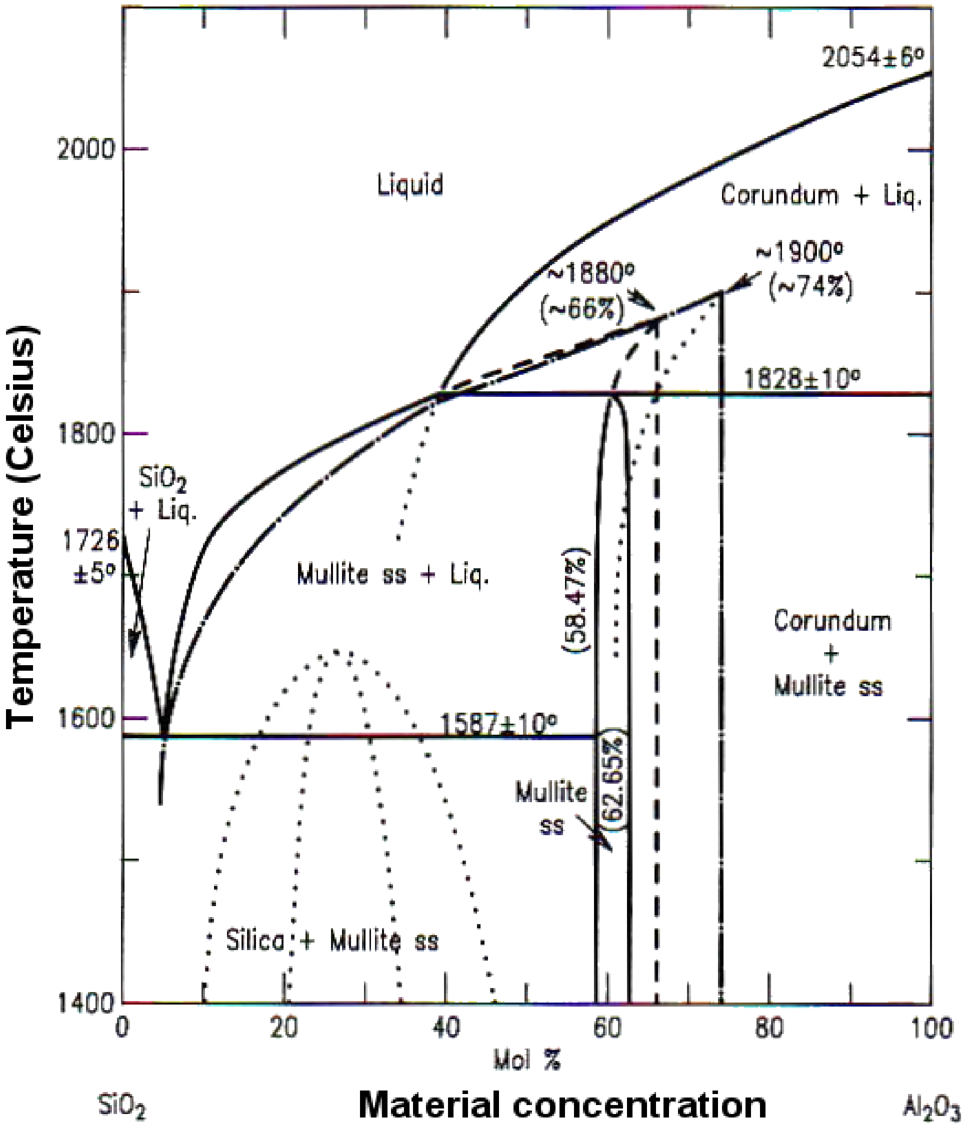

FIGURE 2.27: Phase diagram for the stable and metastable equilibria for the silica alumina system. Figure adapted from [77]

The formation of mullite from silica and alumina precursor materials depends on both the concentration of each material within the formulation and also the temperature to which the materials are exposed. For the purposes of this research the temperatures for all materials will be consistent and determined to closely reflect those experienced by mould materials during the casting cycle. Shell formulations based on these materials are featured in Chapter 5. The sintering behaviour of each formulation is inferred through observing changes in the sample dimensions during sintering using dilatometry (see section 3.1). The behaviour of the trial materials are compared to materials observed in the literature.

The silica-soda system

The previous section discussed the effect of silica and alumina concentration on the properties of materials based on this system during thermal cycling. Another material which can alter the behaviour during the firing cycle, and one which is often present within investment casting slurries as part of the colloidal silica binder is sodium oxide or soda as it is more commonly referred to. The effects of soda, on the sintering behaviour of ceramic materials such as silica and alumina are well known and documented within scientific literature. It was reported by Louet *et al.* that at temperatures as low as 800 °C a liquid phase can be formed between soda and silica. However it was also observed that soda content within the alumina powder reduced the rate of sintering at temperatures below 1280 °C, at temperatures exceeding 1280 °C the rate for materials containing soda were increased compared to those without. The resulting density of the soda containing samples post firing was reduced compared to soda-free samples indicating that relative differences in the sintering rates did not compensate for each other [78].

3

Methods and Materials

3.1 Methods

This section contains information relevant to the experimental work undertaken during the completion of this thesis; it details all of the processes involved in both the manufacture of ceramic shells and also their characterisation. The work has predominantly been performed in the laboratories of the Interdisciplinary Research Centre (IRC) at the University of Birmingham (UOB). Due to equipment availability some additional testing was performed at other locations.

3.1.1 Ceramic slurries: Mixing and Monitoring

3.1.1.1 Laboratory scale trials

The primary objective of this thesis is the formulation of recrystallisation (RX) reducing shell materials, in order to facilitate the mixing of a large number of candidate shell systems four small scale slurry tanks were developed. These allowed test bars required for characterisation to be manufactured by dipping into a slurry rather than by the often used technique of painting the slurry onto test bars. It was proposed that this would allow more representative shell behaviour and therefore reduce scale-up problems. The schematic layout of the slurry mixer rig is shown in Figure 3.1; the rig comprised 4 varibale speed Fisher FB15028 overhead stirrers equipped with 60 mm diameter ringed impeller-type mixer blades, 4 polypropylene slurry tanks with a 3 litre capacity and a water bath. The rig was operated in the shell laboratory under nominal conditions of 21 °C ± 2 °C and 50 % relative humidity ± 3 % RH to ensure consistency with Rolls-Royce shell workshop conditions. Excluding periods of mould dipping the slurry tanks were covered in order to prevent excessive dehydration through evaporation and reduce the possibility of contamination. Slurry rheology was monitored using a Zahn-4 type flow cup and a digital stopwatch; de-mineralised water additions were made to counteract losses due to evaporation based on Zahn-4 measurements. Mould drying was performed in the shell laboratory drying cabinet under nominal conditions of 21 °C, 50 % relative humidity and 10 ms^{-1} pulsed air speed with a period of approximately 20 seconds.

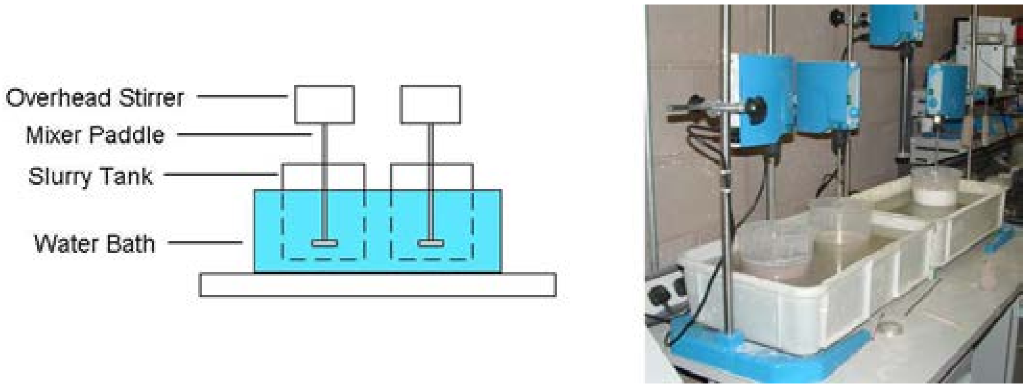

FIGURE 3.1: Schematic and photographic illustration showing the set-up of the lab-scale overhead mixer slurry tank rig.

3.1.1.2 Large scale trials

Systems progressing through laboratory scale trials were migrated into larger tanks, this was done in order to facilitate shelling of larger moulds and to monitor the long-term stability of the slurry systems in an industrially representative environment. The tanks selected were 120-litre conventional, rotating-drum stationary-blade type, installed in the robot shell cell in the UOB shell laboratory. Figure 3.2 shows the slurry tank with the safety guard removed for clarity. The paddle is a manufactured from stainless steel with a 45 degree profile as presented to the flow of slurry; stainless steel is used to resist corrosion and wear and hence slurry contamination.

Migration into the larger tanks permitted Rolls-Royce small-bore furnace moulds (150mm maximum diameter) to be dipped automatically using the Motoman MRC16 robot, and sanded using the automated sanding tower. Through ensuring the dipping and sanding cycles were consistent for each dip and each mould the variability of shelling was reduced. Mould drying was performed using the shell laboratory drying cabinet as per test bar moulds.

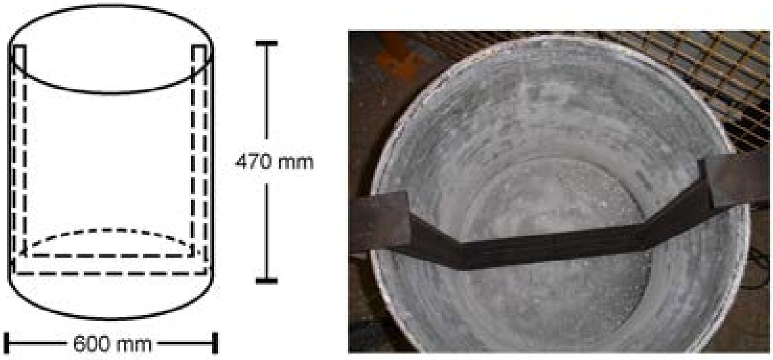

FIGURE 3.2: 120 litre robot-cell slurry tank used for the dipping of Rolls-Royce small-bore furnace moulds. Agitation provided by rotation of drum with respect to stationary paddle.

3.1.1.3 Slurry mixing

In order to produce defect free moulds with predictable mechanical properties it is important to ensure correct mixing of ceramic slurries during the initial mixing period. In industry this stage is performed using an overhead type high-shear mixer equipped with a turbine-type mixer blade. Slurries are mixed in 366 kg batches for 30 minutes [79]. The set-up employed in the UOB shell room to replicate this consists of a single Fisher FB15028 overhead mixer equipped with a turbine-type mixer blade inserted into a 12 litre beaker; during the initial mixing stage slurries are made up in batches using this set-up and sheared for 10 minutes before being added to the rotary slurry tank. The addition of this step ensures that ceramic powder within the slurry is correctly dispersed preventing clogging issues during flow-cup measurement.

3.1.1.4 Slurry characterisation

A number of techniques were employed to monitor the conditions of the ceramic slurries used in the shell trials, they comprised;

- Flow time

- Plate weight
- Specific gravity
- pH

During small scale trials slurries were only retained for periods of 2-3 days to facilitate the manufacture of ceramic test bars, slurry monitoring over this period was limited to flow cup measurements to ensure correct slurry viscosity for dipping. Larger scale slurries, which would be retained for longer, were subjected to all of the above testing throughout the duration of their life. Slurry lifetimes in excess of 12 weeks were common for larger scale slurries.

3.1.1.5 Flow-time

Measurement of flow-time is the standard technique used in the investment casting industry to characterise the viscosity of ceramic slurries, there are a number of different variations of the flow cup; the designs used in this thesis were of the International Standardisation Organisation (ISO) and Zahn types shown in Figure 3.3. ISO cups used in this thesis were manufactured and calibrated by Sheen Instruments.

Viscosity testing using flow-cups was performed according to BS EN ISO 2431:1996 [81]. Slurry samples for testing were collected by dipping a container into the slurry and decanting from the container into the flow cup. As the cup is filled the operator covers the orifice preventing flow until the cup is full, the end point of the test is defined as the point where the orifice becomes visible when viewed from above the cup; at this point the flow time is recorded. Each measurement is repeated 3 times and the mean value is recorded. If slurry viscosity exceeds the specified limit an addition of de-mineralised water is made; the amount required to correct the viscosity is often determined through empirical observations of the flow-time

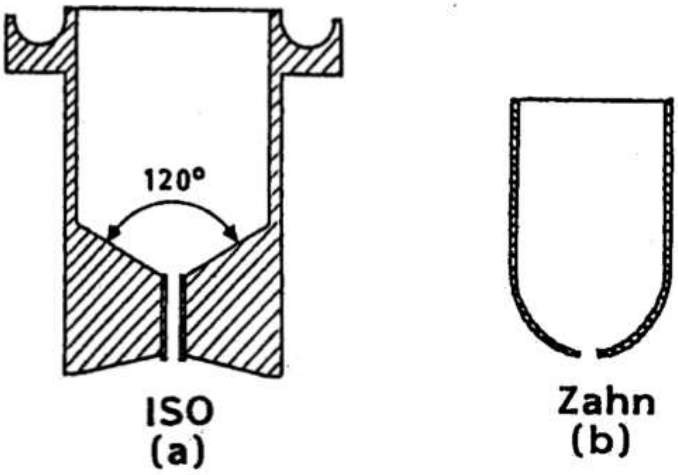

Figure 3.3: Cross sectional schematic of (a) ISO-type and (b) Zahn-type flow cups; orifice angle in the ISO cup is designed to promote parabolic flow through orifice. Adapted from [80].

reaction to the addition and is hard to quantify. For Zahn-type flow cups the measurement process differs from the above in that the entire cup is submerged into the slurry and measurement of flow time begins as the cup is withdrawn and flow begins. Whilst other measurements are used to characterise the slurry flow-time is generally the technique used as the control parameter. Slurry control data for a range of relevant slurries is given in Table 3.1.

Table 3.1: Flow-cup specifications for Rolls-Royce standard slurry systems.

Shell system	Flow Cup	Flow time (s)
Std SX Primary	ISO B5	28 - 31
Std SX Primary + 1	ISO B4	36 - 39
Std SX Backup	ISO B4	55 - 60
Hi-Shell Backup	ISO 6	28 - 30
NG backup trials	Zahn 4	11 - 12

3.1.1.6 Plate weight

The plate weight test is another method available for characterising the condition of investment casting slurries, the test is performed by dipping a polished stainless steel plate into the slurry, allowing it to drain for 120 seconds and measuring the mass of slurry retained on its surface; the process is illustrated in Figure 3.4. Mass measurements were made using a digital balance accurate to ± 0.005 g.

FIGURE 3.4: Schematic diagram showing the measurement process for plate weight slurry retention test.

The plate used during the test is made from polished stainless steel and features a wire hanger to enabling it to be fully submerged into the slurry, plates are cleaned and checked routinely to determine the presence of surface imperfections. The design of the plate is illustrated in Figure 3.5.

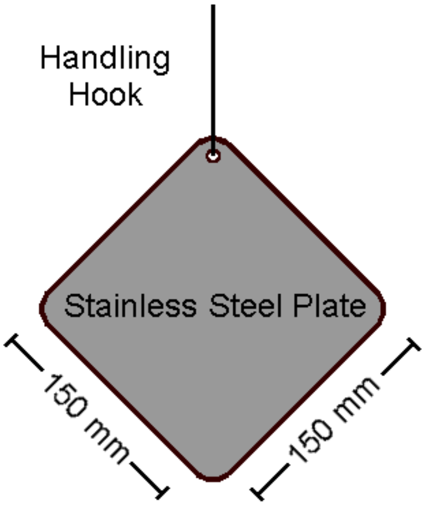

FIGURE 3.5: Schematic diagram showing the plate weight apparatus.

Whilst plate weight does not characterise viscosity directly it is known to exhibit correlation to flow-cup measurements whilst also providing an indication of the coating ability of the slurry; Equation 3.1 [82] gives the relationship between viscosity of the medium μ, and the coating thickness h. Other parameters within the

Equation are the gravitational force g, the density ρ, the withdrawal rate of the plate U, and the surface tension of the liquid σ.

$$\mathrm{h} = 0.945\sqrt{\frac{\sigma}{\rho g}}\left(\frac{\mu U}{\sigma}\right)^{\frac{2}{3}} \tag{3.1}$$

The applicability of the equation to non-newtonian fluids such as investment casting slurries is debated within the literature, however, these are beyond the scope of this thesis since the plate weight test operates independently of the equation. The test is particularly applicable to primary slurries and is able to detect any coating issues which may be present.

3.1.1.7 Specific Gravity

Specific gravity measurements are used to reveal any change in slurry composition over time. Particle instability within the slurry can cause formation of aggregates which increase the observed flow time or plate weight, these can precipitate over-dilution of the slurry to counteract an apparent increase in viscosity. Observations of specific gravity will characterise any drift in slurry density caused by this.

Specific gravity measurements were made using either a 100 ml container or a 25 ml measuring cylinder, by measuring the mass of a known volume of slurry it is simple to calculate the bulk density.

3.1.1.8 pH

Measurement of pH is particularly important for characterising the stability of colloidal systems relying on charge stabilisation; this is discussed in detail in sections 2.7 and 7.2. Daily measurements were taken using a Fisher AB15 pH meter which was calibrated weekly using buffer solutions at pH values, 4, 7 and 10. Slurry samples were decanted from the slurry tank into a plastic beaker for measurement. Measurements were only recorded once the pH value had stabilised.

3.1.2 Shell manufacture

In order to evaluate the candidate shell materials it was necessary to manufacture shell samples for the range of characterisation tests to be performed. This section details the procedures necessary for manufacturing test bars including the manufacture of wax patterns.

3.1.2.1 Wax patterns

The wax patterns used throughout the research were made using an MPI injection moulding machine equipped with a range of wax pattern dies for making flat MOR bars, edge test specimens and compression test specimens. Blaysons FR60 pattern wax was used throughout at injection-nozzle pressure and temperatures of 35 Bar and 64 ℃ respectively.

After injection the wax formers are cleaned by hand dipping into Trisol 60 Plus wax pattern cleaner for 3 seconds; this process ensures that the slurry is able to adhere to and coat the surface of the pattern to produce a good quality facecoat.

3.1.2.2 Mould dipping

Two dipping processes were employed during mould manufacture; shell test specimens were dipped by hand and Rolls-Royce small bore moulds were dipped automatically using the shell room robot. Hand dipping was performed by manually inserting wax patterns (and subsequently partially dipped moulds) according to the procedure shown in Figure 3.6. During slurry draining the moulds were slowly rotated along their axis whilst simultaneously being moved through an arc of approximately ± 30 ° relative to horizontal, this was done to ensure even coating across all dimensions of the shell. Stucco application was also performed manually using a sieve with large enough apertures that all stucco particles could pass freely through it. The final coat known as the seal was applied by dipping into the slurry in the same manner as before but the stucco was omitted.

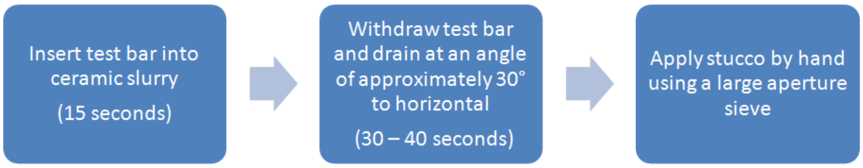

FIGURE 3.6: Schematic diagram showing the hand-dipping process for manufacturing shell test specimens.

In order to shell small bore moulds using the shell room robot it was first necessary to generate a correct robot program which would mimic that used by Rolls-Royce; all robot programming was performed by the author. To provide comparison between robot programmes a video was recorded of the Precision Casting Facility (PCF) robot and the programme was characterised by observing both the angle of the mould and the duration of each manoeuvre. The tanks in the PCF shell room are larger in diameter than those in the UOB shell room, this resulted in the angle of mould insertion being closer to vertical than that of the PCF robot. Moulds dipped using the UOB robot were however comparable in terms of shell thickness and surface finish and deemed suitable for casting. Stucco application in this case was performed by a Drytech automatic rainfall sander which is shown schematically in Figure 3.7. The stucco is housed within a hopper where it passes under gravity into the bottom of the Archimedes screw which conveys it to the shaker. The function of the shaker is to separate the stucco into a dispersed 'rain-like' stream, the mould is placed into the stream whereby the wet surface becomes covered. Stucco which is not adsorbed passes through the grate (whose function is to collect large particulates or fragments of broken mould) and into the hopper.

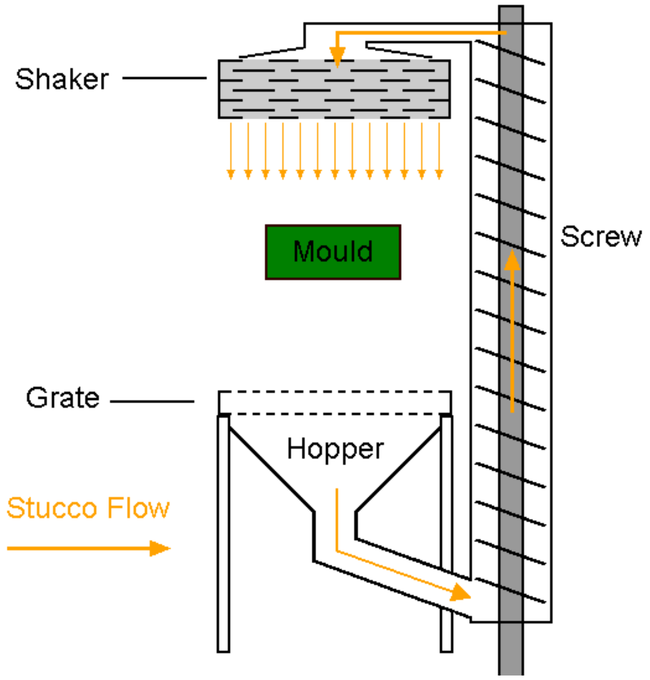

FIGURE 3.7: Schematic diagram showing the operation of the rainfall sander. Stucco is drawn from the hopper and elevated by the Archimedes screw, it is then passed through a shaker to disperse it before passing over the mould. Non-adsorbed stucco passes through the grate and back into the hopper.

It should be noted that the UOB drying area only has the capacity to hold ten Rolls-Royce small bore moulds on the drying carousel at any one time. Using a standard inter-coat dry time of 3 hours this restricted the number of shell dips which could be applied to 3 per working day necessitating a 48 hour dipping period per ten moulds (based on 6 dips per mould). Coupled with the fact that the robot is restricted to semi-automatic operation and requires continual supervision during dipping the number of moulds which could be practically shelled was limited.

3.1.2.3 De-wax process

In both the manufacture of test specimens for material characterisation and for the manufacture of components it is necessary to remove the wax former from within the mould before firing. For moulds processed both at the University of Birmingham (UOB) and at the Precision Casting Facility (PCF) this is performed by high pressure steam using a Leeds and Bradford Boilerclave Company (LBBC) Quicklock Boilerclave. Steam is introduced from the boiler section into the vessel section at between 9 - 10.3 bar and 180 - 200 ℃. Cycle times at pressure range from 5 minutes for small moulds to 8 minutes for larger moulds containing more wax.

3.1.2.4 Mould firing

Two firing stages were employed for test-bar moulds during the course of this work. All shell materials other than those retained in the green-state were subjected to the firing cycles given in Table 3.2.

Table 3.2: Furnace cycles for mould firing conditions. All mould firing performed in a single furnace for repeatability. Requested dwell times reflect the duration entered into the furnace programme and do not account for lag in the actual furnace temperatures.

	Temperature (℃)	Req'd Dwell (mins)	Heating Rate (℃.min^{-1})
Green	N/A	N/A	N/A
Pre-fired	800	60	20
Fired	1550	30	20

All firing was performed using a Lenton Thermal Designs (LTD) 1700 ℃ electric furnace equipped with a Eurotherm controller. The use of a single furnace enabled repeatable firing conditions for each firing cycle. The furnace was calibrated using a B-type thermocouple connected to a Fluke digital thermocouple calibrator; the results of calibration are shown in Figure 3.8.

The blue symbols show the specified temperature for the furnace cycle, shown in red and green respectively are measurements recorded for the furnace control thermocouple and a thermocouple located in the sample firing area. During testing a

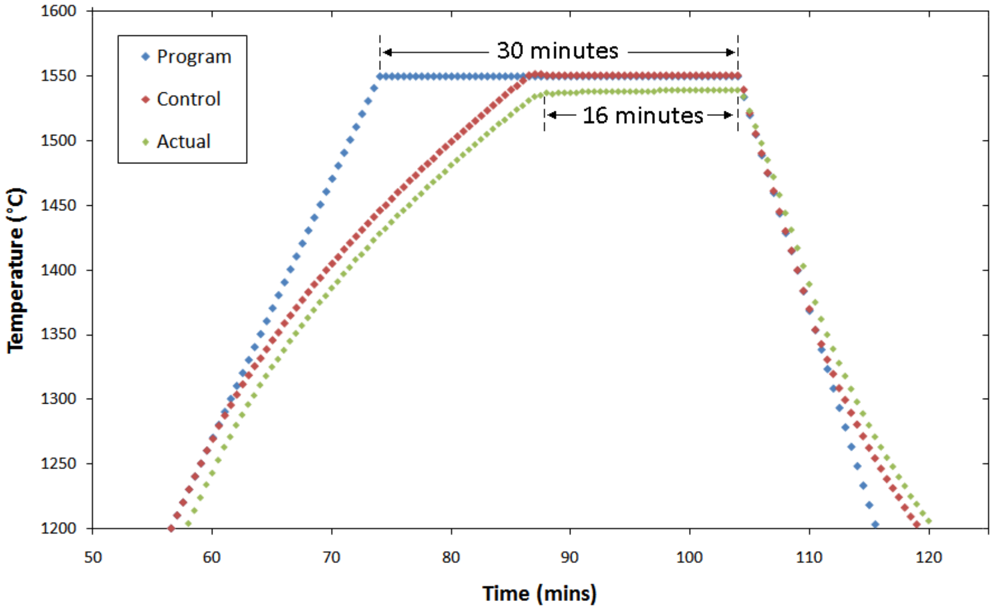

Figure 3.8: Thermocouple monitoring of Lenton Thermal Designs 1700 ℃ furnace during a simulated firing cycle to 1540 °C.

representative mass of shell specimens were placed in the furnace to ensure results were reflective of normal firing cycles. It was found that the control thermocouple gave a reading approximately 20 °C higher than that of the calibration thermocouple during the initial heating ramp; during the dwell time the value dropped to approximately 11 °C. From ambient temperature to approximately 1270 °C there was no difference between the specified temperature and that measured by the control thermocouple, beyond this temperature the furnace was unable to maintain the specificed 20 °C min^{-1} heating rate; this effectively reduced the dwell time experienced by the control thermocouple. The resulting firing cycle experienced by the samples was approximately 15 minutes at 1538 °C; this is similar to that experienced by the small-bore casting furnaces utilised in the Precision Casting Facility.

3.1.3 Mechanical Evaluation of shells

A number of techniques were employed to characterise the behaviour of shell materials, this section contains information relating to the evaluation of their mechanical properties using three techniques; flexural, edge and compression testing. Test parameters and geometries will be given including details of the test equipment utilised. Prior to testing samples were subjected to a range of heat-treatments reflective of those experienced by shell moulds during the casting cycle, the details are summarised in Table 3.3.

TABLE 3.3: Heat treatment cycles for shell test specimens. All firing performed in same furnace to ensure repeatability.

Condition	Heat treatment	Testing conditions
Green	None	Room temperature
Pre-fired	800 ℃ for 60 minutes	Room temperature
Fired	Pre-fired + 1550 ℃ for 30 minutes	Room temperature
Hot	Pre-fired + 1540 ℃ for 20 minutes	Tested at 1540 ℃

3.1.3.1 Flexural testing

The flexural strength of shell specimens was measured predominantly in 3-point bend configurations, but some limited testing was also performed in 4-point bend mode. Room temperature testing was performed in the UOB laboratory using an Instron 4467 load frame equipped with a 1 kN load cell calibrated by Instron. Parameters for testing are shown in Table 3.4. The test geometry is shown in Figure 3.9A; samples were supported by two fixed rollers and load was applied by another fixed roller. For 4-point bend tests both crosshead rollers and one of the support rollers were articulated, the final roller is fixed. Unless otherwise stated all flexural testing was performed with the primary coat face down.

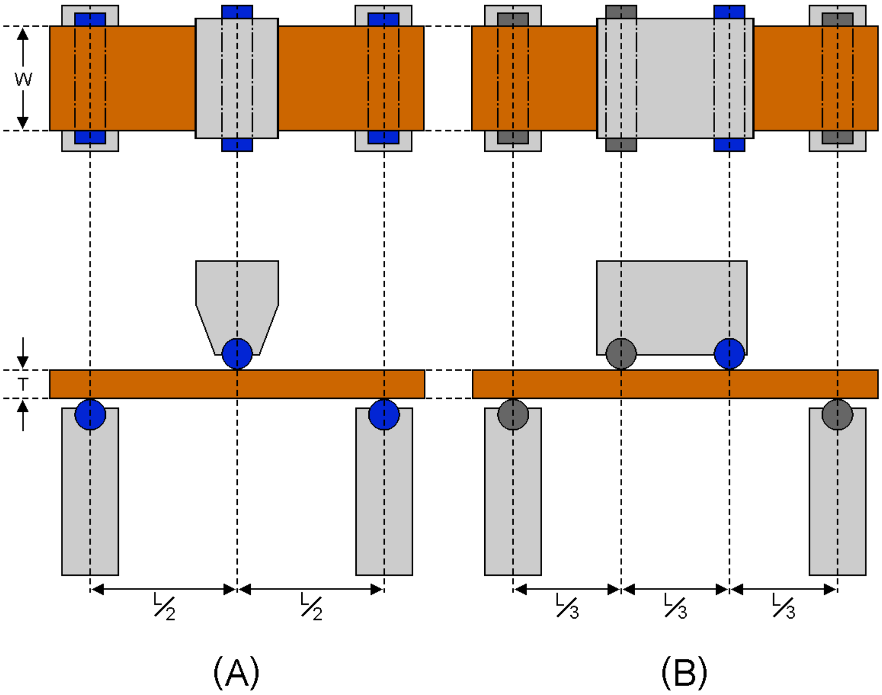

FIGURE 3.9: Schematic diagram showing the flexural test geometries used throughout testing. (A) shows test setup for 3-point bend; (B) shows set-up for 4-point bend. Articulated rollers are shown in grey, fixed rollers are highlighted in blue.

Shell samples suitable for flexural testing were manufactured by coating rectangular wax formers measuring 200 x 25 x 10 mm using the standard shell dipping process and the relevant shell material. Samples were wet-cut using an overhead-type diamond saw to approximately 20 x 65 mm for testing; additional sample preparation such as polishing was not possible due to the low green strength inherent to the manufacturing process and as such the number of surface defects was likely to have been high. Prior to testing sample dimensions were measured using a combination of digital callipers and a digital micrometer for width and thickness measurements respectively; for better accuracy and to take into account the uneven surface of the shell 3 measurements of thickness were performed across the centreline of the shell as shown in Figure 3.10. Measurements of load and crosshead displacement were recorded automatically by computer; the maximum load prior to failure (F) was used to calculate the so-called Modulus of Rupture

(MOR)[1] using Equation 3.2 in which (L) is the length of the support span, (W) is the width of the sample and (T) is the thickness of the sample [83]. The equivalent equation for calculation of MOR in 4-point bend is given in Equation 3.3.

$$\sigma = \frac{3\mathrm{FL}}{2\mathrm{WT}^2} \tag{3.2}$$

$$\sigma = \frac{\mathrm{FL}}{2\mathrm{WT}^2} \tag{3.3}$$

Flexural testing at elevated temperatures was split across two load frames. The first was a custom made Isoheat rig based at Intertek Testing Services (ITS) in Bristol, UK. Load was applied to specimens using a pneumatic actuator and measured using a load cell. The second was a rig made by Kiln Control Services for Ross ceramics in Denby, UK. For clarity the two rigs will be referred to as the ITS and Ross rigs respectively. During the course of testing the original load frame at ITS used for hot testing failed and was irreparable, it was therefore necessary to switch to the Ross rig as an alternate source. The components and specifications for each rig are shown in Table 3.5.

Table 3.4: Test parameters for room-temperature 3-point bend testing.

Load Frame	Instron 4467
Load Cell	1 kN
Support Span	50 mm
Crosshead speed	0.8 mm.min^{-1}

Both high temperature test rigs used were capable of accepting test bar insertion at elevated temperature, in both cases this was performed by passing the test bar through an aperture in the furnace and fully inserting it with a ceramic pushrod. The orientation of insertion was different for each rig and is shown in Figure 3.11.

---

[1] MOR is a measure of stress throughout the sample not an actual modulus.

Due to the loading channel present on the Ross rig sample width is limited to 10 mm.

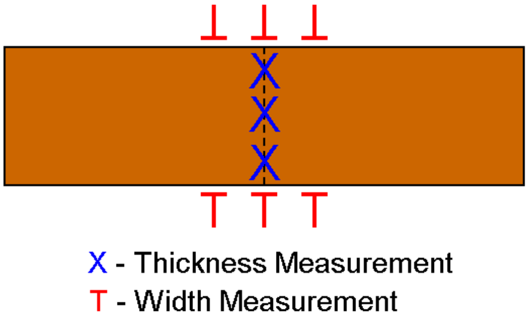

Figure 3.10: Schematic diagram showing the points at which dimensional measurements were made on flexural test specimens; blue crosses indicate thickness measurements made using a digital micrometer; red tees indicate width measurements made using digital callipers.

Table 3.5: Details and specification for elevated temperature flexural test rigs.

	Ross rig	ITS Rig
Load Frame	Lloyds LR10k Plus	N/A
Load Cell	250 N	250
Max Temp	1600 ℃	1550 ℃
Manufacturer	Kiln Control Services	Isoheat
Support assembly	Alumina rollers	Fixed alumina rods
Test Temperature	1540	1540
Crosshead speed	0.8 mm.min^{-1}	0.8 mm.min^{-1}

Four-point bend testing was only performed at room temperature, and was performed using a Zwick Z010 load frame equipped with a 500 N load cell. The test geometry is shown in Figure 3.9B and featured fully articulated supports and partially articulated crosshead.

3.1.3.2 Edge testing

Edge testing was performed using the same Instron 4467 load frame as used for MOR testing, however due to reduced sample strength in this geometry it was

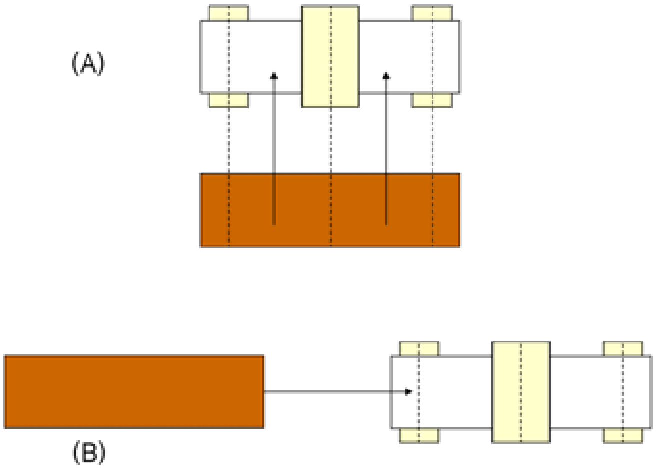

FIGURE 3.11: Schematic diagram showing the orientation of test bar insertion employed by A) the ITS rig and B) the Ross rig.

equipped with a 100 N load cell and test geometry as shown in Figure 3.12. The crosshead used in this test is a flat cylinder and the bottom platen is replaced by a knife edge in order to transmit force to the sides of the test bar in order to place the edge of the specimen into tension. As per MOR testing the maximum load at the point of failure is recorded by computer and used along with Equation 3.4 to calculate the stress at failure; the equation is only valid in this form for a 'knife-edge' with an angle of 30 degrees.

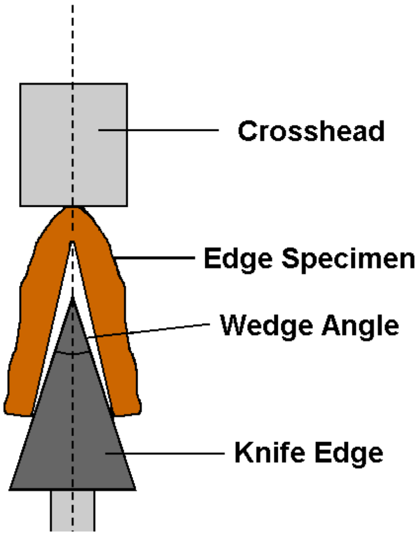

FIGURE 3.12: Schematic diagram showing the test geometry for edge testing.

$$\sigma = \frac{3 \cdot Fd}{WT^2} \tag{3.4}$$

Comparing Equations 3.2 and 3.4 it can be seen that for an equivalent applied load the stress experienced at the trailing edge is double that generated at flat sections; this result can be generalised to all high-angle features within ceramic shells and supports casting observations that shells often break at such locations. This is often evident as cracking during the dewax process.

3.1.3.3 Compression testing

The compressive strength of shell specimens cannot be characterised using conventional compression techniques as it is not possible to manufacture suitable test pieces without inducing high levels of machining damage. As a result a test geometry which was co-developed by the author and Rolls-Royce plc & can be seen in Figure 3.13) was used. The geometry is such that after cutting the specimens they feature flat, parallel surfaces at each end, this overcomes the difficulty of machining such edges into the test piece. In order to manufacture these test-pieces it was necessary to have a die manufactured to facilitate injection moulding of the wax-patterns, following this the patterns were shelled as per other samples. The dimensions of the resultant test pieces featured an internal diameter of approximately 15 mm and a height of approximately 40 mm. Cut-up was performed using an overhead wet-cut saw equipped with a diamond blade.

Compressive testing was performed using an a combination of the Instron 4467 load frame equipped with a 30 kN load cell and an Instron 5507 load frame equipped with a 200 kN load cell. The latter was used for the majority of testing as typically the shell specimens required compressive loads greater than 30 kN to achieve failure, however for weaker specimens the lesser load was sufficient; unless otherwise

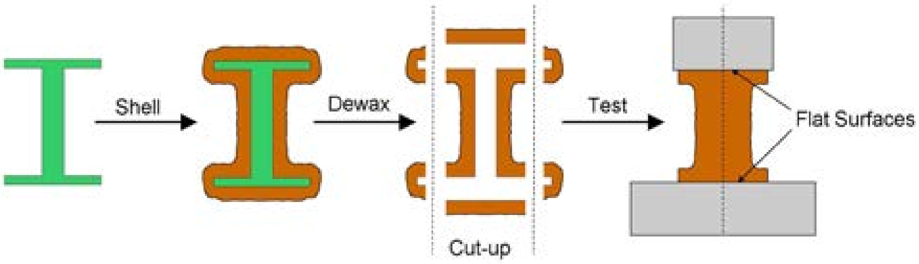

Figure 3.13: Schematic diagram showing the test geometry for compressive strength of shell materials.

stated results are measured using the 200 kN load cell. Load is applied to the samples using non-articulated hardened steel plates with a constant crosshead speed of 3 mm.min^{-1}. This value was chosen as the initial speed and to ensure comparability between test results remained consistent throughout all testing. However due to the failure mechanisms occurring within the shell due to the difference in thermal expansion coefficients between the shell material and the alloy the speed should be significantly reduced.

Measurements of load and extension were recorded automatically by a computer controlled datalogger attached to the frame. Compressive strengths are reported based on the maximum stress, σ within the sample prior to failure; this was calculated using equation 3.5.

$$\sigma = \frac{4F}{\pi(d_o^2 - d_i^2)} \tag{3.5}$$

where...

$$F = \text{Load at failure}$$

$$d_o = \text{Outer diameter of specimen}$$

$$d_i = \text{Inner diameter of specimen}$$

3.1.3.4 Creep Testing

Elevated temperature creep deformation was characterised using the Ross ceramics hot rig with the same 3 point bend geometry as used for flexural testing. Unlike the flexural strength characterisation test creep testing is performed by applying a constant load of 3.2 N to the specimen and measuring the amount of deflection occurring in 5 minutes; the crosshead speed is therefore dependant on the creep behaviour of the material. Sample dimensions are the same as those used in flexural testing and the loading mechanism is also identical. As with all MOR testing creep specimens are also characterised primary-coat down.

3.1.3.5 Porosity testing

The amount of open porosity present in shell specimens was tested using an Archimedes water immersion method; the measurement process is described in Figure 3.14.

Figure 3.14: Measurement process for Archimedes porosity testing of shell specimens.

Samples used for porosity testing were machined from the broken pieces of post-test MOR samples. Samples were suspended using 0.25 mm diameter nickel chrome wire wrapped around the centre and held in place by notches machined into each side as shown in Figure 3.15.

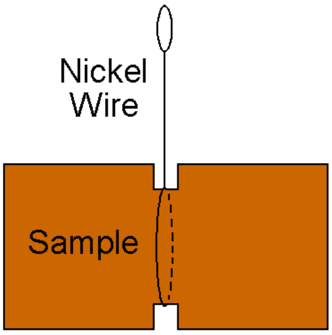

FIGURE 3.15: Shell test specimen for Archimedes porosity testing.

Since the technique relies on filling the pores with water it is restricted to measuring the open or connected porosity only, that is, pores which have an open path to the surface. Open porosity is calculated from experimental measurements using equation 3.6.

$$\phi_o = \frac{M_{wet} - M_{dry}}{M_{wet} - M_{app}} \tag{3.6}$$

where...

M_{wet} = Mass of wet sample

M_{dry} = Mass of dry sample

M_{app} = Mass of wet sample suspended in water

Porosity measurements were only made on samples in the pre-fired and fired conditions since wax residues present in and on the surface of the green samples would have affected the measured porosity.

3.1.3.6 Thermal Expansion

In order to understand the performance of the shell material during the heat-treatment experienced during the casting cycle their thermal expansion was characterised. Mould contraction during casting is closely related to the dimensional stability of the cast article therefore it is important to understand both the amount and the repeatability of shell materials. The technique was also able to detect volumetric phase transformations occurring in shell materials containing species exhibiting such behaviour.

Initially thermal expansion measurements were performed at Ross Ceramics using a Linseis L75 Platinum Series vertical dilatometer, however due to several failures of this machine and its subsequent limited availability it was necessary to switch to another Linseis L75 vertical dilatometer of similar design and performance. Each machine was calibrated using a polycrystalline alumina standard to ensure repeatability between measurements. In order to gain the most accurate reproduction of the shell expansion during the casting cycle thermal expansion measurements were performed on shell specimens cut from test pieces which had been subjected to the pre-fire cycle of 800 °C for 60 minutes. Sample dimensions were approximately 20 mm x 5 mm x 5 mm and prior to measurement had primary and primary + 1 coats ground off using a diamond saw; this ensured that any variation inherent in the behaviour of these coats did not influence the measurements. The temperature cycle for the measurements is given in Figure 3.16. In order to ensure repeatability of the measurement 2 samples of each material were tested, unless otherwise stated the results of each run were in agreement.

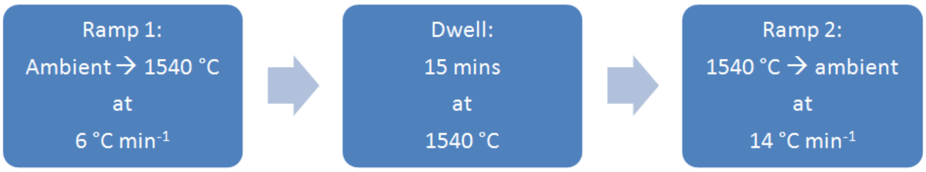

FIGURE 3.16: Temperature cycle used for thermal expansion testing.

Thermal expansion samples are orientated such that expansion is measured parallel to the shell layers since the largest contraction experienced by the mould during the casting is in this direction, that is along the aerofoil. In relation to RX performance it is the contraction in this direction that is potentially responsible for inducing strain in the metal during cooling.

3.1.4 Particle Size Distribution

The particle size distribution (PSD) of raw materials can affect both the mechanical properties of the shell materials themselves and also in the case of filler materials the rheology of slurry systems. Although material suppliers provide PSD information about their products it was still necessary to verify these results on raw materials using the same technique to eliminate any variation in supplier measurement techniques. The PSD of raw materials was measured using a combination of sieving and laser-diffraction which are discussed in the following sections. It was necessary to use the techniques in combination as a wide range of particle sizes are employed in the manufacture of shell moulds ranging from several microns for the finest filler materials to almost 800 microns for the coarsest stucco materials.

In order to perform accurate and meaningful measurements of PSD it was necessary to obtain samples that were representative of the raw material. Generally sampling within the investment casting industry is performed by simple grab sampling in which samples are physically removed from the material surface. In order to perform more robust measurements samples taken for this work were generated using a manual riffle. Incoming samples of initial mass 25 kg were subdivided into two equal portions, one of these portions was then riffled again and the process repeated until a sample of approximately 100 g was obtained.

The spread of the particle size distribution was calculated using equation 3.7; d_{90}, d_{50} and d_{20} were estimated from particle size distributions measured using a combination of sieve analysis and laser diffraction.

$$\text{Spread estimate} = \frac{d_{90} - d_{20}}{d_{50}} \tag{3.7}$$

3.1.4.1 Sieving

Sieving was performed using an Endecotts Octagon 200 automatic sieve shaker with a nest of sieves featuring an approximate Renard R20/3 progression as shown in Table 3.6. The Renard progression recommended by Merkus [84] is calculated from a first sieve with 45 micron apertures; subsequent sieves in the nest feature apertures with apertures approximately 1.413 larger than the previous; see Equation 3.8. Due to equipment availability it was not possible to use sieves which concurred exactly with the Renard series however the discrepancy was minimal; for greater resolution in the 125 µm - 180 µm range a 150 µm sieve was also included. Samples were sieved for 30 minutes with the machine amplitude set at 6; 50 g samples were used unless otherwise stated.

$$\text{R20/3} \Rightarrow \text{progression} = 10^{\frac{3}{20}} \approx 1.413 \tag{3.8}$$

Sample mass of approximately 100 grammes was used in order to ensure sufficient sample material to represent the whole. Typically sieve agitation was carried out for 20 minutes which was sufficient to ensure a change in retained material of less

TABLE 3.6: Typical U.S. Mesh sizes and their S.I. equivalents.

Sieve Aperture μm	
Renard	Actual
1423	1400
1007	1000
713	710
505	500
357	355
253	250
179	180
-	150
127	125
90	90
64	-
45	45

than 1 % for any given sieve. Particle size distributions measured by sieving are reported for each measured material in section 3.2.

3.1.4.2 Laser Diffraction

The passing fraction during sieving was further analysed using laser diffraction. The machine used was a Coulter LS130 capable of measuring a typical sample mass of 0.5 g. Prior to measurement the sample is dispersed in de-ionised water; to aid this process Dispex A40 dispersing agent and ultrasonics are employed. In order to commence measurement the machine tests the obscuration of the sample, if this is incorrect this can be adjusted by varying the concentration of the sample. Due to this adjustment process it was not possible to record the final concentration. PSD measurements were made using the Mei model. Results were recorded computationally and are presented for each material in the following section.

3.1.5 Scanning Electron Microscopy

In order to investigate the microstructure of shell specimens they were examined using a JEOL 6060 Scanning Electron Microscope (SEM). Prior to imaging the samples required processing using the steps shown in Figure 3.17.

FIGURE 3.17: Process for preparing shell samples for SEM analysis

Shell samples were mounted in Struers EpoFix epoxy resin, and vacuum impregnated using a Struers Epovac; this caused the resin to be drawn into pores within the shell material. Impregnation was performed at room temperature. Following evacuation samples were held at the minimum pressure achieved (indicated as -800 mbar) for 120 seconds before being cycled back to room temperature; to ensure the samples were thoroughly impregnated this process was repeated 3 times. Samples were polished using a Struers DAP-7 automatic sample polisher; polishing pads and media used are listed in Table 3.7.

TABLE 3.7: Details of plates and media used during polishing process for shell specimens. Polishing was performed in descending order.

Polishing Plate	Duration (mins)	Polishing medium	RPM
Piano	9	Water	250
Allegro	9	9 kds	125
Largo	9	3 kds	125
Dac	9	1 kds	125

In order to image using the SEM polished samples must be coated with a conductive material such as gold or carbon for imaging or elemental analysis respectively; this was performed using a Polaron SC7640 sputter coater using an acceleration current of 20-30 mA for 180 seconds. The final step is to paint Acheson Silver DAG 1415M onto the edges of the coated samples to ensure adequate conductivity to prevent charging of the sample surface during imaging. Imaging was performed under high vacuum using primarily secondary electron detection; acceleration potentials are given on micrographs.

3.1.6 Image analysis

Electron micrographs produced using the SEM technique described in the previous section were analysed using a freeware program known as ImageJ. Using this technique it was possible to estimate the level of porosity and also the volume percent stucco and other particles within the shell material. It is pertinent to mention that due to the SEM images representing cross-sections of the shell material all measurements of area % will only provide an indication of the true volume % of any features contained within the shell material.

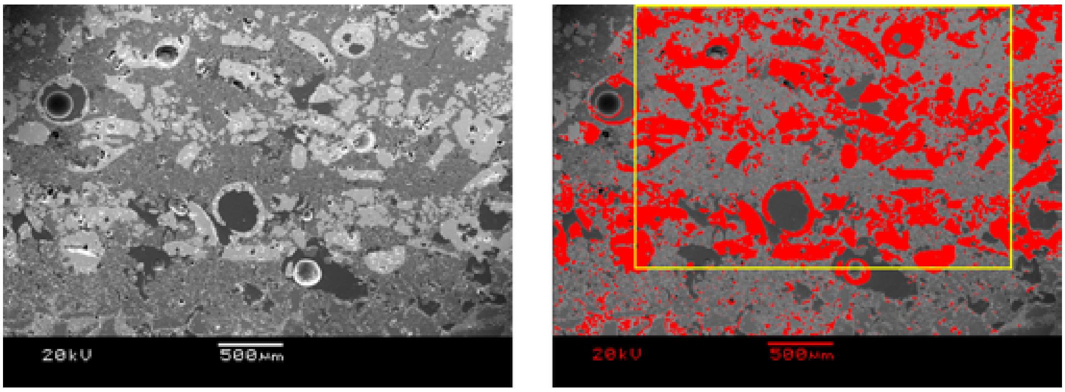

FIGURE 3.18: SEM micrograph of a zirconia containing shell system analysed using ImageJ. In this example threshold levels have been set to an appropriate level to correctly highlight stucco particles.

In order to reduce areas of brightness associated with charging of the sample surface during the SEM process, images were processed using a median filter with a radius of 2-pixels followed by a Gaussian blur again with a radius of 2-pixels. The final step before measurement was to set an appropriate threshold value to select the species to be analysed; this was done manually for each image to ensure that measurements correctly reflected the structure of the samples. Figure 3.18 shows an example of a micrograph of a shell material containing unstabilised zirconia stucco. The threshold has been chosen to highlight the presence of zirconia particles; area measurement is performed automatically by the software. For all images the area of analysis (denoted by yellow rectangle) is chosen to be away from both the black information bar and the primary and primary + 1 stucco coats to prevent skewing the measurements. Results of image analysis are presented within the thesis however for clarity, analysed images are omitted.

3.1.7 Zeta Potential

Zeta potential measurements were performed on several colloidal silica binders and also some ceramic filler powders in order to assess their stability towards particle aggregation across a range of pH values. Measurements were performed at Leeds University using a Colloidal Dynamics ZetaProbe which is shown schematically in Figure 3.19.

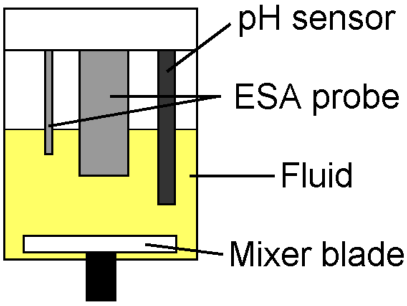

Figure 3.19: Schematic diagram showing the configuration of the ZetaProbe fluid vessel

Zeta potential measurements are calculated automatically from measurements of the Electro-Sonic Amplitude of the fluid (ESA) (see Section 2.8) and are recorded by computer along with the output from the built-in pH meter. The ESA probe features an integral temperature sensor the output of which was also recorded. The rotary mixer blade at the bottom of the vessel provides agitation during testing which serves to both allow acid and base additions to be dispersed and also keep dispersed powders in suspension during the test. The machine features an automated dosing system for acid and base additions, however on this particular machine this system was non-functional and as such acid and base additions were made manually using a pipette. For all testing acid and base additions were hydrochloric acid and potassium hydroxide respectively both of which were obtained from Sigma Aldrich. Zeta potential measurements subsequent to pH alteration were not made until the pH had stabilised; for each pH value the Zeta potential measurement was performed 5 times. Inputs required by the machine to enable calculation of zeta potential include particle concentration (wt %), particle density (kg.m^{-3}) and dielectric constant; where measurements are subsequently presented values used for calculation will be stated.

3.1.8 Viscosity Measurement

Viscosity measurements were made on a number of slurries based on the alumina and silica system. In order to understand the effect of the surface charge of the particles within the slurry on the slurry stability these measurements were performed at a number of different pH values. The viscosity measurements were made using a TA Instruments AR500 rheometer equipped with a stainless steel 40 mm flat plate geometry. Testing was performed using a continuous ramp (up and down) shear stress rate over a period of ten minutes; all testing was performed at a constant temperature of 20 °C. The results of these experiments are presented in Chapter 7 along with supporting data from sedimentation and zeta potential experiments.

3.1.9 Sedimentation Experiments

To characterise the flocculation behaviour of several silica and alumina slurries a number of sedimentation experiments were performed; details of the slurries tested can be found in Table 7.1. Slurries were mixed in batches of approximately 400 grams for 30 minutes using an overhead mixer as used previously. Following this, slurries were decanted into 50 ml centrifuge vessels prior to having their pH adjusted to the required level through the addition of acid or base. The acid and base used were as described in section 3.1.7 and additions were as before made manually using a pipette. Following pH adjustment the slurries were transferred into 25 ml measuring cylinders and allowed to settle; an initial measurement of the height of each sediment was made using digital vernier callipers after 30 seconds. The final sediment height was recorded after 48 hours. In order to prevent error due to evaporative losses, the tops of the measuring cylinders were sealed.

3.2 Materials

A number of materials were utilised during experimental work to support this thesis. A number of techniques were employed to determine their properties and characteristics, the results of these tests are presented in the following sections. The properties of some widely used ceramic materials are given in Table 3.8.

Table 3.8: Material property data for ceramic materials employed in trial formulations. All information (unless otherwise stated) from [85]

Material	Density	Melting Temperature	Thermal Expansion
	(kg.m^{-3})	(℃)	(x10^{-6} K^{-1})
Alumina	3.4 - 4.0	2050 [86]	9.6 (1000℃) [36]
Mullite	3.15	1850 [87]	5.3 (1000℃) [87]
Zirconia	5.73	2700 [37]	15.3 (1273) [88]

3.2.1 Binders

A number of colloidal silica binders were evaluated over the course of shell development, details are given in Table 3.9. The difference in performance of colloidal silicas stabilised by aluminium modification and sodium stabilisation are discussed in sections 2.7.3 and 2.7.2 respectively.

TABLE 3.9: Details of colloidal silica binders used during formulation trials. Data reproduced from material datasheets.

Name	Type	Polymer	Natural pH	Silica Content (wt %)
Ludox HSA	Al-modified	None	3.5 - 5	25
Ludox SK-CV	Al-modified	PVOH	3.5 - 5	25
Ludox SK-R	Al-modified	PVOH	3.5 - 5	25
Wexcoat	Na-stabilised	None	10.2 - 10.5	25
Hi-S	Na-stabilised	None	10.5	32.7
Remasol Ultra	Na-stabilised	Latex	9.9 - 10.5	24
Morrisol	Na-stabilised	None	9.5 - 10.3	30
EHT	Na-stabilised	None	9.2 - 10.2	38

Figures 3.20 and 3.21 show zeta potential variation as a function of pH for 5 relevant binder materials; both Ludox SK-CV and SK-R are based on Ludox HSA and hence the results of HSA were taken to be representative of all Ludox binders. All binders other than Ludox HSA were sodium stabilised and had natural pH in the alkali range. All binders however exhibit acceptable surface charge at intermediate and alkali pH values.

It was observed that the aluminium-modified silica particles within the Ludox HSA binder exhibited a minimum Zeta potential greater than 40 mV across all pH values tested. In contrast, all sodium stabilised binders exhibited significantly lower zeta potentials at acidic pH. These results were consistent with the theory that aluminium modified binders retain surface charge due to the embedded aluminate ions on their surface. Sodium stabilised binders, which rely on the presence of

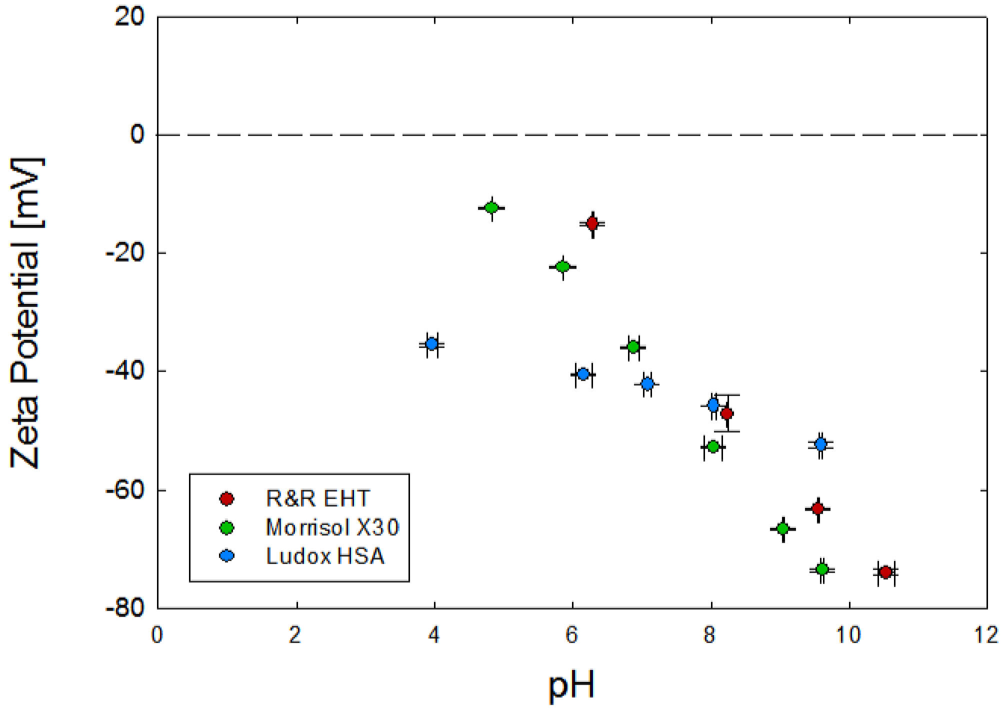

FIGURE 3.20: The effect of pH variation on zeta potential for 3 Rolls-Royce binder materials. Ludox HSA is an aluminium modified binder with native pH 4.0. Morrisol X30 and R&R EHT are both sodium stabilised and have native pH approximately 10.

hydroxyl ions for their surface charge, lose their stabilisation in the presence of hydrogen ions.

3.2.2 Aluminium Oxide

Aluminium oxide, otherwise known as alumina, is a widely used refractory mineral with chemical composition Al_2O_3; a number of different alumina types are available, however alpha alumina was used throughout this work. Three types of alumina were utilised in trial formulations as part of this thesis, tabular alumina made via the Bayer process is a standard Rolls-Royce stucco material (28/48 mesh) and was also evaluated as a filler material in 200 mesh grade. Reactive alumina, so-called for its high surface area, is another standard Rolls-Royce material featured in the Hi-shell system as one of the ingredients designed to enhance the

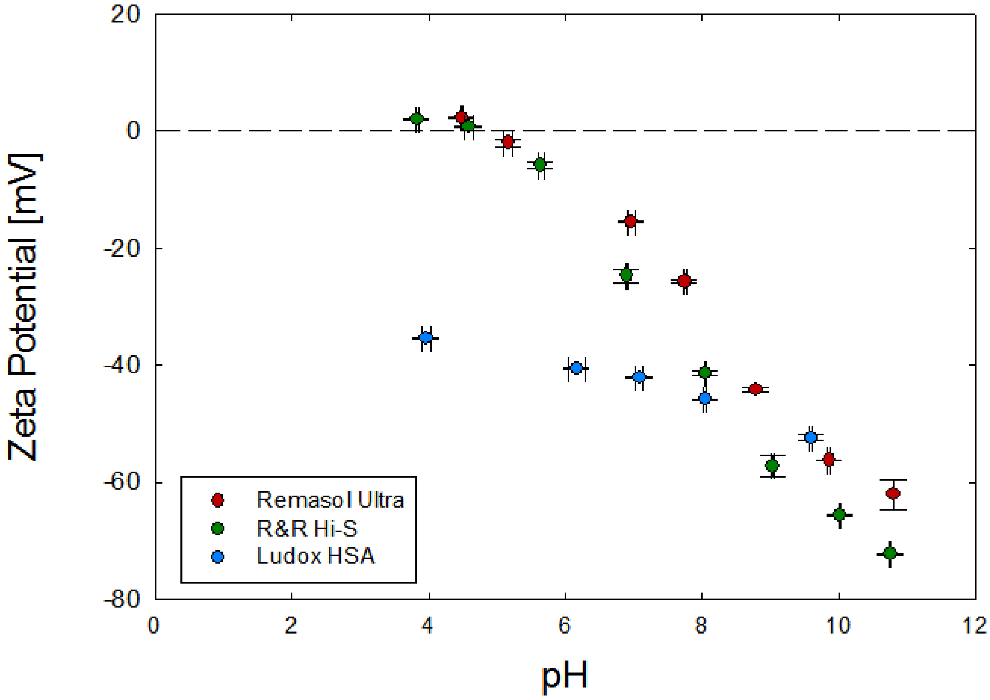

FIGURE 3.21: The effect of pH variation on zeta potential for 3 binders used in trial shell systems. Ludox HSA is an aluminium modified binder with native pH 4.0. Remasol Ultra and R&R Hi-S are both sodium stabilised and have native pH approximately 10.

synthesis of mullite in the shell. Fused alumina, produced by electro-fusing tabular alumina is used as a standard primary coat stucco by Rolls-Royce in an 80 mesh (180 µm) grade, it was also evaluated as a 200 mesh (75 µm) filler material for trial purposes. The alumina types used in the trial shell systems are reported along with their properties in Table 3.10.

TABLE 3.10: Details of various types of alumina featured in candidate shell systems

Material	Supplier	Type	Application
PFR15	Rio Tinto Alcan	Reactive	Filler
WRG IC-F200	Treibacher Schleifmittel	Fused	Filler
Duralum F80	Washington Mills	Fused	Stucco
CerTab 200 #	Cermatco	Tabular	Filler
CerTab 28/48	Cermatco	Tabular	Stucco
Aluchem	Aluchem	Tabular	Filler

The particle size distribution of each alumina powder was determined through a combination of sieve analysis and laser diffraction, particle size distributions are shown in Figure 3.22.

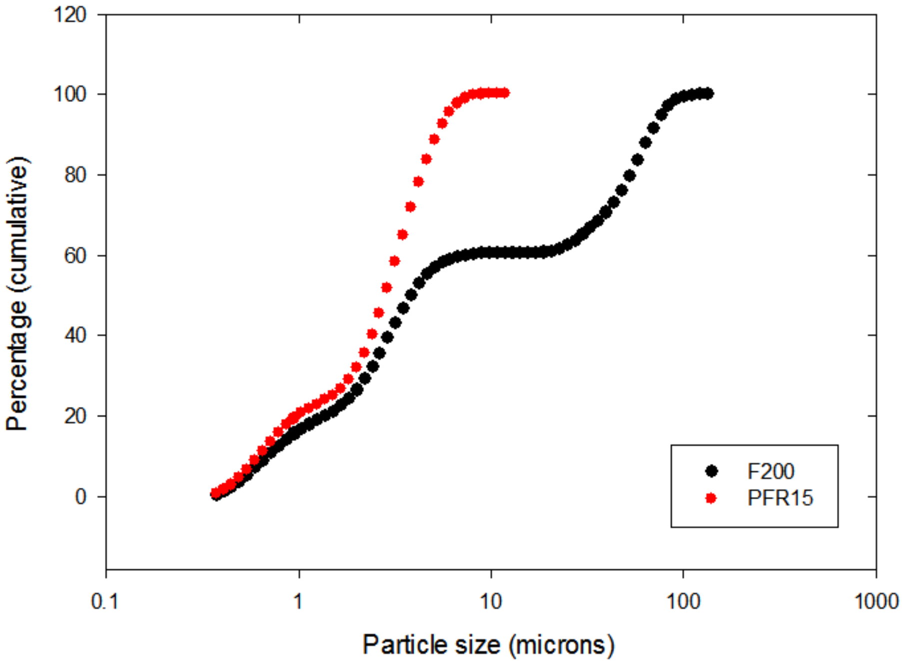

FIGURE 3.22: Particle size distribution for F200 and PFR15 alumina powders analysed using laser diffraction.

To understand the stability against aggregation of fused alumina and reactive alumina the zeta potential of each was measured over a range of pH values, the data is presented in Figure 3.23.

The results of zeta potential testing on different alumina types were consistent with expectations. Assuming the surface charge density of the alumina particles was approximately constant, it is natural to assume that the higher surface area PFR15 would exhibit greater overall charge than the larger F200 particles. The results suggested that in isolation, dispersions of PFR15 should be more stable to aggregation than dispersions of F200 particles, however no allowance was made for the physical effects of having larger particles. The stability of alumina in suspension is discussed in greater detail in Chapter 7.

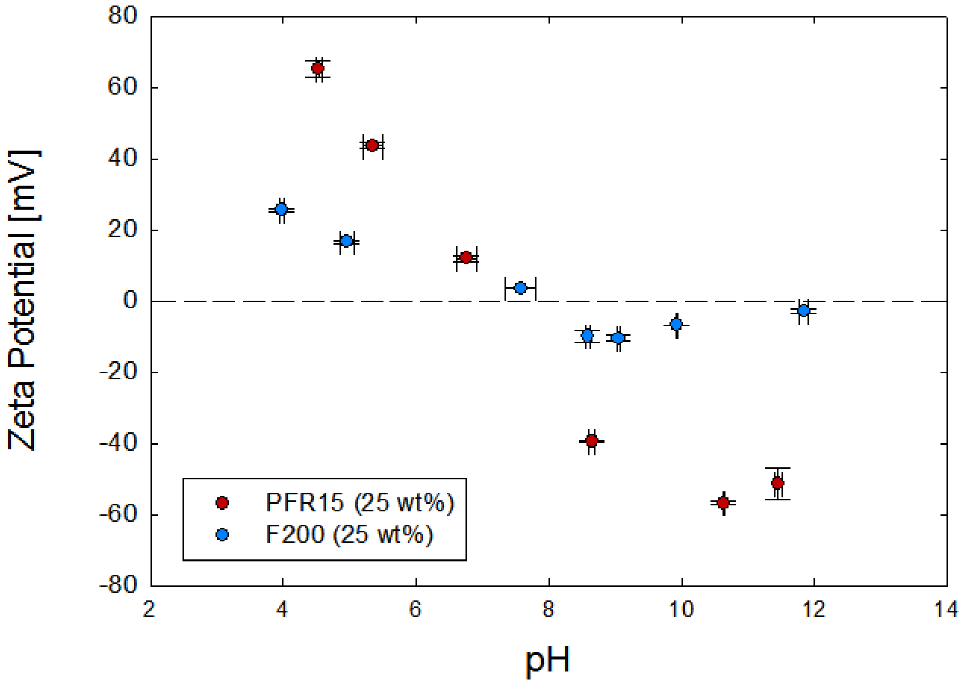

FIGURE 3.23: The zeta potential variation with pH of PFR15 reactive alumina and F200 fused alumina

3.2.3 Zirconium Dioxide

One of the main aims of this thesis is the formulation of a shell system with reduced propensity to induce recrystallisation. One of the proposed techniques to achieve this was the inclusion of unstabilised zirconia as discussed in Chapter 2.

During the early formulation stages it was proposed that zirconia should be used both within the shell as a filler constituent and as a stucco material; the initial grades selected from ABSCO materials reflect this, see Table 3.11. During initial development however it was observed that systems containing zirconia as a filler material exhibited undesirable slurry behaviour, this is discussed further in Chapter 5. A number of stucco materials used during the trials in order to explore the effect of particle size and also the type of particles used. The ABSCO material referred to as *blown* hereafter, is known to have hollow grains and therefore reduced density, all other materials have dense solid grains; this effect is shown in Figure 3.24. Unfortunately the supplier of the material was not willing to reveal the manufacturing process used to produce the hollow zirconia material, however it is likely that the material was produced in a process similar to spray drying.

TABLE 3.11: Various zirconia types and grades utilised during the development of the ZF shell system.

	Particle Size				
Supplier	Mesh size	d_{50} (µm)	Spread	Type	Application
ABSCO	30/60	500	0.43	Blown	Stucco
WM	35/60	401	0.21	Dense	Stucco
	20/35	661	0.38	Dense	Stucco
UCM	30/100	325	0.71	Dense	Stucco
	30/60	363	0.37	Dense	Stucco
Foskor	30/60	362	0.44	Dense	Stucco

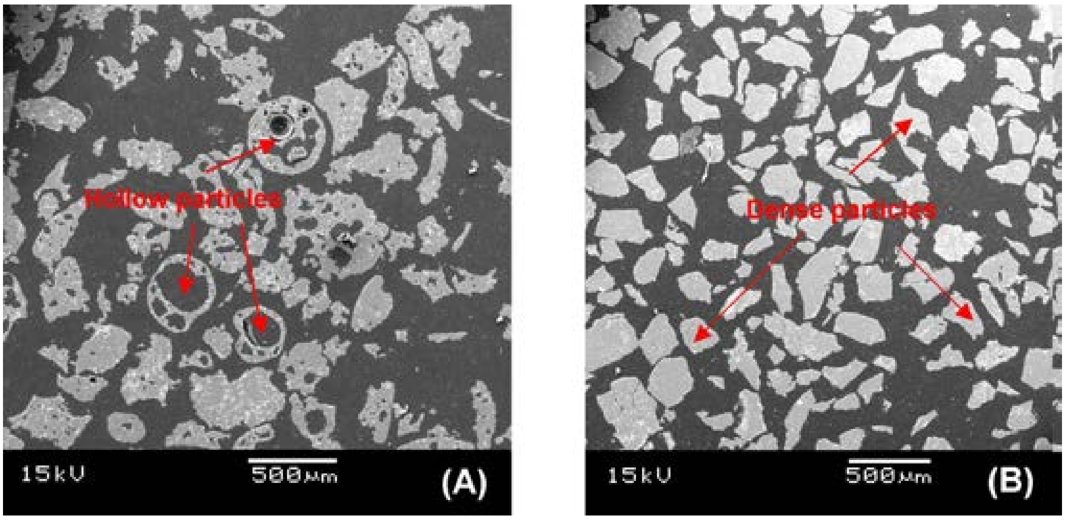

FIGURE 3.24: Polished section micrographs of two zirconia stucco materials; (A) shows ABSCO blown zirconia particles, (B) shows Washington Mills conventional dense particles.

The particle size distribution of each zirconia stucco was analysed using sieve analysis, the results are summarised in Table 3.11 and shown graphically in Figures 3.25 to 3.30.

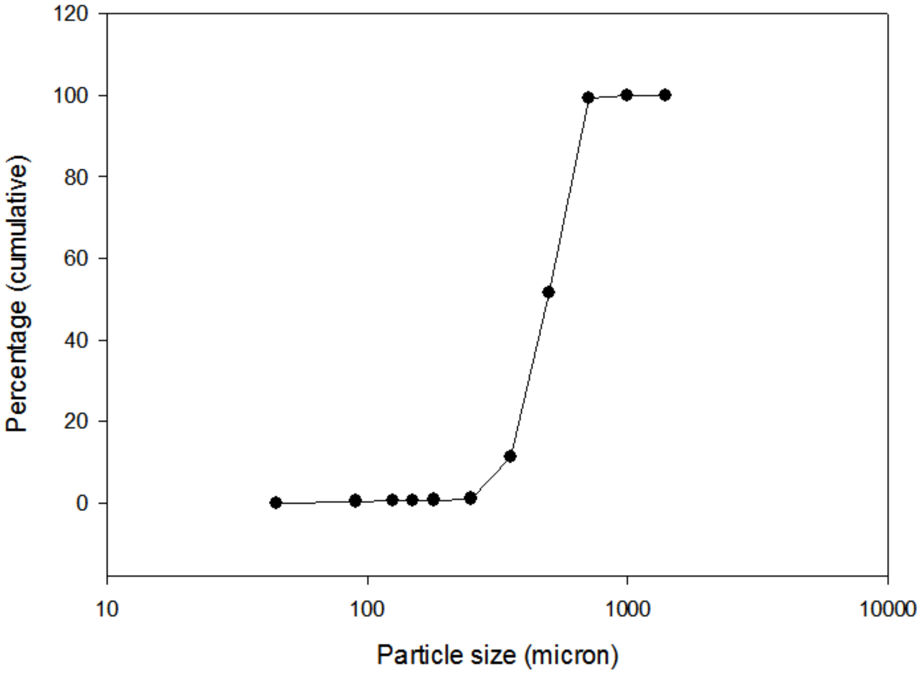

FIGURE 3.25: Particle size distribution for 30/60 mesh ABSCO unstabilised zirconia stucco analysed through sieve analysis.

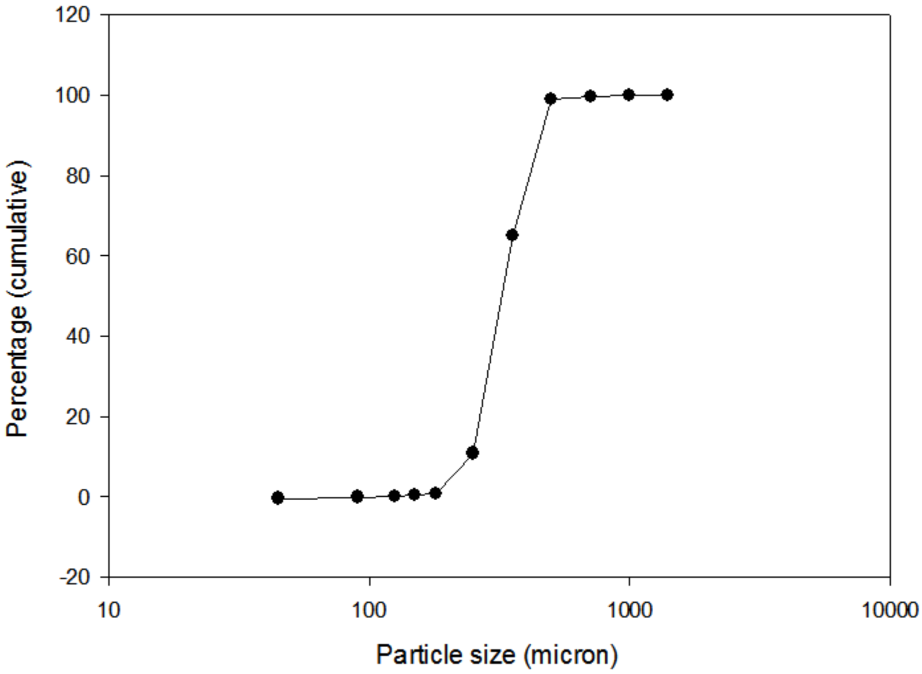

FIGURE 3.26: Particle size distribution for 30/60 mesh Foskor unstabilised zirconia stucco analysed through sieve analysis.

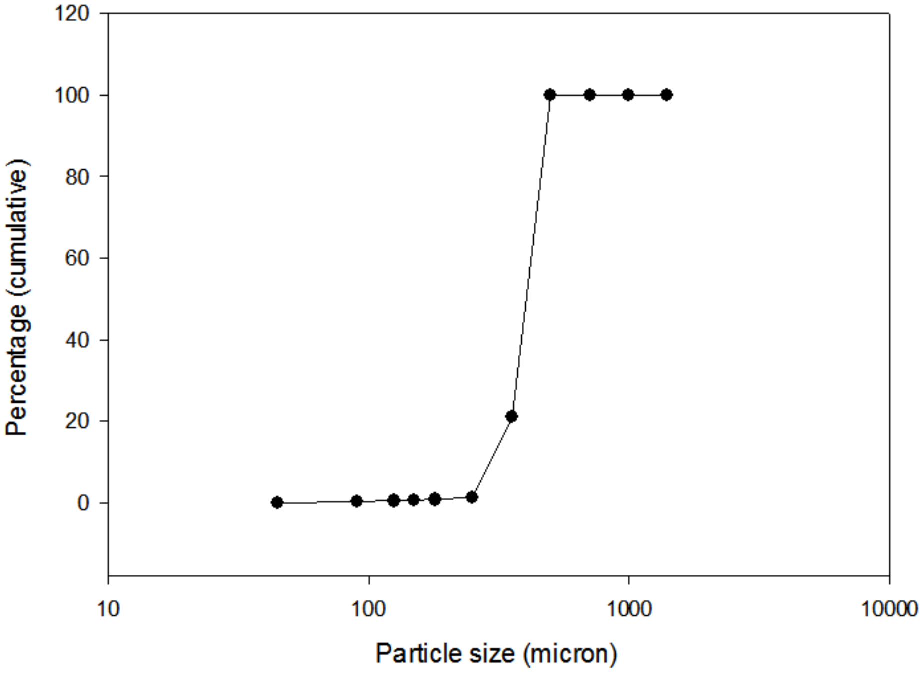

Figure 3.27: Particle size distribution for 30/60 mesh Washington Mills unstabilised zirconia stucco analysed through sieve analysis.

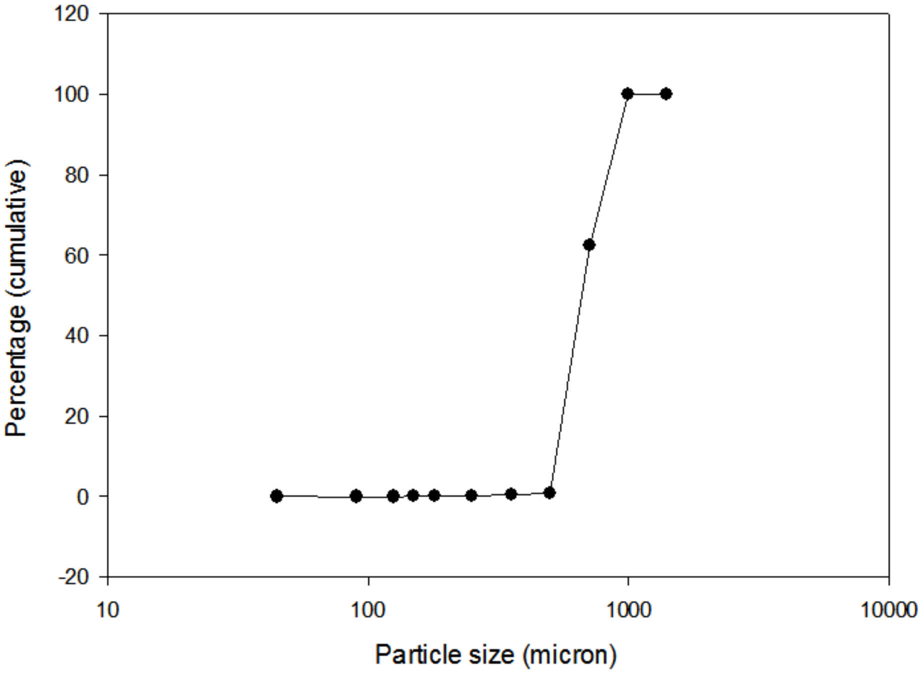

Figure 3.28: Particle size distribution for 20/35 mesh Washington Mills unstabilised zirconia stucco analysed through sieve analysis.

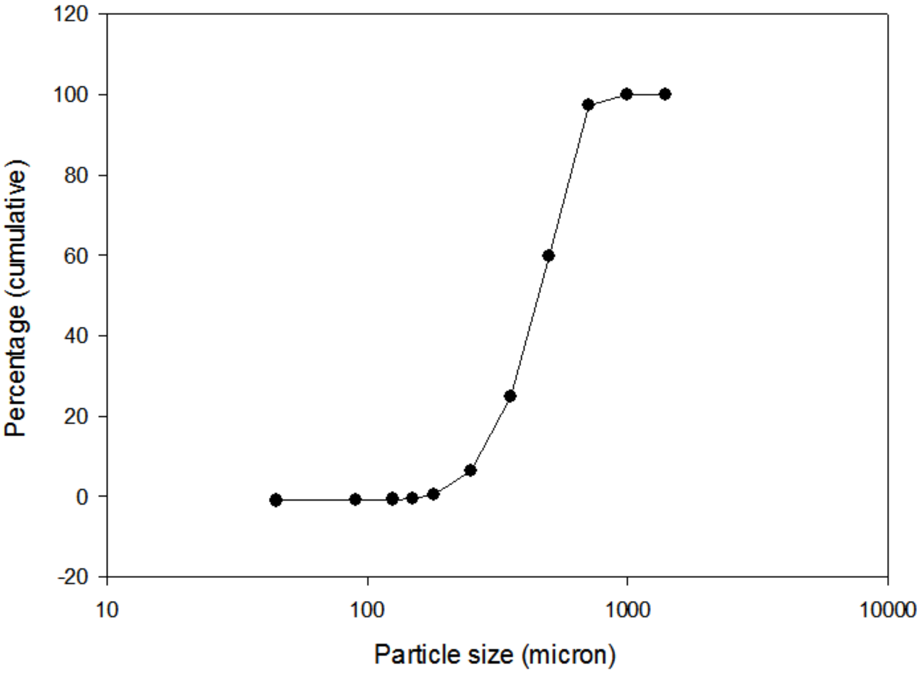

FIGURE 3.29: Particle size distribution for 30/100 mesh UCM unstabilised zirconia stucco analysed through sieve analysis.

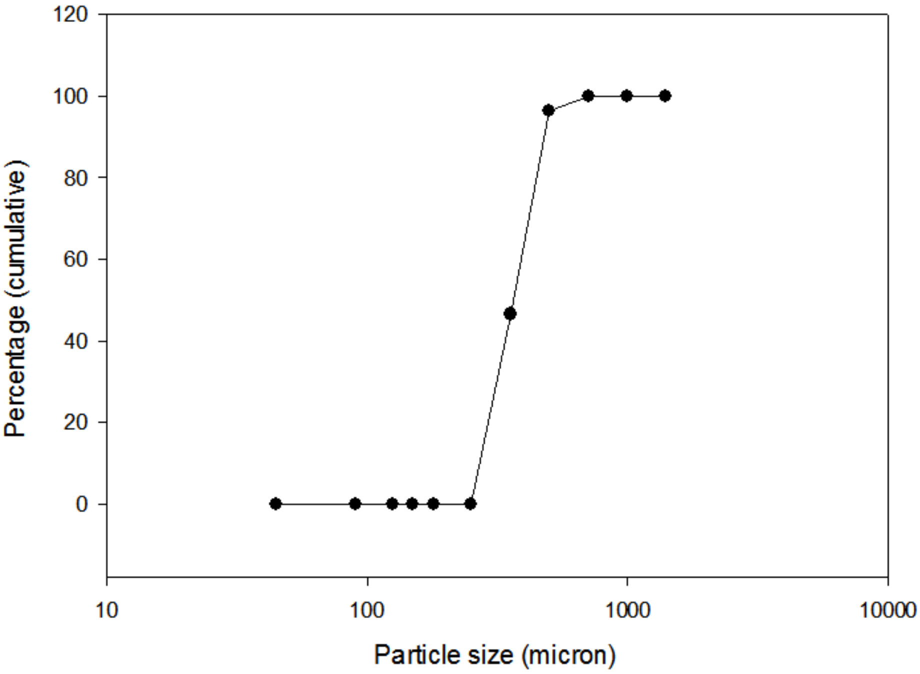

FIGURE 3.30: Particle size distribution for 30/60 mesh UCM unstabilised zirconia stucco analysed through sieve analysis.

3.2.4 Mullite

Mullite is a refractory alumino-silicate material with composition $3Al_2O_2.2SiO_2$. It is widely used in ceramic materials due to its high creep resistance at elevated temperatures (see section 2.3.2). The materials utilised in this thesis were supplied by Washington Mills, USA via Rolls-Royce and are identical to those used in the Hi-shell system shown in Table 3.12.

Table 3.12: Mullite grades utilised within Next-Generation candidate shell systems.

Name	Supplier	Type	Application	Spread
Duramul 0.04	Washington Mills	Fused	Filler	2.41
Duramul 0.07	Washington Mills	Fused	Filler	2.78
Duramul 0.25 - 0.50	Washington Mills	Fused	Stucco	0.51

A large number of suppliers exist for fused mullite, however, the existing agreement between Rolls-Royce and Washington Mills simplifies the process of acquiring and validating material should it be required for production. Logistically it is also favourable to have commonality between raw materials for different shell systems where possible.

As mullite is used as a slurry material it was also useful to characterise its zeta potential, this was performed as detailed in the previous section. The zeta potential curve is given in Figure 3.33 along with that of Wexcoat, a conventional sodium stabilised binder and also Ludox HSA, an aluminium modified binder.

It can be seen from the zeta potential data that at pH 5.5 the mullite powder exhibited its isoelectric point. Above and below this point the surface charge of the particles were positive and negative respectively. Although the results suggest that Ludox HSA is capable of operating in an acidic pH range, the results also show that the silica and mullite particles are stabilised by opposite surface charges in the acidic pH range. This could lead to a process known as hetero-coagulation in

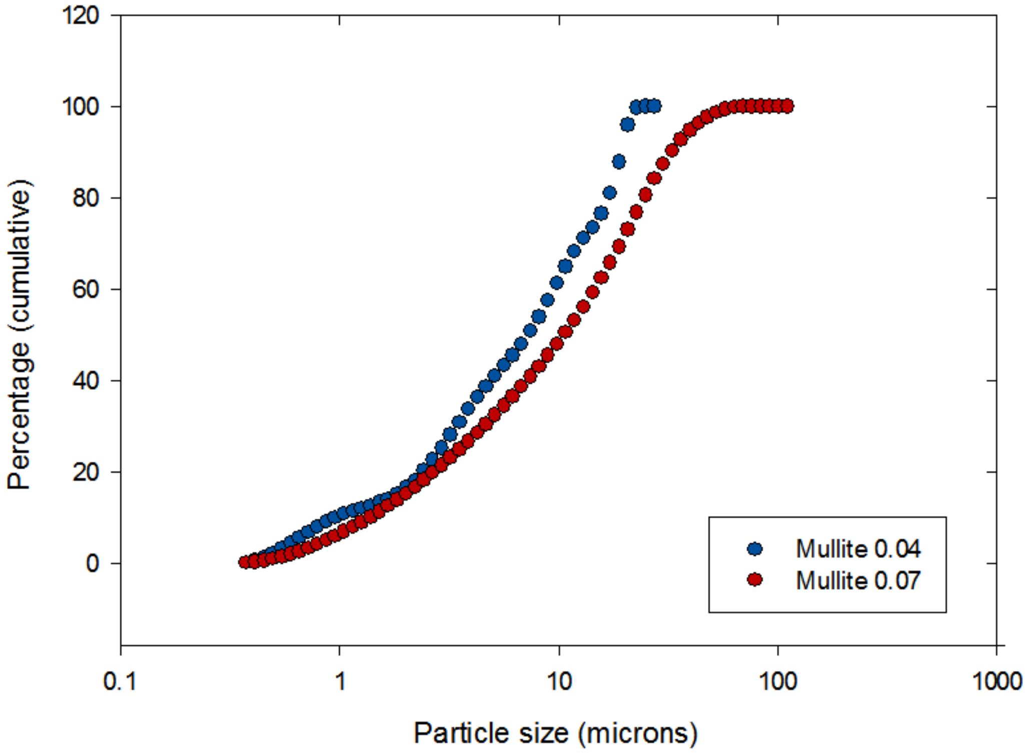

FIGURE 3.31: Particle size distribution for fused mullite filler powders analysed by laser diffraction

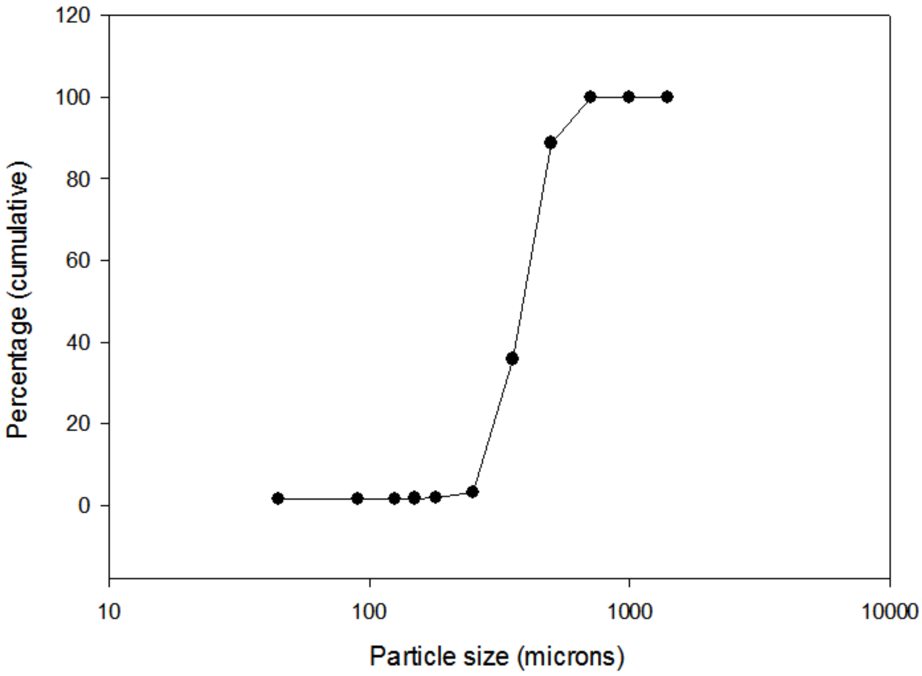

FIGURE 3.32: Particle size distribution for 35/60 mesh fused mullite stucco analysed through a combination of sieve analysis and laser diffraction

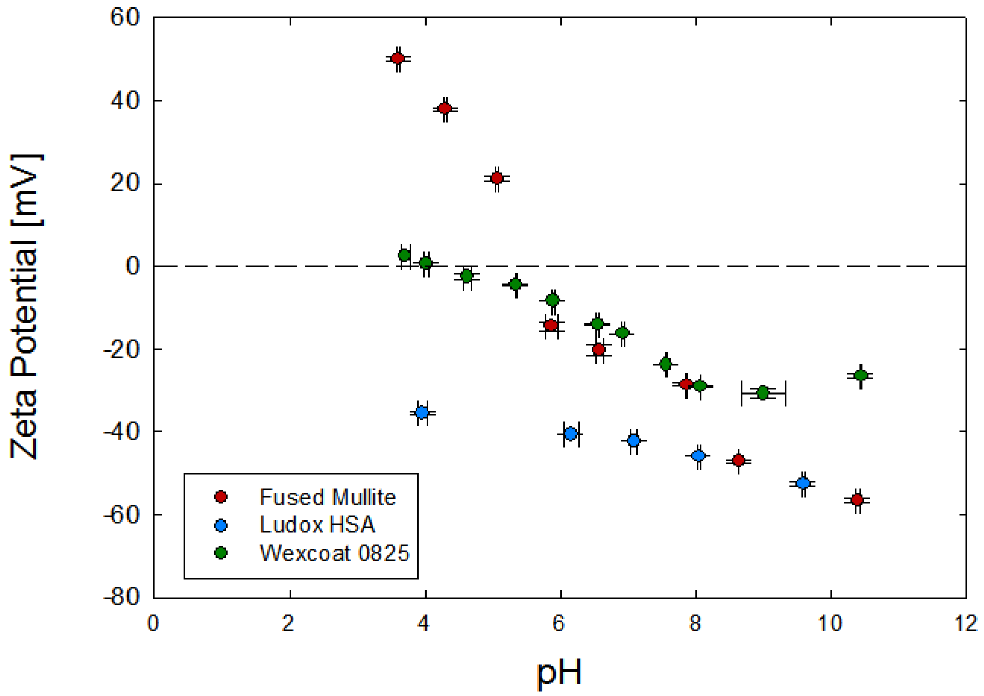

FIGURE 3.33: The zeta potential variation with pH of fused mullite shown along with that of Wexcoat, a conventional sodium stabilised binder and also Ludox HSA, an aluminium modified binder

which particles of opposite surface charge attract one another to form aggregates; this process is discussed further in Chapter 7.

3.2.5 Polyethylene

Polyethylene (PE) powder was chosen as the pore forming agent (PFA) for candidate shell systems featuring fugitive behaviour. The reasons for its choice were the relative cleanliness of its burnout products and good availability; for further discussion see Section 2.5. PE is a widely used raw material in the plastics industry and the particle size distributions of available powders reflect this, the smallest particle size commercially available was approximately 500 microns. This corresponds to the upper range of particles used as stucco materials in investment casting and is well above the range traditionally used as filler materials. The PE powder selected for the project was 500 micron ICORENE high density polyethylene (HDPE) powder from ICO Polymers. As with other powder materials the particle size distribution was characterised by sieving; the results of this can be seen in Figure 3.34.

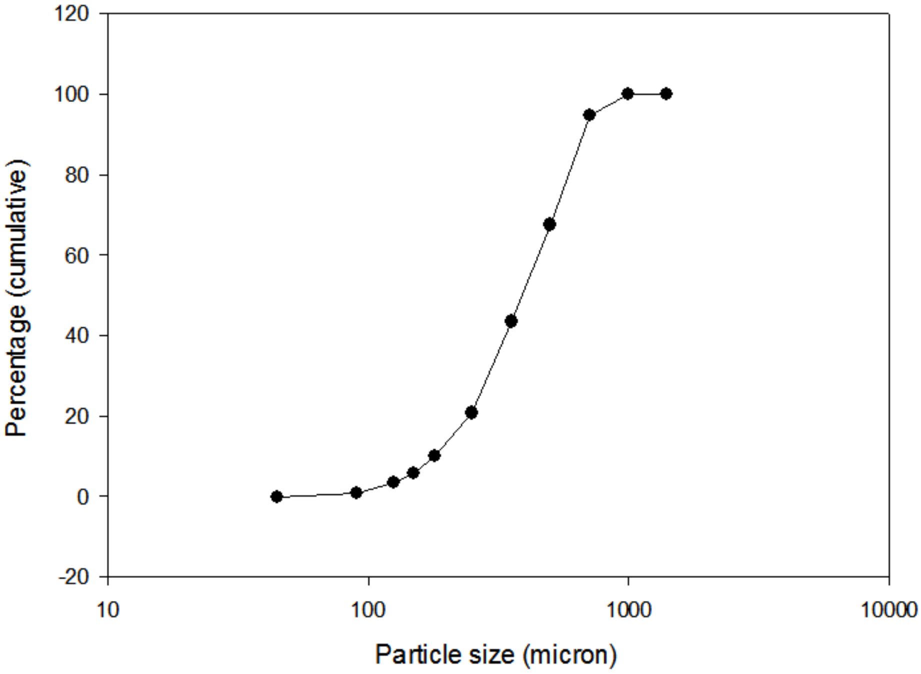

Figure 3.34: Particle size distribution for Icorene polyethylene powder analysed through sieve analysis

3.2.6 Titanium Dioxide

Titania is the oxide of the metal titanium, with the chemical formula TiO_2. It was included in a number of formulations in order to generate tialite via the solid state reaction between alumina and titania within the casting furnace. A 0.2 micron (d_{50}) powder was sourced from ABSCO materials. Due to the small particle diameter the PSD was measured only using laser diffraction, the results are presented in Figure 3.35. The spread value was 9.57.

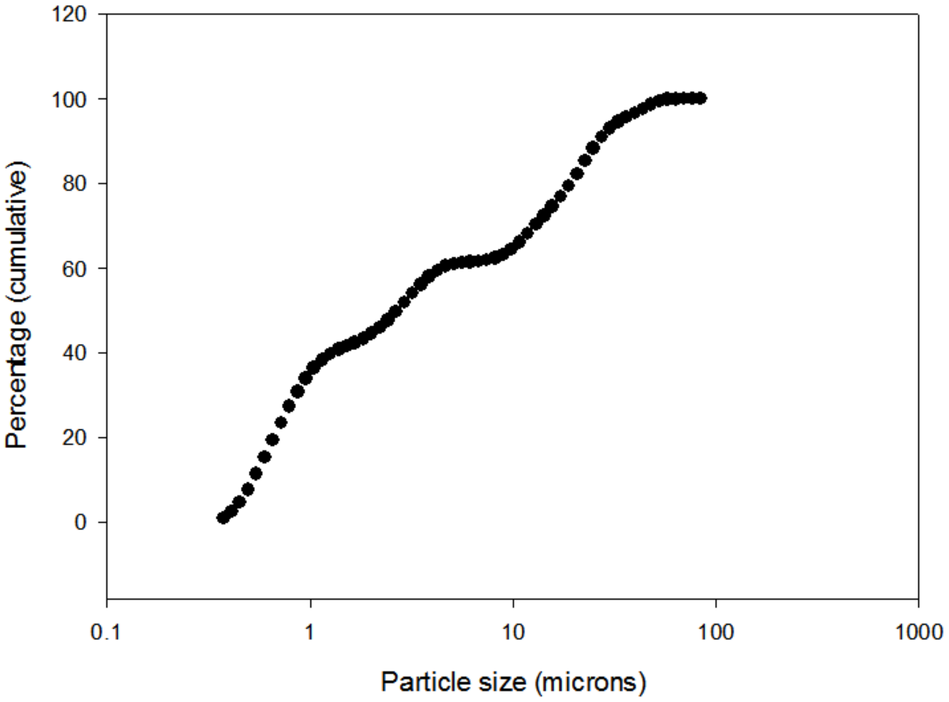

Figure 3.35: Particle size distribution for ABSCO titania powder analysed using laser diffraction

4

Thermally disruptive shell systems

4.1 Introduction

This chapter reports the development of investment casting shell systems employing the use of thermally disruptive materials in order to deliberately reduce their mechanical properties as the mould material cools from the casting temperature. The different stages of research are presented in separate sections containing trial formulations used, results and discussion relevant to each. Finally conclusions about the use of thermally disruptive shell systems are drawn in the final section.

4.2 Trial formulations: Stage 1

Initial trials were conducted on systems containing unstabilised zirconia as both a stucco and a filler material; the properties of this material were discussed in more detail in section 2.4.2. A number of trial systems were formulated to investigate the effect of thermal disruption on mechanical and thermal properties and are described in the following sections.

Zirconia systems

Four trial formulations were developed utilising unstabilised zirconia as the stucco material; three slurry matrix materials were used in the trial including tabular alumina, fused mullite and a finer grade of zirconia powder. The latter created what was, excluding the silica binder, a shell material consisting entirely of unstabilised zirconia. The mullite matrix featured a similar formulation to the Rolls-Royce Hi-shell material, which contained fine reactive alumina (d_{50} = 3.1 µm) along with two grades of mullite (d_{50} = 10.7 µm and 7.9 µm); the presence of the fine alumina along with colloidal silica particles present in the binder promotes the formation of mullite in-situ during the firing cycle. For clarity the system utilised in this trial was designated as SiAl2773 to reflect the silica alumina molar-ratio present within the slurry (27 mol % silica and 73 mol % alumina); this naming convention is used throughout this thesis for all systems utilising a combined silica alumina slurry. Table 4.1 shows the formulations of the three ceramic slurries utilised within the trials.

The fourth variant was a hybrid shell system featuring layers of both the mullite and zirconia shell systsms; for clarity the shell build is shown in Table 4.2.

Table 4.1: Slurry formulations utilised for investigation of unstabilised zirconia. Each slurry was stuccoed using the ABSCO unstabilised zirconia stucco material.

			Concentration	
Slurry	Material	Product	Wt %	Mol %
SiAl2773	Silica	Ludox HSA	8.9	27.3
	Alumina	PFR15	58.5	72.7
	Mullite	Duramul 0.04	11.7	
	Mullite	Duramul 0.07	20.8	
Alumina	Silica	Ludox HSA	26.3	-
	Alumina	CerTab 0.07	73.7	-
Zirconia	Silica	Ludox HSA	24.1	-
	Zirconia	ABSCO 0.07	75.9	-

Table 4.2: Shell build for zirconia - mullite hybrid shell system.

	Slurry	Stucco
Coat 1	Zirconia	Zirconia
Coat 2	SiAl 2773	Mullite
Coat 3	Zirconia	Zirconia
Coat 4	SiAl 2773	Mullite
Coat 5	Zirconia	Zirconia
Seal	SiAl 2773	None

It should be noted that all shell specimens discussed within this section were manufactured using 5 stuccoed backup coats; in each case the zirconia stucco material employed was 30/60 grade (500 µm - 250 µm) supplied by ABSCO materials.

Investigating zirconia content

In order to further investigate the effect of zirconia inclusions within a silica alumina (SiAl) based system three additional trial formulations were developed. These trials were conducted simultaneously with those detailed in Chapter 5 into the effect of relative silica alumina concentration within the shell. The SiAl2773 system was therefore developed into four trial systems one of which contained a silica alumina molar ratio of 40:60 as per the Rolls-Royce Hi-Shell system, because of this it formed high levels of mullite during the firing cycle. In order to further investigate the strength reduction effect associated with unstabilised zirconia stucco this system was chosen as the slurry matrix. The formulation of SiAl4060 is shown in Table 4.3. It should be noted that unlike the SiAl2773 system the new variant only contained the larger mullite grade, whilst this had little effect on mechanical properties it simplified the formulation making it more production friendly.

Table 4.3: Formulation of SiAl4060 slurry utilised for investigation of unstabilised zirconia stucco.

			Concentration	
Component	Material	Product	Wt %	Mol %
Binder	Silica	Ludox HSA	9.0	40.8
Filler	Alumina	PFR15	20.8	59.2
Filler	Mullite	Duramul 0.07	70.2	

In order to investigate the influence of zirconia stucco on the shell properties each system contained a different amount of zirconia stucco including full, partial and none; mullite was chosen as the second stucco material. Given the disparity in densities between mullite and zirconia stucco the most repeatable way to perform this was by alternating stucco material between shell layers. Shell builds for the three trial systems are given in Table 4.4.

Table 4.4: Slurry formulations utilised for investigation of unstabilised zirconia. M and Z respectively reflect the use of fused mullite or unstabilised zirconia stucco on a shell layer.

	Stucco material				
System	Layer 1	Layer 2	Layer 3	Layer 4	Layer 5
None	M	M	M	M	M
Partial	M	**Z**	M	**Z**	M
Full	Z	Z	Z	Z	Z

4.3 Results: Stage 1

The shell system utilising unstabilised zirconia as a filler material presented problems during the initial mixing and slurry monitoring stage. The density of zirconia is relatively high at 6 kg.m^{-3} compared to that of other filler materials such as mullite and alumina at 3 and 4 kg.m^{-3} respectively. The mixer blades utilised throughout the initial development (discussed in section 3.1.1) were unable to keep the high-density filler material in suspension; a more traditional non-ringed propeller type mixer blade was employed to counteract this (impeller geometries are shown in Figure 4.1). The rotational speed of the mixer was set such that a slight vortex was apparent at the slurry surface but not so high as to induce air entrainment.

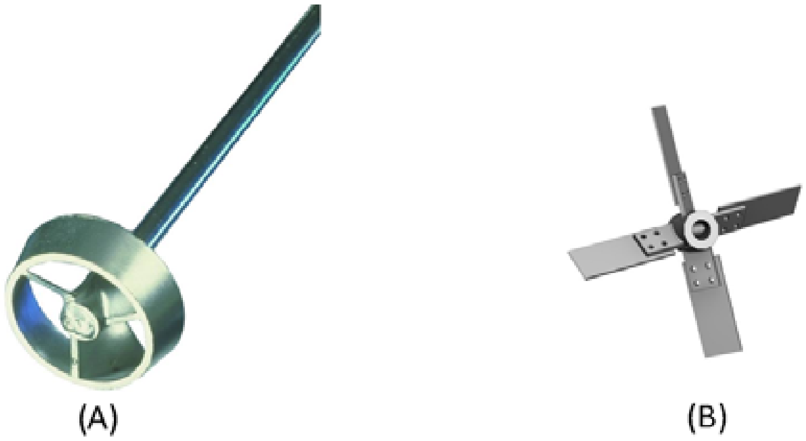

Figure 4.1: Different impeller geometries utilised during lab scale trials. (A) shows ringed impeller utilised for all slurries except that containing zirconia filler which required the non-ringed impeller shown in (B).

The modification allowed the manufacture of shell test specimens but posed a potential problem in terms of up-scaling the system. One of the aims of the thesis was to develop an industrially relevant shell system which could be employed using standard shell-room processing equipment, since the ringed impellers provided insufficient agitation to maintain the zirconia particles in suspension it is likely that a conventional slurry tank would encounter the same problem. It is likely that the level of capital investment required to replicate the shear environment required to retain the zirconia filler material in suspension would, in an industrial application, be prohibitively high.

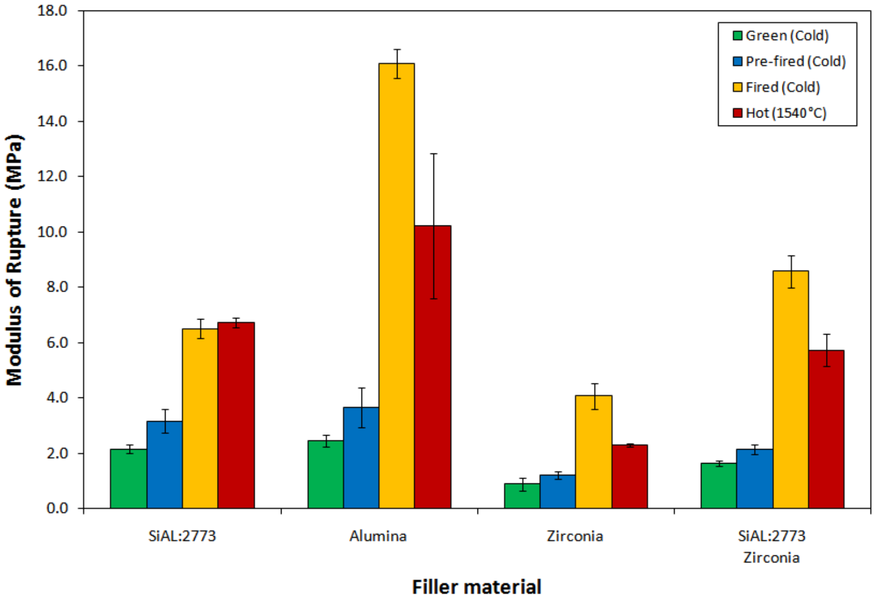

FIGURE 4.2: Results of flexural testing for initial zirconia stuccoed shell materials grouped by slurry matrix. Results are presented for specimens tested across a range of heat treatments; all data excluding those in red were tested at room temperature. Samples in red were tested at 1540 ℃.

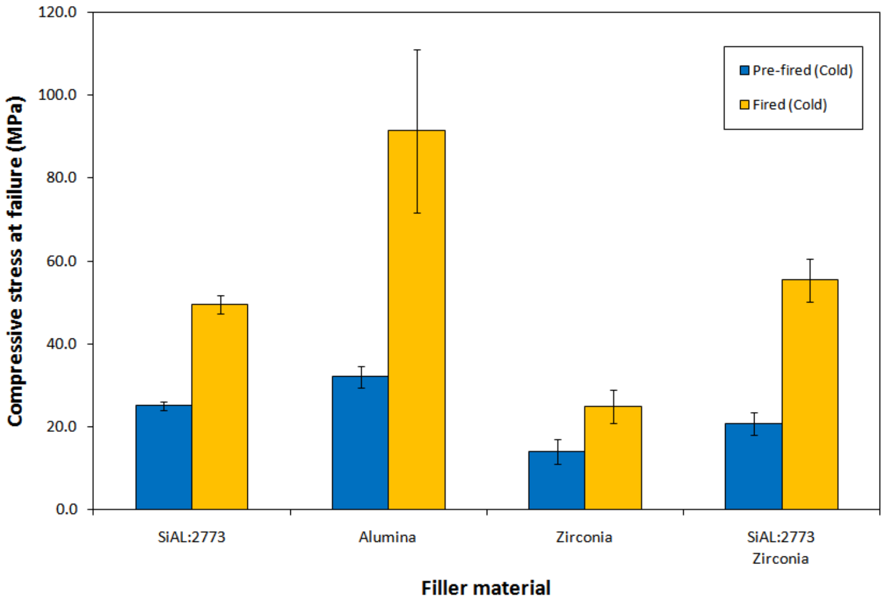

Figure 4.3: Compressive testing results for initial formulations utilising zirconia stucco grouped by filler constituent. Results are presented for specimens tested in pre-fired and fired conditions; all testing was performed at room temperature.

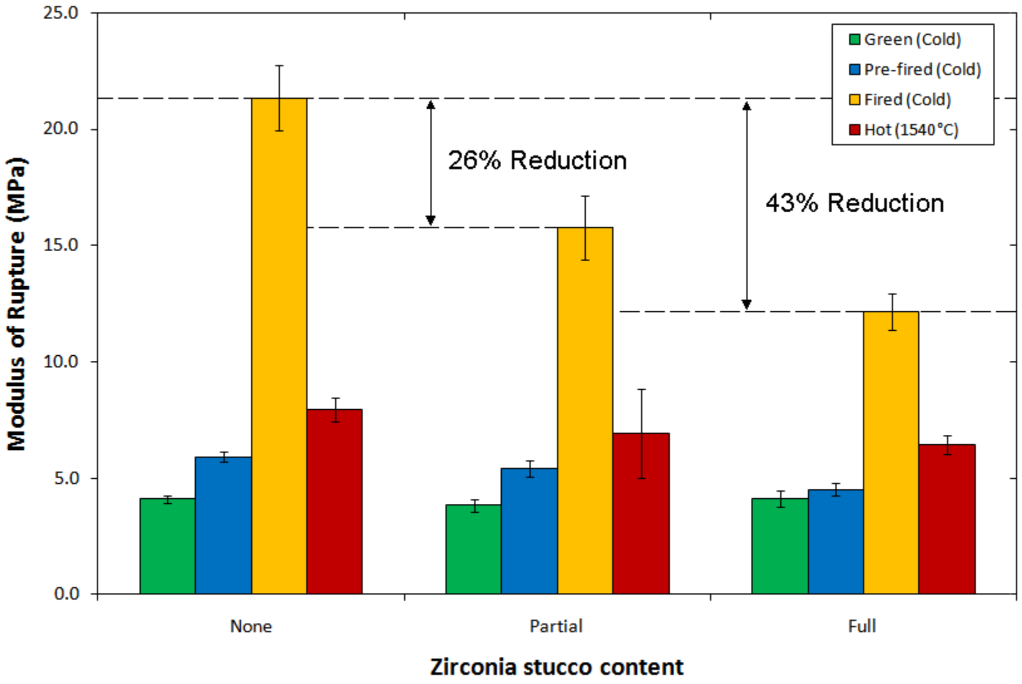

FIGURE 4.4: Results of flexural testing for shell formulations containing varying amounts of zirconia stucco; specimens containing no zirconia were stuccoed using fused mullite, partially specimens featured 2 coats stuccoed with zirconia and 3 with fused mullite, specimens marked full were stuccoed only using zirconia. Results are presented for specimens tested across a range of heat treatments; all data excluding those in red were tested at room temperature. Samples in red were tested at 1540 ℃.

Figures 4.2 and 4.3 show the results of flexural and compressive testing for shell materials containing unstabilised zirconia stucco. It is well known that the combination of colloidal silica and alumina generates shell materials which are high in fired strength [89]; this was also observed in the zirconia containing shell. It was also expected and observed that the system containing zirconia as both a filler and stucco material exhibited the lowest level of fired strength. It is likely that this was due in part to the destructive behaviour of the phase transition, however reduced green and pre-fired strengths compared to other variants would suggest that particle packing and morphology may also have had an effect. Interestingly it was observed that the SiAl system and the SiAl-zirconia hybrid had similar strengths across all states other than in the Fired condition. It is likely that the presence of the full-mullite layers acted to contain cracks generated by the full-zirconia layers thereby reducing the weakening effect. These trends were also noted in the results of compressive testing.

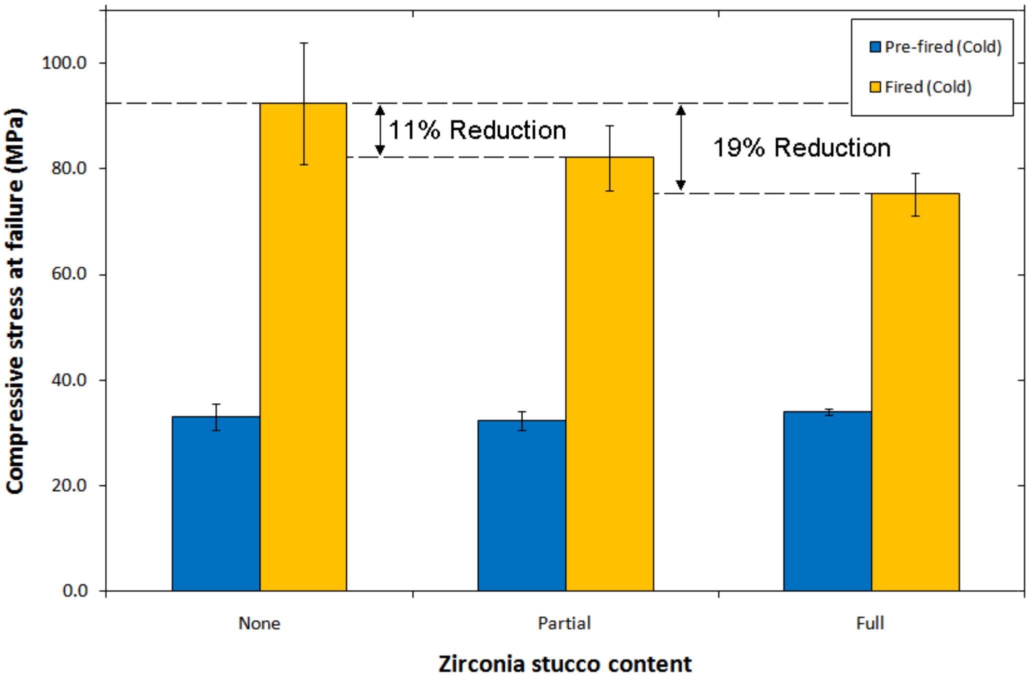

FIGURE 4.5: Results of compressive testing for shell specimens containing varying amounts of zirconia stucco; zirconia-free specimens used mullite stucco throughout. Partially zirconia stuccoed systems featured two coats stuccoed with zirconia stucco with the remainder using mullite. Fully stuccoed specimens featured zirconia stucco throughout.

Figures 4.4 and 4.5 show the results for flexural and compressive testing of shell materials containing various levels of zirconia stucco content. Examination of each data set shows that the measured strength of test samples having been through a simulated casting cycle to 1550 ℃ decreases with greater zirconia content. The partially stuccoed system exhibited a 26 % reduction in fired strength compared to the zirconia free shell whilst the reduction for the fully zirconia stuccoed shell was 43 %. For both systems the flexural strengths of specimens measured in all other states (i.e. green, pre-fired and hot) were comparable to that of the zirconia-free system. Since only the fired specimens underwent the zirconia phase transition prior to testing, this supported the hypothesis that it was the destructive effect linked to the transition process that caused the reduction in strength rather than another effect linked to the presence of zirconia. Results of compressive testing also exhibited a reduction in strength based on the presence of zirconia stucco; partially and fully stuccoed specimens exhibited reductions in compressive strength of 11 % and 19 % respectively. As with flexural testing it was observed that the strength in the pre-fired state was unaffected by the presence of zirconia stucco. Reduction in shell strengths in the fired state were reflected in observations of increasing open porosity with increased zirconia content characterised by water absorption shown in Figure 4.6.

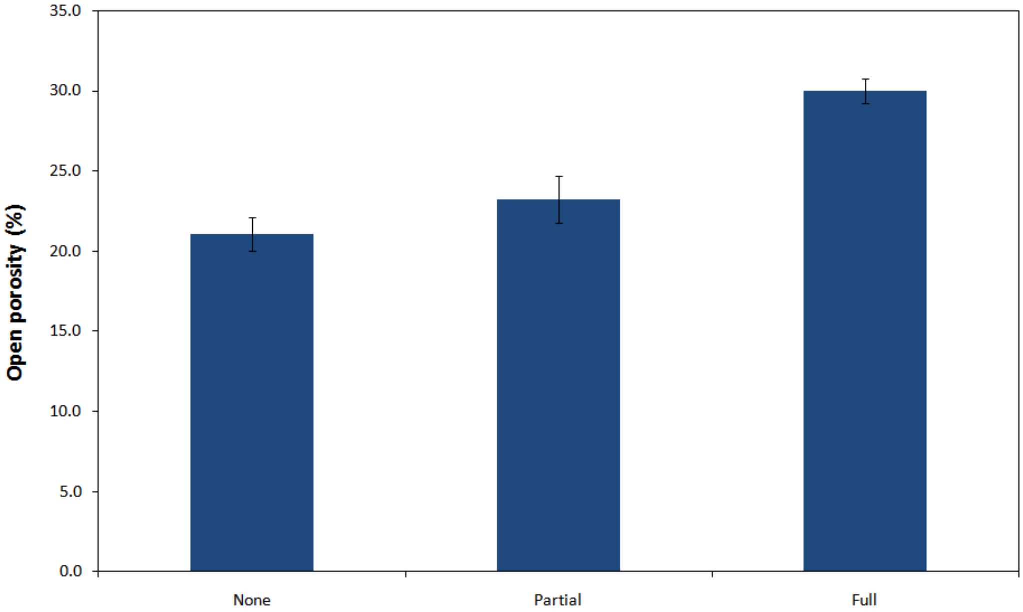

FIGURE 4.6: Open porosity of SiAl4060 shell specimens manufactured using various unstabilised zirconia contents. As expected from flexural strength measurements increased zirconia content led to increased porosity indicating shell cracking.

Thermal expansion measurements were performed on samples containing each level of zirconia stucco in order to determine the occurrence of the phase transition and the extent of which it affected the linear expansion (black dots) during firing. Figure 4.7 shows a summary of thermal expansion traces for samples manufactured using mullite, zirconia & mullite (in alternate layers) and zirconia stucco only.

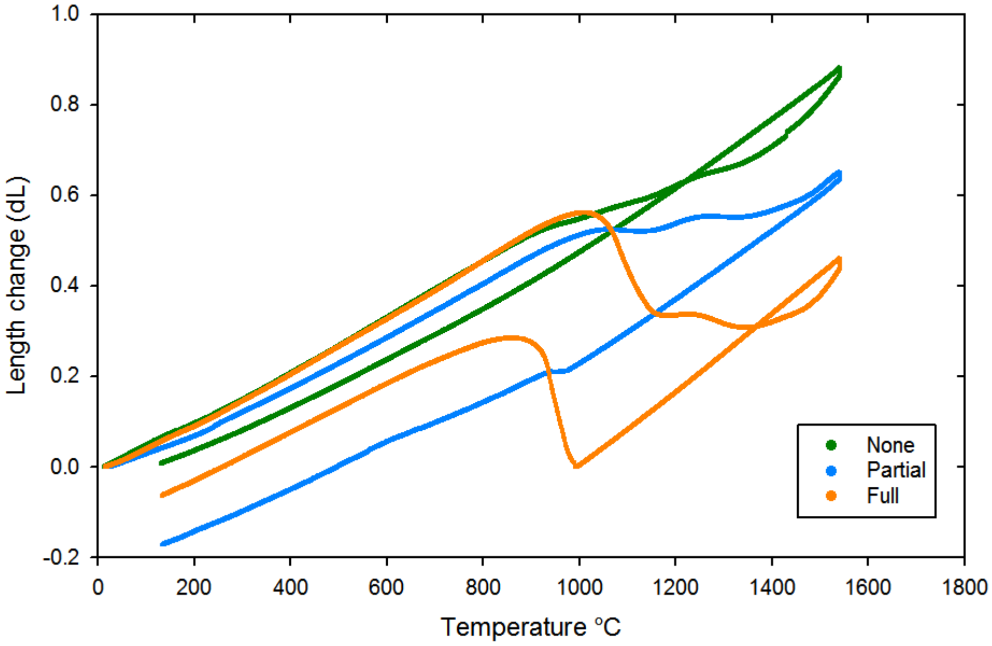

FIGURE 4.7: Thermal expansion traces for shell specimens containing varying numbers of coats stuccoed with unstabilised zirconia.

Thermal expansion was characterised in terms of percentage linear expansion relative to the original sample length; the behaviour of samples containing zirconia stucco reflected the occurrence of the phase transition during testing. For greater clarity, traces for heating and cooling are presented separately for the three shell variants in Figures 4.8 to 4.10. In order to more clearly determine the occurrence of the phase transformation, linear expansion was differentiated with respect to temperature (red dots). The phase transition was characterised by a peak in the gradient of the expansion; the onset of the process was defined as the point immediately preceding the peak at which the gradient reached zero (or a point of inflection). Conversely the end of the process was defined as the point immediately after the peak at which the gradient became zero or experienced inflection. Using this technique it was possible to estimate the temperatures at which the transition occurred and also the corresponding amount of expansion; Table 4.5 summarises results for shell specimens partially and fully stuccoed using unstabilised zirconia.

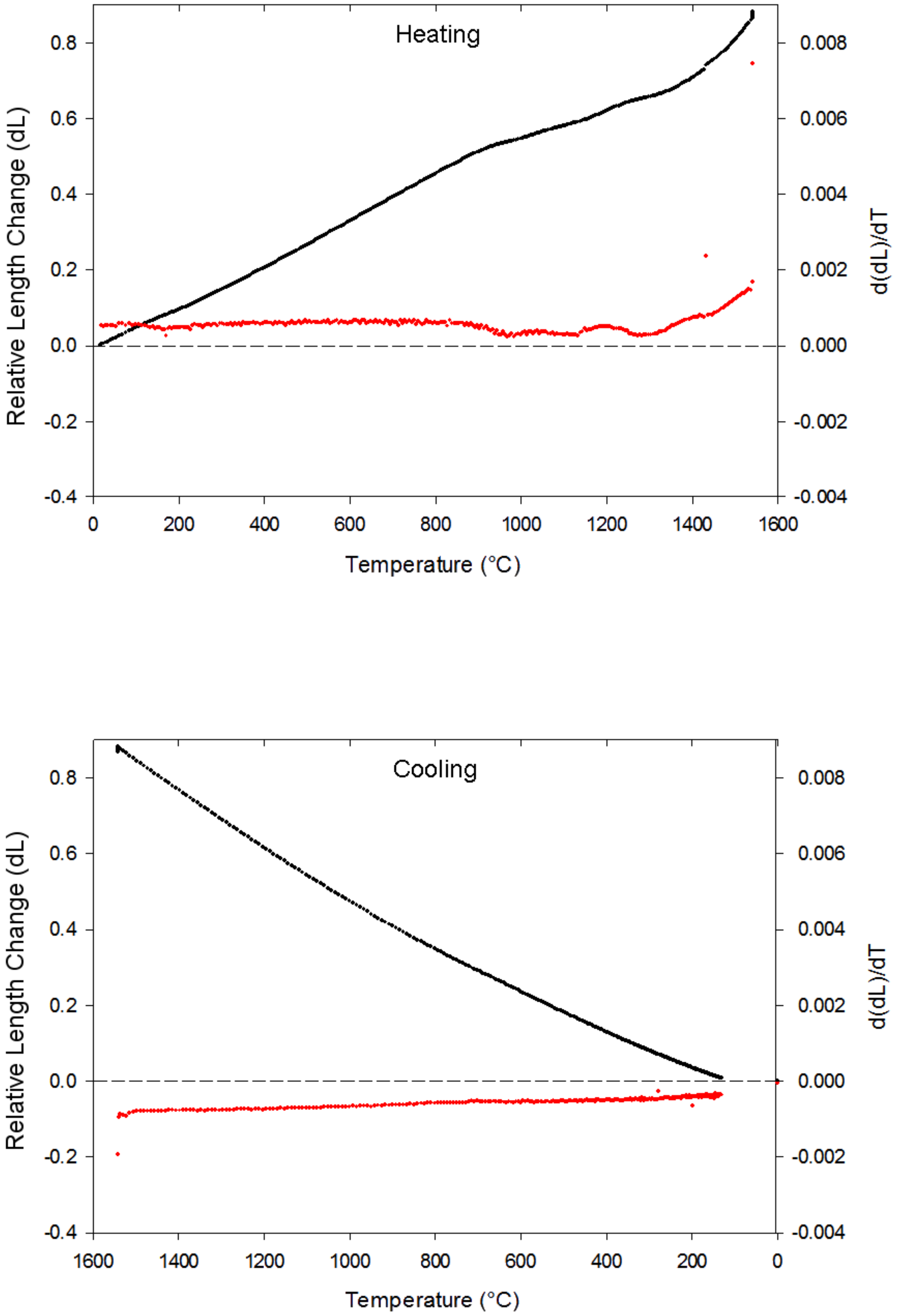

FIGURE 4.8: Thermal expansion data for SiAl4060-M system. Relative change in length is shown in black, rate of length change is shown in red.

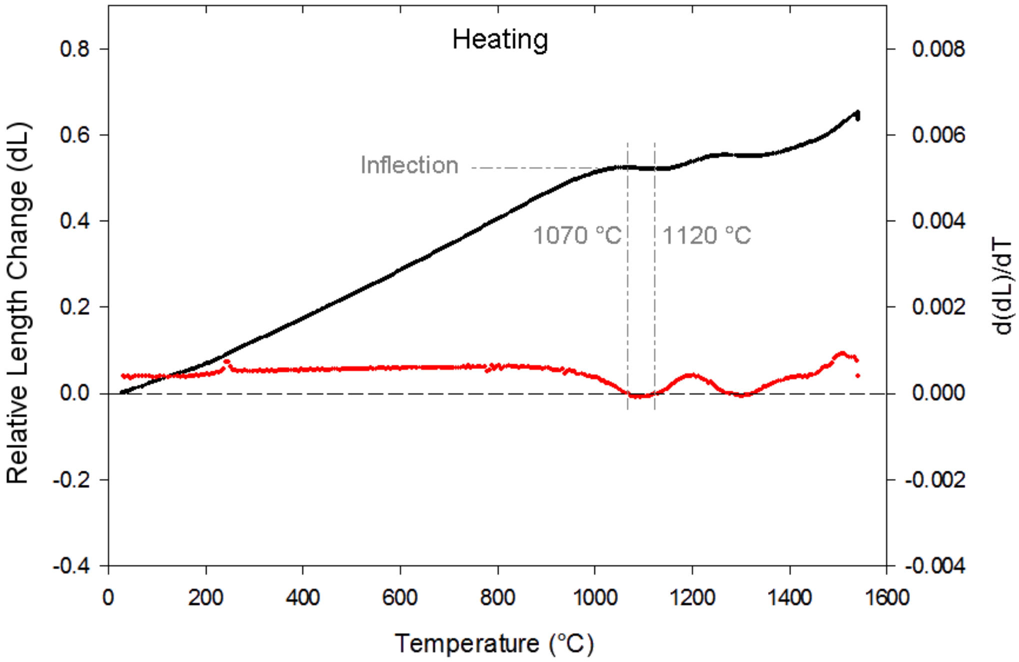

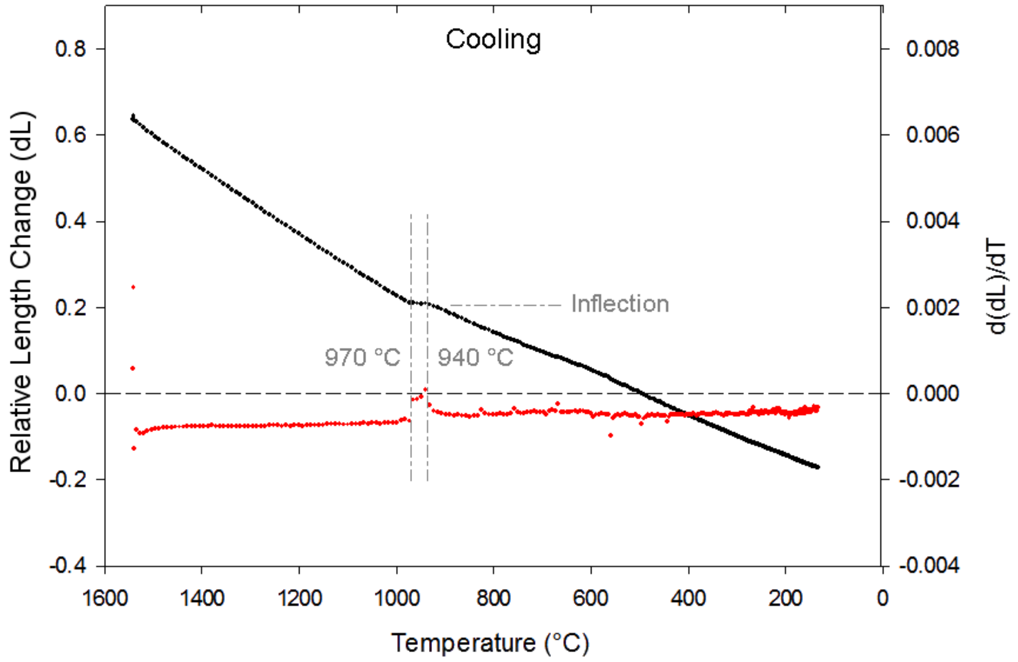

FIGURE 4.9: Thermal expansion data for partially zirconia stuccoed system. Relative change in length is shown in black, rate of length change is shown in red.

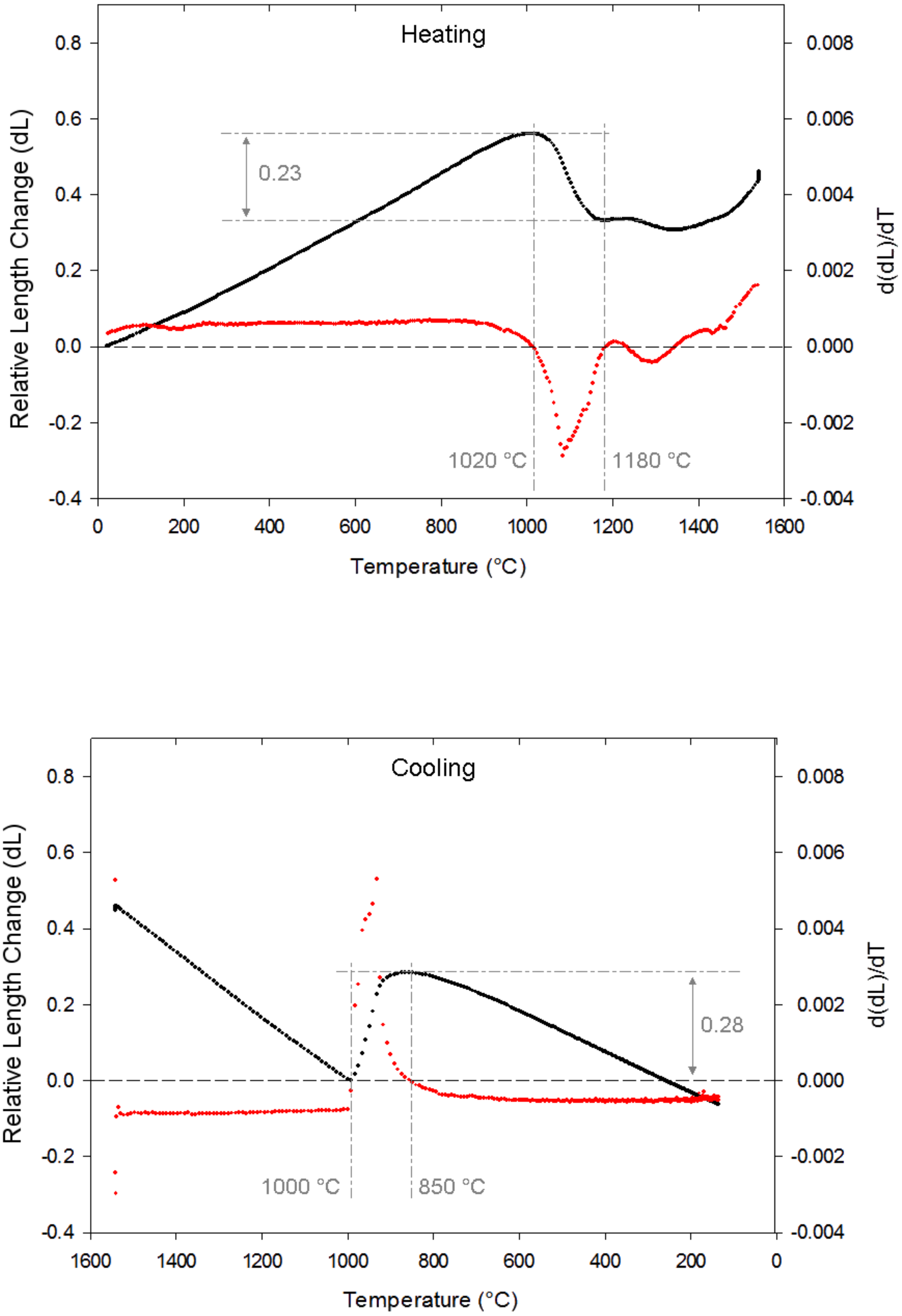

Figure 4.10: Thermal expansion data for fully zirconia stuccoed system. Relative change in length is shown in black, rate of length change is shown in red.

Table 4.5: Transformation temperatures and relative change in length for shell specimens containing unstabilised zirconia stucco. Partial denotes systems stuccoed with 2 layers of zirconia and 3 mullite. Full denotes the use of zirconia stucco throughout.

	Transformation temperature (℃)					
	Heating			Cooling		
	Monoclinic (Start)	Tetragonal (End)	(dL)	Monoclinic (Start)	Tetragonal (End)	(dL)
Partial	1070	1120	N/A	970	940	N/A
Full	1020	1180	-0.23	1000	850	0.28

As expected the zirconia-free system exhibited no phase transition during either heating or cooling. A period of reduced expansion occurred between 1250 and 1320 ℃ and is thought to be characteristic of the early mullitisation process; since all three variants shared a common slurry matrix it was expected each system would exhibit this behaviour.

It should be noted that during testing the temperature recorded is that within the test chamber rather than that of the sample itself; it is likely that the sample temperature lagged that of the chamber somewhat. Transition temperatures are however in approximate agreement with those reported in the literature for both forward and reverse transitions (see section 3.2.3). It should also be noted that for all samples manufactured using a silica-alumina matrix a loop was exhibited in the linear expansion trace in the extreme high-temperature region; due to separating cooling and heating cycles this is only evident in the summary diagram; Figure 4.7. The mullitisation process is discussed in greater detail in Chapter 5, however it is likely that the loop is due to the formation of mullite grains from silica and alumina during the firing cycle rather than the presence of zirconia.

The length contraction of the fully stuccoed system was significant exhibiting a relative contraction of 0.23 % due to the forward transition and an expansion of 0.28 % during the reverse process. In contrast no significant change in relative length was observed for the partial system, the transformation instead manifesting as a point of inflection in each direction. The amount of zirconia within the shell was estimated from analysis of electron micrographs to be approximately 40 vol %, Adams *et al.* reported a linear thermal expansion value for single-crystal zirconia of 1.2 % [90] for material in the virgin state. It was also reported that samples in the study exhibited a permanent overall length increase of 0.3 % following the initial cycle and that for all subsequent thermal cycles the linear expansion dropped to 0.9 %. This behaviour indicated that the sample had become cracked during cycling (this was substantiated by the sample changing from transparent to translucent after cycling). Assuming that the fully zirconia stuccoed shell specimens contained 40 vol % zirconia it is reasonable to expect the thermal expansion of the zirconia stucco particles to exhibit a 1.2 % linear expansion giving a total value of 1.2 % (linear expansion) x 0.4 (zirconia volume fraction) = 0.48 % linear expansion for the overall sample. As stated before the actual value measured was only 0.28 %, it is possible that cracks and defects inherent to the matrix material provided voids to accommodate the expansion during the transformation. It was known from SEM micrographs that ABSCO zirconia stucco grains were hollow, it is likely that this would also have served to accommodate some of the expansion during the phase transformation. The effect of hollow grains is further discussed in section 4.6.

The difference in measured expansion between partially and fully stuccoed systems was consistent with that reported by Pontin *et al.* during thermal expansion measurement of alumina-zirconia laminates containing varying vol % concentrations of 0.3 - 0.4 µm unstabilised zirconia particles. It can be seen in Figure 4.11 that the measured expansion (and also transition temperature) during the cooling cycle was proportional to the level of zirconia content [91]. To understand this observation it is necessary to consider the effect of the matrix surrounding the zirconia

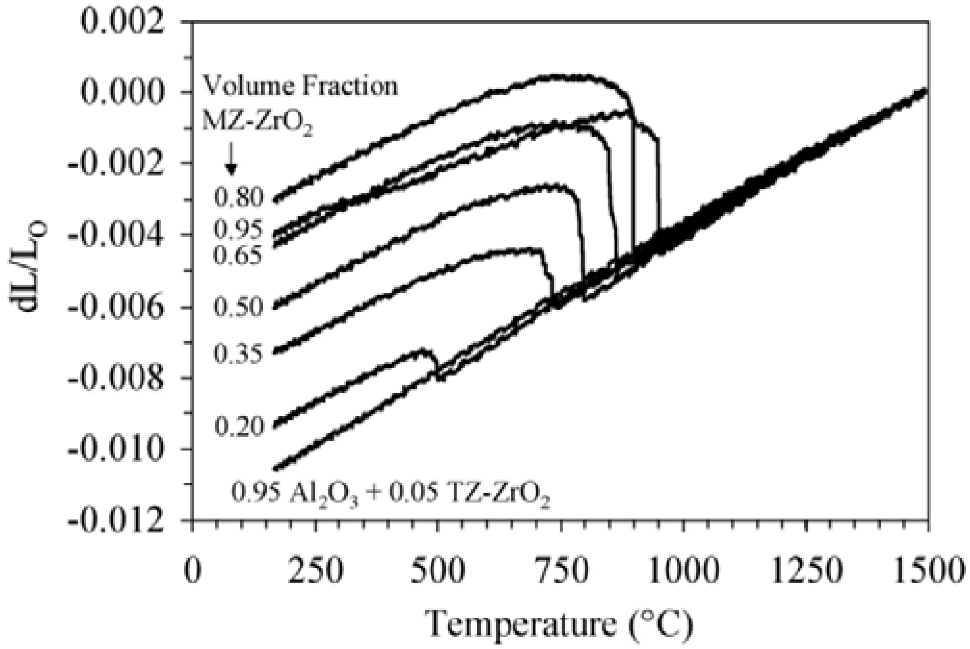

FIGURE 4.11: Thermal expansion measurements for thin-layer laminar specimens manufactured using alumina and varying amounts of unstabilised zirconia reported by Pontin *et al.*. Data presented reflects cooling cycle from 1500 ℃. Reproduced from [91].

particles. It is widely reported in the literature relating to zirconia toughened alumina (ZTA) that the tetragonal to monoclinic phase transition is influenced by the surrounding material. If the energy required to induce fracture in the surrounding matrix is greater than that required to retain the tetragonal structure it is thermodynamically favourable to do the latter and the zirconia will exist in a meta-stable tetragonal state [92]. The effect of zirconia content on transition temperature can be explained by the fact that it becomes increasingly thermodynamically unfavourable for zirconia particles to remain in the tetragonal state as the temperature drops. For larger particles it is likely that the balance shifts in favour of transformation at higher temperatures than for smaller particles due to the energy required to constrain them, this was reflected in the data shown in Figure 4.11. To a reduced extent this was reflected in the thermal expansion traces measured for shell test specimens with the full system beginning transformation 30 ℃ earlier than those only partially stuccoed. It is likely that the effect was not as dramatic as that observed by Pontin *et al.* due to the size of the zirconia stucco particles. For each matrix material there is a critical zirconia particle size below which transformation is unfavourable and above which spontaneous transformation will occur during thermal cycling. It is generally accepted that for alumina matrices this size is around 1 µm for particles within the bulk material and around 1 nm for particles near the specimen surface [93] [94].

It was calculated by Claussen that hot-pressed alumina specimens containing unstabilised zirconia particles between 3 - 5 µm generated tensile stresses of 2000 $\mathrm{MN\,m^{-3}}$ at the particle-matrix interface. Since this exceeded the fracture strength of the matrix by an order of magnitude cracking was observed at and around the interface [95]. The effect this had on the flexural strength of specimens is shown in Figure 4.12 (A). It can be seen that the fracture toughness of the zirconia doped alumina matrix increases with increasing zirconia concentration up to the peak value, above this concentration the transformation toughening mechanism breaks down allowing spontaneous transformation of the zirconia and subsequently reducing the toughness. This phenomenon had a marked effect on the flexural strength of the specimens, beyond the peak fracture toughness the flexural strength of the specimens dropped significantly. It is likely that this was due to the formation of cracks within the material during the zirconia transformation process.

A similar relationship between increased zirconia content and reduced sample strength was observed by Green and is shown in Figure 4.12 (B). Through image analysis of Figures 4.13 to 4.15 it was possible to estimate the level of unstabilised zirconia within the shell specimens. As expected and consistent with measurements reported in the literature increased zirconia content led to a reduction in shell mechanical properties. Considering the porous, heterogeneous structure of the investment casting specimens it was expected that cracking would be exhibited at the interface between the zirconia stucco particles and the matrix; observations from SEM micrographs confirmed this.

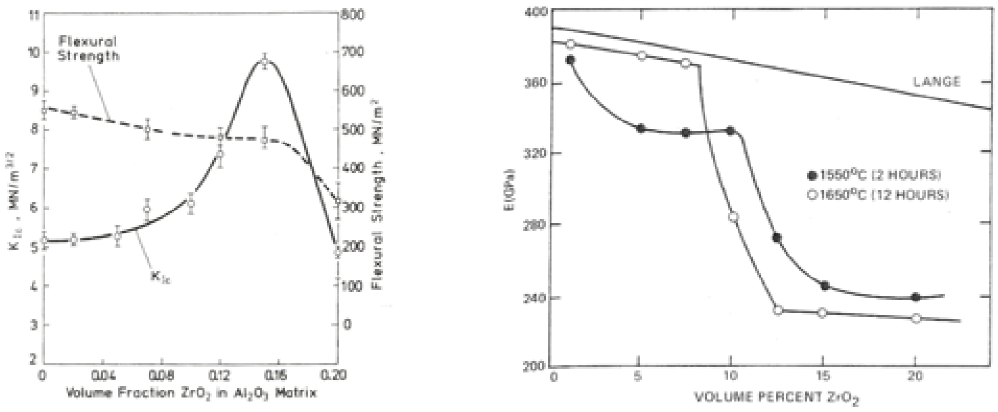

(A) (B)

FIGURE 4.12: Young's modulus and flexural strength results for alumina ceramics containing unstabilised zirconia particles. (A) shows trend for decreasing strength with increasing zirconia concentration. (B) exhibits a similar trend in Young's modulus. Figures (A) and (B) reproduced from [95] and [96] respectively.

Although the tensile strength of the shell-matrix is not known, it is likely to be significantly lower than that of the hot-pressed alumina samples used by Claussen due to the presence of defects and the inherent heterogeneity of shell materials. Additionally the zirconia particles utilised within shell materials were between 1-2 orders of magnitude larger than those used by Claussen and those reported by Pontin *et al.* as the critical size for inhibiting transformation. It is therefore reasonable to conclude that the reduction in fired strength exhibited by shell materials containing unstabilised zirconia is due to transformation induced cracking during cooling. This was further substantiated by the absence of cracking within the zirconia free shell material.

4.3.1 The forward transformation

The destructive effect of the reverse transformation (from tetragonal to monoclinic) has been widely discussed with regard to the deliberate weakening of shell materials. However it is also necessary to consider to the effect of the forward transformation during heating. It was clearly shown in Figures 4.7 and 4.10 that

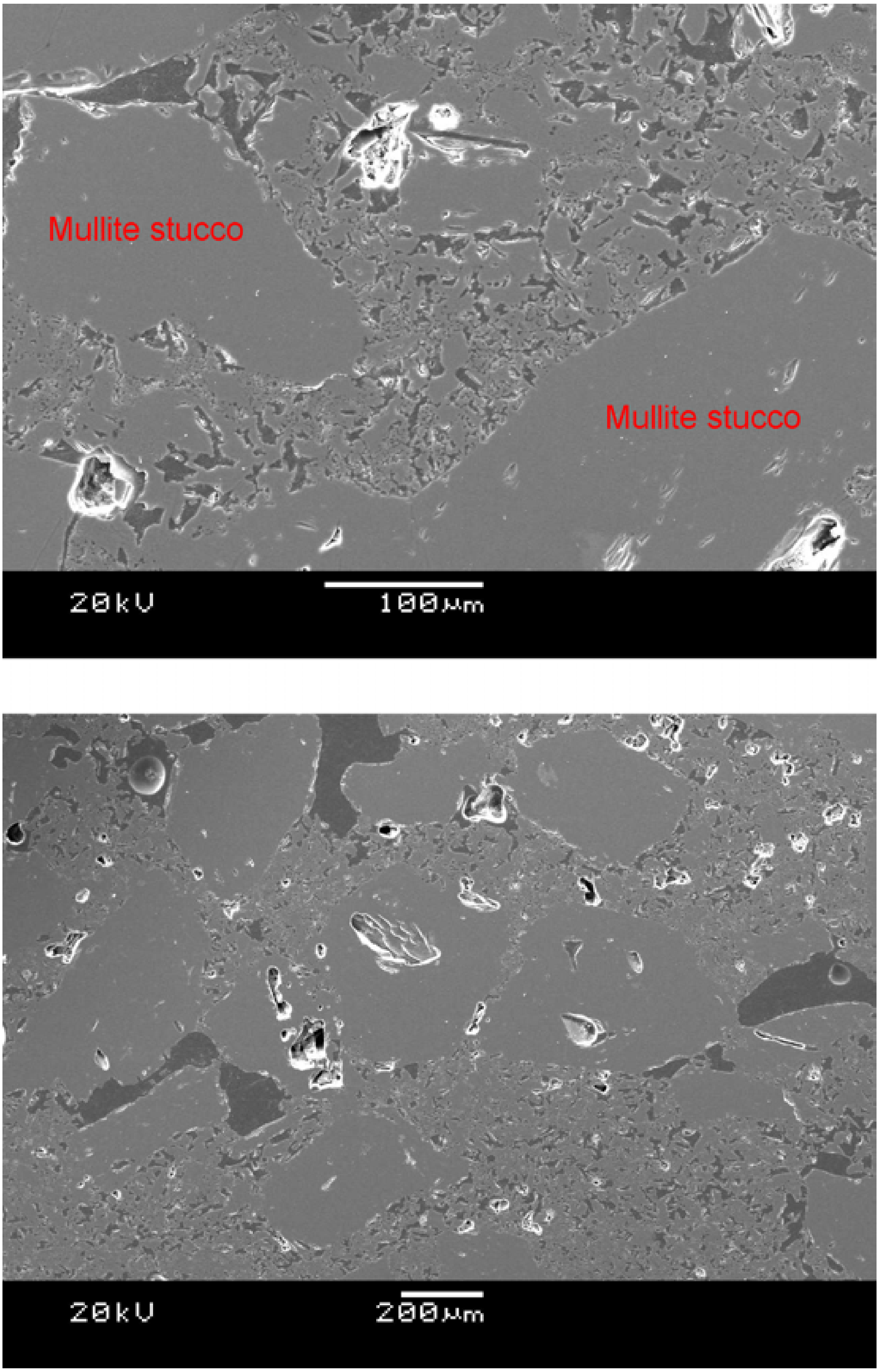

FIGURE 4.13: SEM micrographs showing the structure of the SiAl4060 system featuring mullite stucco throughout. Specimen was examined in the fired condition.

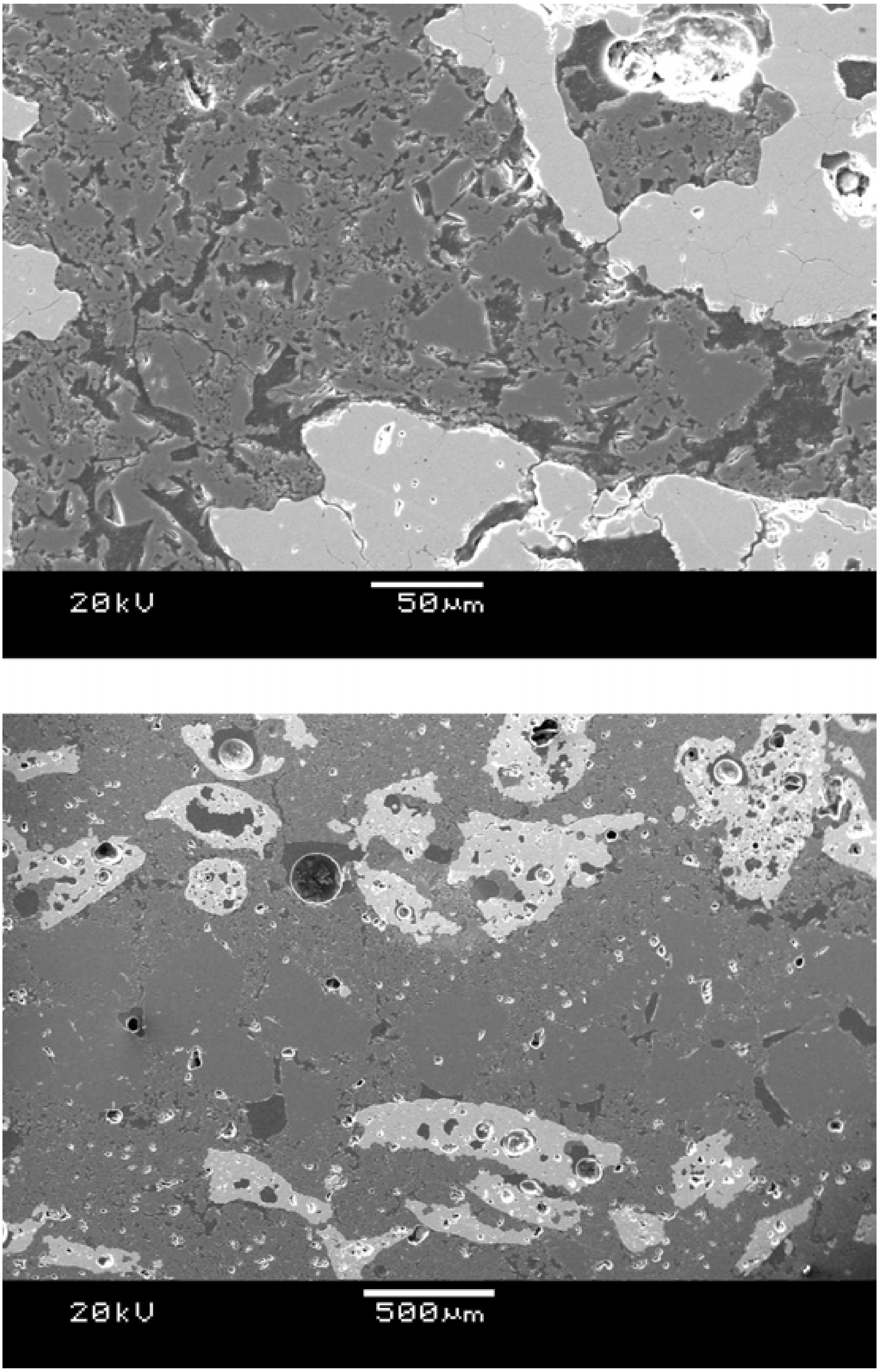

FIGURE 4.14: SEM micrographs showing the structure of the SiAl4060 system partially stuccoed with unstabilised zirconia; due to higher atomic number the zirconia grains appear lighter than the mullite stucco and matrix.

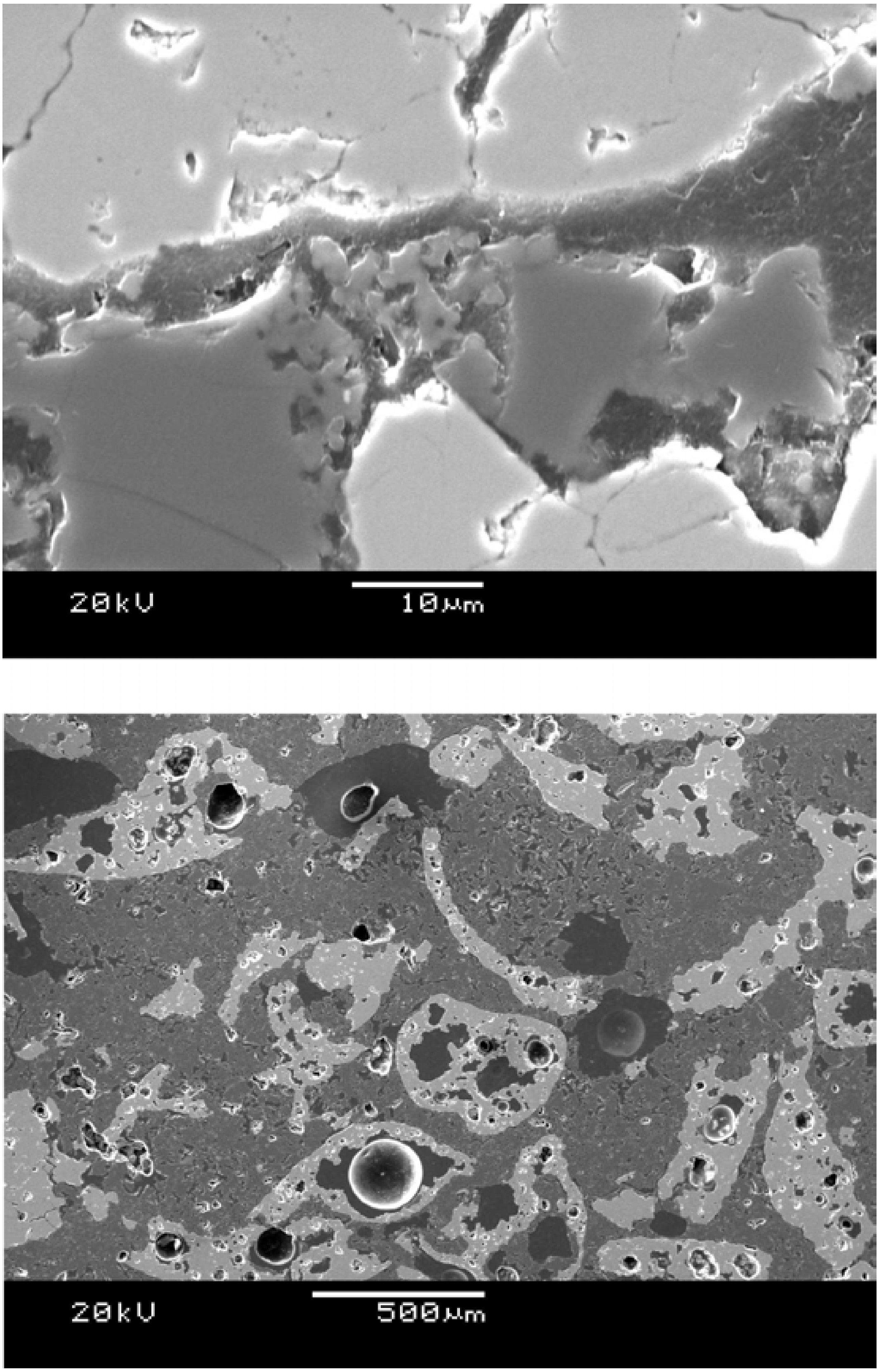

FIGURE 4.15: SEM micrographs showing the structure of the SiAl4060 system fully stuccoed with unstabilised zirconia; due to higher atomic number the zirconia grains appear lighter than the mullite stucco and matrix.

the forward transformation causes a comparable change in specimen length (albeit a contraction rather than expansion) during thermal expansion measurement.

Since high-temperature testing is performed at 1540 °C it is assumed that zirconia particles within the shell material have been through the forward transformation and are in the tetragonal state. This makes the high-temperature test particularly relevant for the determination of the effect of the forward transition on the strength of shell specimens. Inspection of flexural strengths presented in Figure 4.4 however showed that the inclusion of zirconia stucco in various amounts had a negligible effect on the high-temperature strength of the shell material. This is in contrast to the significant reductions experienced by the shell materials tested in the fired condition which showed that cycling through both forward and reverse transformations caused significant reductions in shell strength.

Inspection of the heating portion of thermal expansion data for the fully zirconia stuccoed shell material, shown in Figure 4.10 reveals a period of sintering occurring after approximately 1180 °C. Unfortunately due to the limitation of the SEM process it was not possible to investigate the structure of the shell specimens at high temperature so it is not possible to conclude the mechanisms at work within the material at high-temperature. However it is likely that during densification, cracks induced within the structure during thermal cycling through the forward transition are healed leading to shell specimens featuring similar shell strengths irrespective of the level of zirconia content within them. Further supporting evidence for this behaviour is presented in the flexural strengths presented in section 4.6.

4.4 SiAl4060-Z Small-bore casting trials

Mechanical testing results indicated that the use of zirconia stucco reduced the mechanical properties of the shell materials both flexurally and in compression. However in order to understand how this would affect the shell manufacturing and casting process it was necessary to perform shelling trials using production moulds. The moulds in question were Rolls-Royce 150 mm diameter 'small-bore' moulds, the part to be cast was the low pressure turbine blade featured in the Pegasus turbine engine referred to hereafter by its short part number 522'. It had been noted throughout trials that all shell systems using Ludox HSA as a binder material exhibited reduced green strength as compared to standard Rolls-Royce shell systems (see section 5.3), one of the primary motivations for completing the 522' trial was to determine the relationship between green strength as measured by flexural testing and the integrity of the moulds during handling and processing. Another important concern and the reason for selection of the 522' blade was observing the effect of shell properties on the presence of recrystallisation (RX).

To facilitate the dipping of small bore moulds, the SiAl 4060 slurry (the basis for the zirconia stuccoed system) was mixed in 10 litre batches as described in section 3.1 and transferred into a 120 litre robot tank for holding. The capacity of the drying carousel limited the number of shell moulds which could be shelled in a single batch to 10 moulds; the number of moulds was also limited by the amount available from Rolls-Royce. Working within this limitation it was possible to manufacture 8 moulds featuring 4 blade waxes each and also 2 moulds with test bar geometries; test bar moulds would provide shell specimens representative of the robot dipped shell material for mechanical testing. This would determine any change in material properties as a result of the scale-up and different dipping process. As was the case during development, flexural and compression testing were performed on shell specimens, the results of which are presented in Figure 4.16.

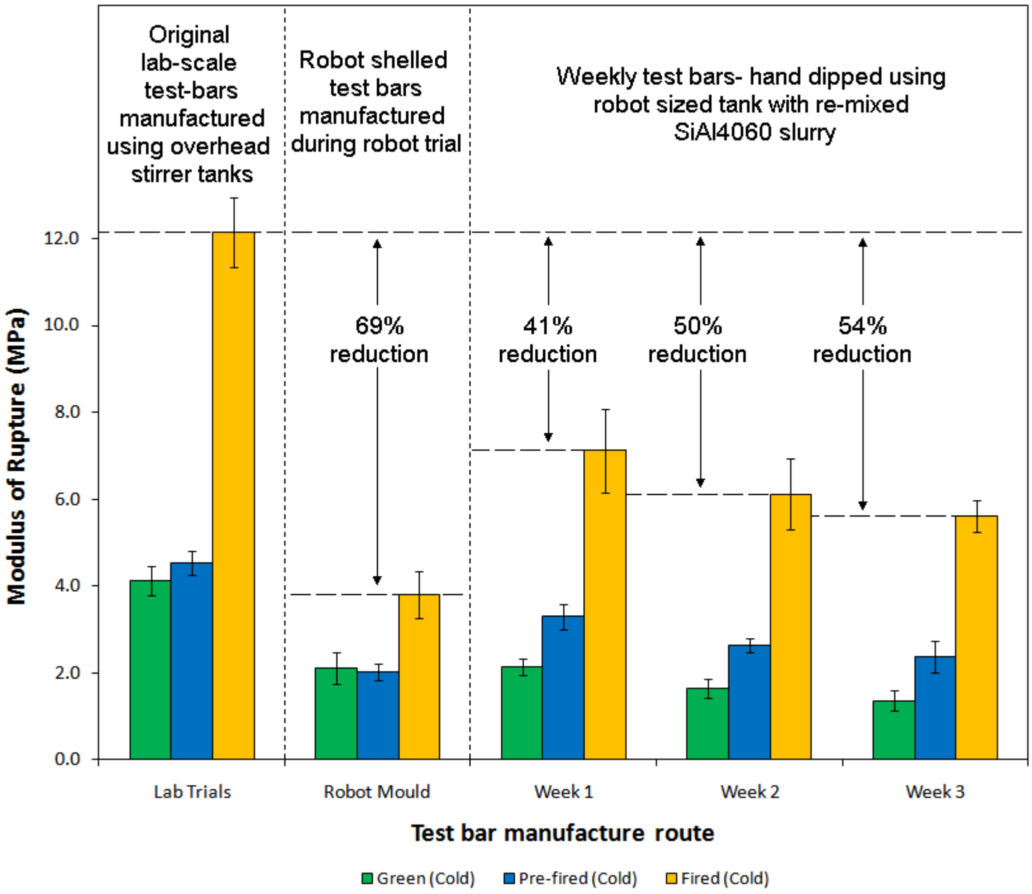

Figure 4.16: Flexural testing results showing the difference in measured strengths for systems manufactured during initial trials and robot trials. Weekly monitoring was performed to track the effect of slurry stability on shell strength.

Initial observations of the zirconia stuccoed shell moulds based on handling and dewax were that the green strength was significantly lower than that of Rolls-Royce standard systems; this was confirmed by subsequent flexural testing. Inspection of Figure 4.16 reveals a significant decrease in mechanical properties of robot moulds across all firing conditions compared to those manufactured during laboratory trials. During pre-cast processing 6 out of 8 of the 522' blade moulds were damaged irreparably due to poor integrity. Figure 4.17 shows the performance of the moulds during crack test in which the shell mould is filled with blue die. Significant damage was observed around the spiral grain-selector highlighted by leakage around these points, leading to all but two of the moulds being scrapped; during production with the standard shell material the level of cracking around this feature is negligible indicating that this was a significant observation. One of the two remaining moulds was cast and exhibited significant metal run-out, a condition where the mould is unable to retain the molten alloy; to avoid further furnace damage the final mould was not cast.

Figure 4.17: Photographs showing Pegasus LP blade moulds shelled using the SiAl 4060-Z shell system during crack-test. Damage was highlighted by the inability to retain the blue dye. Notable damage was observed around the grain selector.

In order to reduce the possibility that the lack of strength was caused by incorrect slurry formulation the original SiAl 4060 slurry was discarded and remixed. The stability of the remixed slurry was characterised using standard slurry-monitoring techniques and also through the weekly manufacture of shell test specimens. These specimens were hand dipped using the same technique as the original lab-scale test bars, however in this case they were dipped into the robot tank. These results are presented in Figure 4.16.

The flexural test results of the specimens shelled alongside the robot moulds revealed a significant drop in strength across all firing conditions compared to lab-scale test bars. Green and pre-fired strengths dropped by approximately 50 % and fired strength by 69 % for the robot shelled test bars. Strength results of test bars hand-shelled in the remixed slurry also showed a reduced strength compared to the original system; specimens shelled in the first week showed reductions in green and fired states of 48 % and 41 % respectively. Test bars shelled in weeks 2 and 3 showed a progressive trend for decreasing shell strength over slurry life; fired strength had dropped by 50 % for week 2 and 54 % for week 3. The trend for decreasing shell strength with time is highlighted in Figure 4.18; it can be seen that an approximately linear relationship between slurry age and decreasing shell strength existed for fired specimens, with green and pre-fired specimens showing a less linear relationship. It should be noted that none of the test bars made from either original or replacement SiAl 4060 slurries in the larger tank exhibited strengths comparable to those measured during small-scale trials.

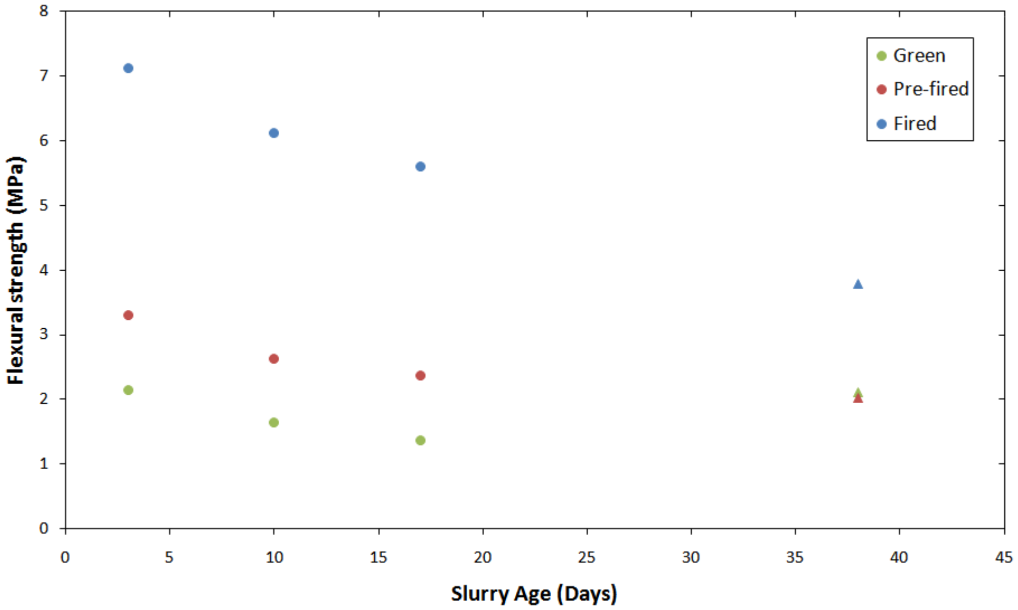

Figure 4.18: Observations of decreasing flexural strength of SiAl4060 based shell system over time. Trend is most apparent in specimens in the fired condition. Circles represent samples manufactured during stability trial; triangles are from robot shelled material.

Measurements of slurry density during the three week period in which shell test bars in 4.16 were manufactured are shown in Figure 4.19. It is likely that the difference in shear provided by different mixer types was responsible for the degradation of slurry density which led to reduced shell strength. Potential causes of the instability are discussed in more detail in Chapter 7. Observations of robot dipped shell specimens under SEM in Figure 4.20 revealed large voids within the shell. These voids reduced the connectivity of the slurry matrix and stucco particles and are believed to be responsible for the significant reduction in strength across all states. Pore sizes observed under SEM were similar to those featured in the fugitive systems described in Chapter 6 and it is likely that shell strength was lowered by the same mechanisms operating in fugitive shell materials.

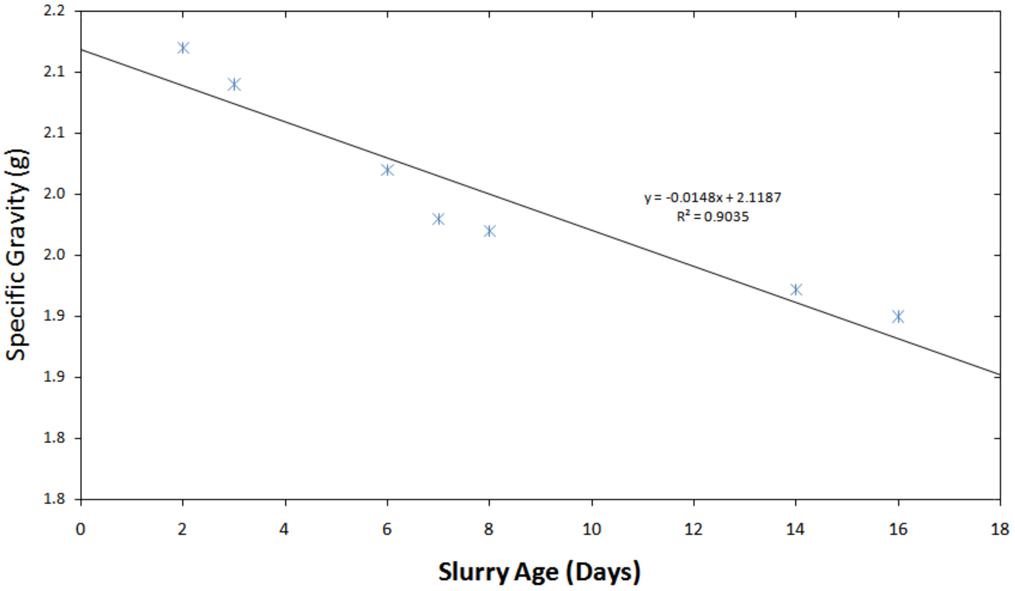

FIGURE 4.19: Specific gravity measurements for SiAl4060 slurry upon which the zirconia containing shell system was based. Note the decrease in density from 2.1 to 1.9 during the observation period; shell material showed a corresponding decrease in mechanical properties.

It is likely that the change in rheology due to the destabilisation of the system led to inhomogeneous viscosity within the slurry and areas of localised gellation. During dipping this would have hindered the formation of smooth slurry layers and potentially formed large defects within the material which caused the strength of the specimens to be reduced.

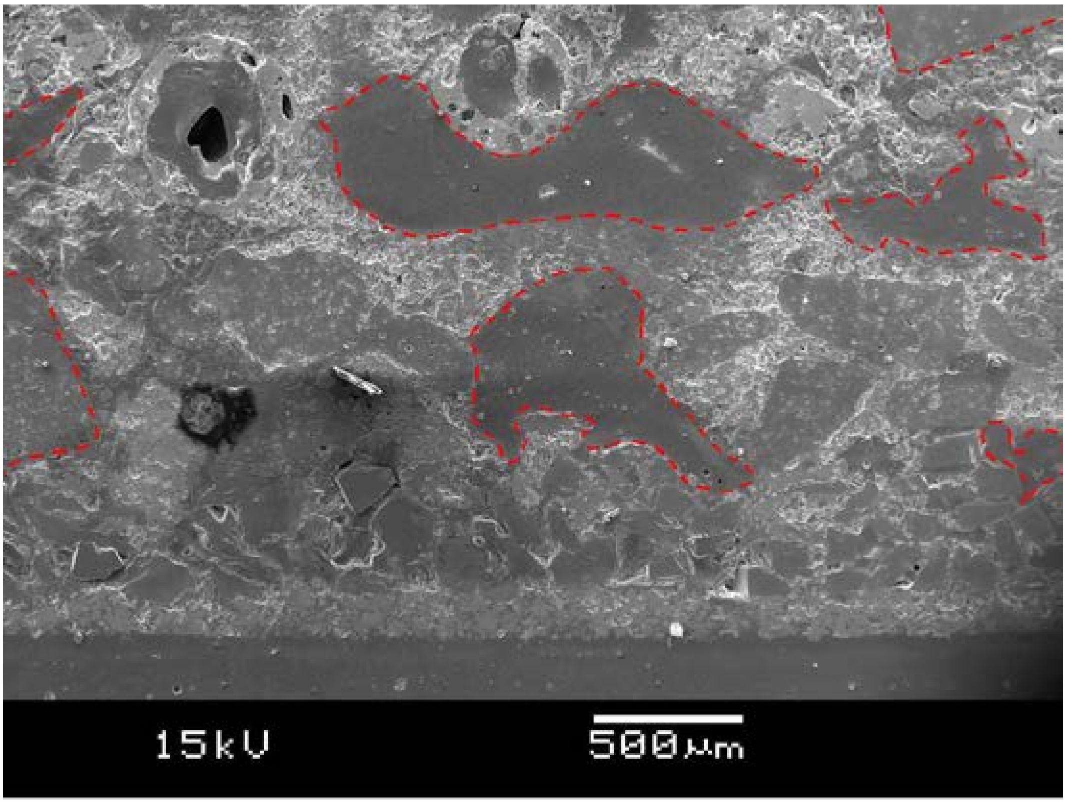

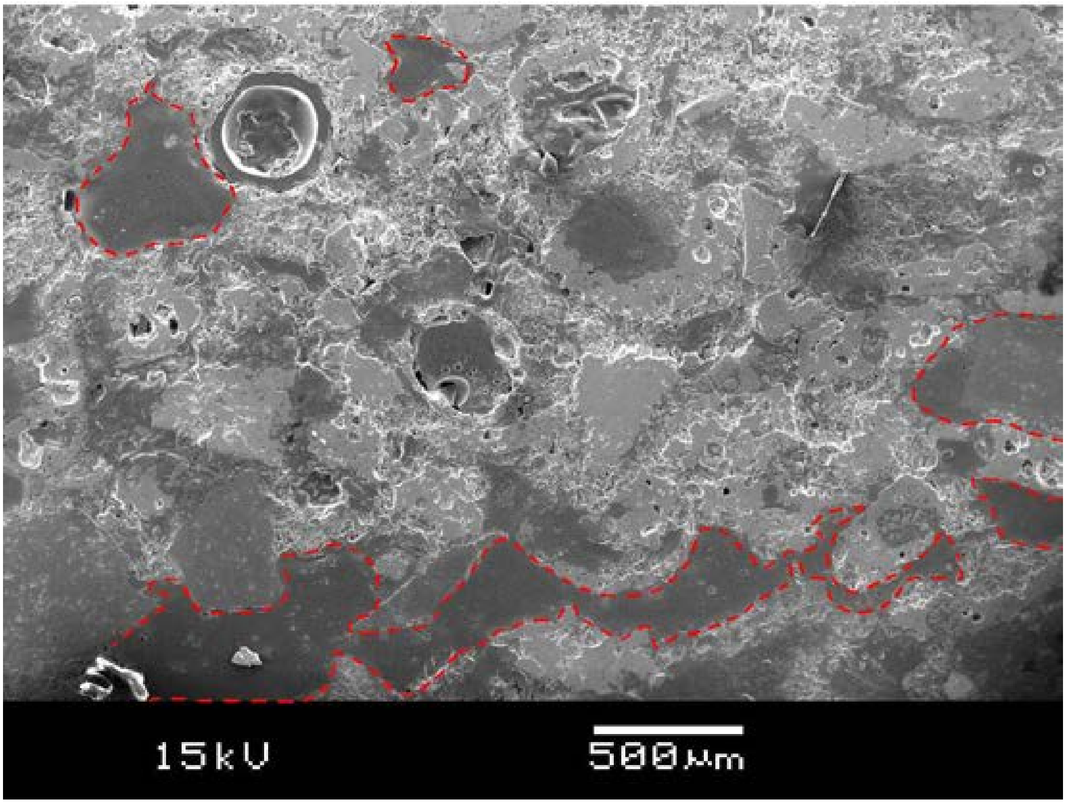

FIGURE 4.20: Micrographs showing the structure of shell specimens manufactured using the SiAL4060 slurry and ABSCO zirconia stucco as part of the Pegasus mould trial. Micrographs show different areas of the same shell specimen. Large voids (highlighted in red) were present within the shell which caused poor binding between the matrix and stucco particles and ultimately led to greatly reduced strength.

4.5 F200 reformulation

The results presented in the preceding section show how the instability of the SiAl4060 system affected the use of the SiAl4060-Z system for mould manufacture. In order to utilise the unstabilised zirconia as a mould material a replacement slurry system was required. During the 522' trial of the mullite stuccoed SiAl2080-M system (reported in Chapter 5) rheological problems were encountered which necessitated reformulation of the system. The reformulated system retained the same (alumina rich) silica alumina ratio of its predecessor but much of the reactive alumina content was replaced by larger fused alumina particles. The reformulation exercise is described in detail in section 5.4. Along with a mullite stuccoed variant, known as F200-M, an unstabilised zirconia stuccoed variant, would be developed known as F200-Z.

4.6 Zirconia supplier considerations

Zirconia containing shell moulds throughout the initial trials and the first small-bore mould trial featured zirconia supplied by ABSCO materials. As discussed in section 3.24 the material from ABSCO was not dense and featured hollow grains. Unfortunately the supplier was not willing to reveal the method by which the material was manufactured. It is believed to have been produced by a process analogous to spray drying in which the molten material is atomised to form droplets and simultaneously cooled during the process. In order to investigate alternative material types, unstabilised zirconia was sourced in similar grades from three competing suppliers; their properties are given in Table 4.6. It should be noted that the material from UCM was evaluated in the as-supplied grade of 30/100 (595 µm - 150 µm) which contained more fines than the 30/60 (595 µm - 250 µm) materials. Although it would have been possible to obtain the same material in 30/60 grade it was not available as a standard product. To prevent excessive material costs it was decided that all materials to be considered for production usage should not rely on custom-made materials. For research purposes however a small amount of material was sieved down to a 30/60 grade; limited results using this material are discussed later in this section. All zirconia stucco materials sourced from the competing suppliers featured conventional dense grains.

Table 4.6: Various unstabilised zirconia materials evaluated for use as stucco materials.

	Particle Size				
Supplier	Mesh Size	µm	d_{50}	Span	Type
ABSCO	30/60	595 - 250	500	0.43	Blown
Foskor	30/60	595 - 250	326	0.44	Dense
UCM	30/100	595 - 150	325	0.71	Dense
WM	35/60	500 - 250	401	0.21	Dense

Shell test specimens were hand shelled using the F200 slurry and zirconia from each supplier and characterised using a mixture of flexural testing and thermal expansion. Data from the latter is summarised in Figure 4.21 and presented in detail in Figures 4.27 to 4.37; in all cases data is the mean of two measurement cycles on different test specimens.

As with previous trials, in order to characterise the behaviour of the base slurry-matrix a mullite stuccoed variant, F200-M, was included in the analysis. In Figures 4.27 to 4.32 the thermal expansion measurement cycle is broken down into heating and cooling cycles; to highlight any changes in expansion behaviour the relative change in length was differentiated with respect to temperature and is plotted in red.

During the heating cycle the mullite stuccoed shell material exhibited two regions of activity which manifested as contractions in the temperature ranges of approximately 900 - 1150 °C and 1200 - 1400 °C. It is known from the literature that

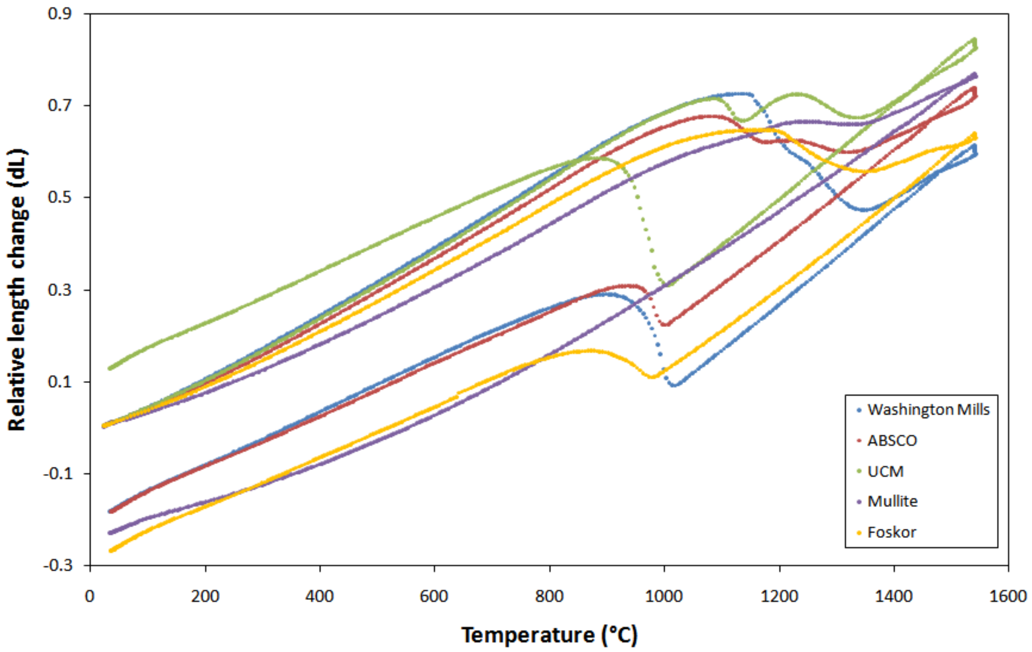

FIGURE 4.21: Summary of thermal expansion measurements performed on F200 shell specimens featuring unstabilised zirconia stucco from different suppliers.

these regions are characteristic of the various stages of mullite formation within the shell material, the first being the formation of precursor mullite and the second being the conversion of this material into stoichiometric mullite. These processes are discussed in detail with references to both experimentally determined results and those reported in the literature in section 5.2. During the cooling cycle the material exhibited no evidence of further transition as was expected since mullitisation had already occurred. Features exhibited by the mullite stuccoed system during heating were present in all zirconia stuccoed variants.

During the heating cycle all zirconia containing shell materials exhibited a contraction between approximately 1000 - 1250 ℃ characteristic of the monoclinic to tetragonal phase transition. This indicated that no reactions were taking place within the shell to prevent the transformation and also that zirconia within the shell provided a detectable change in shell dimensions. Transition temperatures and dimensional changes estimated from thermal expansion data are presented in

Table 4.7. The thermal expansion traces from which this data was acquired are presented in Figures 4.27 to 4.32.

TABLE 4.7: Zirconia phase transition temperatures estimated from thermal expansion measurements. For specimens made using UCM material the change in delta L was unusual as the sample exhibited a net expansion during testing. dL/L represents the relative length change of the specimen during measurement.

	Transformation temperature (℃)					
	Heating			Cooling		
	Monoclinic (Start)	Tetragonal (End)	(dL/L)	Monoclinic (Start)	Tetragonal (End)	(dL/L)
ABSCO	1090	1170	-0.05	1000	940	0.05
Foskor	1150	1350	-0.06	980	870	0.09
UCM	1090	1140	-0.05	1000	870	0.28
WM	1140	1250	-0.12	1020	900	0.20

Shown in Table 4.8 are measurements of the zirconia stucco content within the shells; these measurements were made using the image analysis procedure detailed in section 3.1.6. Also shown are the measured reductions in fired strength compared to the mullite stuccoed system. It was observed that specimens containing the hollow ABSCO zirconia material exhibited the smallest change in dimensions during thermal cycling. This was consistent with the reduced amount of stucco present within the shell and also the relatively low reduction in fired strength compared to shells containing dense stucco particles. It may have been the case that the reduced volume of material within the hollow particles led to the reduction in measured expansion, however it may have been the case the cavity within the stucco accommodated some of the expansion during the phase transition and hence reduced the stress on the shell this is shown schematically in Figure 4.22. The process was also modelled using a finite element analysis technique, the results of which are presented in Figure 4.23. The boundary conditions used for the model were a particle radius of 10 µm and a square matrix with side-length 30 µm. The starting temperature for the model was 1200 °C. The conditions are presented in Figure 4.24.

Table 4.8: Zirconia phase transition temperatures estimated from thermal expansion measurements. Specimens made using UCM material the change in delta L was unusual as the sample exhibited a net expansion during testing.

Stucco	Particle Size		Particle	Stucco	Strength
supplier	Mesh	µm	type	content (%)	reduction (%)
ABSCO	30/60	595 - 250	Blown	28.9	27.3
Foskor	30/60	595 - 250	Dense	41.3	44.5
UCM	30/100	595 - 150	Dense	43.9	45.0
WM	35/60	500 - 250	Dense	51.0	60.9

The dense material from UCM exhibited a similar contraction during heating to that of ABSCO however the expansion during cooling was similar to that of the dense Washington Mills material. It is possible that the fine material present within the 30/100 grade UCM zirconia acted as a grain refiner and caused greater densification of the surrounding matrix during sintering. It was observed by Prochazka *et al.* that the addition of zirconia promoted enhanced densification of mullite ceramics regardless of the amount present [97]. This was linked to the fact that the presence of zirconia grains reduced the amount of grain growth within the matrix; more numerous small grains were shown to have formed thereby enhancing sinter-ability. It is possible that the finer particles present within the 30/100 material formed more intimate contact with the surrounding matrix thus increasing the above process. It was also reported that the presence of zirconia within silica-alumina systems containing excess alumina eliminated the occurrence of alumina grains within the matrix; given the alumina rich nature of the F200 matrix this is an important observation and may be linked to the reduction in mechanical strength due to the presence of zirconia. It should however be noted that the zirconia particles used by Prochazka *et al.* had an average diameter of 1.0 µm and the mullite grains formed had similar size at 1.3 µm. In contrast shell materials featured zirconia grains between 590-250 µm and mullite particles as large as 70 µm. It is unlikely that particles this size would have sufficient mobility at the relatively low firing temperatures employed to experience grain refining.

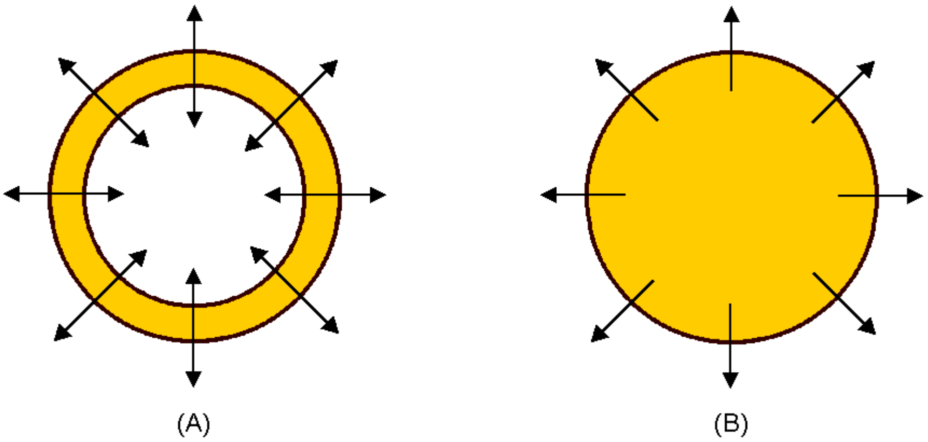

FIGURE 4.22: Schematic representation of the expansion behaviour of hollow and dense zirconia particles.

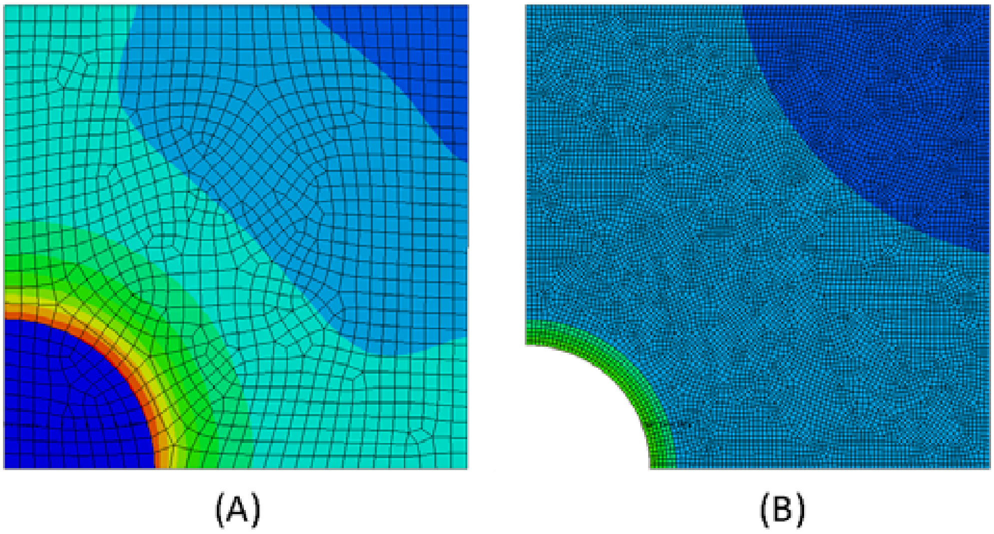

FIGURE 4.23: Finite element analysis representation of the expansion of zirconia stucco particle embedded within a dense alumina matrix. Areas of increased stress are shown in red. Dense and hollow zirconia grains are shown in Figures (A) and (B) respectively. Figure modified from [98].

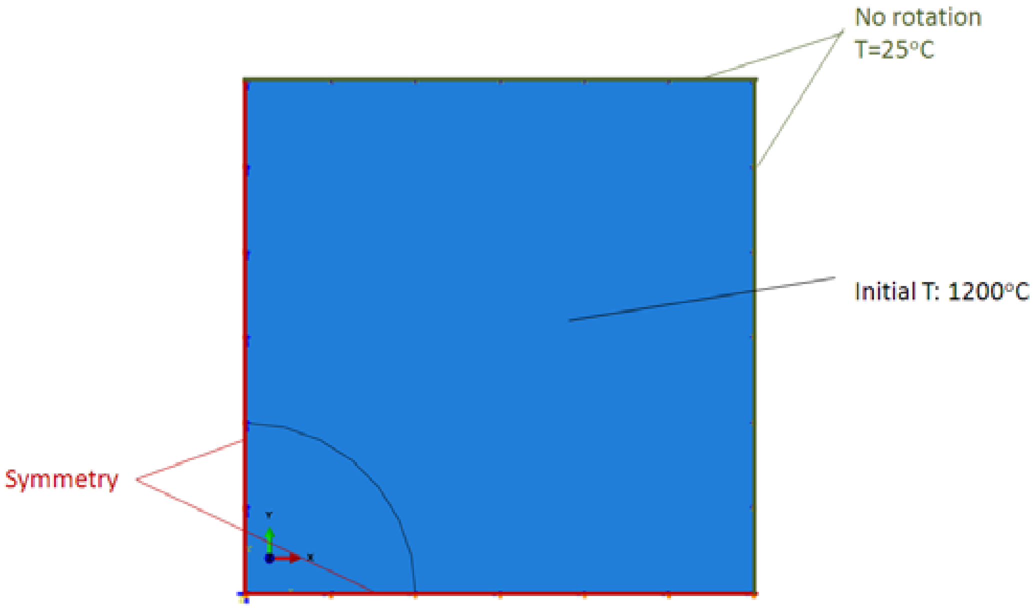

FIGURE 4.24: Boundary conditions used for modelling expansion of zirconia stucco particle within alumina matrix. Starting temperature of model selected as 1200 °C Particle radius 10 µm, domain dimension 30 µm. Figure modified from [98].

Inspection of thermal expansion data show that each shell system behaves differently during cycling. It was necessary to understand the thermal expansion behaviour of the shell matrix itself in order to de-convolute the effect of the zirconia particles. Although it would have been possible to manufacture test bars without stucco it would have dramatically altered the structure of the material and therefore influenced the results. Instead a mullite stuccoed variant was evaluated; since the slurry matrix is essentially mullite-based it was hoped that the use of mullite stucco within the shell would not influence the result due to any difference in thermal expansion coefficient. It was however possible that the presence of mullite within the shell could have seeded the growth of mullite particles from silica and alumina during firing. Other than the loop present at the extreme high temperature (as discussed in section 4.3) the only notable feature is the inflection and subsequent zero gradient between 1230 and 1320 ℃. The behaviour of mullite formation from silica and alumina materials is discussed in detail in Chapter 5. Transition temperatures and dimensional changes estimated from thermal expansion data are presented in Table 4.7.

Thermal expansion behaviours of zirconia stuccos from ABSCO, Foskor and Washington Mills (WM) exhibited similar behaviour during thermal cycling with transition temperatures consistent with those observed in the literature (see section 2.4.1).

It was observed that WM zirconia exhibited the greatest length change during both forward and reverse transitions; this behaviour was reflected in the results of flexural testing shown in Figure 4.26. In the fired state WM-stuccoed test bars exhibited the greatest reduction in fired strength compared to the mullite stuccoed system (which was included as a zirconia-free baseline), it also exhibited greater reduction in strength than other zirconia containing systems which exhibited lower levels of overall expansion. In comparison to data presented in Figure 4.4 flexural strengths for test bars in green and pre-fired states are consistent between all stucco materials including mullite. This reinforced the observation that the phase transformation was responsible for strength reduction in the fired state rather than the shape or surface chemistry of particles. High temperature strengths were also largely unaffected by stucco type; due to machine failure it was not possible to record high-temperature strengths for the Foskor stuccoed material.

Figure 4.25 shows the correlation between strength reduction and the amount of expansion exhibited by samples during the cooling cycle. As expected the blown ABSCO zirconia exhibited the smallest reduction in strength at just 27 %. Although featuring different particle size distributions zirconia stuccoes from UCM and Foskor exhibited similar properties reducing fired strength by 45 %, the greatest reduction was 61 % exhibited by the material from Washington Mills. To better understand the effect of the expansion on the microstructure, shell specimens in

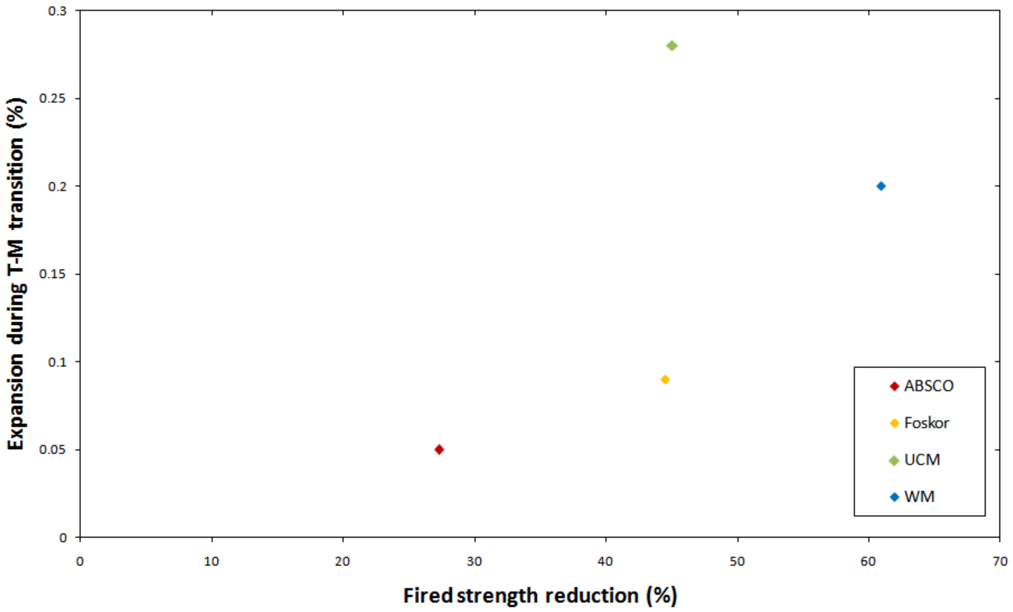

FIGURE 4.25: Correlation between measured expansion of samples during phase transition and reduction in flexural strength in the fired condition. UCM stuccoed variant exhibited unusual thermal expansion behaviour and did not fit the trend.

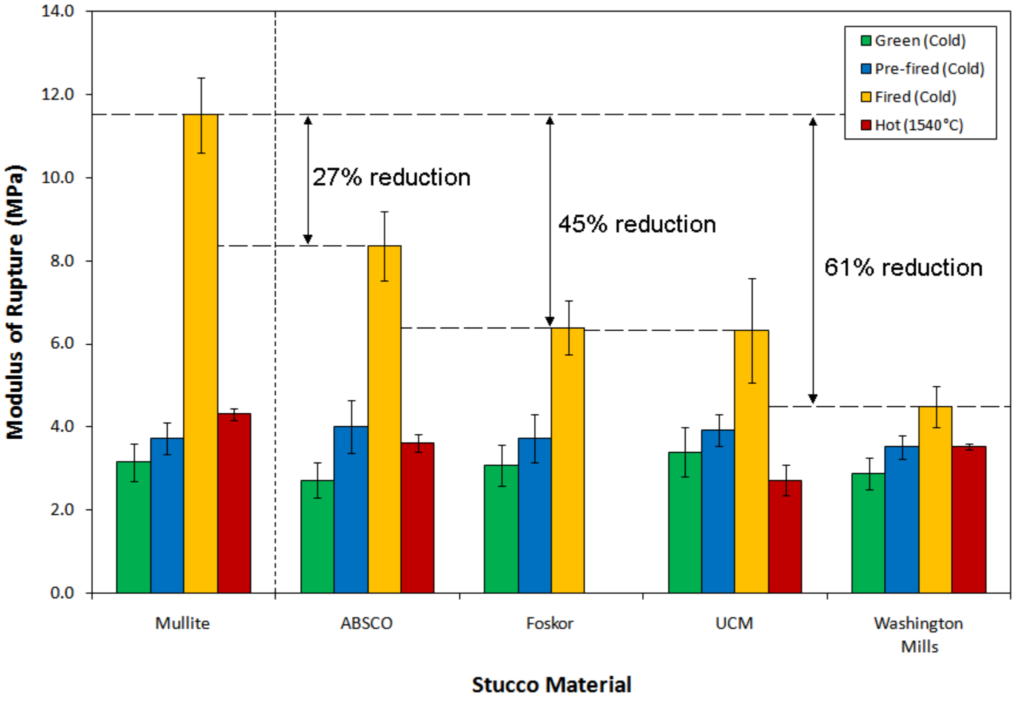

FIGURE 4.26: Flexural strength results for shell specimens manufacture using the F200 slurry stuccoed with zirconia from various suppliers. For comparison a zirconia free variant stuccoed using mullite was included.

the fired state were examined using SEM; micrographs from each can be seen in Figures 4.33 to 4.37.

The structures of samples containing dense zirconia (Figures 4.33 to 4.36) showed similar cracking behaviour; trans-granular cracks several microns in width were observed around and through the majority of stucco particles and a number of intergranular cracks were also evident. Matrix material in the proximity of zirconia particles and particularly that closely constrained by two or more particles was observed to be heavily cracked with many cracks being several microns in width and in excess of 100 µm in length. Different behaviour was observed for specimens containing the hollow ABSCO grains shown in Figure 4.37. Little evidence of trans-granular cracks surrounding the hollow zirconia stucco particles was observed, however cracking of the matrix material was essentially unchanged. It was apparent that whilst the particle size distribution of the stucco is similar to the dense variants the way in which this is achieved is different. Particles toward the upper limit of the size range, those around 500 µm, were hollow in nature as expected, however smaller particles appeared to be fragments of the larger hollow particles. It is not believed that the material was broken down during the stuccoing procedure as this structure was evident in both the as received material and that which had been applied to the shell; Figure 3.24 shows the structure of as-received particles. Considering both structural observations and the measured strength reductions it appears that the strength reduction is more dependant on trans-granular cracks surrounding the stucco than those extending into the matrix. The reduced stress generated by hollow ABSCO particles was insufficient to induce this and therefore lower strength reduction was observed.

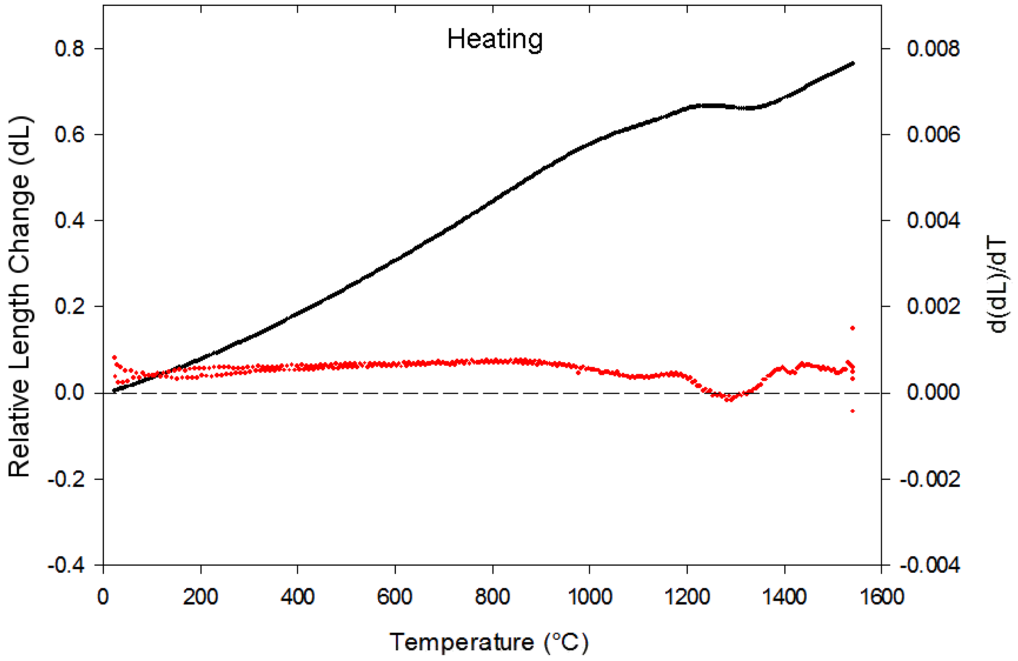

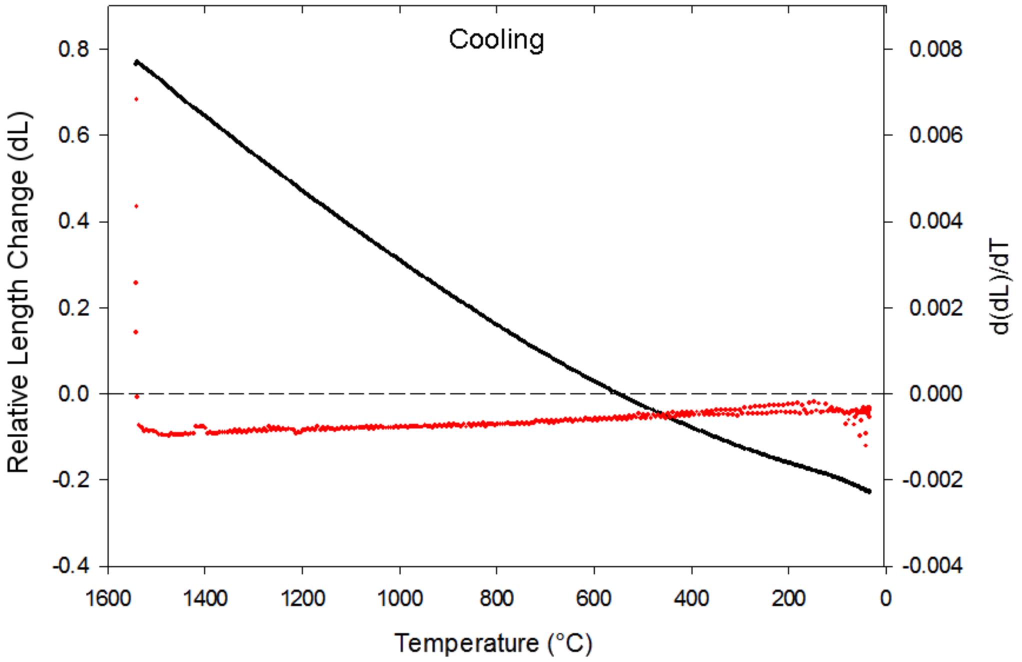

FIGURE 4.27: Thermal expansion data for F200-M system. Relative change in length is shown in black, rate of length change is shown in red.

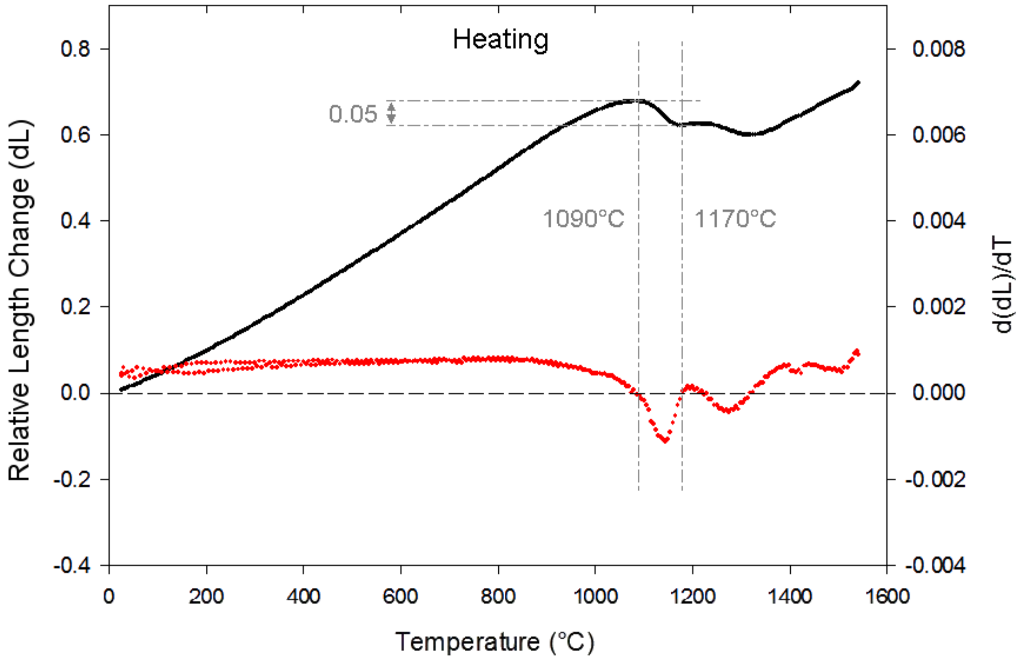

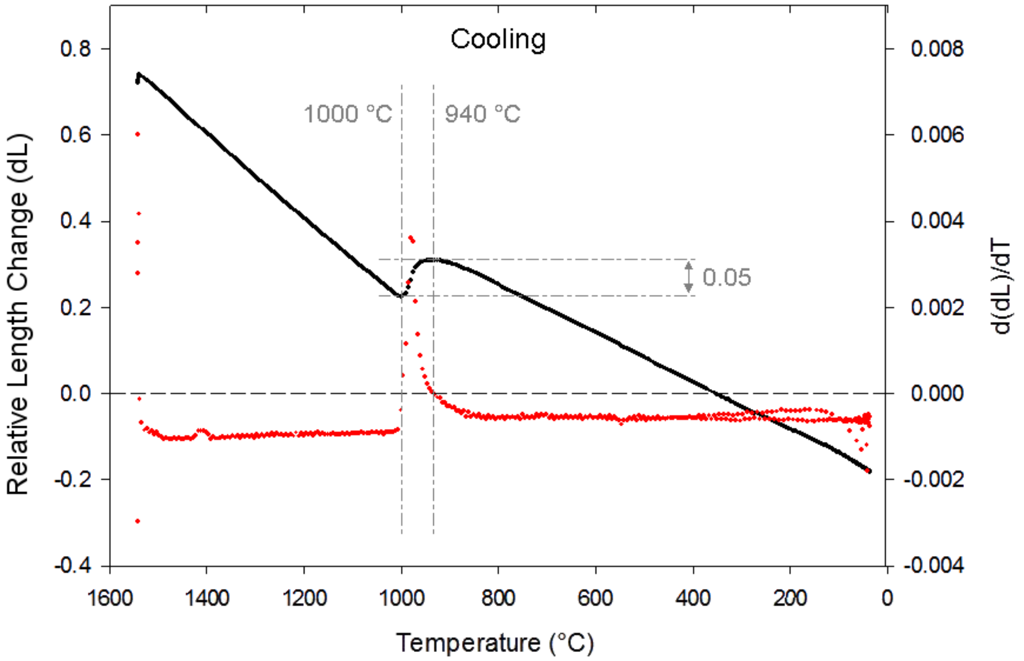

FIGURE 4.28: Thermal expansion data for ABSCO stuccoed system. Relative change in length is shown in black, rate of length change is shown in red.

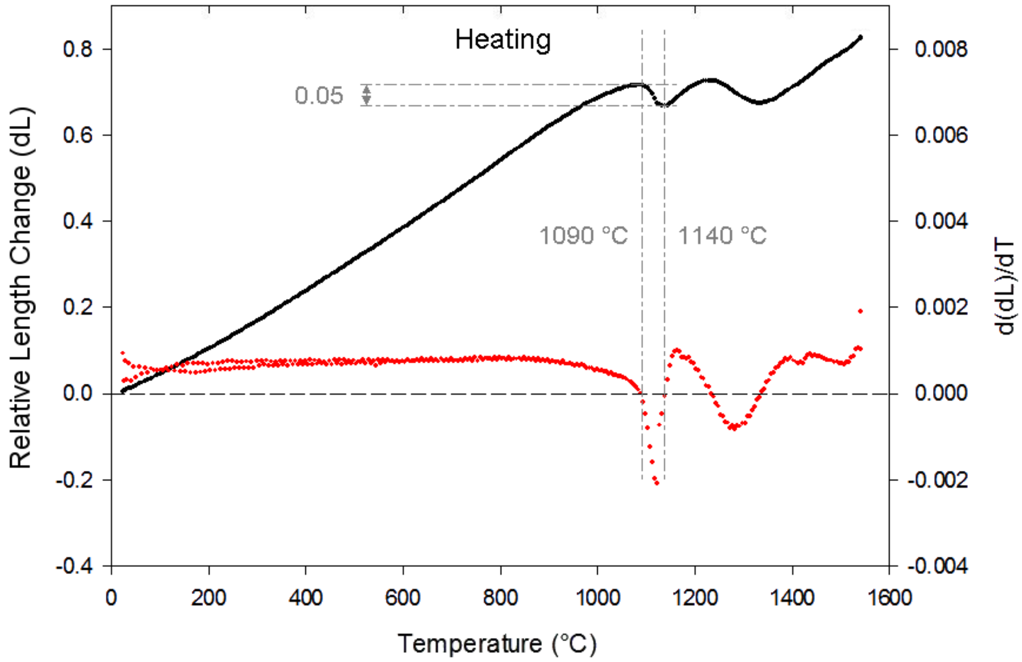

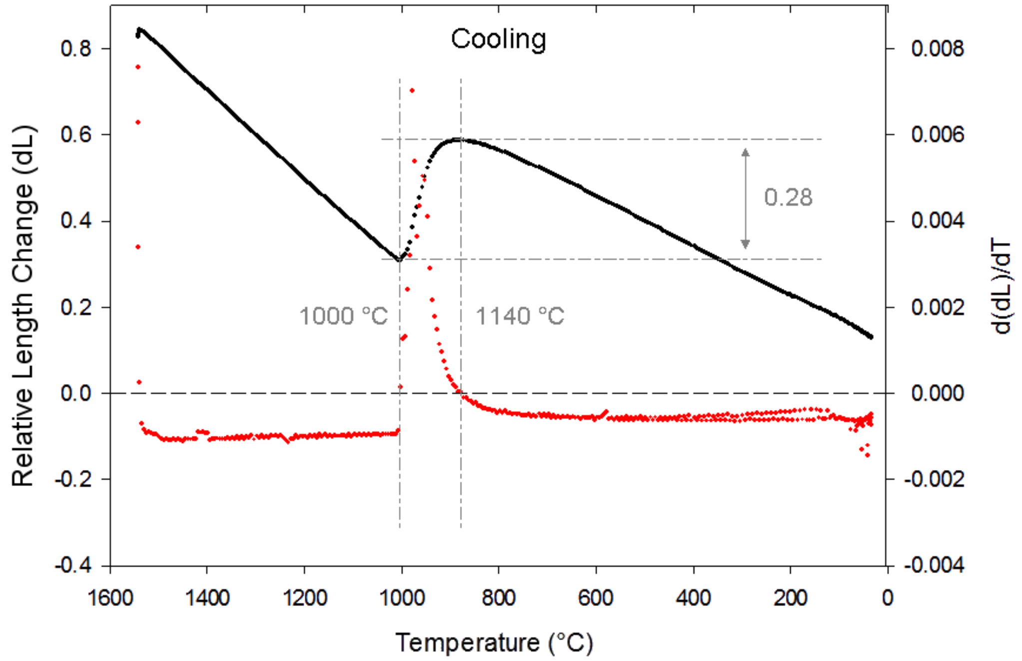

FIGURE 4.29: Thermal expansion data for UCM 30/100 stuccoed system. Relative change in length is shown in black, rate of length change is shown in red.

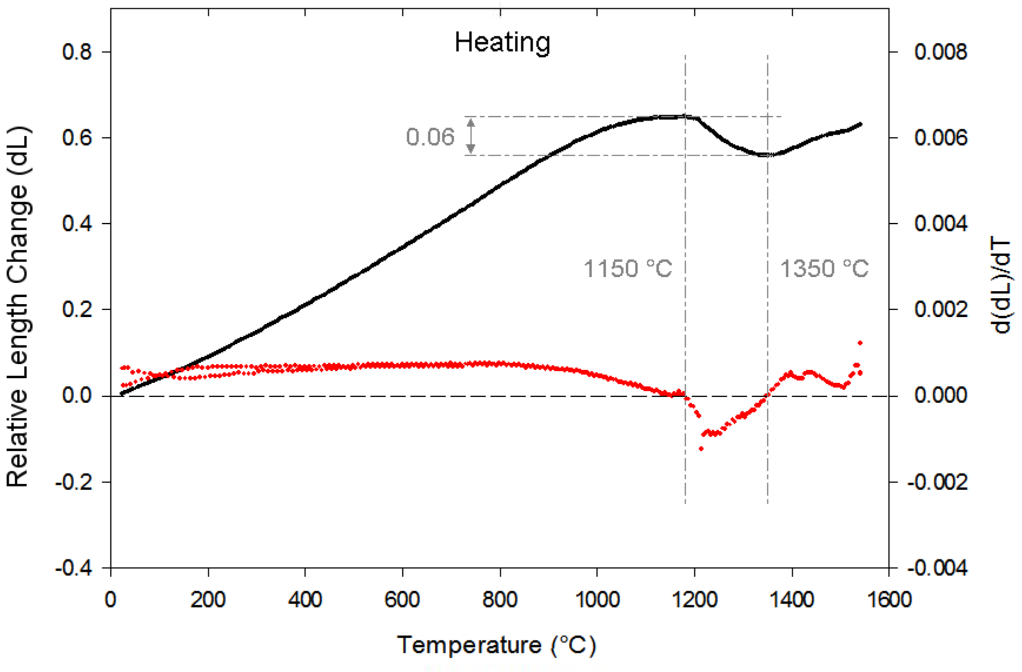

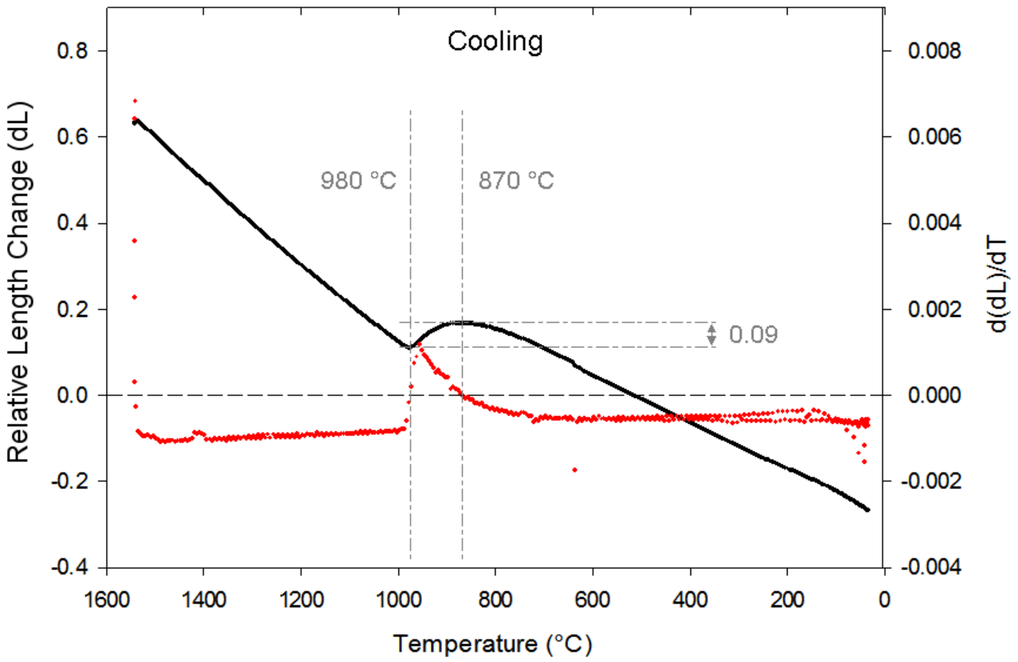

Figure 4.30: Thermal expansion data for Foskor 30/60 stuccoed system. Relative change in length is shown in black, rate of length change is shown in red.

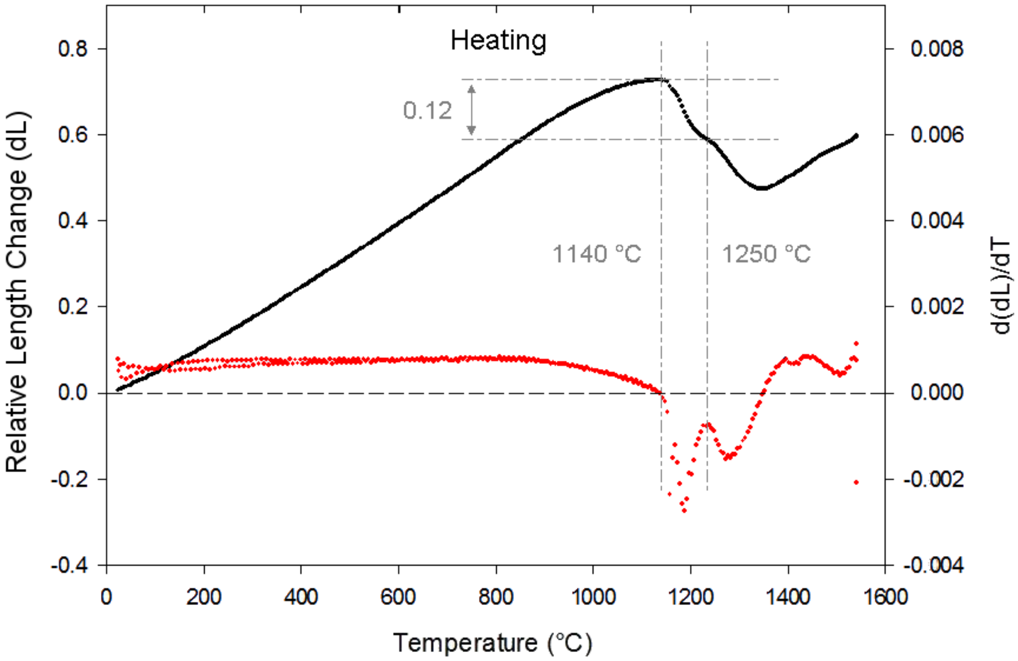

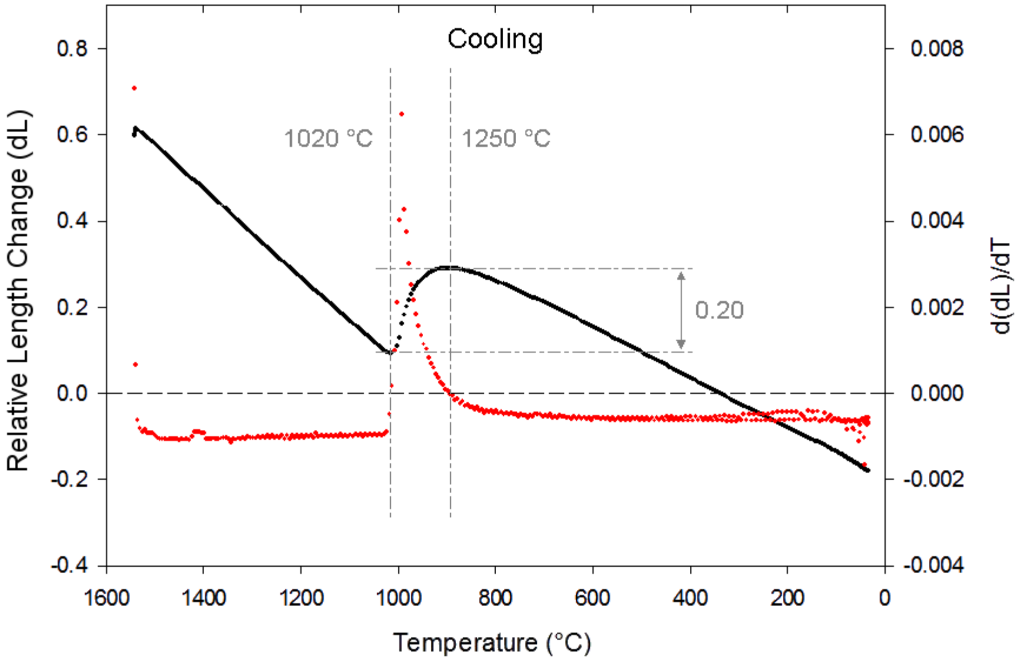

FIGURE 4.31: Thermal expansion data for Washington Mills 35/60 stuccoed system. Relative change in length is shown in black, rate of length change is shown in red.

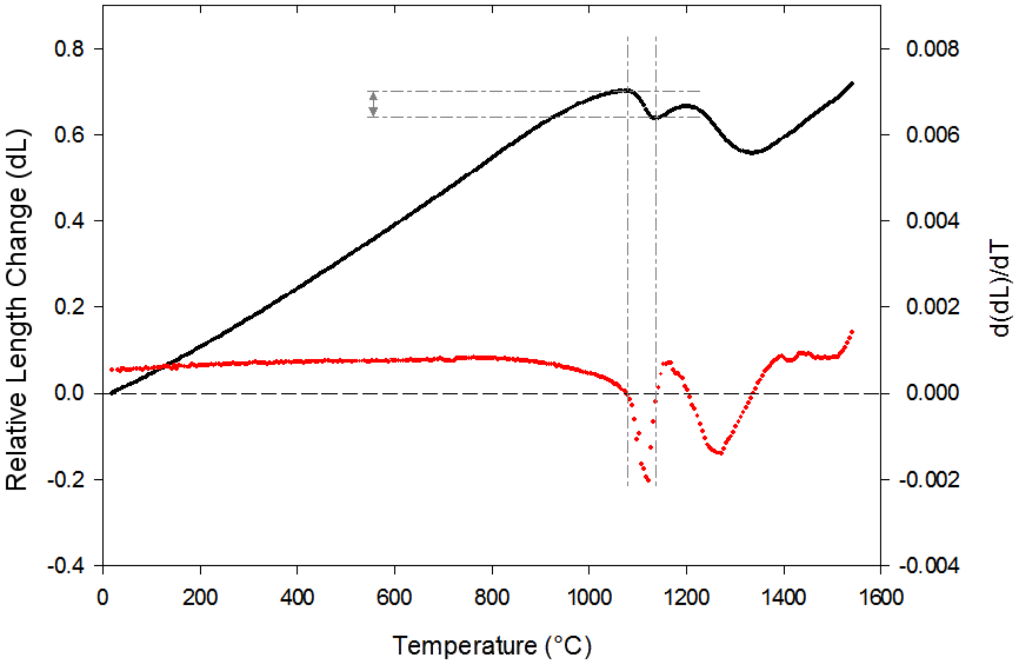

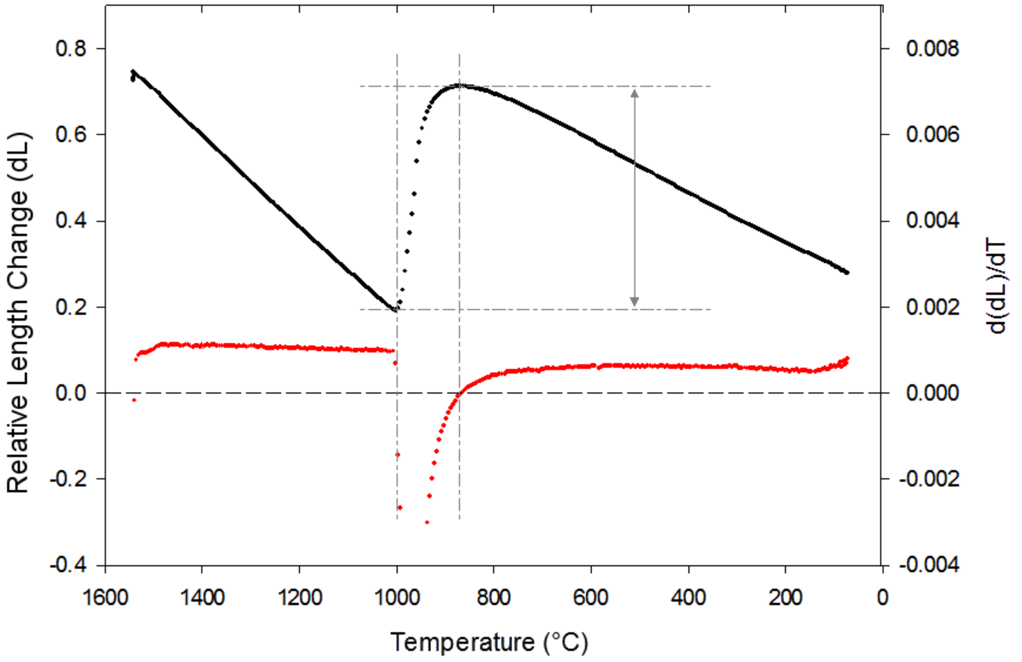

FIGURE 4.32: Thermal expansion data for UCM 30/60 stuccoed system. Relative change in length is shown in black, rate of length change is shown in red.

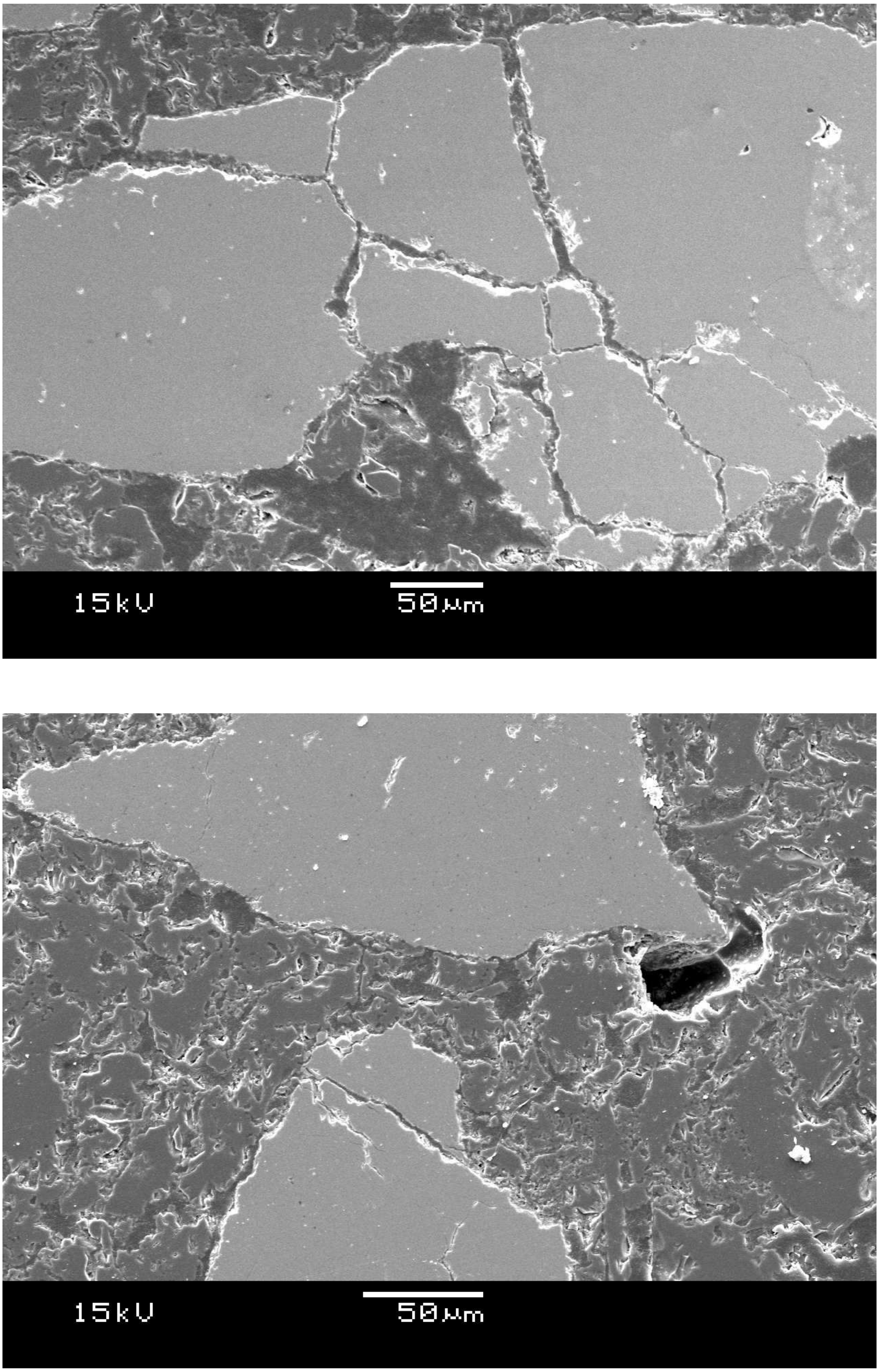

FIGURE 4.33: Ludox HSA based F200-Z shell specimen manufactured using Washington Mills 35/60 zirconia stucco in the fired state. Extensive cracking was observed both throughout the grains themselves and propagating into the interconnecting matrix.

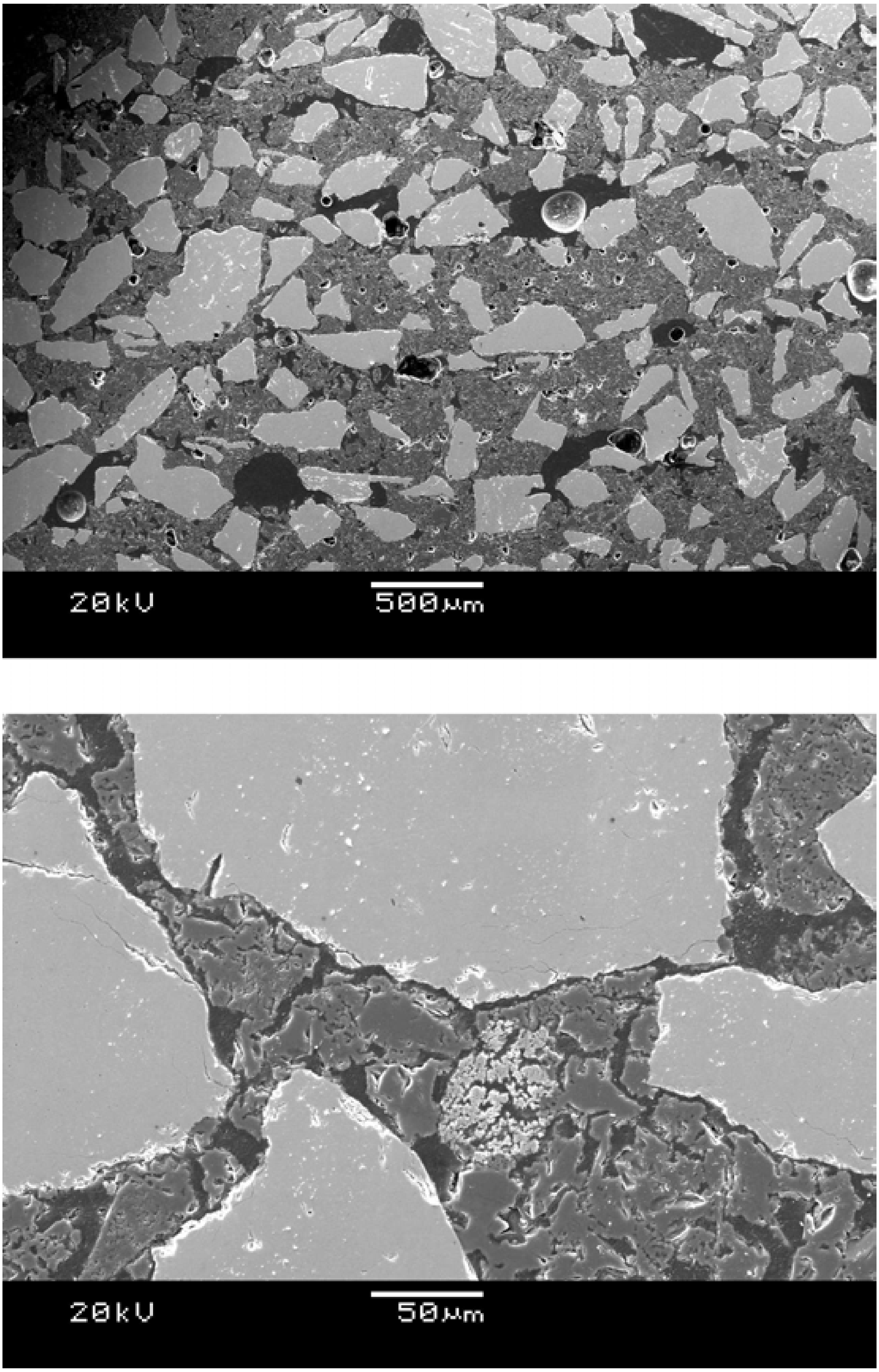

Figure 4.34: Ludox HSA based F200-Z shell specimen manufactured using UCM 30/100 zirconia stucco in the fired state. Extensive cracking was observed both throughout the grains themselves and propagating into the interconnecting matrix.

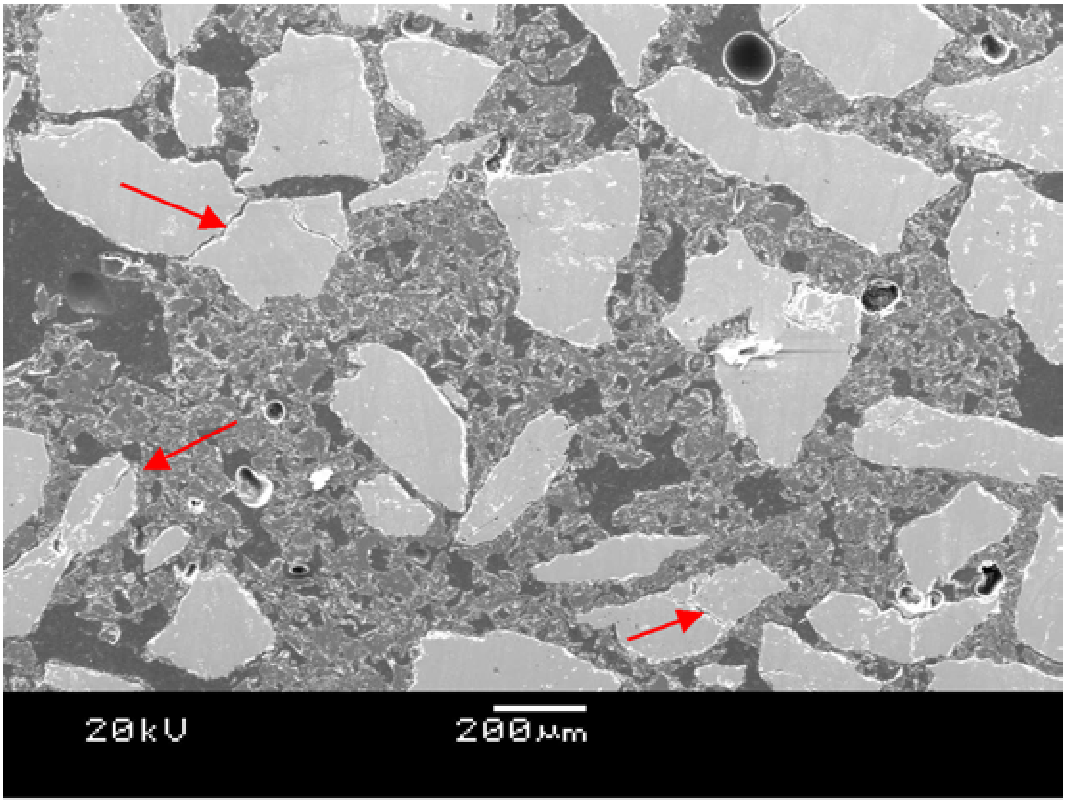

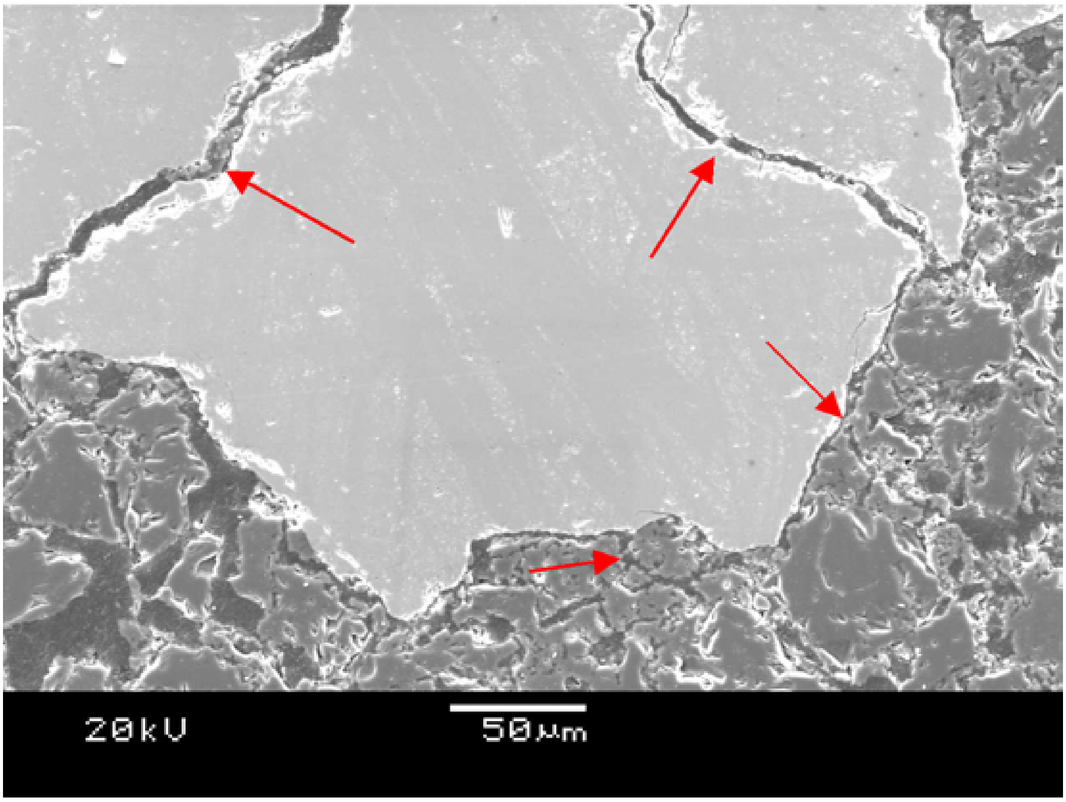

FIGURE 4.35: Ludox HSA based F200-Z shell specimen manufactured using UCM 30/60 zirconia stucco in the fired state. Extensive cracking was observed both throughout the grains themselves and propagating into the interconnecting matrix.

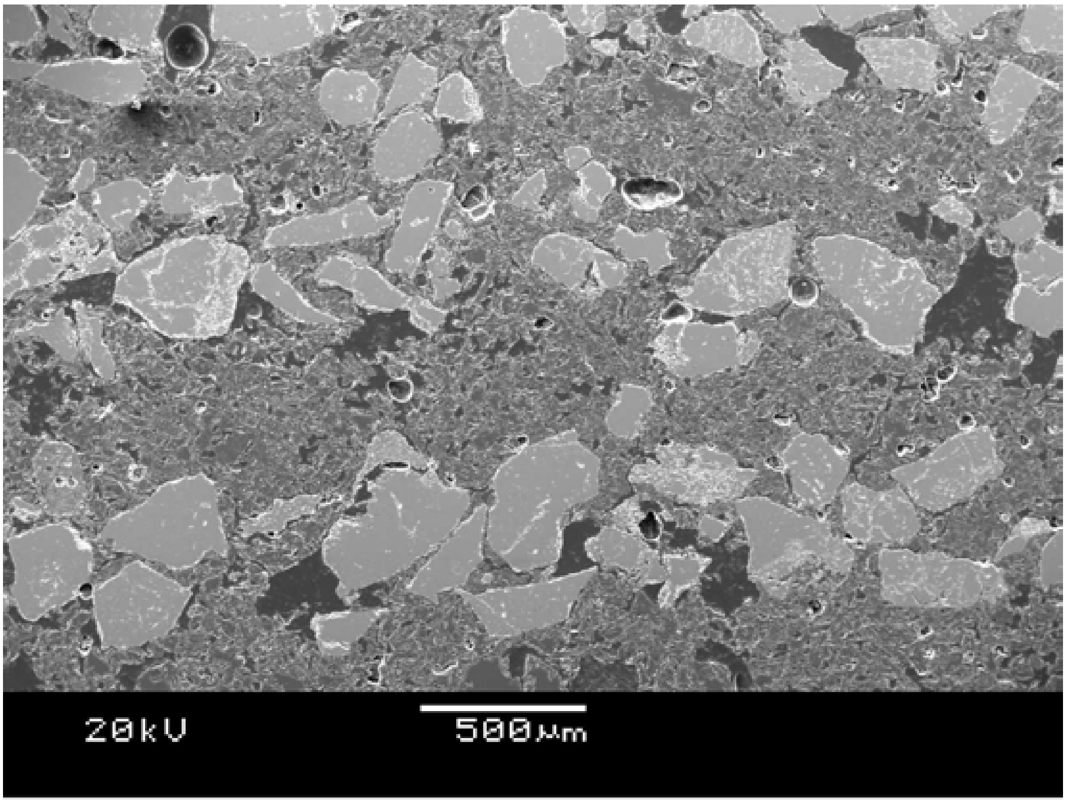

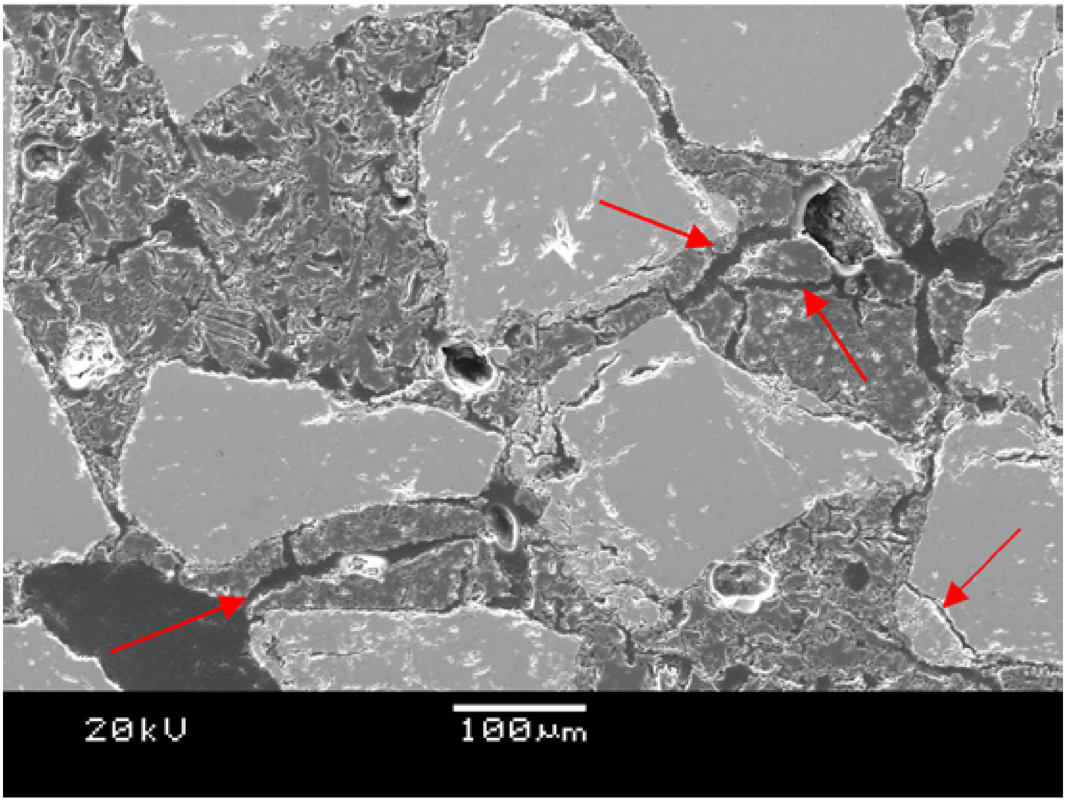

FIGURE 4.36: Ludox HSA based F200-Z shell specimen manufactured using Foskor 30/60 zirconia stucco in the fired state. Extensive cracking was observed both throughout the grains themselves and propagating into the interconnecting matrix.

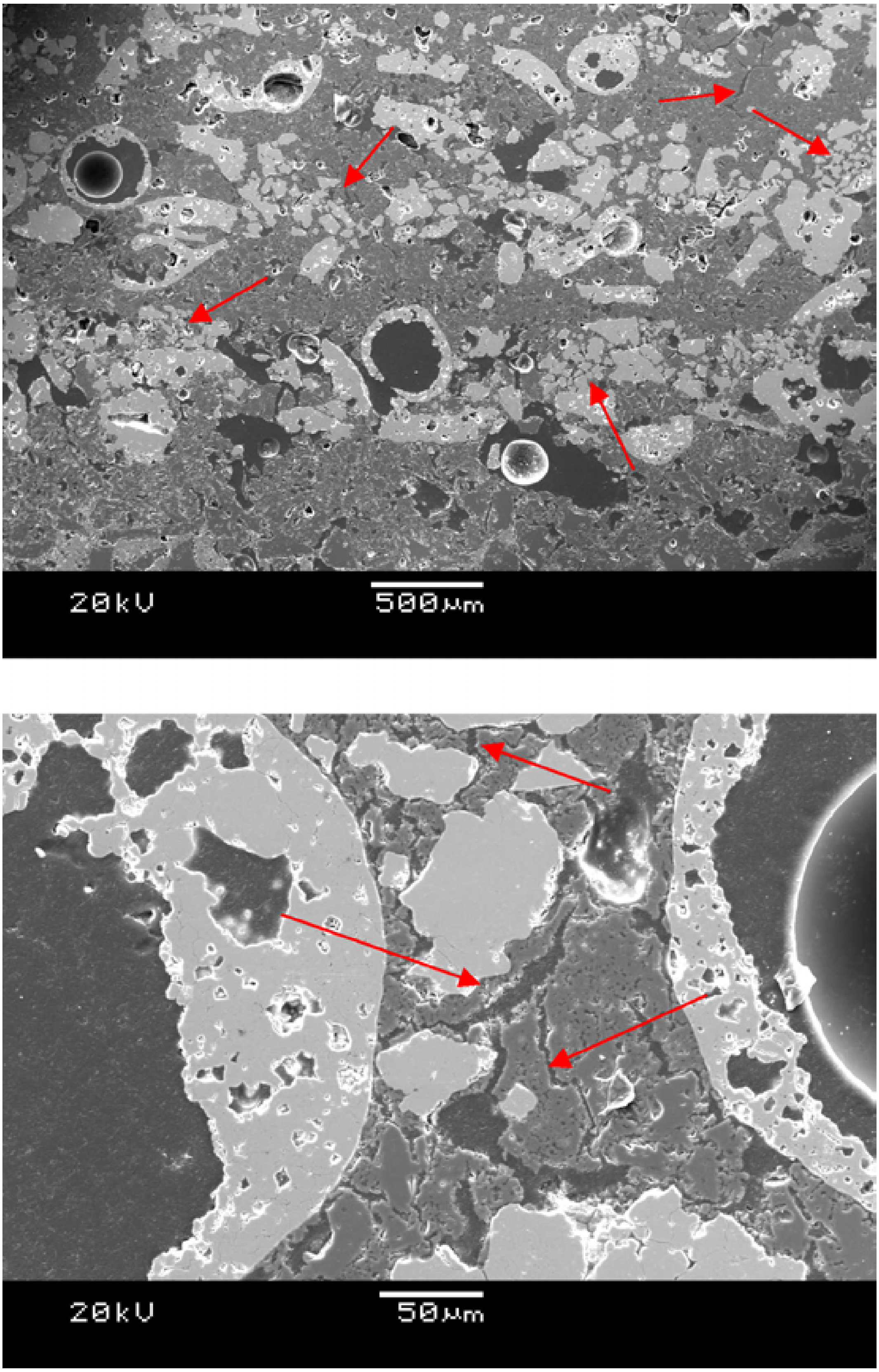

FIGURE 4.37: Ludox HSA based F200-Z shell specimen manufactured using ABSCO 30/60 zirconia stucco in the fired state. Unlike other materials zirconia particles were hollow. Reduced cracking aroung the grains however the matrix showed evidence of cracking.

4.6.1 UCM stucco sizes

It was mentioned previously that material from UCM was supplied as a 30/100 grade; in order to understand the effect this had on thermal expansion behaviour a small amount of material was sieved to 30/60 and used to manufacture shell specimens and thermal expansion samples. Due to the limited amount of material available flexural specimens were only evaluated in the fired condition. To allow direct comparison and negate variation due to slurry condition, specimens stuccoed with fused mullite and UCM 30/100 stucco were manufactured in the same batch. Thermal expansion and flexural testing results are presented in Figures 4.39 and 4.38 respectively.

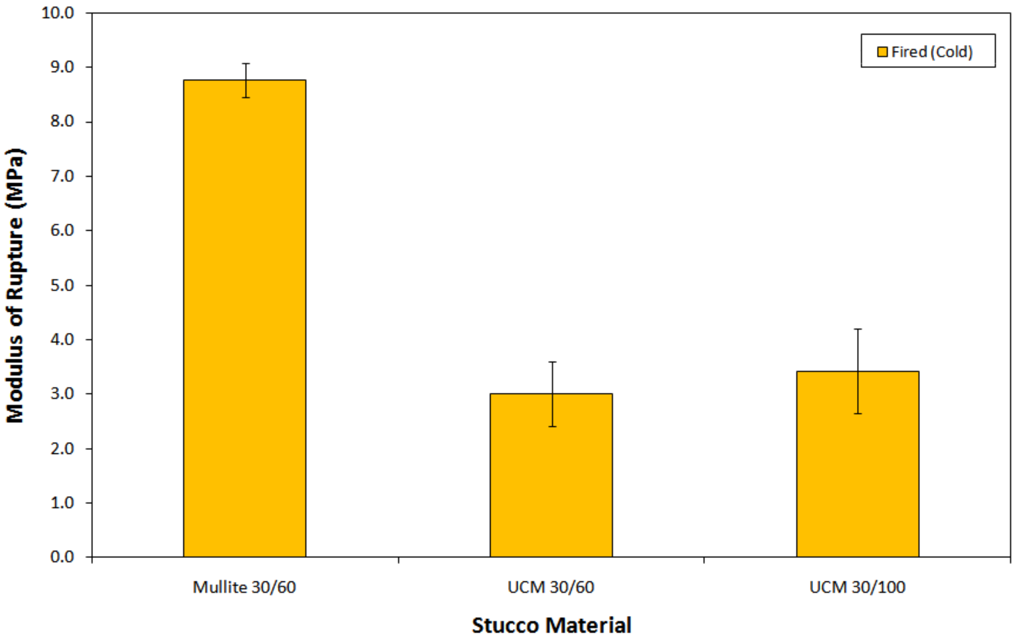

FIGURE 4.38: Measured flexural strengths for shell specimens containing UCM zirconia in both 30/60 and 30/100 grades. Mullite stuccoed F200-M variant included for comparison. All specimens fired to 1550 °C for 30 mins and tested at room temperature.

It can be seen from flexural strength measurements of specimens in the fired condition that the effect of 30/60 grade (590 µm-250 µm) zirconia stucco compared to that of the broader 30/100 (590 µm-150 µm) grade is minimal. Samples made with both stuccoes exhibited a reduction in strength compared to the mullite stuccoed variant. It should also be noted that the trial was performed using the same F200 slurry as used for the manufacture of the previously mentioned samples. Since the trials were performed a number of months after the original trial it was noted that the strengths of samples in each state were reduced, however since the specimens presented in Figure 4.38 were manufactured at the same time the comparison between them remains valid.

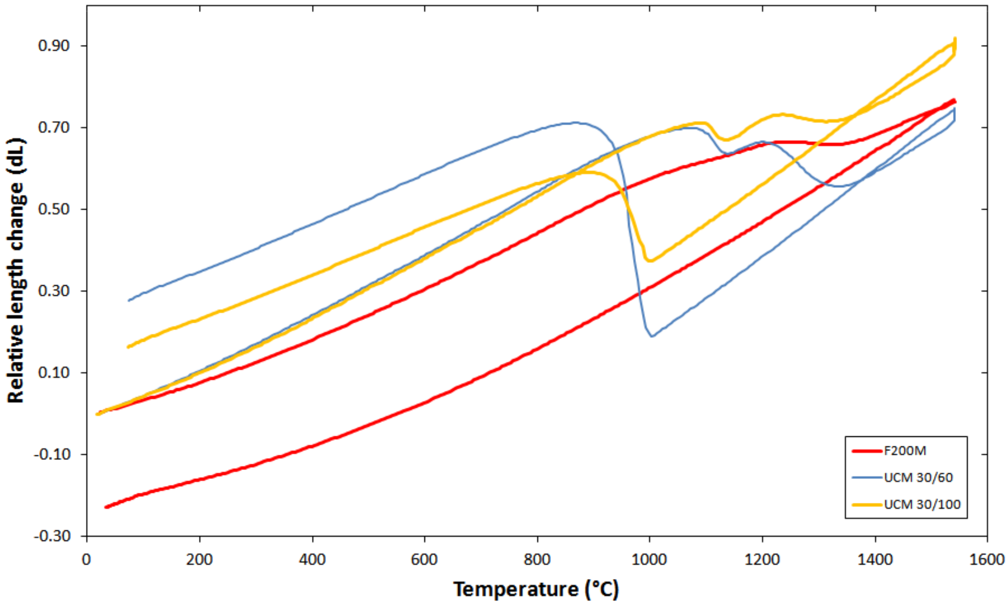

FIGURE 4.39: Thermal expansion data for shell specimens containing UCM zirconia in both 30/60 and 30/100 grades. Mullite stuccoed F200-M variant included for comparison

The results of thermal expansion testing of both the 30/60 and 30/100 grades of stucco revealed very little difference in behaviour during thermal cycling. The removal of the fine content through sieving had no effect on the expansion behaviour during the cooling cycle with both the 30/60 and 30/100 samples exhibiting expansion beyond their original dimensions following testing.

4.7 Stage 2 Small bore trials

Since it gave the greatest reduction in fired strength compared to the mullite stuccoed variant a second round of casting trials were performed using the F200-Z system with Washington Mills 35/60 zirconia as the stucco. As before trials consisted of moulds shelled using standard primary and primary +1 coats at the Precision Casting Facility (PCF) which were subsequently transported to the University of Birmingham for application of backup coats. Mould transport was temperature controlled to minimise any cracking due to thermal expansion of the wax former.

Figure 4.40 shows the progression of moulds during manufacture including incidents of mould loss. During processing it was noted that F200-Z (and also F200-M) moulds were notably weaker than standard PCF moulds, however the level of green and fired strength was greatly enhanced over moulds produced in Stage 1 using the unstable SiAl4060 system. Properties of the shell materials were not recorded directly using a robot mould as extensive slurry monitoring and regular F200-M test bar manufacture had proven the system to be stable during the dipping period. As the slurry is common to both the mullite and zirconia stuccoed variants stability of the latter was implied due to stability of the former.

Figure 4.40: F200-Z mould progression and losses during processing. Mould lost on drier is related to a drier fault rather than material properties.

Due to mould losses during processing and casting only 13 blades were finally produced. A number of inspection operations are routinely performed on all castings to ensure their compliance with the specification. RX is determined during the grain size assessment (GSA) operation during which, etched single-crystal blades are manually examined for the presence of any secondary grains indicative of RX. It was observed during this operation that of the 13 F200-Z blades examined, only 1 (7.6 %) was designated as scrap due to the presence of RX. Comparative data from PCF standard production showed that during an 11 month period, 1933 Pegasus 522' blades were manufactured using the Std. SX shell system, of those 957 (55 %) were scrapped due to the presence of RX.

However it should be noted that during the trial three PCF Std. SX control moulds were cast alongside the trial moulds; all 12 blades were cast RX-free (0 % RX). This suggested that the observed reduction in RX occurrence was not statistically significant. The trial did however generate useful information regarding the performance of the shell material during the various stages of the casting cycle.

4.8 Green strength concerns

The green and pre-fired strengths of the F200 shell systems were greater than that of the unstable SiAl4060 system, however an unacceptable level of mould cracking was still evident during mould trials. It is well known that prior to sintering, shell strength is largely dependent on the siloxane bonding between silica binder particles. It is also known that aluminium modified binders, such as Ludox HSA used in the F200 system, exhibit lower levels of green and pre-fired strength than sodium stabilised varieties. To counteract this various green strength additives are available to enhance the green strength of ceramics made with these binders; a number of these were trialled with Ludox HSA and are discussed in section 5.3. During flexural testing the level of increase offered by the enhancers however was low at around 1 MPa, in comparison the use of a sodium stabilised binder gained around 4 MPa. It is unlikely that an increase of 1 MPa in the green state would have significantly reduced the mould cracking issues, therefore a new formulation for the F200 shell system was developed using Wexcoat 0825, a conventional sodium stabilised binder in place of the aluminium modified Ludox HSA. The resulting systems were named W200-M and W200-Z for mullite and zirconia stuccoed variants respectively. Shell specimens were manufactured in both variants and their flexural strengths determined as before using 3-point bend testing, the results of this are presented in Figure 4.41. For comparison flexural strength measurements for the original F200 shell systems (both mullite and zirconia stuccoed) are also presented.

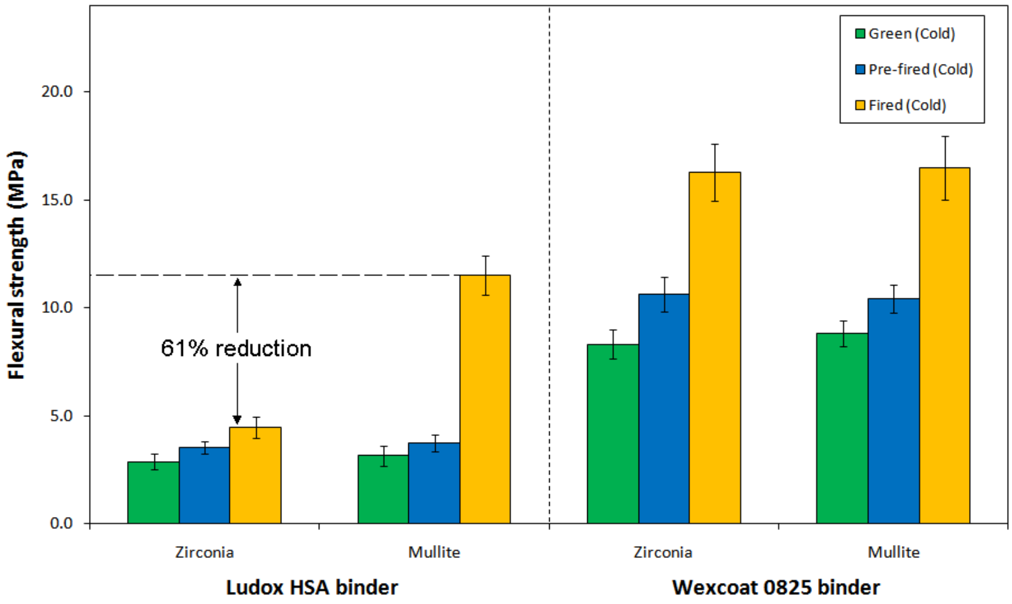

FIGURE 4.41: Flexural strengths measured for zirconia and mullite stuccoed shell systems based on both Ludox HSA and Wexcoat 0825. It was observed that samples bound with Wexcoat exhibted increased strength in all conditions; the presence of zirconia stucco did not reduce fired strength in these samples.

As expected, it was observed that replacing Ludox HSA with Wexcoat significantly increased the green and pre-fired strengths on average by 5.6 and 6.9 MPa corresponding to 285 % and 290 % respectively. It was also observed that unlike the Ludox HSA based systems which exhibited a 61 % reduction in fired strength between the mullite and zirconia stuccoes, no significant reduction in strength was observed for Wexcoat based systems. To understand what effect the sodium-stabilised binder had on the zirconia phase transition samples of each material were subjected to thermal expansion testing and examined by SEM; results of the former are presented in Figure 4.42.

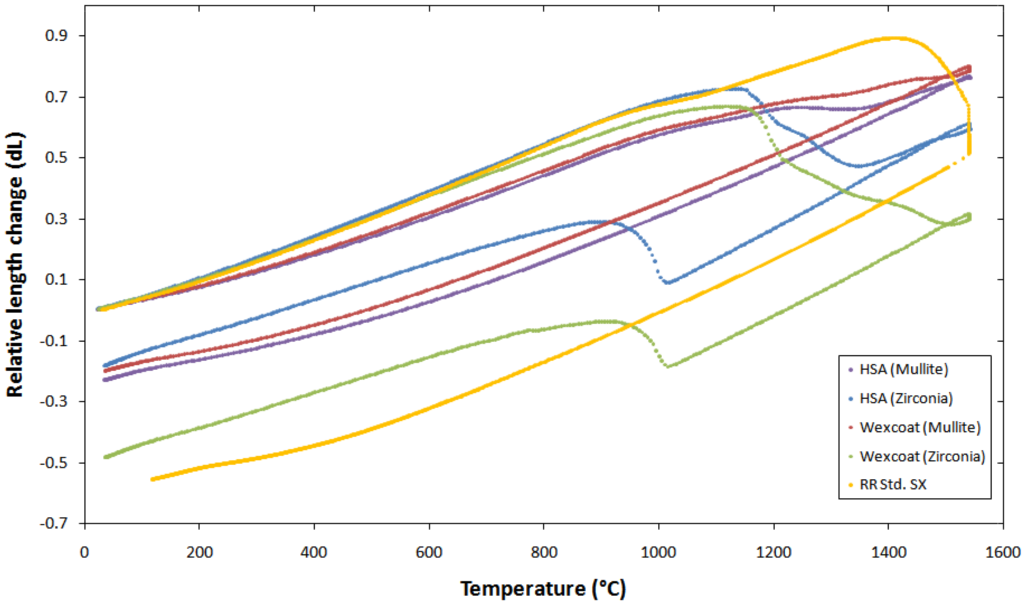

FIGURE 4.42: Comparison of thermal expansion behaviour for mullite and zirconia stuccoed shell systems featuring Ludox HSA and Wexcoat binders.

Inspection of the data revealed that the transition was present and occured across a similar temperature range irrespective of binder with the forward transition beginning around 1135 °C and continuing until 1250 °C; similar length changes due to transformation also in both variants. As reported in the literature and observed for all other zirconia containing shell samples the reverse process occurs over a narrower temperature range from 1020 to 920 °C. Transformation data is summarised in Table 4.9.

The overall relative sample contraction was greater for the Wexcoat bound system at 0.488 compared to 0.187 for the HSA equivalent. This was not observed for mullite stuccoed variants with overall contraction measured at 0.231 for both Wexcoat and HSA bound materials. It is suspected that this was due to sintering effects linked to the presence of sodium within the shell material; this process is discussed further in Chapter 5. For comparison the thermal expansion behaviour

Table 4.9: Thermal expansion of shell specimens measured during phase transitions in both forward and reverse directions for specimens containing different silica binder materials.

	Transformation temperature (°C)					
	Heating			Cooling		
	Monoclinic (Start)	Tetragonal (End)	(dL)	Monoclinic (Start)	Tetragonal (End)	(dL)
Ludox HSA	1140	1250	-0.12	1020	900	0.20
Wexcoat	1130	1250	-0.21	1020	910	0.14

of the zircon-filled Rolls-Royce standard single-crystal (Std. SX) shell system is presented in Figure 4.42, it can be seen that whilst the overall contraction of the wexcoat based zirconia shell system is larger than the HSA variant it remains comparable to the Std. SX shell (which also featured a sodium stabilised binder).

Samples of the Wexcoat bound shell material were examined using Scanning Electron Microscopy (SEM) and observations of the microstructure in the fired condition were compared to those made on the HSA bound shell material; Figures 4.33 and 4.43 show samples in the fired state.

It was observed that Ludox HSA samples featured extensive cracking both within the stucco grains and also extending into the surrounding shell material; transgranular cracks extending around the perimeter of stucco grains were also observed and are likely to have been caused by the expansion experienced during cooling through the tetragonal to monoclinic phase transition. In contrast the Wexcoat based samples exhibited reduced levels of cracking; the occurrence of transgranular cracking was minimal and although cracks were still observed within stucco grains themselves their propagation into the matrix was either not present or minimal. Analysis of these micrographs showed that the level of zirconia within the shell had fallen from 43 % for the HSA shell to 29 % for the Wexcoat shell; it has been shown previously that reduced zirconia content lead to lower levels of fired

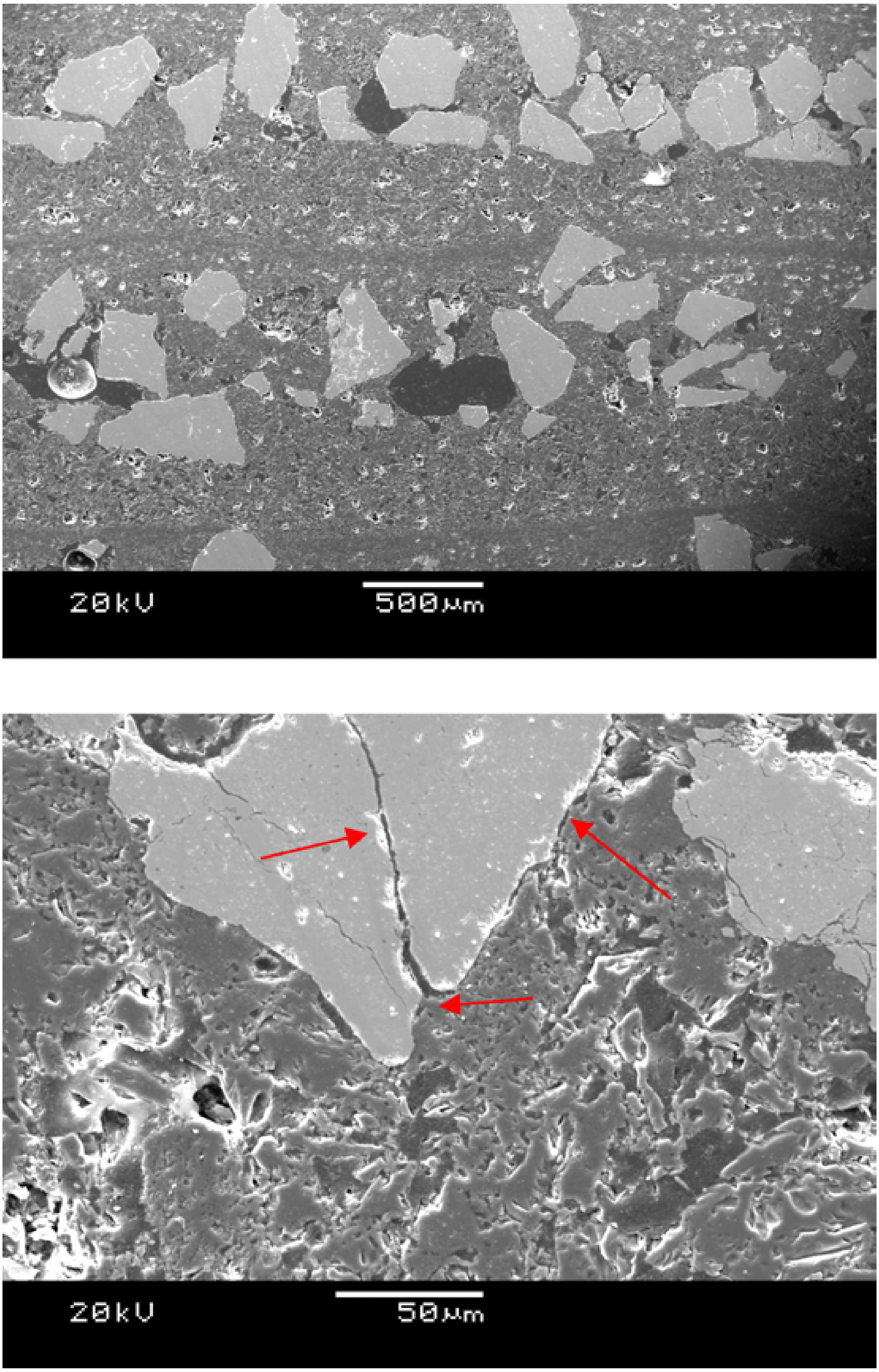

Figure 4.43: Wexcoat based W200-Z shell specimen manufactured using Washington Mills 35/60 zirconia in the Fired state. Unlike the HSA based variant samples made from this material exhibited little cracking.

strength reduction although for all previous systems some weakening effect had been retained. The reduction in relative zirconia content was due to the increased shell thickess related to the shell build of the Wexcoat bound system.

Based on the mechanical test results and the lack of cracking observed in the matrix of Wexcoat samples, it was necessary to reformulate the shell. It is likely that the addition of sodium within the matrix of the W200 allowed the silica to form a glassy phase which promoted sintering and densification around the stucco particles. Due to this the system was sufficiently strong to resist the formation and propagation of cracks associated with the transformation of zirconia stucco particles. Without these cracks to act as sites for failure initiation and stress concentration the bulk materials were better able to resist applied forces during testing and therefore exhibited greater strength. To capitalise on the volumetric phase transition and once again induce cracking into the matrix it was necessary to increase the effect of the stucco within the shell. Due to the manufacturing process the amount of stucco which can be applied is limited to that which adheres to the surface area. In order to increase the stucco volume percent to the levels observed in the HSA shell two methods were employed; the use of larger stucco particles would increase the volume of zirconia contained within each coat and the viscosity of the slurry was reduced in order to reduce the thickness of the shell matrix. To investigate this the slurry viscosity was reduced from 50-55 seconds on a B4 flow-cup to 45-50 seconds; shells were also manufactured using a 20/35 mesh (840 µm - 500 µm) unstabilised zirconia stucco from Washington Mills. Flexural strength results of these tests are presented in Figure 4.44.

Another mechanism used within the investment casting industry to reduce shell strength is the inclusion of a so-called slip-layer within the shell. The layer is generated by omitting the stucco during a dipping cycle in a similar process to the application of the seal coat [1], however unlike the seal-coat further (stuccoed) shell

---

[1] The seal coat is the final un-stuccoed slurry layer applied to the shell mould.

coats are applied on top of the slip-layer. Due to the lack of stucco the surface of the slip-layer is much smoother than conventional shell coats, it is believed that the interface between the slip-coat and subsequent layers acts as a failure initiation point. There is anecdotal evidence within the investment casting industry that this relieves the stresses linked to RX which build up during the cool-down cycle [99]. To investigate the efficacy of this technique shell specimens were made featuring an un-stuccoed slip-layer on the third backup dip; samples were otherwise identical to the reduced viscosity 35/60 stuccoed samples.

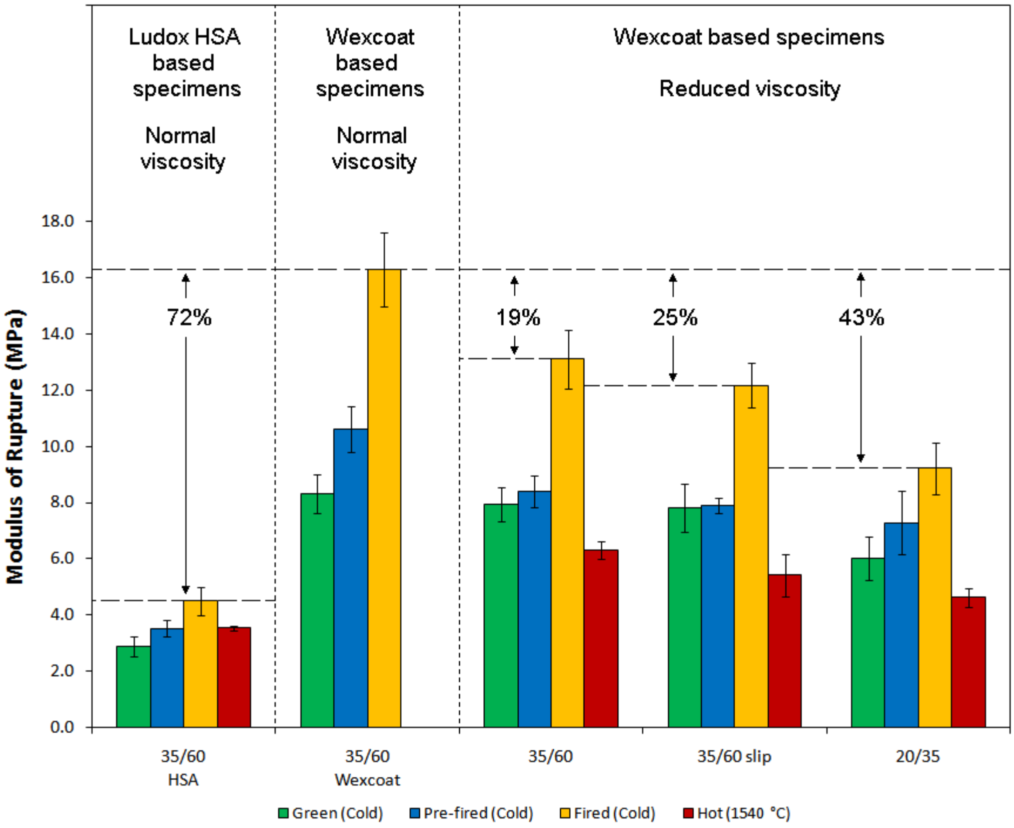

FIGURE 4.44: Flexural strengths for test bars manufactured using Washington Mills zirconia stucco with various manufacturing techniques.

The reduction in slurry viscosity caused a reduction in flexural strengths of fired specimens of 19 % compared to specimens made at the original viscosity; this modification had little effect on green strength and a modest reduction in pre-fired strength at 4 % and 20 % respectively. The strength was further reduced through the incorporation of the larger zirconia stucco material with a fired strength 43 % lower than the original system, however the accompanying loss of green and pre-fired strengths at 28 % and 31 % suggested that this may have been due to a difference in particle packing and sample density rather than enhanced cracking due to the larger particles. Samples incorporating an unstuccoed slip-coat exhibited little difference in flexural strength compared to the conventionally built specimens, this may have been due to the force being applied perpendicular to the slip-layer during testing. Rather than encouraging failure at the interface this would have ensured that the layers remained in intimate contact; compressive testing may have yielded different results but was not performed for these shell materials.

Water absorption porosity measurements made using the shell specimens of each type are presented in Figure 4.45; the occurrence of the reduced porosity of the weaker systems, namely 20/35, was not expected based on the reduction in mechanical properties and cannot be explained through observations of the microstructure.

To further investigate the structure of the above shell materials specimens were examined by SEM; micrographs of the reduced viscosity, slip-coat and 20/35 mesh stucco variants are presented in Figures 4.46, 4.47 and 4.48 respectively.

From the micrographs it is clear that reducing the thickness of the matrix has increased the number of cracks generated during thermal cycling, it is likely that this is due to the reduced volume of material supporting the load generated by the phase transition. Slip-coated samples exhibited identical microstructure in the regions away from the slip-layer however within the layer itself few cracks were observed. This observation is concurrent with that observed in the samples made using the original, higher viscosity slurry; a thicker slurry layer better resists the stresses generated during the phase transition. This was substantiated

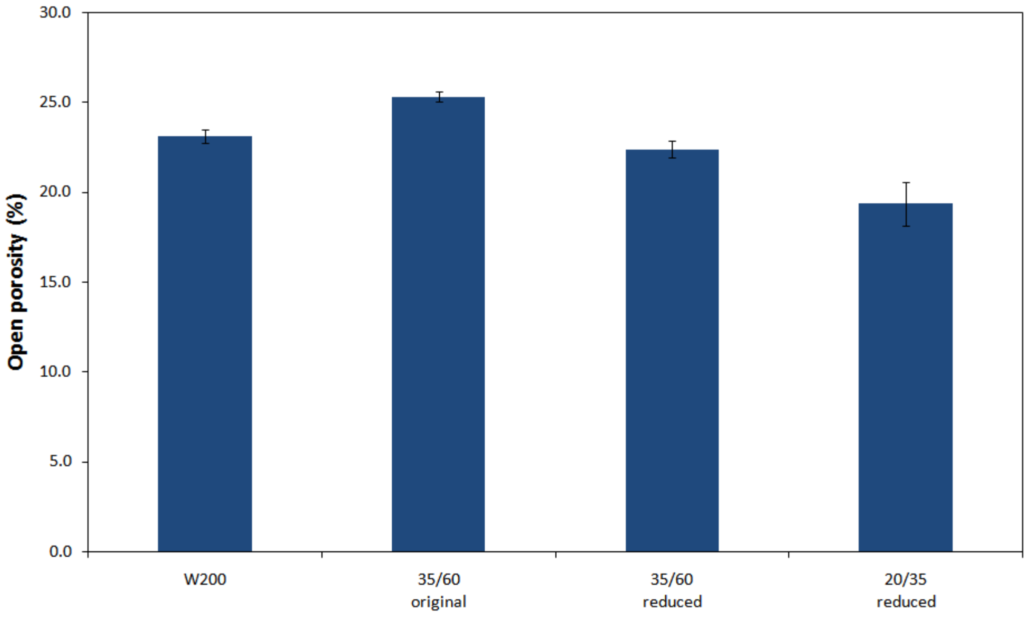

FIGURE 4.45: Open porosity of Wexcoat based zirconia stuccoed shell materials as measured by water absorption.

by analysing the stucco content of the original and reduced viscosity specimens from micrographs. Reducing shell viscostiy and hence the matrix thickness increased relative stucco content from 29 % to 42 %. The trend for reduced fired strength with increased stucco content was consistent with that observed for all other zirconia containing shell materials.

The microstructure of shell specimens containing 20/35 stucco exhibited extensive cracking both of the grains themselves and also of the surrounding matrix. Cracking around the perimeter of the grain was particularly evident with the larger stucco material. This system exhibited the largest number of cracks propagating into the surrounding matrix. This can be explained by considering the expansion of individual grains and is discussed in the following section.

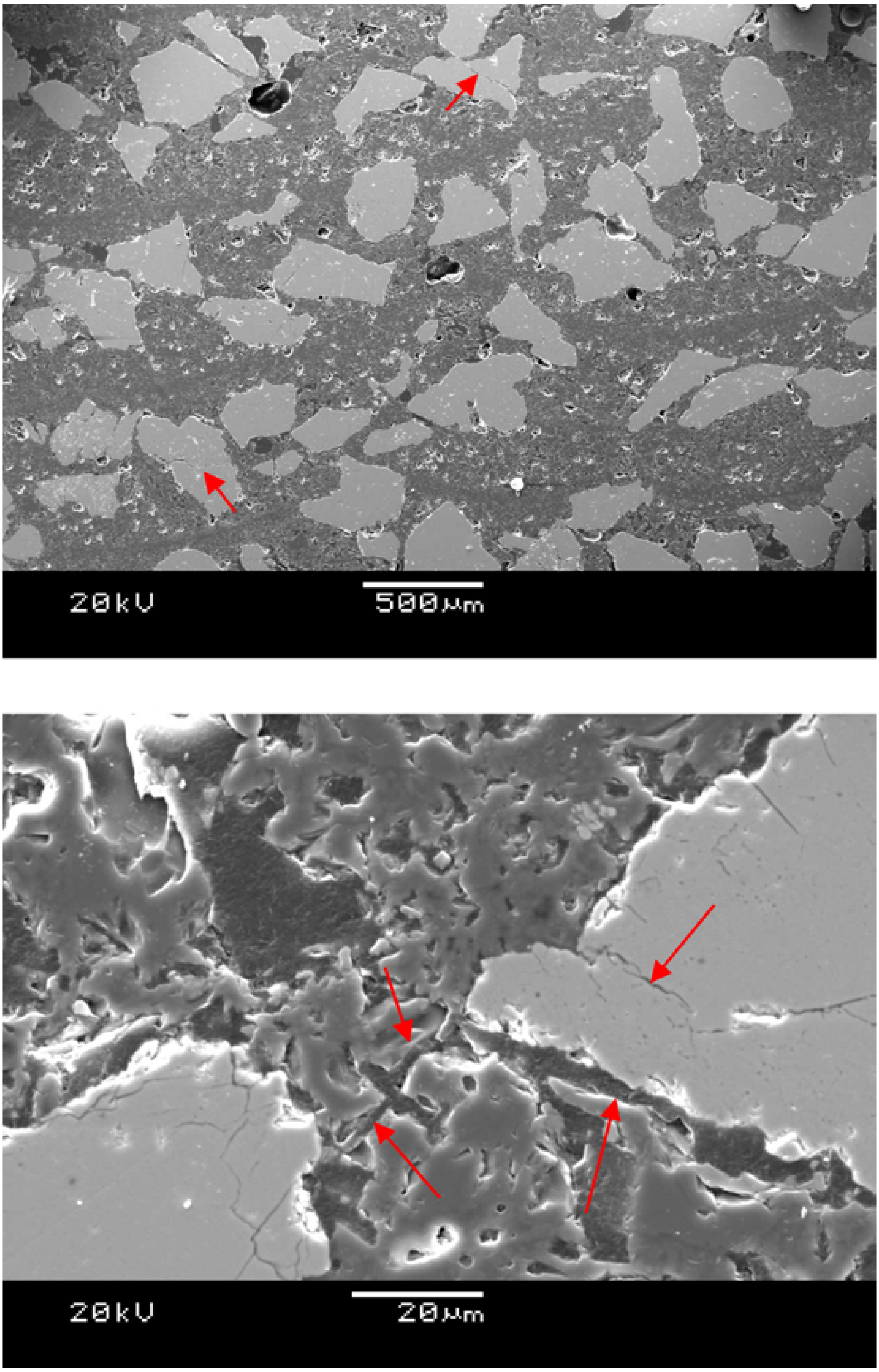

FIGURE 4.46: Reduced viscosity Wexcoat based W200-Z shell specimen manufactured using Washington Mills 35/60 zirconia in the Fired state. Red arrows indicate the locations of cracks within both stucco grains themselves and also the matrix

.

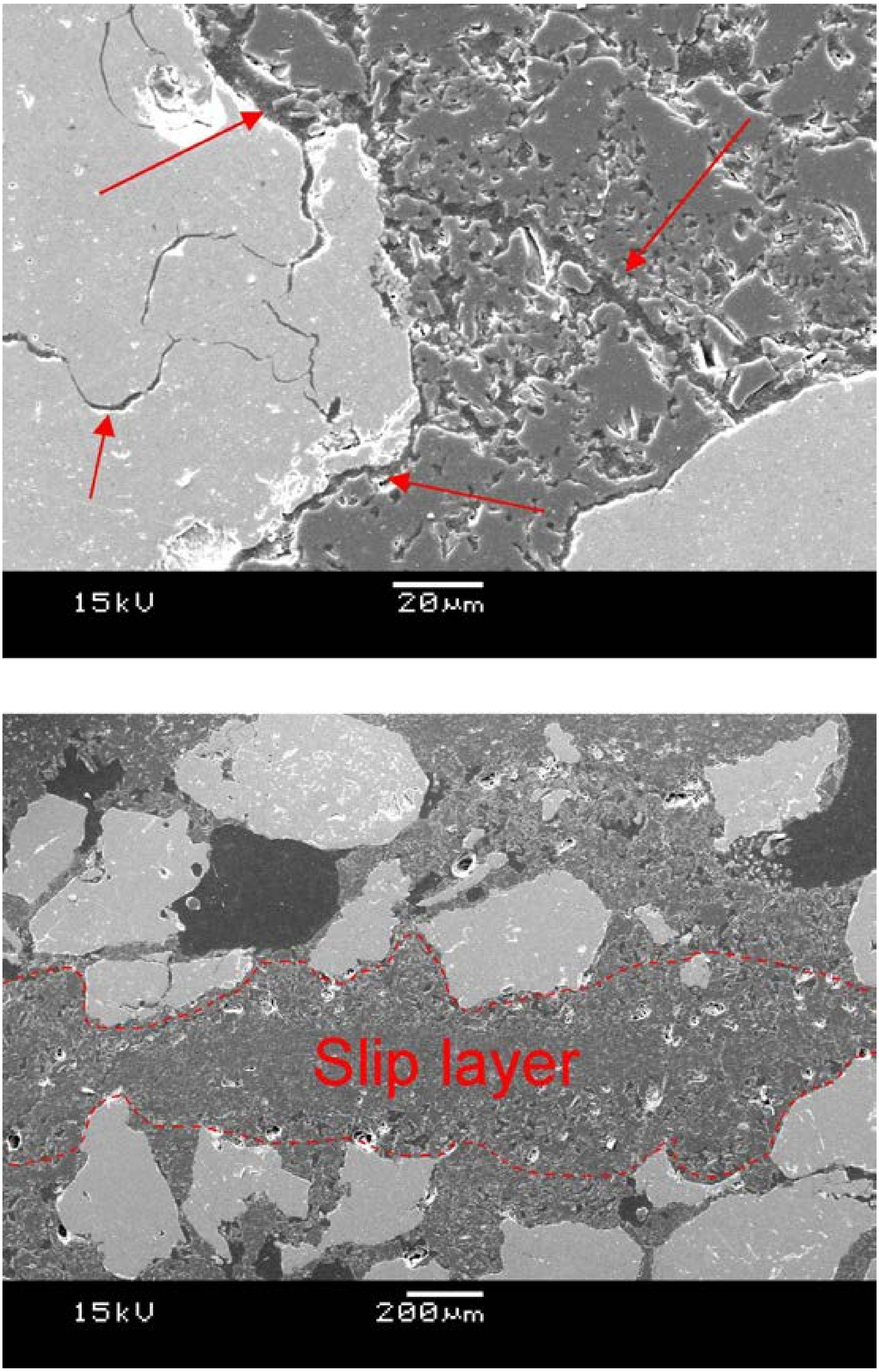

FIGURE 4.47: Wexcoat based W200-Z shell specimen manufactured using Washington Mills 35/60 zirconia stucco featuring an un-stuccoed slip-layer. Sample was examined in the Fired state. Cracking around grains was observed (red arrows) however no propagation through the slip-layer was evident.

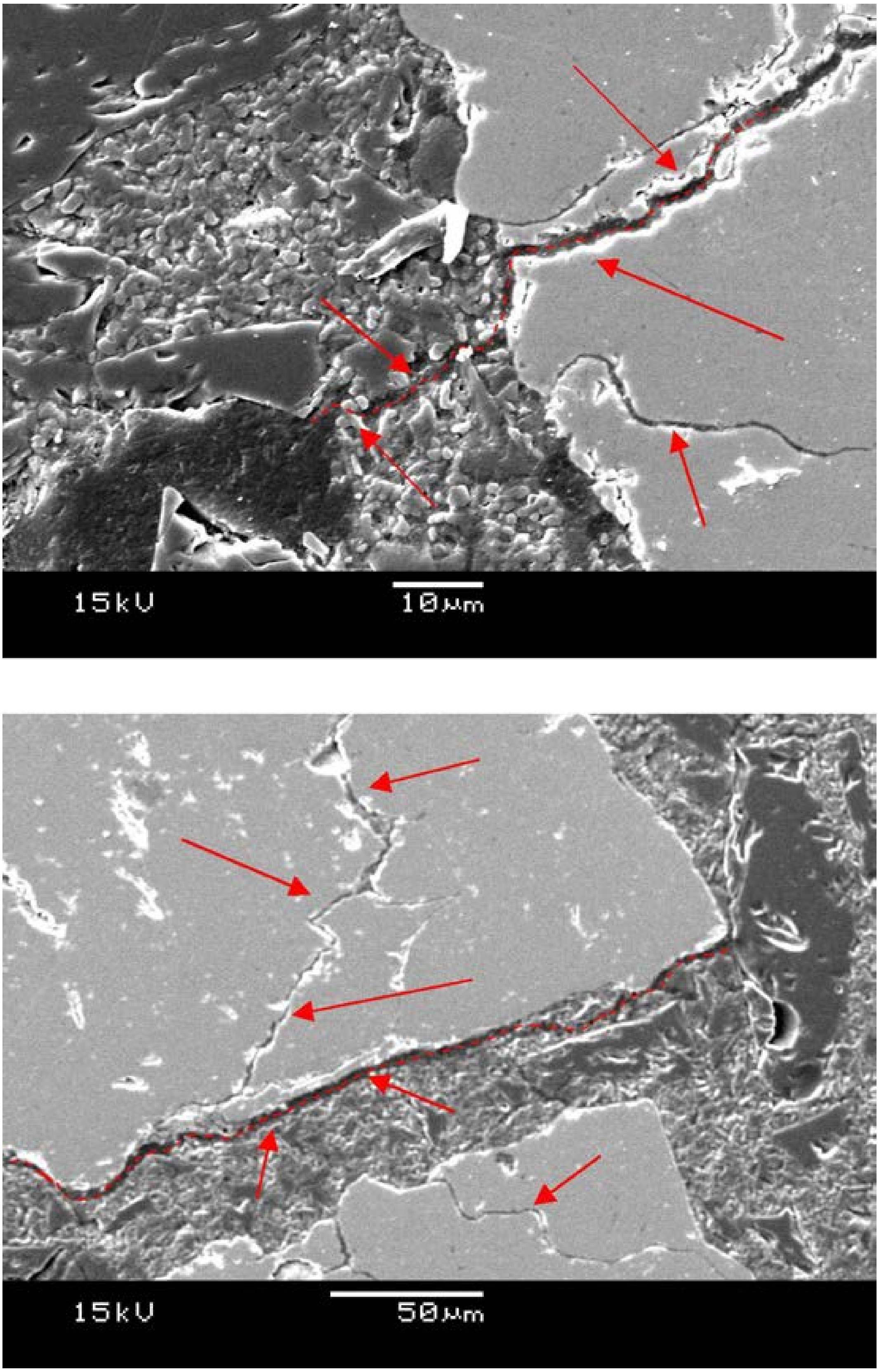

Figure 4.48: Wexcoat based W200-Z shell specimen manufactured using Washington Mills 20/35 zirconia in the Fired state. Extensive cracking was observed both throughout the grains themselves and propagating into the interconnecting matrix.

4.9 Effect particle size during phase transformation

In order to better understand the effect of the phase transformation on mechanical properties it is necessary to consider the linear effect of the volume expansion. Although stucco particles are neither spherical nor cubic (in terms of morphology rather than crystal structure) assumption of either simplifies the volumetric calculations. Table 4.10 shows the omnidirectional linear expansion based on a spherical stucco particle experiencing a volume change of 5 % during transformation. Although the ratio of expansion to diameter is constant the absolute expansion varies from 3 µm for a 150 µm particle up to 14 µm for an 850 µm particle. Inspection of SEM micrographs reveals stucco separations of less the 50 microns, considering the extreme case of two neighbouring 850 micron stucco particles the distance between them would change by more than 50 % during cycling. The observation that increasing the size of stucco particles and reduction in their separation reduces shell strength is therefore not unexpected.

TABLE 4.10: The effect of monoclinic - tetragonal phase transformation on linear expansion of particles. All values given in microns and calculated using spherical particle approximation. Note the reduced particle size for material in the tetragonal state corresponding to the volume reduction associated with transformation in this direction.

Particle size (µm)		
Monoclinic	Tetragonal	Linear change
850	836	14
750	737	13
650	639	11
550	541	9
450	442	8
350	344	6
250	246	4
150	147	3

Figures 4.49 and 4.50 present the results of thermal expansion measurements of W200-Z shell materials stuccoed with Washington Mills unstabilised zirconia in

both 35/60 and 20/35 grades; results are, as before, mean values taken from two independent measurements.

It was observed that material featuring 20/35 stucco exhibited larger expansion and contraction behaviour during thermal cycling; values in Table 4.11 were estimated from thermal expansion data. Considering the maximum stucco particle size is approximately 850 microns for the 20/35 grade and 500 microns for the 35/60, the observation that thermal expansion (and contraction) during phase transformation was approximately double in the larger stucco are consistent with estimates in Table 4.10. That this also increased both the amount of shell cracking observed in the shell micro structure and the reduction in measured fired strength suggests that stucco particle size (and hence the amount of expansion) is an important factor in terms of the ability to deliberately weaken shell materials.

Table 4.11: Thermal expansion of shell specimens measured during phase transitions in both forward and reverse directions for materials containing different stucco grades.

	Transformation temperature (°C)					
	Heating			Cooling		
Stucco grade	Monoclinic (Start)	Tetragonal (End)	(dL)	Monoclinic (Start)	Tetragonal (End)	(dL)
20/35	1140	1260	-0.25	1020	880	0.35
35/60	1130	1250	-0.21	1020	910	0.14

4.10 Stage 3 Small bore trials

A final round of small bore trial work was completed in order to determine the efficacy of the sodium stabilised binder in increasing green strength for moulds. The selection of a new trial part was necessary for a number of reasons. At the time of the trial the Pegasus 522' blade was no longer in production at the

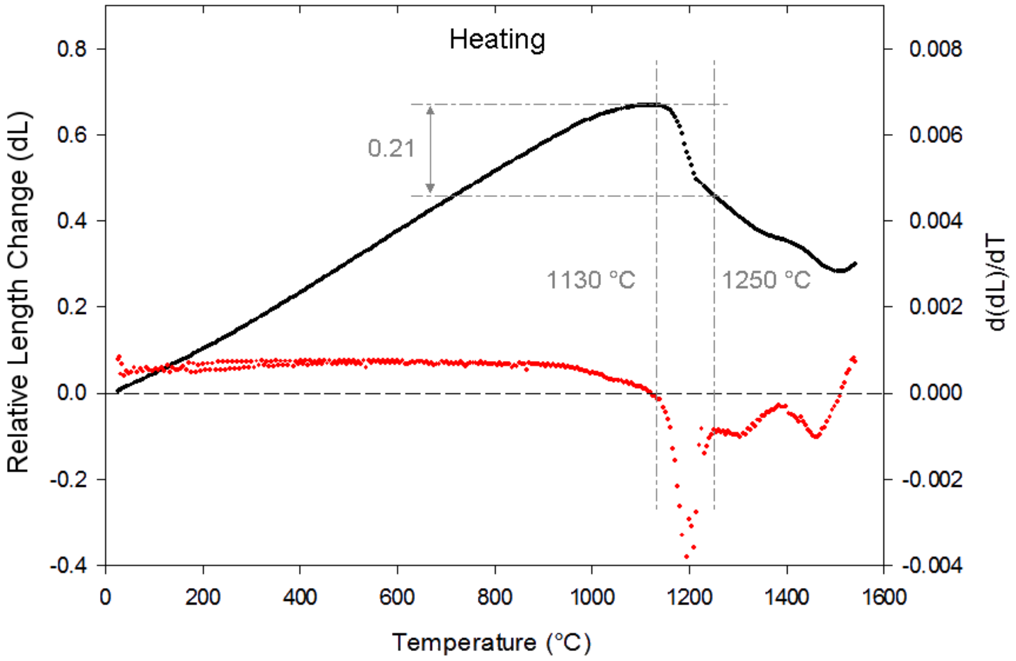

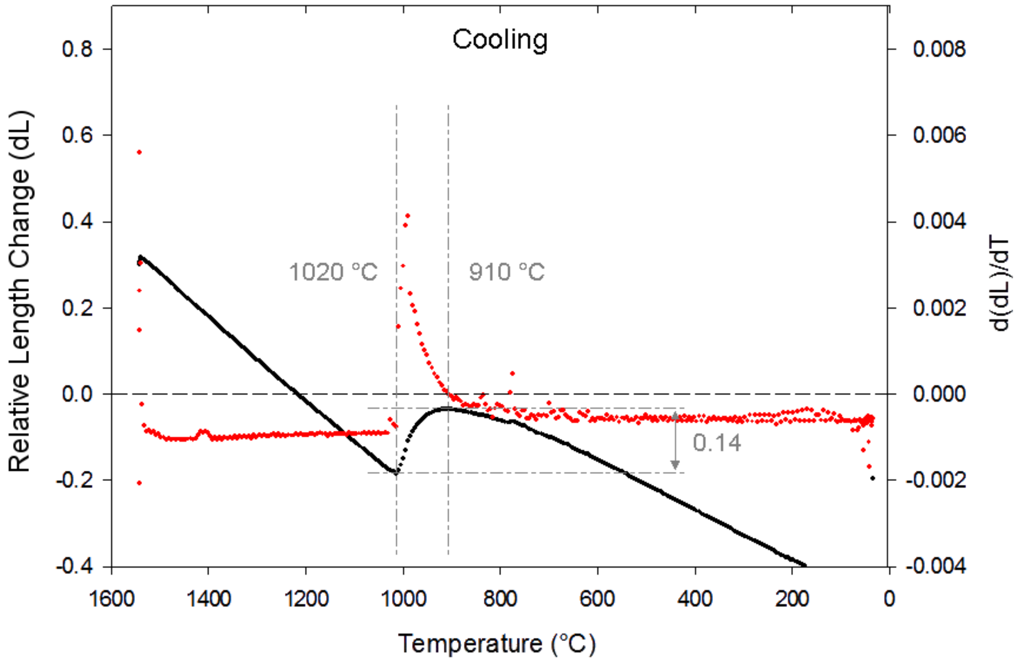

Figure 4.49: Thermal expansion data for Washington Mills 35/60 stuccoed system manufactued with Wexcoat binder. Relative change in length is shown in black, rate of length change is shown in red.

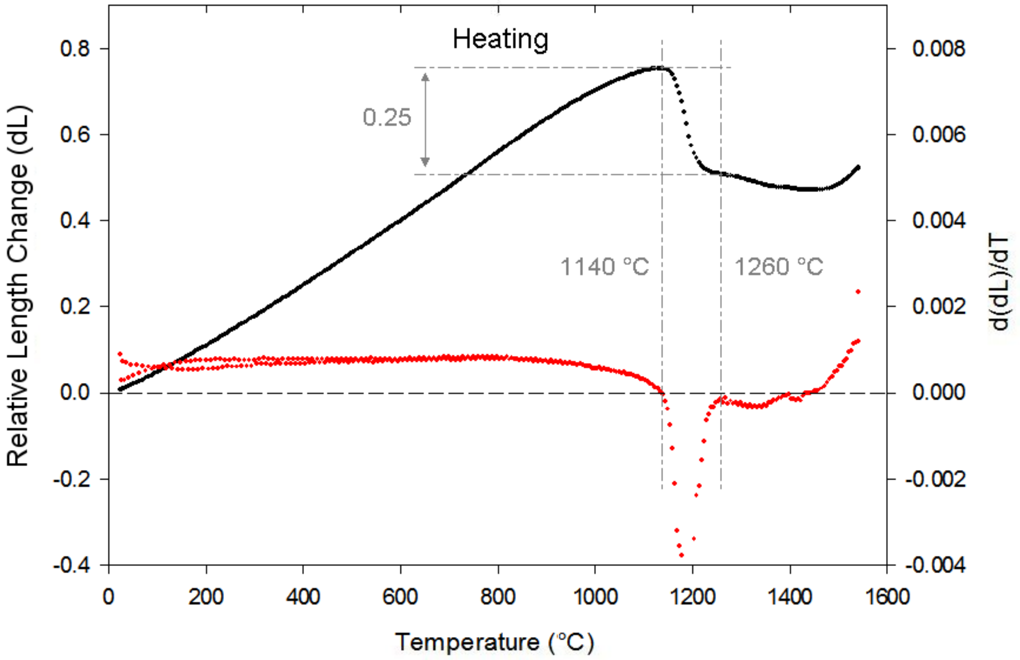

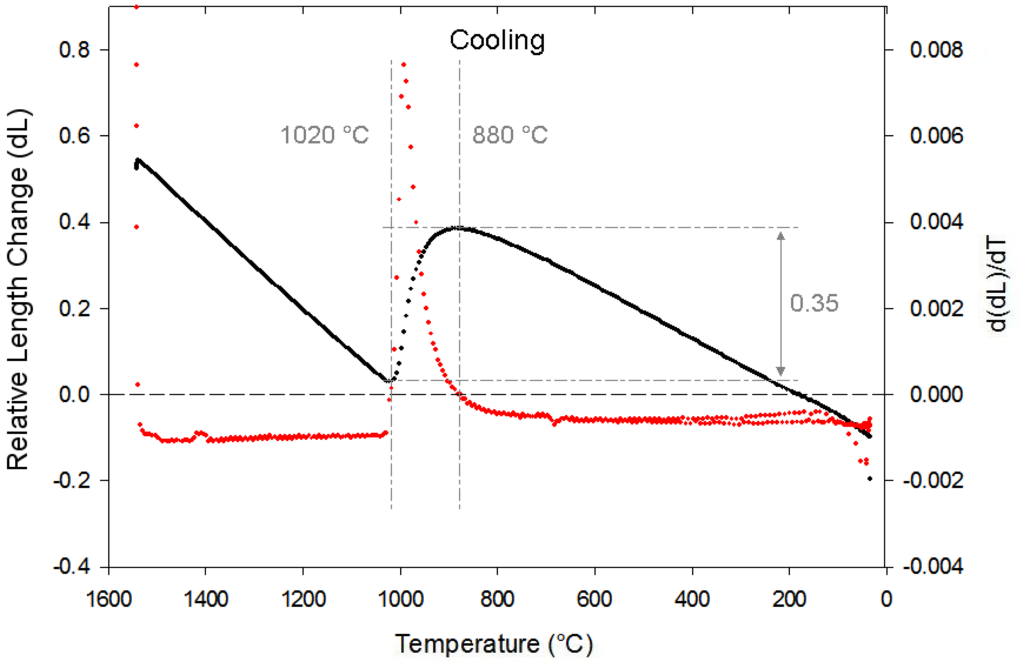

Figure 4.50: Thermal expansion data for Washington Mills 20/35 stuccoed system manufactued with Wexcoat binder. Relative change in length is shown in black, rate of length change is shown in red.

Precision Casting Facility (PCF), this led to a logistical issue concerning the supply of wax patterns. It also posed a problem in terms of heat-treatment; prior to its discontinuation [2] the 522' blade was the only part cast using the superalloy SRR99. After its discontinuation there was no longer a requirement for a regular SRR99 heat-treatment cycle and hence any parts cast in this alloy would require a one-off run. Due to these logistical concerns a new part, the Trent 700 Intermediate Pressure (IP) blade (referred to as part number 579') was selected. A number of reasons existed for its selection including it being cast in the superalloy CMSX4, a widely used alloy within the PCF, and also the high volume of production parts which were regularly being manufactured. Trial parts would no longer require dedicated heat-treatment runs as they could be included with standard production. Due to the low level of RX (3-4 %) exhibited by the 579' blade when cast using the Std. SX system, the number of blades required to gain statistical confidence in any RX reduction was impractically large to manufacture in the UOB shell laboratory. However as with previous mould trials it provided information pertaining to the performance of the shell material during processing and the casting cycle.

As with previous trials primary and primary + 1 coats were applied at the PCF before moulds were transported to the University of Birmingham for the application of backup coats. All subsequent processes were, as before, performed in the PCF. A quantity of 26 off 579' moulds were available for the trial, of those 20 were shelled using a standard shell build with 5 backup coats and the remainder were shelled using a stucco-free slip-coat at backup layer 4. Mould losses during this trial were notably lower with just 2 moulds being lost prior to cast and none lost during the casting cycle. The qualitative observation of shell-room operatives responsible for processing the moulds was that their behaviour was more consistent with the Std. SX shell material (which also features a sodium stabilised binder) than previous trial materials. Due to operational constraints within the PCF, the

---

[2] at the time of writing

RX results were not available at the time of writing this thesis, however as before with the 522' trial, any reduction in observed RX would not be statistically significant and should therefore be disregarded.

4.11 Conclusions

A number of zirconia containing shell materials were evaluated during the completion of this work; variations in the material included both different shell matrices and different zirconia stucco types and sizes. It was shown that the inclusion of unstabilised zirconia as a stucco material was able to reduce the strength of shell materials based on various silica-alumina matrices in terms of both flexural and compressive strengths. However due to the mechanisms responsible for failure in each case it was observed that flexural strength was more greatly affected than compressive strength. The reduction in shell strength was shown to be linked to the expansion of the test bar during the tetragonal to monoclinic phase transition, and the expansion itself was shown to be proportional to the size of the zirconia stucco particles present. It was also shown that hollow 'blown' stucco particles were less effective at reducing strength than dense particles.

It was not however possible to link reduced shell mechanical properties to the occurrence of strain-induced re-crystallisation (RX) within single-crystal (SX) castings. This was in part due to the variability exhibited by RX occurrence and in part due to the lack of a definitive RX test. At the time of writing it is not fully understood which mechanisms are responsible for the manifestation of RX, along with shell strength it is believed to be due to a number of effects including the geometry of the cast article, the surface finish of the cast article prior to heat-treatment and the way in which the heat-treatment cycle itself is performed.

5

Conventional shell systems

5.1 Introduction

The shell systems reported in this chapter were designated as conventional since they did not contain materials intended to induce disruption during thermal cycling, nor did they contain pore-forming-agents to deliberately increase the level of porosity within the shell. The materials contained within them are conventional ceramic materials which include silica, alumina and mullite. As with the preceding chapter a number of trial formulations were utilised to manufacture both test-bar specimens and larger scale shell moulds. Materials were characterised using a mixture of thermal, mechanical and observational techniques. In the following sections trial formulations are presented and discussed along with evaluation of their properties. Conclusions about the various shell materials are drawn in the final section.

5.2 Silica-alumina shell systems

5.2.1 Formulations

One of the main aims of this thesis was the development of a shell material exhibiting reduced strength in order to reduce the occurrence of strain induced recrystallisation (RX) within single-crystal (SX) castings. The Rolls-Royce Hi-shell system was developed in order to cast large non-heat-treated components, and features a matrix composed of reactive alumina, colloidal silica and mullite which upon heat treatment generates a highly mullitic structure. It has been observed by Rolls-Royce that in general the system is excessively strong for the manufacture of heat treated SX blades inducing unacceptably high levels of RX within them. Since the system relies upon the formation of mullite from alumina and silica during firing, it is possible to alter the proportions of each constituent to vary the mullite content in the final shell. The silica alumina system was discussed in section 2.9; it is well known that ceramic materials featuring formulations within the different regions of the phase diagram exhibit significantly different properties both during and after firing. In order to determine the applicability of this effect to investment casting shell material a number of trial formulations were developed and are presented in Table 5.1 and illustrated graphically on the silica alumina phase diagram in Figure 5.1.

The naming convention for silica alumina systems was based on the relative silica alumina molar concentration within the slurry and takes into account the silica

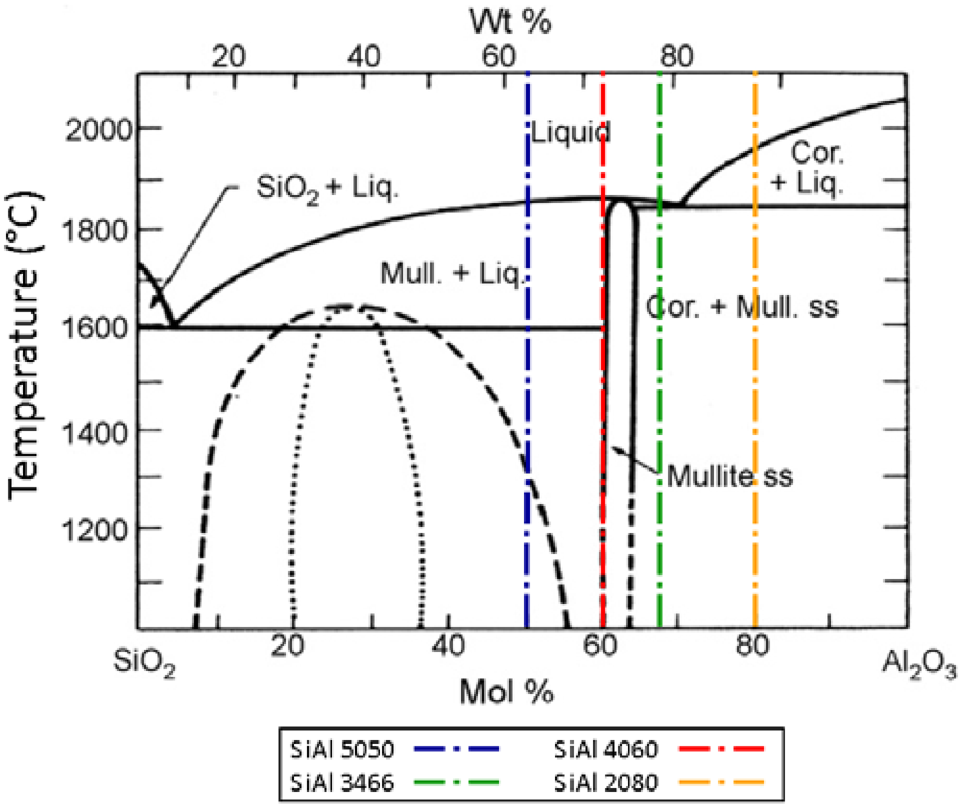

FIGURE 5.1: Modified silica alumina phase diagram indicating the relative silica - alumina concentrations of SiAl trial slurries. Stucco is in all cases fused mullite. If all slurry constituents reacted the 34:66 formulation would produce stoichiometric mullite. Figure adapted from [77]

present within the binder and alumina filler content within the slurry; also included in the calculation are the contributions to each material from mullite particles in the slurry. All SiAl shell systems described in this chapter featured fused mullite stucco; due to the difficulty in measuring the amount of stucco present within the shell the contribution to the silica alumina ratio from these particles was omitted. For example in terms of initial formulation the SiAl5050 system contained approximately equimolar concentrations of silica and alumina as reflected in the designation; the alumina rich SiAl2080 system contained approximately 20 mol % silica content and 80 mol % alumina content. Two additional formulations with ratios 34:66 and 40:60 were also evaluated, according to the silica-alumina phase diagram the 34:66 formulation lies inside the mullite region with the 40:60 in close

TABLE 5.1: Slurry formulations utilised for investigation of silica alumina content on the mechanical properties of shell materials. Note that silica content represented as solid content only.

			Concentration	
Slurry	Material	Product	Wt %	Mol %
SiAl2080	Silica	Ludox HSA	9.1	21.1
	Alumina	PFR15	74.9	78.9
	Mullite	Duramul 0.07	16.0	
SiAl3466	Silica	Ludox HSA	9.0	32.5
	Alumina	PFR15	44.4	67.5
	Mullite	Duramul 0.07	46.6	
SiAl4060	Silica	Ludox HSA	9.0	40.8
	Alumina	PFR15	20.8	59.2
	Mullite	Duramul 0.07	70.2	
SiAl5050	Silica	Ludox HSA	9.6	47.9
	Alumina	PFR15	0.0	52.1
	Mullite	Duramul 0.07	90.4	

proximity (being slightly enriched in alumina) at the temperatures relevant to the investment casting process. Due to the properties of mullite ceramics and the Rolls-Royce Hi-shell system (both of which are discussed in section 2.3.2) which shares the same ratio as SiAl4060 it was expected that formulations within the mullite region would exhibit good creep resistance and high-temperature strength.

From inspection of the phase diagram it was also expected that the silica rich system would experience reduced strength at high-temperature due to the proximity of the firing temperature (1539 °C) to the melting temperature of silica (1587 °C); it is likely that creep would reduce the high-temperature strength. However it was expected that this would increase the strength of the ceramic in the fired condition at room temperature due to the formation of glassy phases within the matrix. The alumina rich SiAl2080 system was expected to exhibit reduced strength due to the formation of alumina grains within the matrix; the difference in thermal expansion rates between alumina ($9.6 \times 10^{-6}\text{K}^{-1}$ below 1000 °C) and mullite ($5.3 \times 10^{-6}\text{K}^{-1}$ below 1000 °C) should induce disruption in the matrix. In order to test these hypotheses shell specimens were manufactured using each system and tested using a number of characterisation techniques; the results of which are reported in the following section.

5.2.2 Results

The strength of shell specimens were characterised flexurally using 3-point bend testing at both room and elevated temperatures and also by compression testing at room temperature; the results are presented in Figures 5.2 and 5.3 respectively.

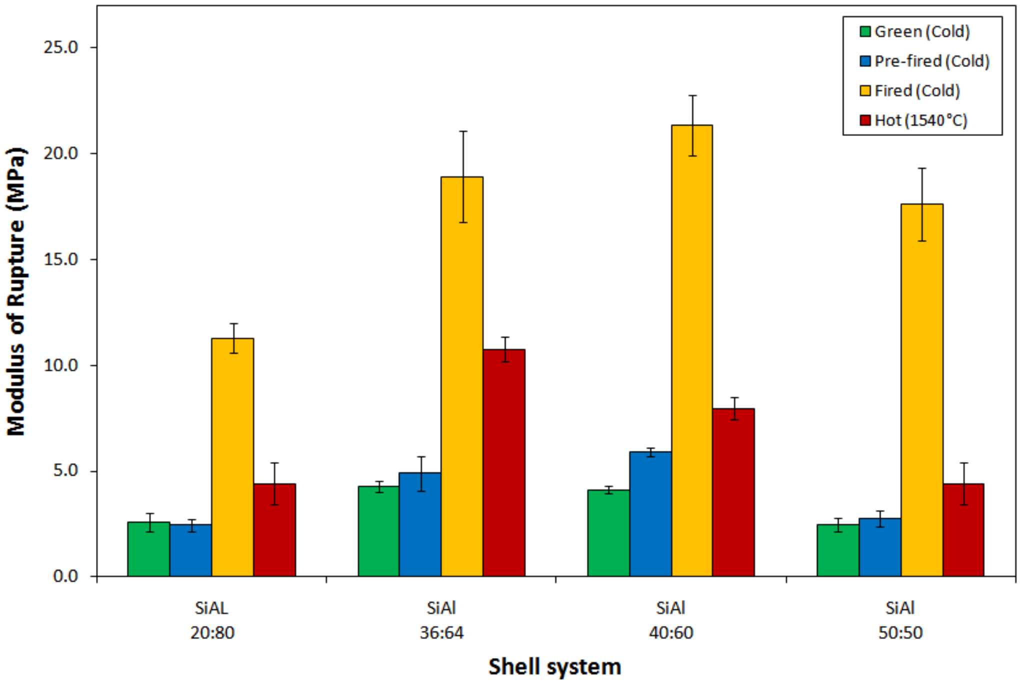

FIGURE 5.2: Flexural strength measurements for test specimens manufactured using various silica/alumina contents. In all cases binder was Ludox HSA and stucco material was fused mullite.

Flexural strengths revealed that the systems with silica alumina ratios correct for the formation of mullite (3466 & 4060) exhibited the greatest strengths in all conditions including green and pre-fired; this trend was also exhibited in the restults of compressive testing.

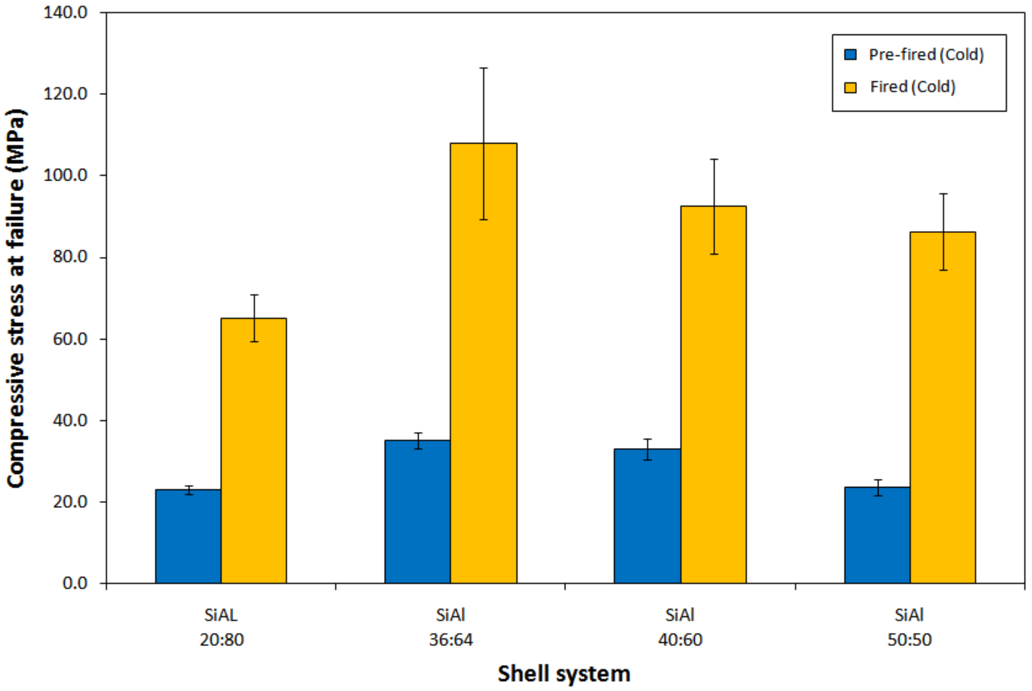

FIGURE 5.3: Compressive strength measurements for test specimens manufactured using various silica/alumina contents. In all cases binder was Ludox HSA and stucco material was fused mullite.

It was expected that the 3466 and 4060 materials would exhibit greater fired and high temperature strengths due to the formation of mullite during thermal treatment. Greater strength prior to high temperature firing was, however, unexpected and potentially due to the particle size distribution of the filler materials. It was shown in Table 5.1 that in order to achieve the required silica-alumina ratio it was necessary to alter the proportions of the mullite and alumina filler powders. These powders featured significantly different particle sizes with supplier quoted d_{50} values of 1.3 µm and 28 µm for alumina and mullite respectively; the proportion of each material within each slurry variant are presented graphically in Figure 5.5.

It is unlikely that in the green and pre-fired states the composition of the materials themselves have exhibited significant effects on the mechanical properties of the shell material, it is more likely that the properties were affected as a result of the different particle packing occurring due to the different particle size distribution within the slurry matrices. It is well known that in bimodal particle distributions it

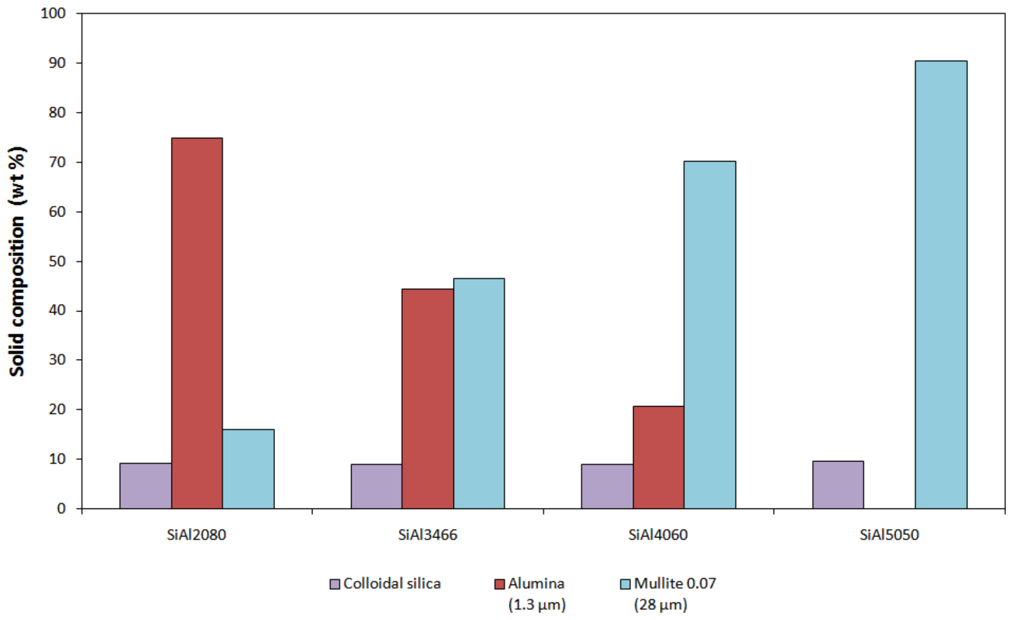

FIGURE 5.4: Graphical representation of the slurry compositions of SiAl slurry matrices. Results presented are for the solid componenet of the slurry only and do not reflect contributions made by mullite stucco particles.

is possible for smaller particles to occupy interstitial sites between coarse particles thus increasing density and particle packing [100]. It was reported by Carneim *et al.* that the flexural strengths of dry-pressed alumina bodies in the green state increased with increasing packing density. They attributed this to the manner in which forces were transmitted through the matrix; greater packing allowed more particle contacts through which forces could be transmitted and hence the green strength was increased[101]. Inspection of Figure 5.2 shows that the strengths of each of the approximately monomodal slurry matrices, that is the 2080 and 5050 materials in the green and pre-fired states is reduced compared to the bimodal system and therefore better packing of the 3466 and 4060 materials. Flexural strengths in green and pre-fired conditions were consistent with expectations.

In order to further characterise the behaviour of the SiAl shell materials specimens were subjected to thermal expansion measurements using the process described in section 3.1. As for zirconia containing shell materials in the preceding chapter a summary of the thermal expansion measurements is shown in Figure 5.5. It was

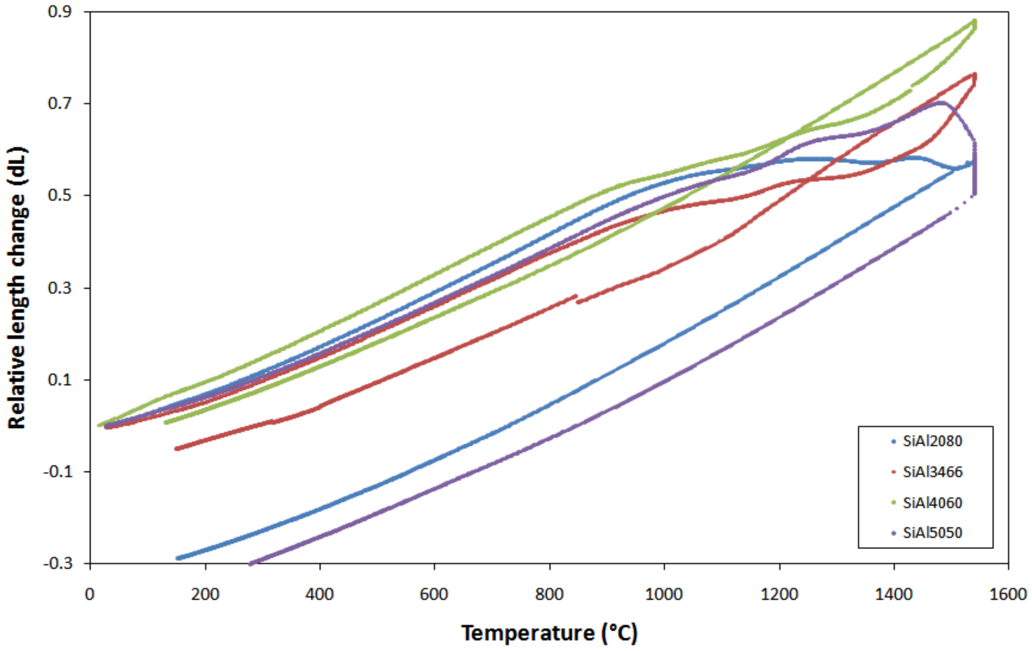

FIGURE 5.5: Thermal expansion measurements for silica alumina based specimens made using various silica alumina ratios.

observed that mullite forming materials exhibited a hysteresis loop at high temperature; it is believed that this is characteristic of the mullitisation process. It was reported by Takei *et al.* that at firing temperatures above 1200 °C, a third stage of mullite development occurs whereby existing mullite crystals begin to coalesce into larger crystals [102]. It is possible that a similar process could have occurred within the shell material thereby inducing the loop. It should also be mentioned that during the casting process this mechanism could alter the strength of mullite containing ceramics should they be exposed to different thermal cycles. Since all samples made and tested within this thesis were fired using the same furnace and the same firing cycle the variation within the samples should be minimal.

The significantly different behaviour exhibited by the SiAl5050 specimens supported the link between mullitisation and the hysteresis, since there was no alumina present in the slurry there was no possibility for the formation of mullite and consequently no loop was exhibited. It is pertinent to mention that the Hi-shell system, with a silica-alumina ratio of 40:60, also exhibited the loop during thermal cycling as was shown in Figure 2.7. Also presented in the aforementioned Figure is the thermal expansion behaviour of the Rolls-Royce standard single-crystal (Std. SX) shell system; its thermal expansion behaviour was similar to that of the SiAl5050 system. It is believed that this is due to the presence of silica within the shell material at elevated temperatures. The discontinuity in the SiAL3466 expansion trace during cooling was due to a machine error rather than any variation in material properties.

To facilitate further analysis and highlight any regions of activity, thermal expansion data for each shell material was analysed by differentiating the thermal expansion data with respect to temperature. For clarity heating and cooling rates are presented on separate graphs; linear expansion (%) is presented as black dots along with the rate of linear expansion ($\% \,°\mathrm{C}^{-1}$) as red dots for each of the SiAl shell materials in Figures 5.6 to 5.9.

Thermal expansion data showed evidence of the formation of mullite during the firing process, this was manifested in a number of stages. It has been widely reported in the literature that the formation of mullite occurs in two stages, the initial stage being the formation of so-called precursor mullite of the form $2\mathrm{Al_2O_3\,SiO_2}$ (2:1 mullite) at temperatures between 930 to 1000 °C [103] [104]. The second stage occurring at temperatures exceeding 1200 °C involves the re-ordering of the structure of the 2:1 mullite to the stable composition $3\mathrm{Al_2O_3\,2SiO_2}$. The activity of the shell specimens inferred from thermal expansion measurements is given in Table 5.2. It was observed that all shell variants exhibited a period of reduced expansion in the temperature range 900 °C to approximately 1100 °C. Since this is coincident with the temperature range reported in the literature it is believed that this was due to the formation of non-stoichiometric 2:1 mullite within the samples.

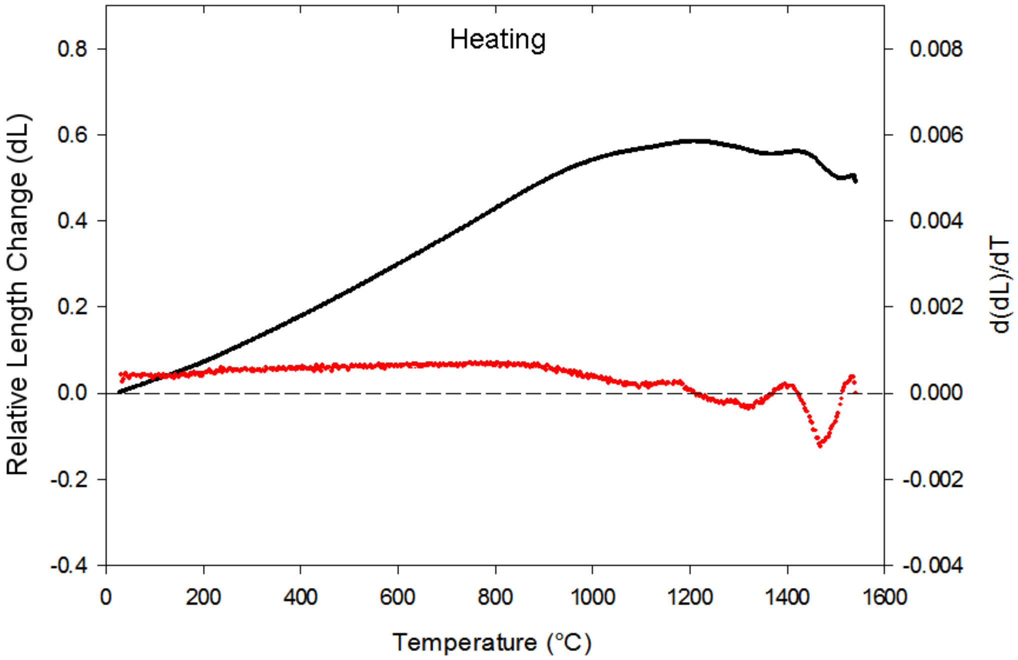

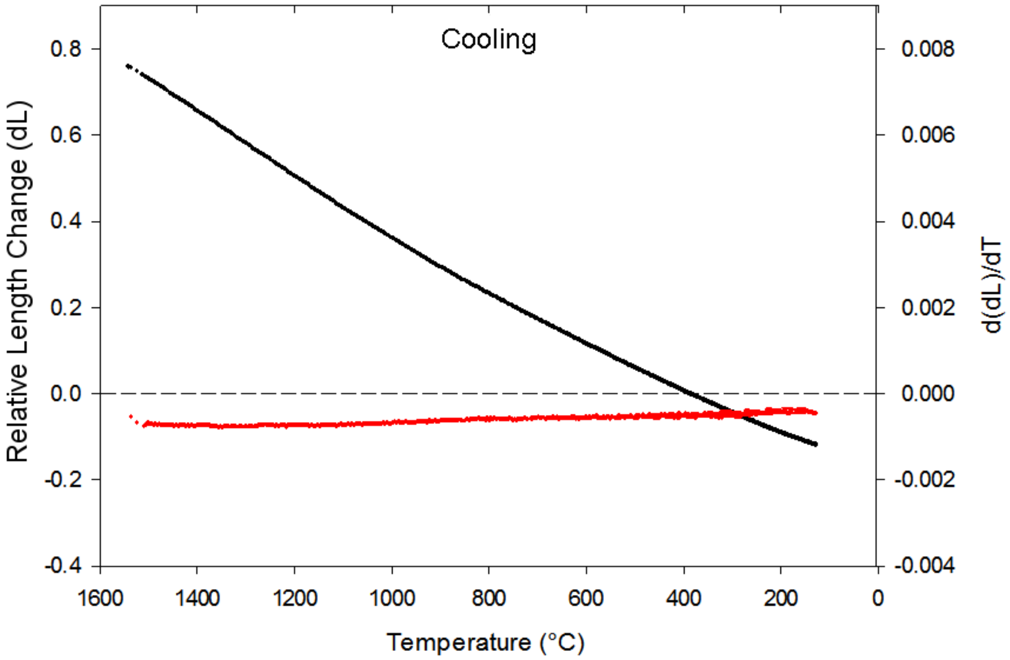

FIGURE 5.6: Thermal expansion data for specimens manufactured using alumina-rich SiAl2080 system. Relative change in length is shown in black, rate of length change is shown in red.

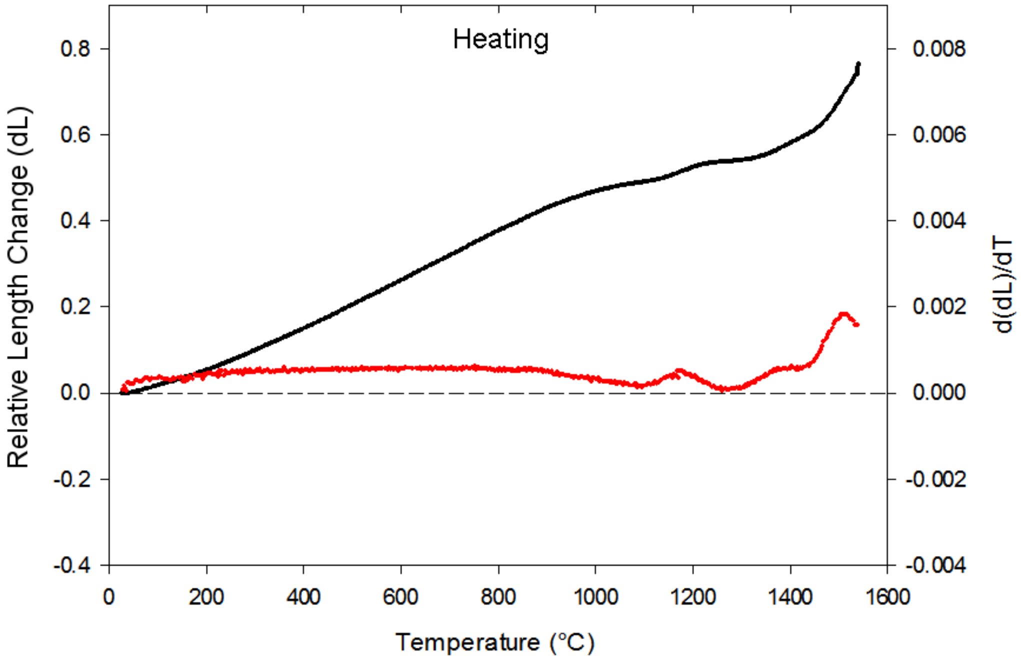

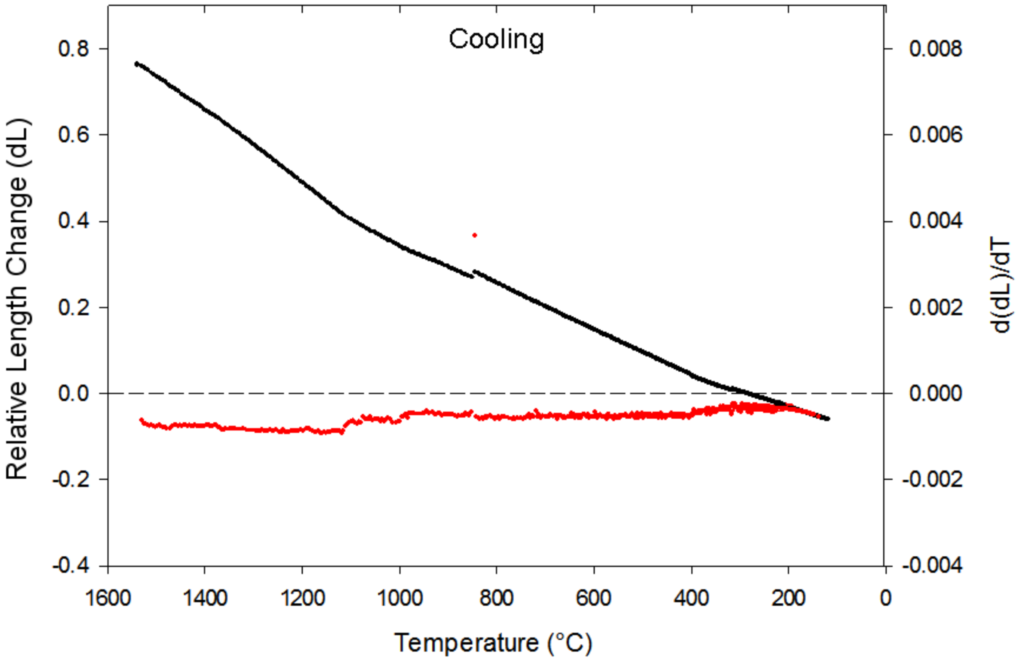

Figure 5.7: Thermal expansion data for specimens manufactured using minimally alumina rich system, SiAl3466. Relative change in length is shown in black, rate of length change is shown in red.

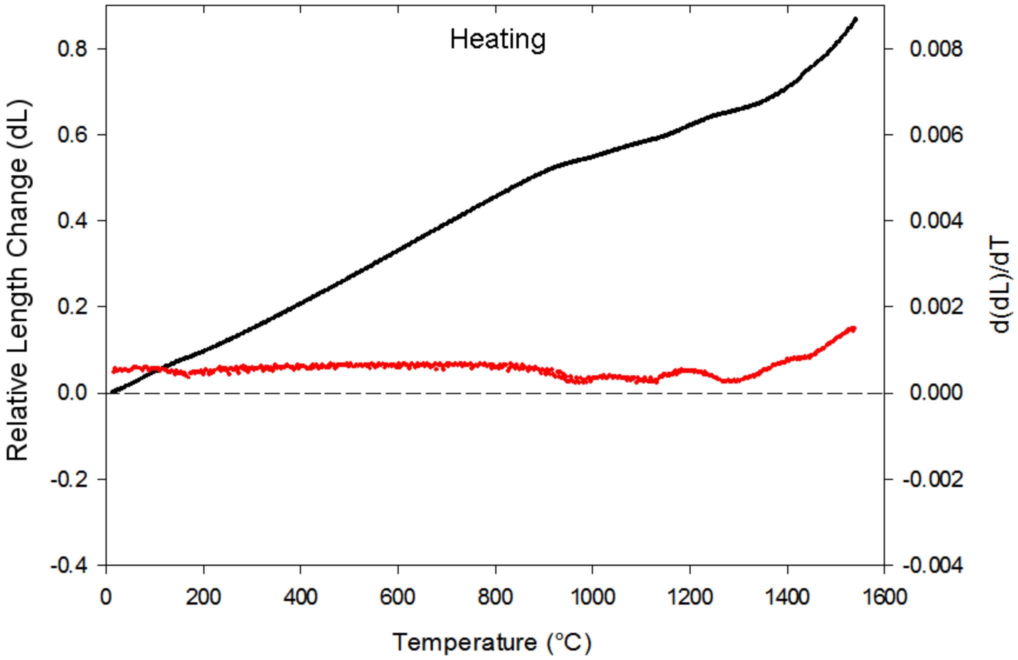

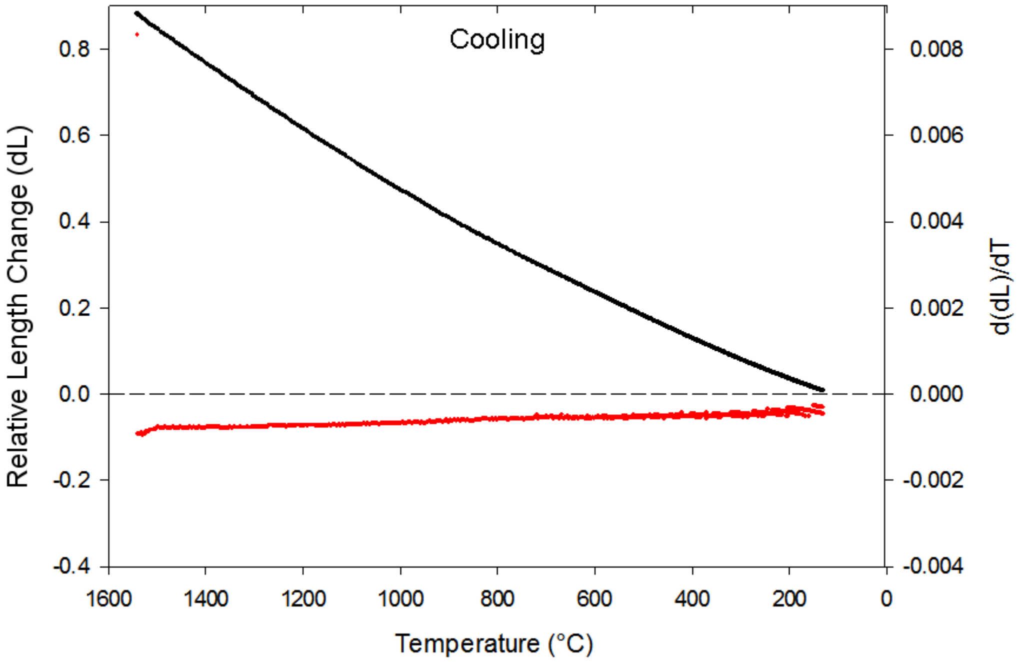

Figure 5.8: Thermal expansion data for specimens manufactured using stoichiometric mullite system, SiAl4060. Relative change in length is shown in black, rate of length change is shown in red.

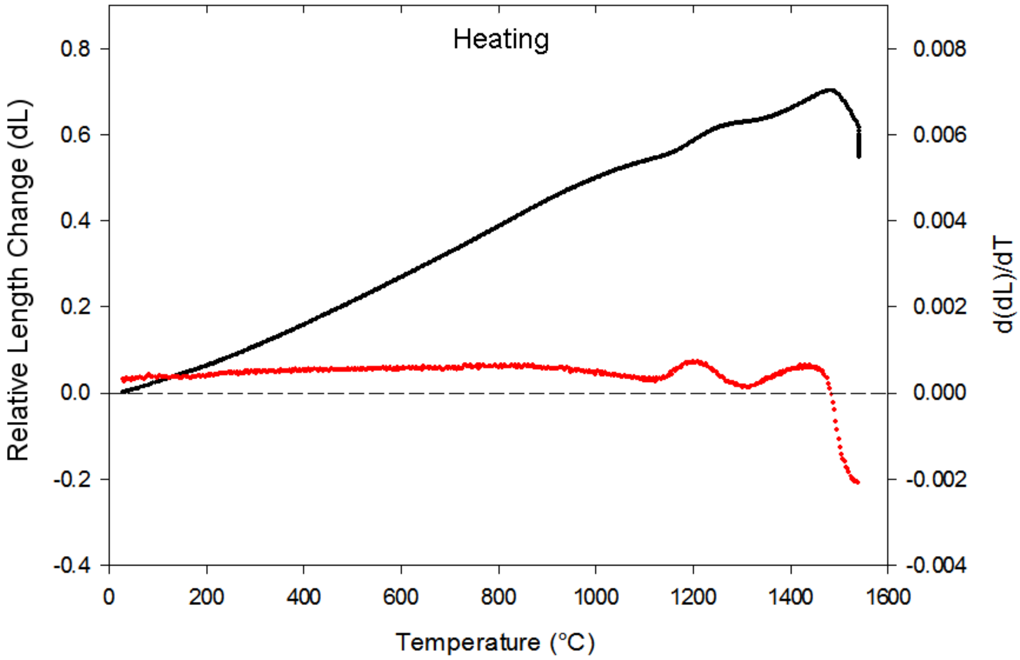

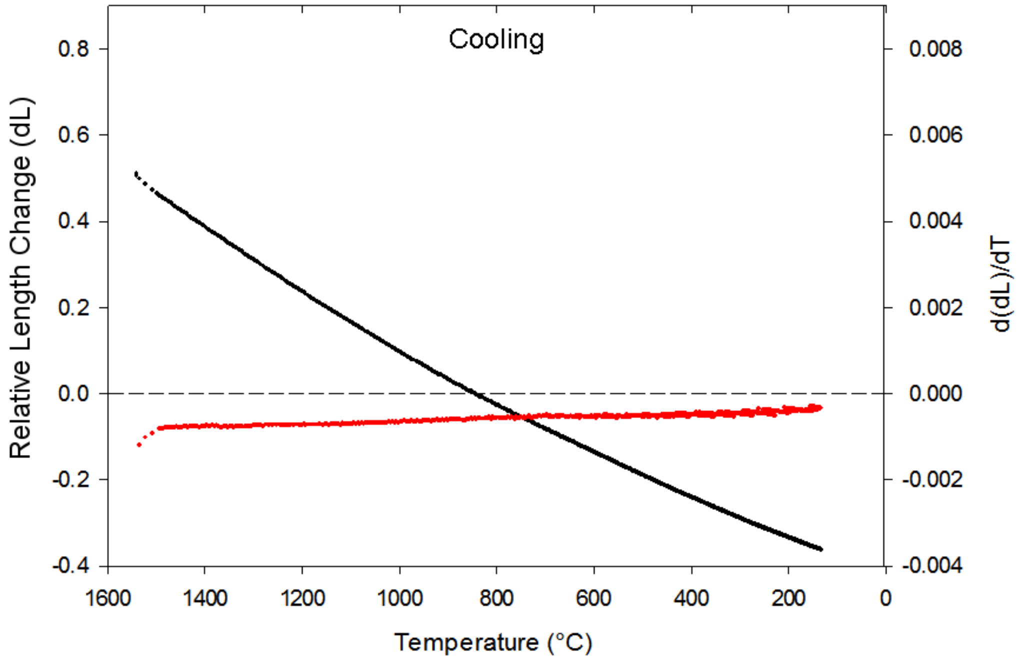

FIGURE 5.9: Thermal expansion data for specimens manufactured using silica rich system, SiAl5050. Relative change in length is shown in black, rate of length change is shown in red.

Table 5.2: Activity observed during thermal expansion measurement of silica-alumina based shell materials.

	Formation temperatures temperature (℃)			
Silica:alumina	Precursor stage		Mullite stage	
(mol %)	(Start)	(End)	(Start)	(End)
20:80	900	1100	1180	1400
34:66	900	1100	1170	1370
40:60	900	1100	1190	1360
50:50	900	1100	1200	1420

A second period of activity was observed for all specimens ranging from approximately 1180 to 1400°C; the temperature range is in broad agreement with that reported in the literature for the secondary phase of mullite formation and was attributed to this process within the shell material. At temperatures above 1400 °C the approximately stoichiometric-mullite formulations continued to expand up to 1550 °C which was the limiting temperature for this test. It can be seen in Figure 5.9 that at temperatures exceeding 1450 °C the silica-rich 50:50 system exhibits a large and sudden contraction, this is due to the proximity of the operating temperature to the melting point of silica at approximately 1580 °C (as shown in Figure 2.27). The reduced viscosity of the silica at this temperature coupled to the small-force applied by the dilatometer during the thermal expansion test caused a significant contraction in the sample of approximately 15 % which was potentially linked to glass-phase sintering. This observation was consistent with those made during hot-creep testing and also from analysis of the microstructure of fired specimens both of which are discussed in greater depth later in this section. The alumina rich shell material, 20:80 also exhibited a deviation from the expected properties during thermal expansion testing. The formation of mullite within this specimen was observed as discussed previously, however at increased temperature the sample exhibited a further period of contraction not consistent with those reported within the literature. Since the level of fine alumina was high, and significantly, that it was in excess of that required to form mullite an amount of contraction due to the sintering of this material itself was expected at high temperature. This was substantiated by thermal expansion measurement of the mullite-stuccoed F200 shell material discussed in section 5.4 and presented as part of thermal expansion characterisation in Figure 5.30. The F200 system was based on the alumina rich 2080 formulation however a large portion of the fine alumina content was replaced by a coarser 200 mesh (70 µm) fused alumina. Due to the increased particle size this material was less prone to sintering, this was reflected in thermal expansion data. Data for the 2080 and F200 systems were almost indistinguishable apart from the lack of the final contraction in the latter indicating that it was sintering of the fine alumina that was responsible.

Similar systems containing fine alumina were investigated in two papers by Louet *et al.*. The 2005 paper [78] investigated the effects of various impurities on the behaviour of a fine reactive alumina powder (d_{50} = 0.3 µm), P172SB manufactured by Rio-Tinto Alcan the same supplier as the PFR15 material (d_{50} = 1.3 µm) utilised in the SiAl shell materials. It was reported during this initial work that the rate of sintering for alumina was significantly reduced in the temperature range 1150 - 1450 °C with increasing silica content. Comparison of the derivative thermal expansion data for the alumina and silica rich systems respectively, reveals a similar trend. This behaviour was further reported by the authors in the 2008 paper [105] in which the same trend was more comprehensively investigated. In this work a highly pure alumina of similar size to the P172SB material was used, with reported d_{50} values of 0.3 µm and 0.36 µm for the trial material and P172SB respectively. Alumina particles were doped with varying amounts of 22 nm colloidal silica by producing a suspension of both particles in a similar method used to produce the slurries used within the shell trials. Once again the trend for reduced expansion in the 1150 - 1450 °C range was detected during thermal expansion measurement; the results are presented in Figure 5.10. It was clearly shown that increased silica content reduced the amount of sintering within the specimens during the 1150 - 1450 °C range, but had the opposite effect for sintering at high temperatures. These observations were again, consistent with those made on the shell specimens; for comparison derivative thermal expansion behaviour for silica and alumina rich specimens are presented in Figure 5.11.

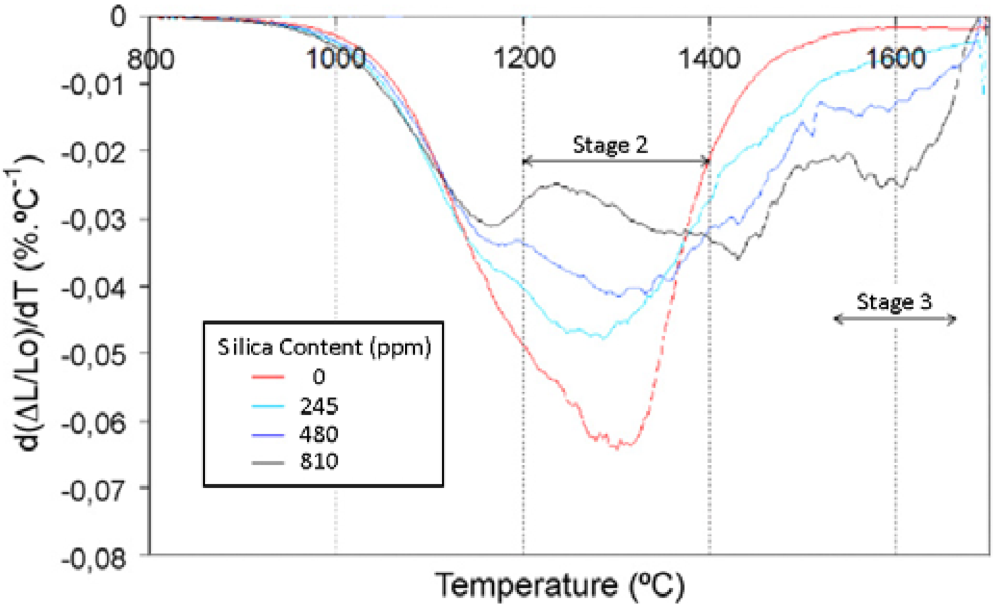

FIGURE 5.10: Thermal expansion results for silica-doped alumina specimens. Modified from [105]

It was concluded by Louet that the reduction in sintering between 1150 - 1450 °C was due to the formation of silica layers at the alumina grain boundaries. This reduced the diffusion process between alumina particles and hence significantly reduced the sintering in this temperature range [105]. Conversely, the sintering process was enhanced at higher temperatures approaching that at which silica melts due to the formation of an intergranular liquid phase. To further investigate the structure of samples having been through the sintering process fired shell specimens were characterised using scanning electron microscopy (SEM). The results are presented in Figures 5.12 to 5.15.

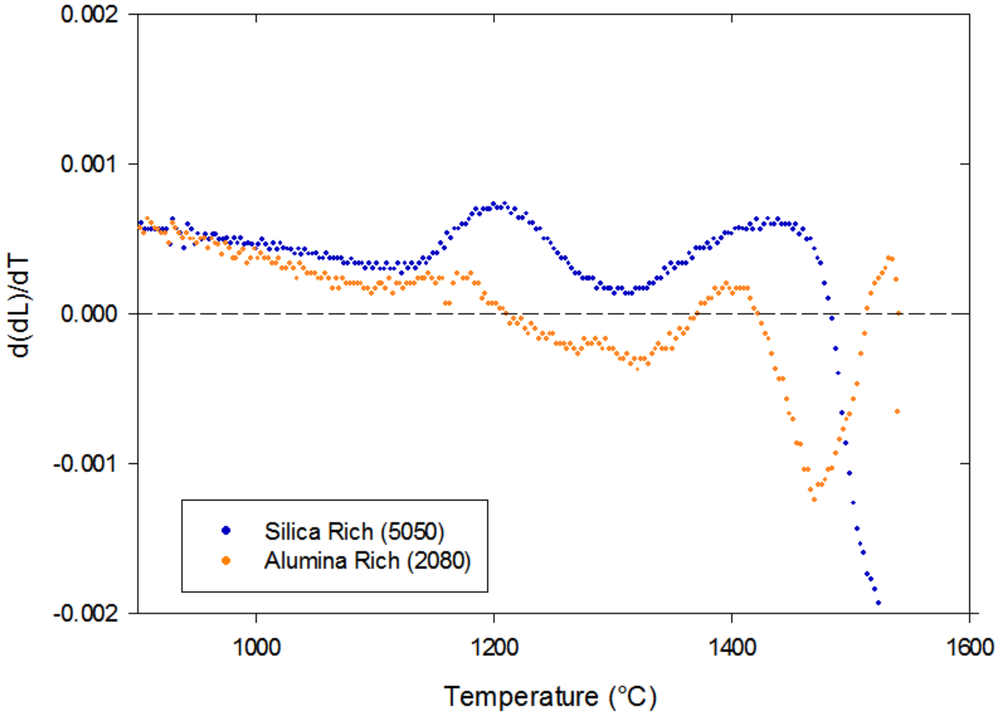

FIGURE 5.11: Comparison of sintering behaviour for silica and alumina rich shell materials.

The structure of the alumina rich 2080 system appeared to be severely cracked in the fired condition with numerous cracks extending up to 500 µm in length and between 5-10 µm in width. From flexural and compressive testing it was shown that the 2080 formulation was the weakest of all SiAl variants in the fired condition exhibiting strengths of 11.3 MPa and 65.2 MPa respectively. This represented a reduction of 47 % in terms of flexural strength compared to the 4060 variant which exhibited the greatest flexural strength and 30 % in terms of compressive strength. Considering the large defects within the structure this was not surprising. To explain the presence of the cracks it was necessary to consider the sintering behaviour of the fine alumina within the matrix. It is proposed that rather than forming due to stresses induced by differential expansion during thermal cycling, cracks were formed due to the stresses generated by different sintering behaviour between the stucco and matrix materials.

It is consistent with thermal expansion observations that the cracks were due to

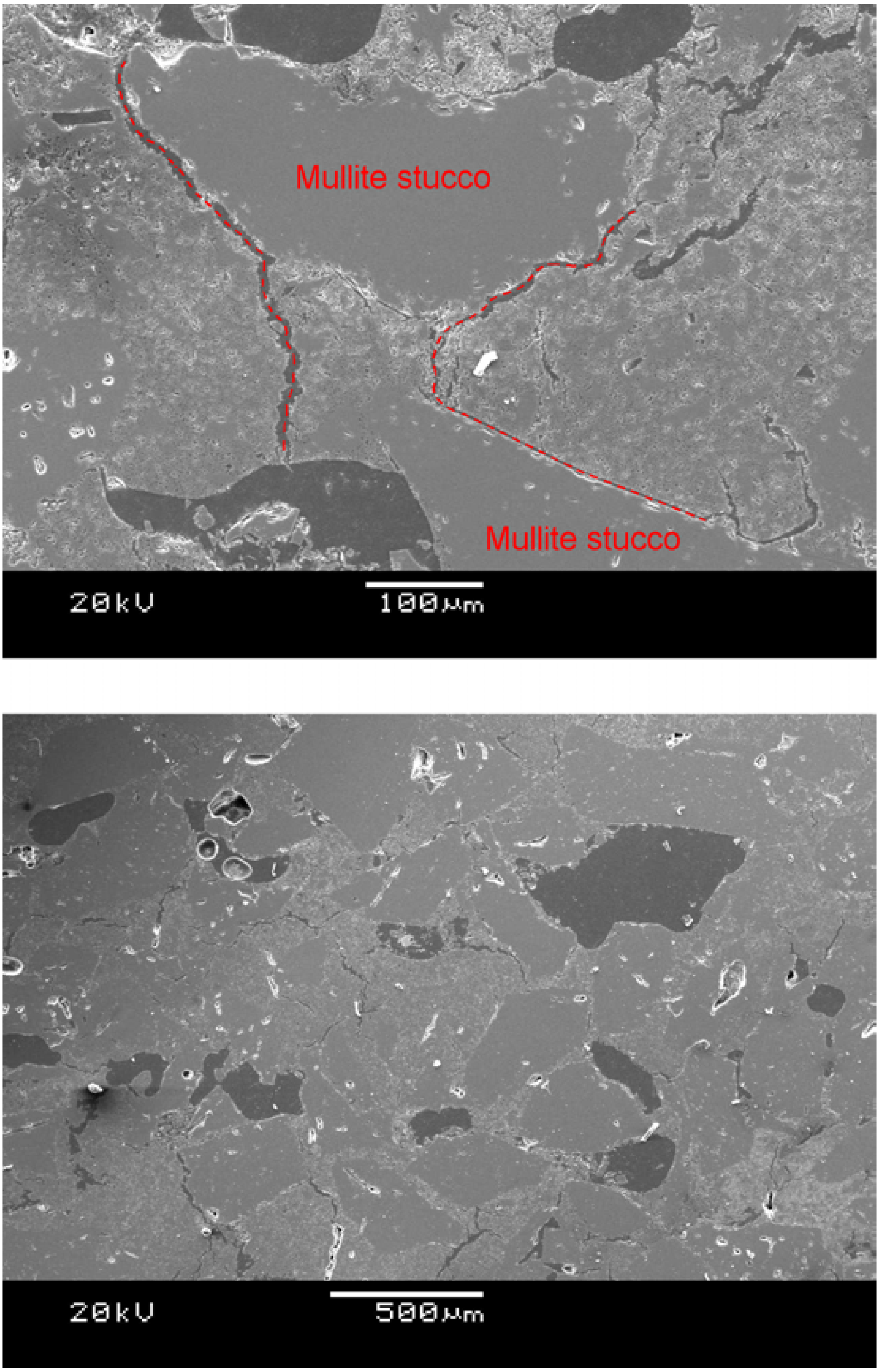

FIGURE 5.12: SEM micrographs showing structure of alumina-rich SiAl2080 shell material. The microstructure was shown to contain a number of large cracks due to the sintering of fine alumina powder within the matrix (indicated by red dotted line).

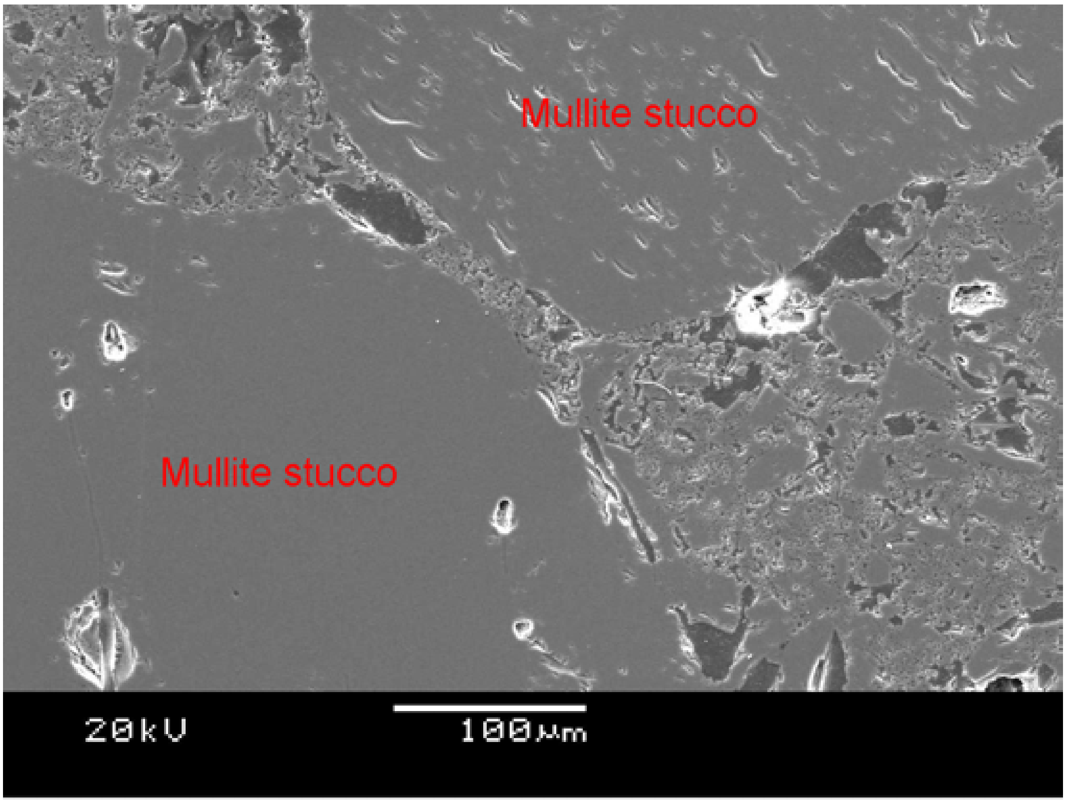

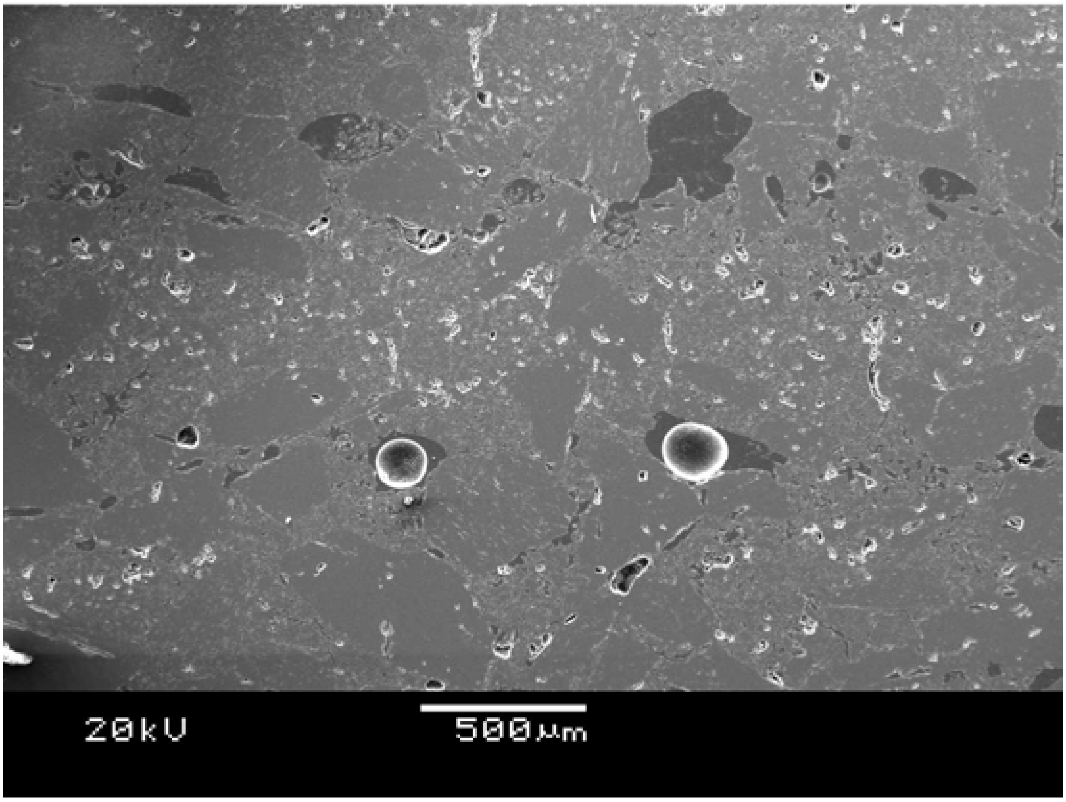

FIGURE 5.13: SEM micrographs showing structure of mullite-forming SiAl3466 shell material. It was noted that the bonding between the stucco particles and the matrix was good in this system, and the structure was essentially crack-free.

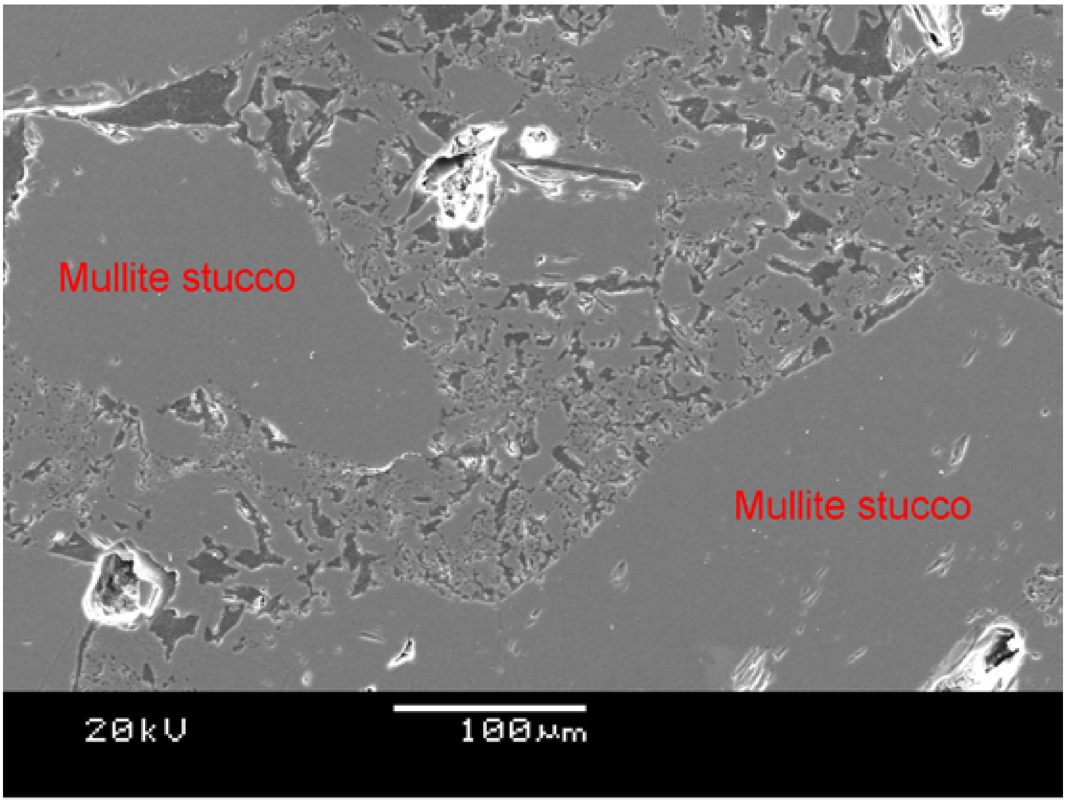

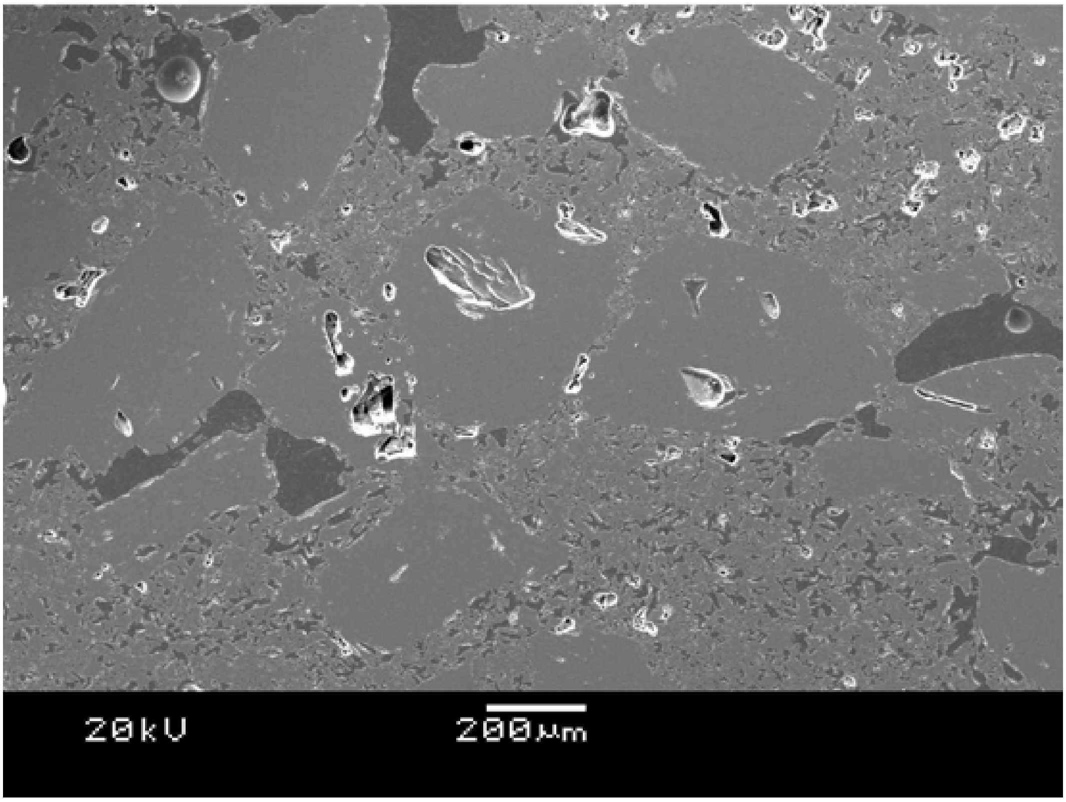

FIGURE 5.14: SEM micrographs showing structure of stoichiometric mullite SiAl4060 shell material. It was noted that the bonding between the stucco particles and the matrix was good in this system, and the structure was essentially crack-free.

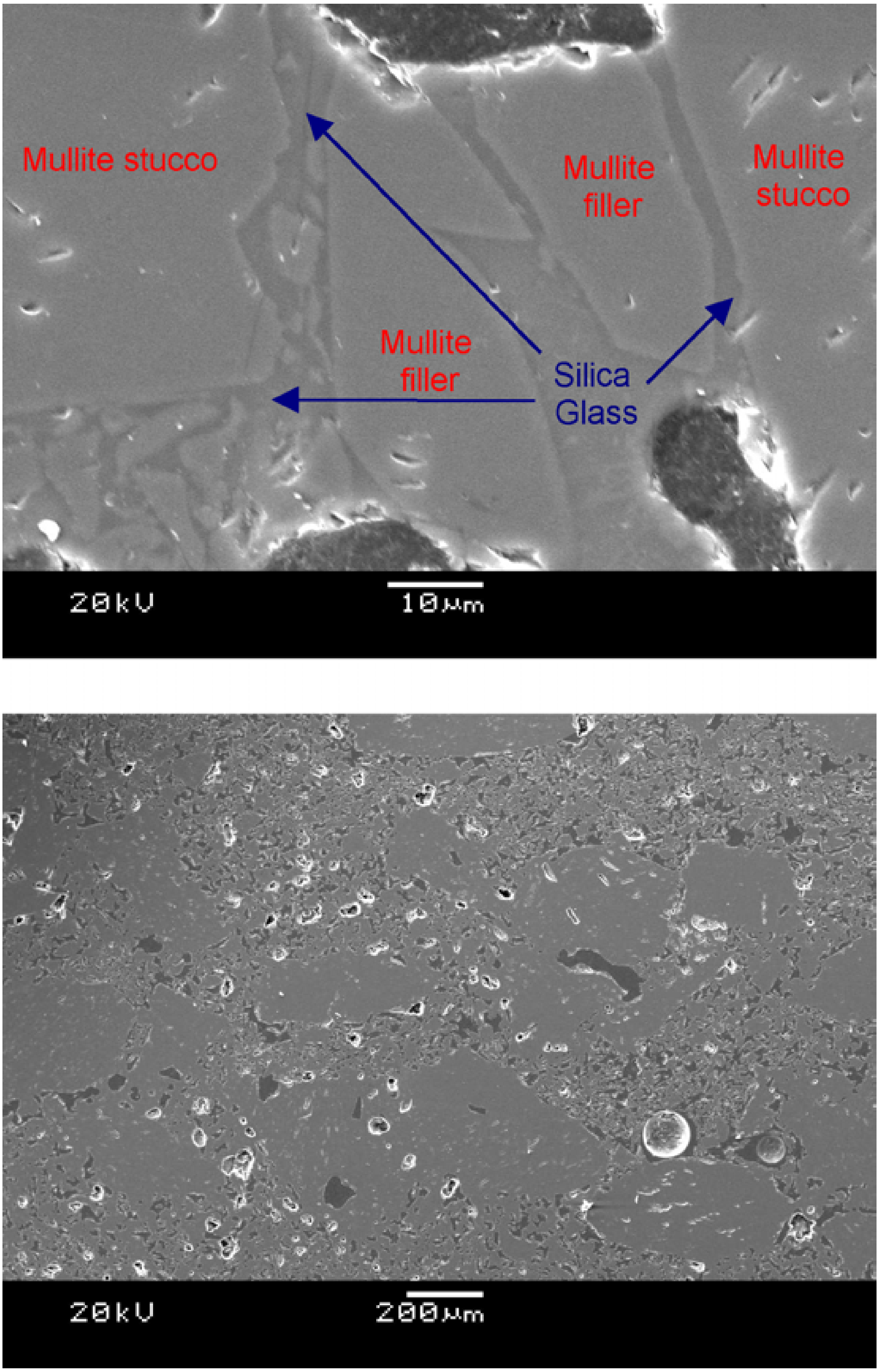

FIGURE 5.15: SEM micrographs showing structure of silica rich SiAl5050 shell material. It was noted that the mullite stucco particles and filler particles within the matrix were surrounded by a glassy silica phase giving high connectivity.

the fine alumina-silica matrix contracting away from the relatively large, immobile stucco particles. The voids left behind created a network of large defects within the matrix which in turn reduced the strength of the material. The defects found in the material were similar to those reported by Liniger during the sintering of a bimodal system of glass spheres [106].

In contrast, the mullite formulations 3466 and 4060 exhibited few large cracks within the matrix and exhibited good sintering and fusion between both the matrix particles themselves and at the matrix-stucco interfaces. The stoichiometric 4060 system exhibited marginally better sintering at the interfaces which led to a minor increase in fired strength over the 3466 variant. It is pertinent to note that a similar behaviour was observed for zirconia systems; shell strength, in particular flexural strength appears to be closely linked to the bonding between the matrix and stucco particles.

Like the alumina rich 2080 material, the silica rich, 5050 variant, also exhibited a significantly different microstructure to the mullite variants. A large amount of glassy phase was observed within the slurry matrix with mullite filler particles visible within it; this is clearly shown at the top of Figure 5.15. It was also observed that due to the presence of the glassy phase and its mobility during sintering, the microstructure featured high levels of connectivity between the matrix particles and the stucco material. Consistent with the observations mentioned above this led to relatively high levels of fired strength at an average value of 17.6 MPa or 83 % of that exhibited by 4060, the strongest recorded for this trial. The high temperature strengths of 2080 and 5050 variants were both relatively low each with an average value of 4.4 MPa; in contrast 3466 and 4060 variants exhibited values of 10.7 and 8.0 MPa respectively. It is likely that the reduction in hot strength for the 2080 system was due to the sintering of the fine alumina; in the case of the 5050 system it was likely due to the occurrence of melting within the silica rich matrix.

Table 5.3: Creep deformation measured flexurally in 3-point bend. Testing performed at 1540 °C under an applied load of 3.2 N. Deformation recorded after 5 minutes. Samples exhibiting creep rates sufficient to prevent measurement are denoted by ∞ symbol.

Shell material	Creep deformation (mm)
SiAl 20:80	0.098
SiAl 34:66	0.125
SiAl 40:60	0.127
SiAl 50:50	∞
PCF Hi-shell	0.061
PCF Std. SX	∞

Samples of these shell materials were additionally characterised in terms of creep deformation at high temperature using the method described in section 3.1. The results, shown in Table 5.3, were consistent with the observations of high temperature flexural testing. Low creep rates, similar to those exhibited for Hi-shell, were measured for both mullite forming systems; this is consistent with the low-creep behaviour of mullite ceramics reported in the literature (see section 2.3.2). The 5050 system exhibited similar behaviour to the Std. SX system; the level of creep observed was too great for the machine to generate the required 3.2 N load. This however illustrated that the system exhibited a high level of creep. The creep deformation for the alumina rich system was observed to be low; this is likely due to the fact that the sintering of the fine alumina had occurred during the 20 minute dwell at 1540 °C prior to testing.

5.2.3 Binder Evaluation

Along with evaluating the effect of silica-alumina concentration on the properties of the shell material a number of variant shell systems were formulated using different colloidal silica binder materials. To enable direct comparison the slurry formulation was consistent between binder variants. The formulation of the SiAl4060 slurry used is presented in Table 5.4; in all cases test specimens were stuccoed using fused mullite. It should be noted that like the Hi-shell formulation, both sizes of mullite powder were included in the formulation of this slurry; since one of the binders in question was Ludox HSA this allowed for a direct comparison between the formulations containing single (as in SiAL4060) and dual-grade mullite filler materials.

Table 5.4: Slurry formulations utilised for investigation of silica alumina content on the mechanical properties of shell materials. Note that silica content represented as solid content only.

			Concentration	
Slurry	Material	Product	Wt %	Mol %
Hi-shell	Silica	Ludox HSA	9.1	40.8
(SiAl4060)	Alumina	PFR15	20.8	59.2
	Mullite	Duramul 0.04	11.7	
	Mullite	Duramul 0.07	58.4	

The trial binders utilised are listed in Table 5.5. The surface of colloidal silica particles within the Ludox HSA binder featured sites modified by aluminate ions. These sites provide the necessary charge repulsion to prevent aggregation during storage and use. Remasol and Hi-S are both of the more conventional sodium stabilised type, relying instead on the presence of negatively charged hydroxyl ions surrounding the silica particles to remain stable. Each of these stabilisation mechanisms were discussed in greater detail in sections 2.7.2 & 2.7.3 respectively. Remasol Ultra additionally featured a latex-based polymer additive to further enhance green strength [107].

Table 5.5: Colloidal silica binders evaluated during trials with SiAl 4060 shell material.

Name	Stabilisation	Polymer	Natural pH	Silica wt %
Ludox HSA	Aluminium-modified	None	3.5 - 5	25
Hi-S	Sodium-stabilised	None	10.5	32.7
Remasol Ultra	Sodium-stabilised	Latex	9.9 - 10.5	24

Initially shell specimens were evaluated using both flexural and compressive testing the results of which are presented in Figures 5.16 and 5.17 respectively.

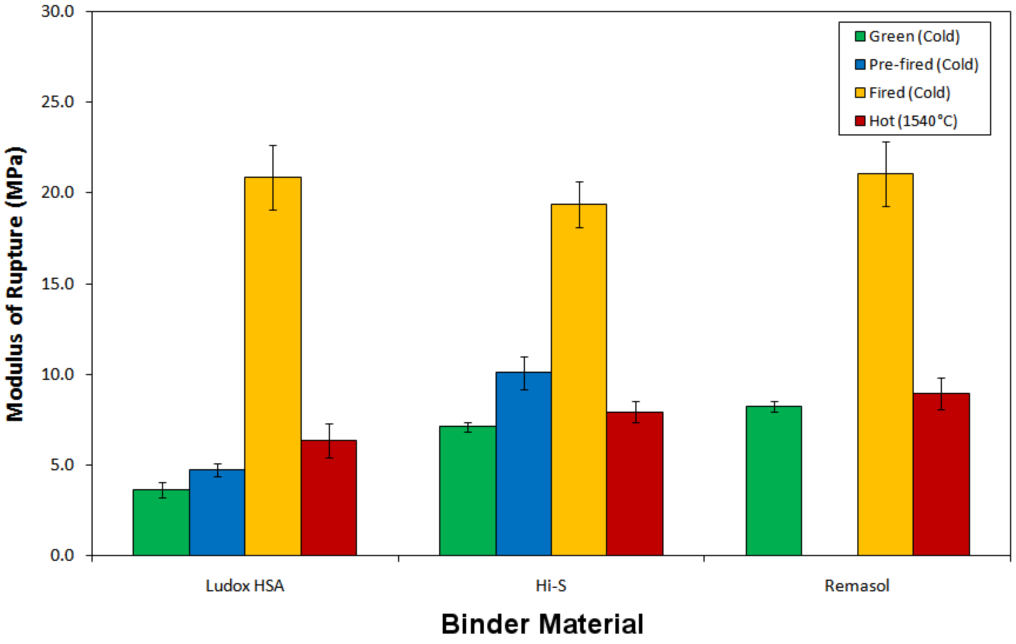

FIGURE 5.16: Flexural strength measurements for test specimens using various colloidal silica binders. Slurry and stucco materials were consistent between test samples.

Similarity in both high temperature and fired strengths were observed in the results of flexural testing; this was consistent with observations made regarding the SiAl4060 system in the previous section. From both mechanical testing and microstructural observations it appeared that the strength of the system was based on the formation and sintering of mullite during the firing cycle. Although the presence of sodium within the binder may have had an effect on the sintering behaviour of the alumina and silica it appeared that the formation of mullite remained the dominant strengthening mechanism. The effect on green and pre-fired strengths was, however, more significant with the sodium-free Ludox HSA binder exhibiting green and pre-fired strengths reduced by 56 % compared to Remasol in the green state and by 53 % compared to Hi-S in the pre-fired condition. It should be noted that due to a machine fault during flexural testing pre-fired strength

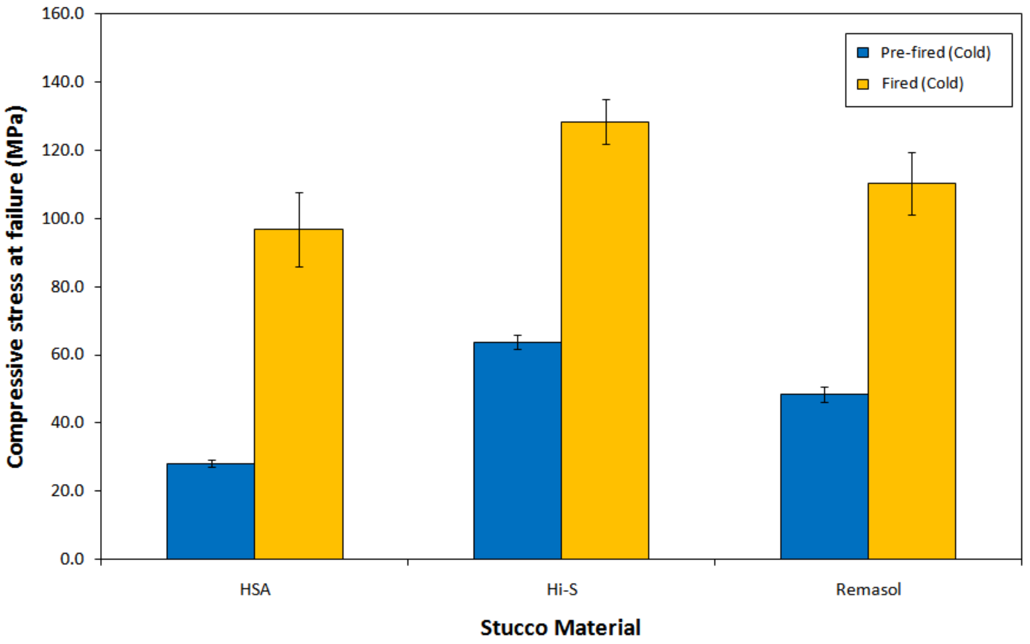

FIGURE 5.17: Compressive strength measurements for test specimens featuring various colloidal silica binders. Slurry and stucco materials were consistent between test samples.

data for Remasol specimens was unavailable. However in the green state polymer-containing Remasol test specimens exhibited the highest level of strength at 8.3 MPa, by comparison the polymer-free Hi-S specimens exhibited 7.1 MPa which represented a reduction of 14 %. The enhancement of green strength through the use of polymer additives is further investigated and discussed in section 5.3.

The trends in compressive strength data were somewhat different to those measured flexurally; Hi-S bound specimens exhibited the greatest strengths in both pre-fired and fired conditions with measured strenghts of 63.7 and 128.3 MPa respectively. Fired Remasol and Ludox HSA specimens recorded average strengths of 110.2 and 96.7 MPa respectively. In terms of pre-fired compressive strength both sodium stabilised variants were significantly stronger than the aluminium-modified Ludox HSA specimens, the latter measuring 28.3 MPa a value which represented a 42 % reduction compared to the Hi-S system. The increased pre-fired strength was consistent with observations in flexural testing and further evidenced the link between reduced pre-sintered strength and the use of aluminium-modified binders.

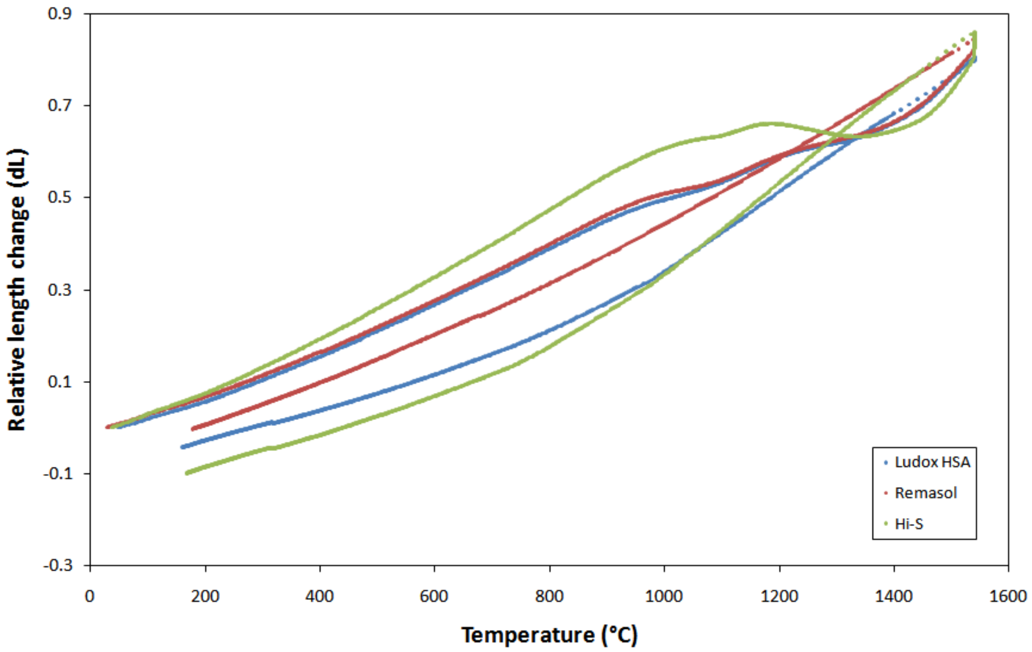

FIGURE 5.18: Thermal expansion measurements for shell specimens manufactured using different binders; all other shell materials were constant between specimens.

In order to understand the effect of binder variation on the thermal behaviour of shell materials during firing, specimens were characterised using thermal expansion testing, the results of which are shown in Figures 5.22 to 5.24. The results are presented in the same format used in the previous section with relative expansion (%) shown in black and the rate of expansion shown in red.

All binder variants exhibited behavioural characteristics of the SiAl4060 material with both regions of mullite formation occurring for each binder during the heating cycle. It was shown in Table 5.5 that the Hi-S binder has a higher silica content (32 wt %) than both Ludox HSA and Remasol Ultra (25 and 24 wt % respectively). During heating the expansion behaviours of Hi-Shell and Remasol were almost indistinguishable, however the higher silica Hi-S binder showed a slightly steeper gradient up to the onset of secondary mullite formation at approximately 1150 °C at which point a significantly larger rate of contraction was observed in the

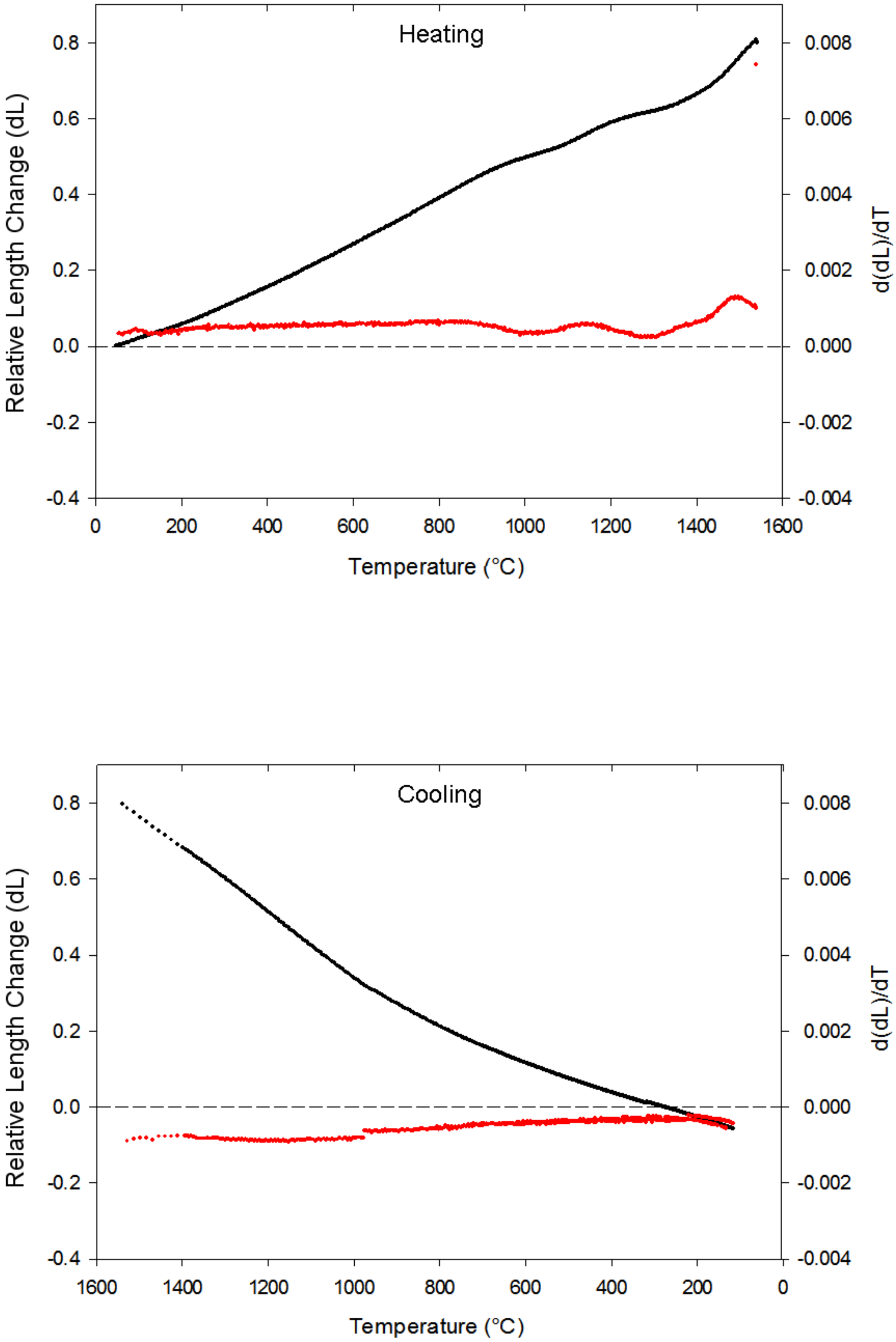

FIGURE 5.19: Thermal expansion of SiAl4060 system featuring Ludox HSA binder. Relative change in length is shown in black, rate of length change is shown in red.

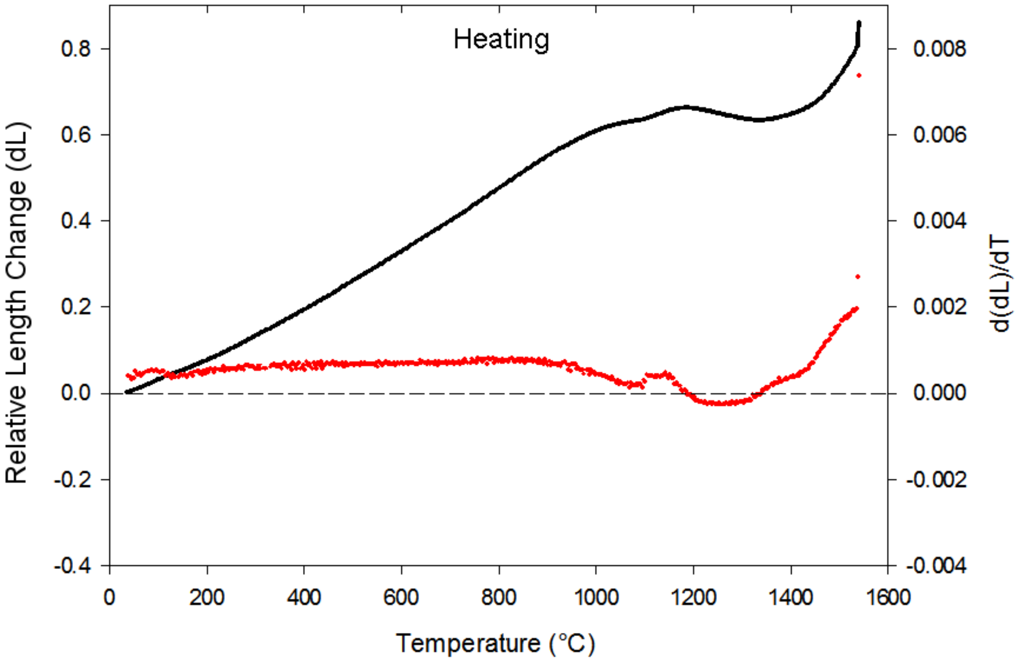

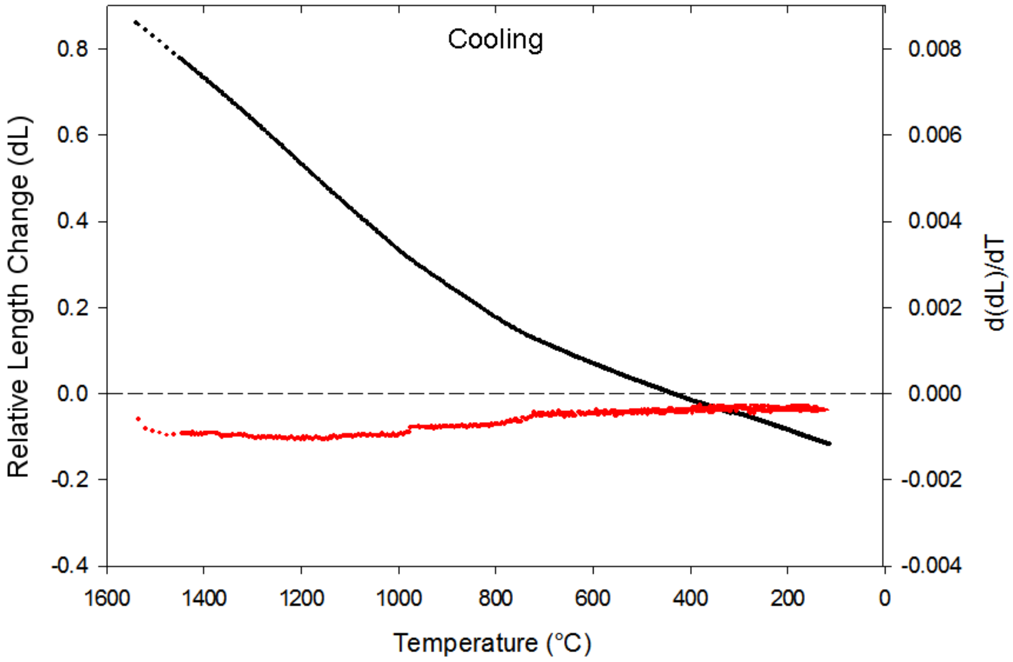

FIGURE 5.20: Thermal expansion of SiAl4060 system featuring Hi-S binder. Relative change in length is shown in black, rate of length change is shown in red.

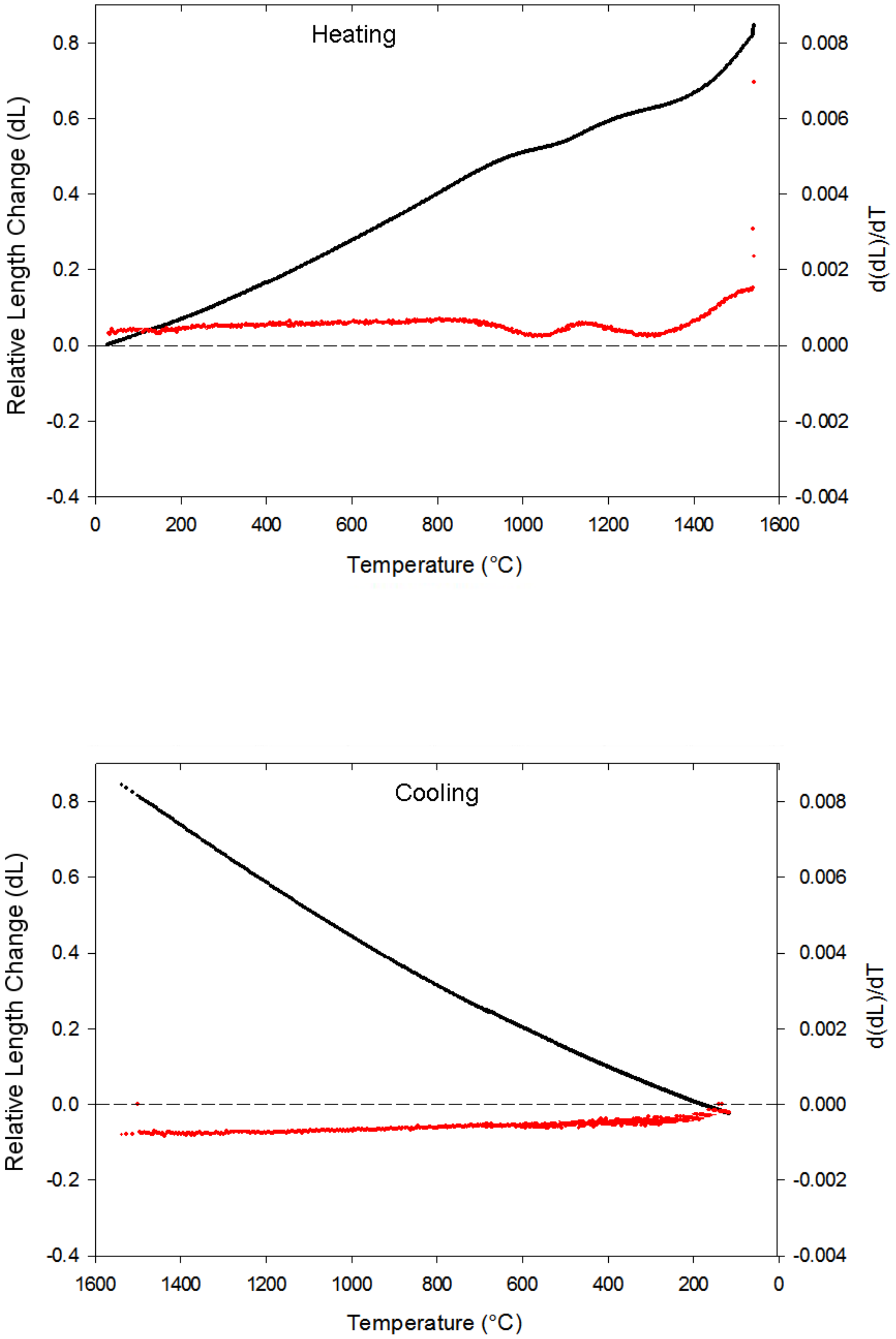

Figure 5.21: Thermal expansion of SiAl4060 system featuring Remasol Ultra binder. Relative change in length is shown in black, rate of length change is shown in red.

Hi-S material. It is possible that the additional silica content within this material enhanced the formation of mullite within the matrix during firing. However as discussed in the preceding section, it has been reported that the presence of sodium and silica reduce the level of sintering between 1050 - 1280 °C and increase it above this range. The reasons for this contradictory behaviour are not understood and unfortunately the relative sodium levels of Remasol and Hi-S binders are not known so definitive conclusions regarding sodium content cannot be made. However assuming that the content per particle was consistent, it is inferred that Hi-S would contain more sodium by virtue of containing more silica particles. Whether or not the level within either binder is significant to alter sintering behaviour and to what extent cannot be determined.

Figures 5.22 to 5.24 illustrate the microstructures of shell material featuring each binder. Both sodium containing materials exhibited better sintering and enhanced connectivity at the matrix-stucco interface, it is likely that this was the due to the effect of sodium-oxide on the sintering of both alumina and silica as discussed in section 2.9.2. By contrast the sodium free Ludox HSA specimen exhibited reduced sintering of the matrix itself and also reduced contact between the matrix and stucco particles. However during flexural testing the presence of greater connectivity did not enhance the fired strength of specimens, this trend is not consistent with that shown by SiAl specimens or zirconia stuccoed specimens and is not well understood.

It was clear from mechanical testing that the presence of a sodium stabilised binder provided shell specimens with greater pre-sintered strength. However it is also necessary to consider the disadvantages of using such a system; it is widely known (and discussed in section 2.7.2) that the stability against aggregation of sodium stabilised binders is dependent on maintaining a stable, highly alkaline pH. As this was an industrial project completed with Rolls-Royce plc. it was necessary to consider the implications of up-scaling systems. It is routine practice within

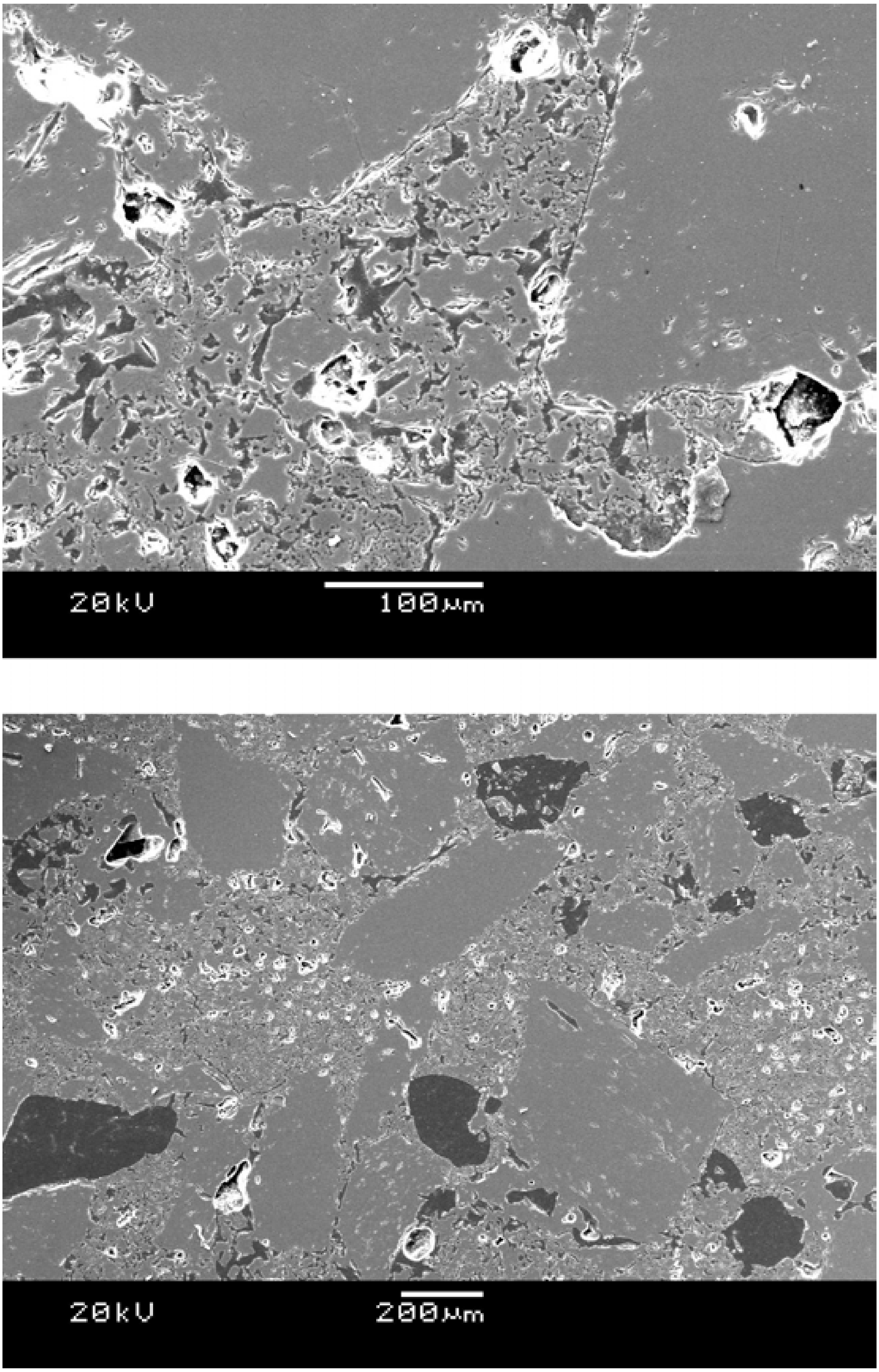

Figure 5.22: Ludox HSA bound SiAl4060 shell material

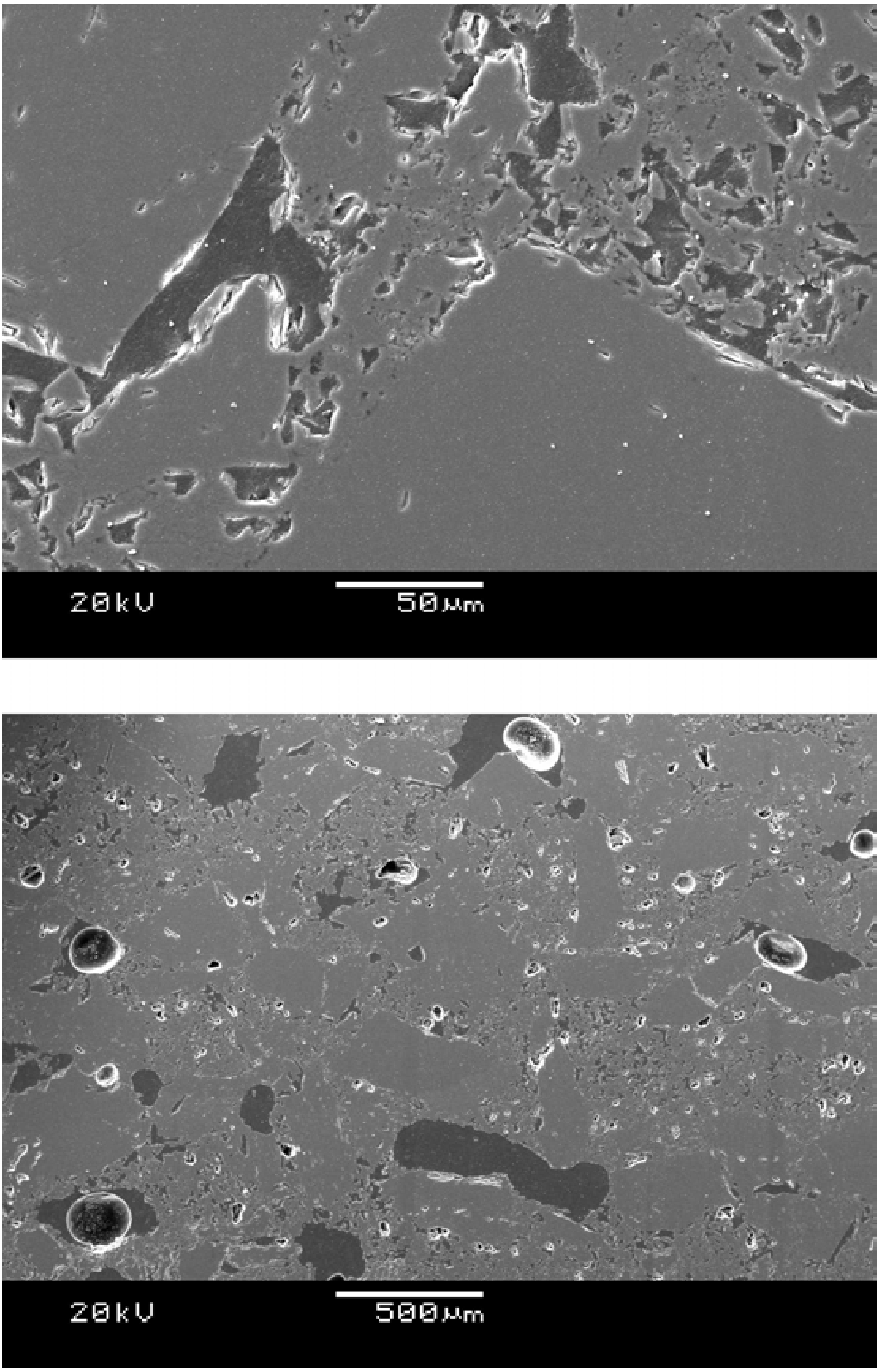

FIGURE 5.23: Hi-S bound SiAl4060 shell material

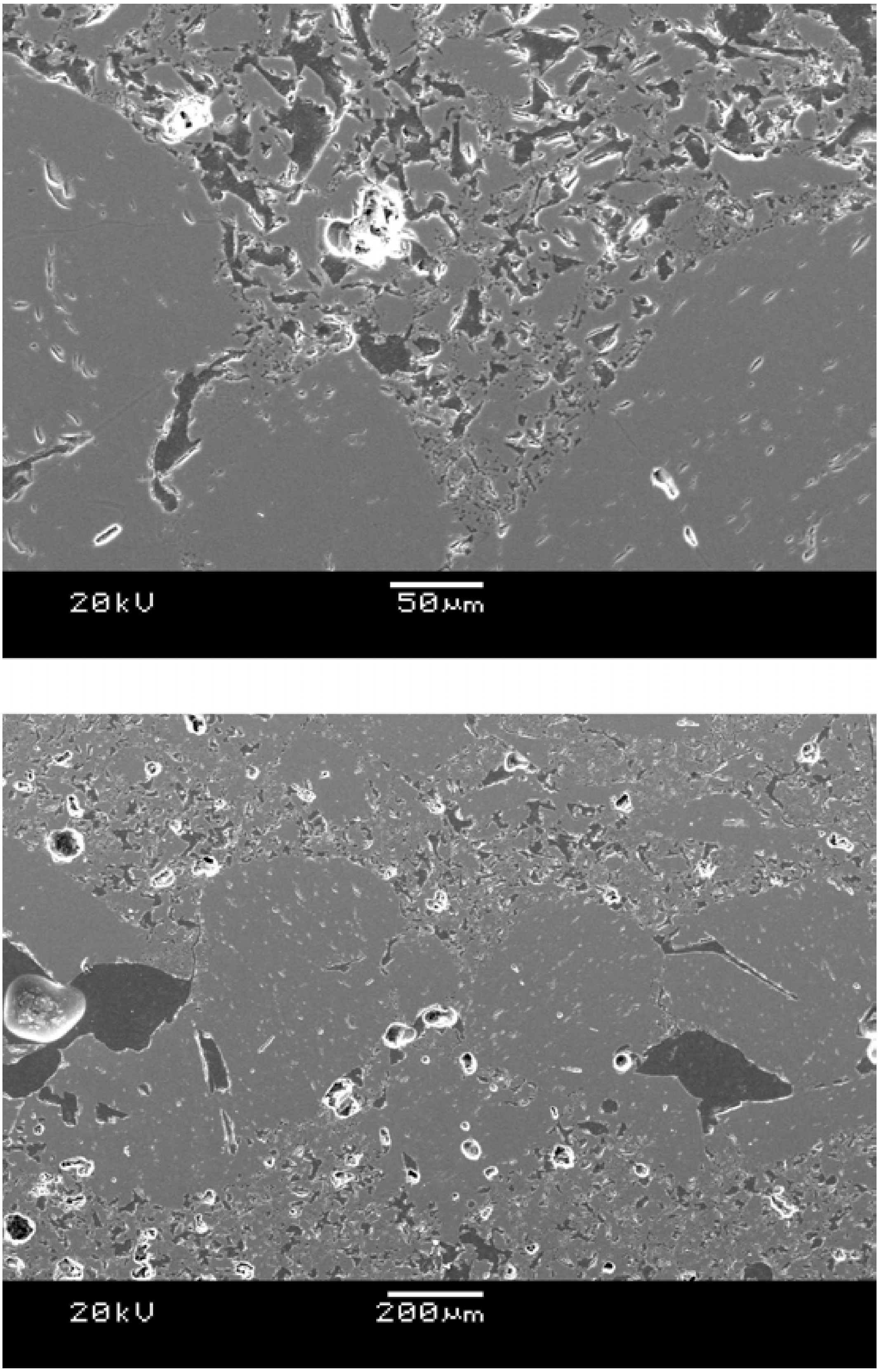

FIGURE 5.24: Remasol bound SiAl4060 shell material

Rolls-Royce foundries to dispose of slurries based on sodium-stabilised binders after a specific lifespan ranging from 12 to approximately 18 weeks; the material cost implications provide a significant business case for the use of more stable systems such as Ludox HSA [67]. Based on this and on the similarity between shell materials using each binder type at both high-temperature and in the fired condition all trial shell materials were chosen to utilise Ludox HSA as the binder material. In order to address the concerns regarding the relatively low levels of green and pre-fired strength a trial was performed to investigate the use of strength enhancing materials such as polymers to increase the green strength of specimens using Ludox HSA; this is discussed in the following section.

Shell materials based on the silica-alumina shell system were investigated in order to determine the most appropriate ratio of each constituent to manufacture shell materials exhibiting desirable mechanical properties. It is known that the SiAl4060 shell material as used in Hi-shell is excessively strong; based on having the greatest reduction in shell strength compared to this system the alumina rich SiAl2080 system was chosen for further evaluation using Rolls-Royce mould trials.

5.3 Green strength considerations

As discussed in the preceding section it was observed that shell materials featuring the aluminium-modified Ludox HSA binder, exhibited reduced green and fired strength compared to sodium stabilised binders. Commercially however, Ludox HSA remains a desirable product as it allows significantly increased slurry life compared to sodium-stabilised variants (typically 12 months compared to 2-3 months). In order to investigate the strength enhancement offered through the inclusion of green strength enhancers a number of systems were formulated; for consistency and based on its selection for larger scale mould trials the alumina rich silica-alumina system, SiAl2080 was used through this trial.

Table 5.6: Binder materials utilised during green strength enhancement trials. It was observed that the polymer Elvanol within Ludox SK-CV was prone to accumulation at the surface. To investigate this the binder was decanted from bulk supply prior to and post agitation; the starred variant is the non-agitated material. PVOH denotes polyvinyl alcohol; SB denotes styrene butadiene.

	Polymer additive		
Binder	Material	Product	Content
Ludox HSA	None	-	-
Ludox HSA	SB	Adbond HSA	8 wt %
Ludox HSA	SB	Adbond HSA	10 wt %
Ludox SK-CV*	PVOH	Celvol	unknown
Ludox SK-CV	PVOH	Celvol	
Ludox SK-R	PVOH	Elvanol	
Wexcoat	None	-	-

Binder materials used during trials are presented in Table 5.6. Although featuring different product names, it was known from discussions with the manufacturer, Grace-Davison, that Ludox SK binders are manufactured through the addition of different polymers to Ludox HSA. As such their comparison to Ludox HSA which had been modified manually through the different additions of the polymer styrene-butadiene (SB) were valid. To provide control data for the trial itself samples were also manufactured using un-modified Ludox HSA. For comparison samples manufactured using the sodium stabilised Wexcoat binder were also included in the analysis to provide context for the observed strength enhancements. It is known that during storage the polymer present in Ludox SK-CV creams (polymer content rises) out to the surface due to the difference in relative density, in order to counteract this the binder is routinely agitated using a high-shear mixer prior to decanting. There is anecdotal evidence to suggest that green strength related shell cracking problems exist relating to the occurrence of separation. In order to determine the significance in terms of flexural strength two Ludox SK-CV formulations were trialled using material sampled before and after mixing. The unmixed variant was denoted by the * symbol.

Consistent with the shell specimens mentioned in the preceding sections, shell specimens were manufactured by hand-dipping. The mechanical strength of these specimens was determined by flexural testing, the results of this are presented in Figure 5.25.

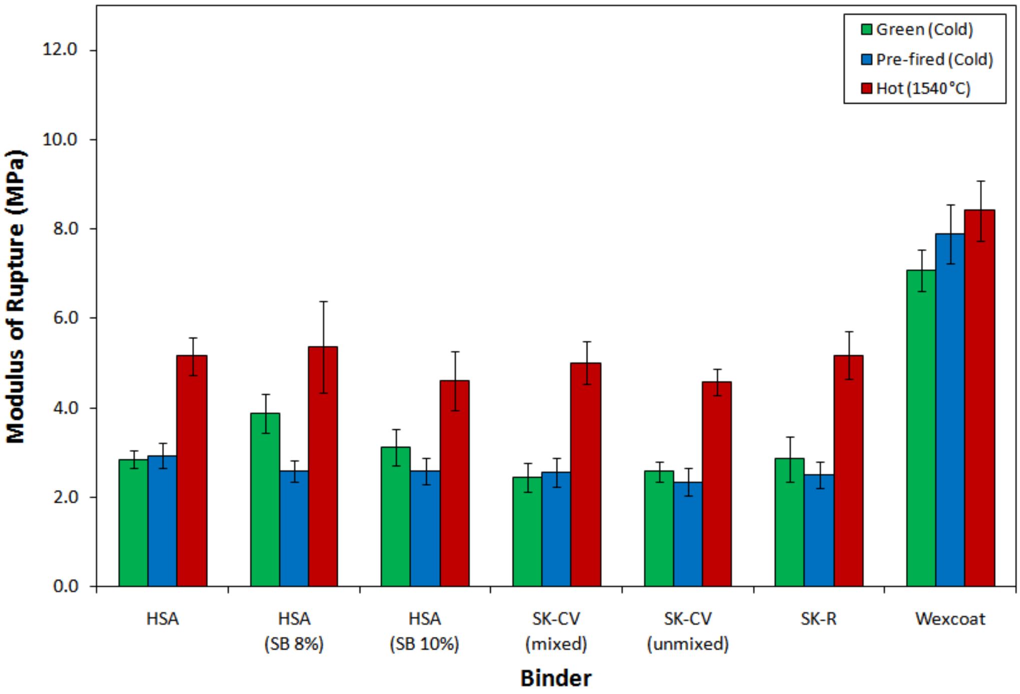

FIGURE 5.25: Flexural strength measurements for test specimens manufactured using various colloidal silica binders and additives. All samples were manufactured using SiAl2080 system with fused mullite stucco.

Inspection of the data revealed that the most significant increase in shell strength was provided through the use of the sodium-stabilised Wexcoat binder. Significant increases in both green (148 %) and pre-fired (170 %) strengths were measured compared to Ludox HSA samples; these observations were consistent with those discussed in the preceding section. Of the Ludox HSA based systems the greatest increase in green strength was recorded for the material containing styrene butadiene in 8 wt % concentration showing a 36 % increase compared to the undoped binder. It was however noted that at the higher concentration the green strength increase was reduced to just 10 %. Surprisingly Ludox SK-R and CV (both mixed and unmixed) variants exhibited lower levels of both green and pre-fired strength compared to the polymer-free binder. In terms of green and pre-fired strengths, it appeared that the segregation of the polymer inherent to the Ludox SK-CV binder during storage had no significant effect. It was also observed that all polymer containing shell materials produced shell specimens with lower levels of pre-fired strength compared to Ludox HSA; it is likely that this was due to the presence of voids within the shell matrix generated by the burn-out of the polymer during the pre-firing process. This process appeared to have no effect on the material at high-temperature with all shell materials except those bound with Wexcoat possessing similar high-temperature strength. Due to the limited slurry material available fired shell specimens were not evaluated in this trial. The significant increase in high-temperature strength for the Wexcoat bound samples was inconsistent with results reported in section 5.2.3, however it is likely that this was related to the difference in silica-alumina ratio within the different shell materials.

Since the level of green strength enhancement provided by the inclusion of a polymer additive was relatively low and due to the associated reduction in pre-fired strength none of the trial systems presented a viable alternative to the original formulation. It was also concluded that the use of a sodium-stabilised binder for the alumina-rich SiAl2080 formulation led to significantly increased levels of high-temperature strength. Since it is believed that this is one of the properties closely linked to the formation of recrystallisation this modification was undesirable.

5.4 SiAl2080 slurry instability and reformulation

The alumina rich system, SiAl2080, was selected as one of two candidate shell systems to be trialled using Rolls-Royce small-bore moulds. To facilitate dipping of the larger moulds it was necessary to mix slurries into 120 litre slurry tanks suitable for robot assisted dipping. During the initial mixing of the slurry it became apparent that the rheology of the slurry would be unsuitable for dipping due to the presence of large flocs on the surface of the slurry. The fact that these flocs were not observed during the initial overhead mixer trial suggested that the instability was linked to a difference in shear environment. The potential causes of the instability are discussed in greater depth in Chapter 7.

Whilst it was necessary to reformulate the shell system to obtain stable rheological behaviour it was important to retain similar mechanical properties. Three candidate formulations were developed featuring different mechanisms to attempt to eliminate the instability; the formulations are given in Table 5.7.

TABLE 5.7: SiAl2080 replacement shell formulations: F200 utilises fused alumina to replace a large proportion of the reactive alumina but still retain overal silica alumina ratio. S20 uses a 40:60 silica alumina content but with binder silica content reduced from 25 wt % to 20 wt % to reduce shell strength. Wex uses the same formulation as the original SiAl2080 material but the aluminium modified Ludox HSA binder is replaced with sodium stabilied Wexcoat.

			Concentration	
Slurry	Material	Product	Wt %	Mol %
SiAl2080 (original)	Silica	Ludox HSA	9.1	21.1
	Alumina	PFR15	74.9	78.9
	Mullite	Duramul 0.07	16.0	
F200	Silica	Ludox HSA	8.3	22.9
	Alumina	PFR15	19.2	77.1
	Alumina	F200	49.1	
	Mullite	Duramul 0.07	23.4	
S20	Silica	Ludox HSA	6.9	40.5
	Alumina	PFR15	16.3	59.5
	Mullite	Duramul 0.07	76.8	
Wex	Silica	Wexcoat 0825	8.5	22.6
	Alumina	PFR15	69.7	77.4
	Mullite	Duramul 0.07	21.9	

It was possible that a number of mechanisms within the slurry may have led to its de-stabilisation, when developing candidate formulations two main causes were addressed. It is known that the silica alumina system exhibits instability at intermediate pH values due to the species being stabilised by opposite charges (for further discussion of this see Section 7.2). Since Ludox HSA is naturally acidic and alumina naturally alkaline (in deionised water) the resulting slurry operated at pH values around 6.6; natural pH refers to the pH of the material without the addition of acid or alkali. To determine if this mechanism was responsible for the observed rheological problem the Ludox HSA binder was replaced with a sodium stabilised binder, Wexcoat. The natural pH of the replacement binder was around 10 and the resulting slurry was similar. This SiAl2080 based system was referred to as Wex.

Another mechanism potentially responsible for the destabilisation was dehydration of the binder due to the level of fine alumina content. Problems with the handling of alumina slurries using the combination of high-solids loading and small particle sizes were reported by Tsetsekou *et al.* [108]. In order to determine this a large proportion of the fine reactive alumina (72 wt %) was replaced with a larger, 200 mesh fused alumina. The silica alumina ratio of this system remained identical to the SiAl 2080 material however the particle size distribution was significantly altered; this system was referred to as F200.

The final trial formulation was based on a reduced silica content variant of the SiAl4060 system. At the time of these trials the long term instability in the SiAl4060 system (used in the SiAL4060-Z shell system described in section 4.5) had yet to be detected. The S20 system was developed based on the SiAl4060 system using the same silica alumina ratio but with reduced amounts of each in order to reduce the amount of mullite formed during firing. It was believed that this would reduce the high temperature and fired strengths of the material such that the mechanical properties of the system would be comparable to the original SiAl2080 system.

Slurries utilised in these trials were mixed using overhead mixers and subsequently transferred into 4.5 litre rotary-tanks for holding and dipping. Whilst these tanks had a relatively low volume they provided a closer representation of the shear environment experienced by slurries in robot tanks than did the overhead mixer-type tanks used during the initial development work. It was hoped that this would more clearly reveal any potential instability similar to that observed in the original SiAl2080 slurry (see Chapter 7).

In order to ensure reproducibility between this experimental set-up and that used previously, the original SiAl2080 system was included in the trial work; whilst it was possible to dip test bars, the instability which had been observed in the 120 litre robot tank was again observed in the smaller tank. During the 10-day slurry life necessary to complete the trial no instability was observed in any of the replacement formulations; the original SiAl2080 system became unstable over a period of around 5 days. Flexural strengths of samples from each system are reported in Figure 5.26.

Shell specimens manufactured using each of the replacement formulations exhibited greater flexural strength in all firing conditions compared to the original SiAl2080 system. As observed in sections 5.2.3 and 5.3 the green and pre-fired strengths of the sodium-stabilised Wex samples were enhanced compared to the original system and both other replacement systems, all of which contained Ludox HSA binder. F200 and Wex samples exhibited similar fired and high-temperature strengths with values increased by 17 % & 10 % fired and 94 % & 91 % at high-temperature respectively. By contrast the fired strength of the stoichiometric mullite formulation, S20 gave a 50 % increase in fired strength and a 33 % increase in high-temperature strength compared to the original system.

Additionally to flexural testing, specimens were subjected to creep testing; results

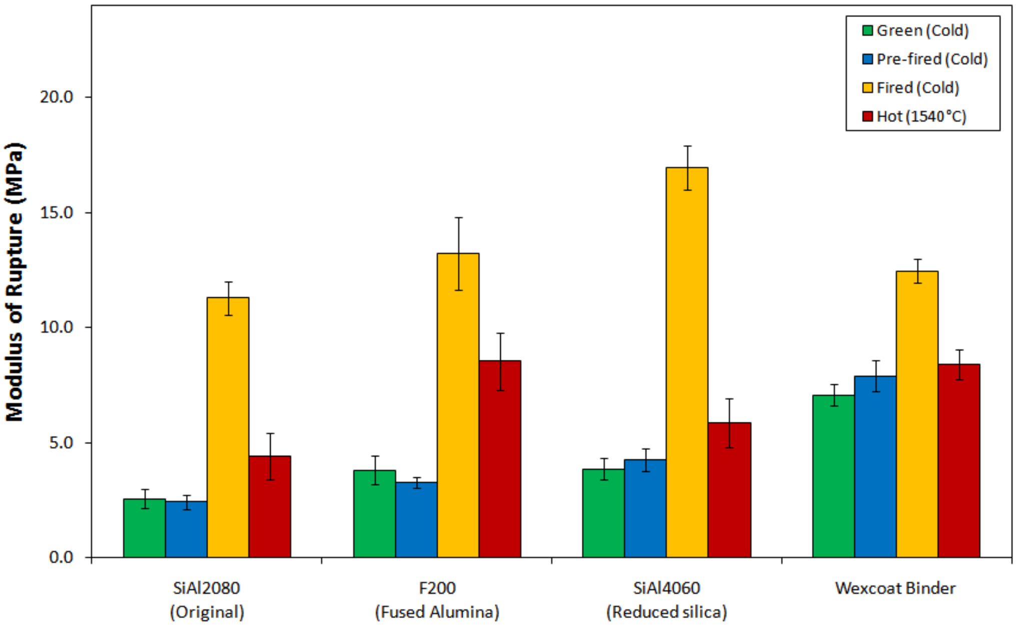

Figure 5.26: Flexural strength measurements for test specimens manufactured using various colloidal silica binders and additives. All samples were manufactured using SiAl2080 system with fused mullite stucco.

of this testing can be seen in Table 5.8. Variation in the amount of creep exhibited by samples of each system were minimal; for reference the amount of creep measured on the Rolls-Royce shell material are included.

Table 5.8: Creep deformation measured flexurally in 3-point bend. Testing performed at 1540 °C under an applied load of 3.2 N. Deformation recorded after 5 minutes. Samples exhibiting excessive creep to generate measurement are denoted by ∞.

Shell material	Creep deformation (mm)
SiAl 20:80	0.098
Wex	0.18
S20	0.31
F200	0.14
PCF Hi-shell	0.074
PCF Std. SX	∞

To further understand the properties exhibited by each shell variant, specimens were examined under SEM. Figure 5.27 shows the structure of the Wex system

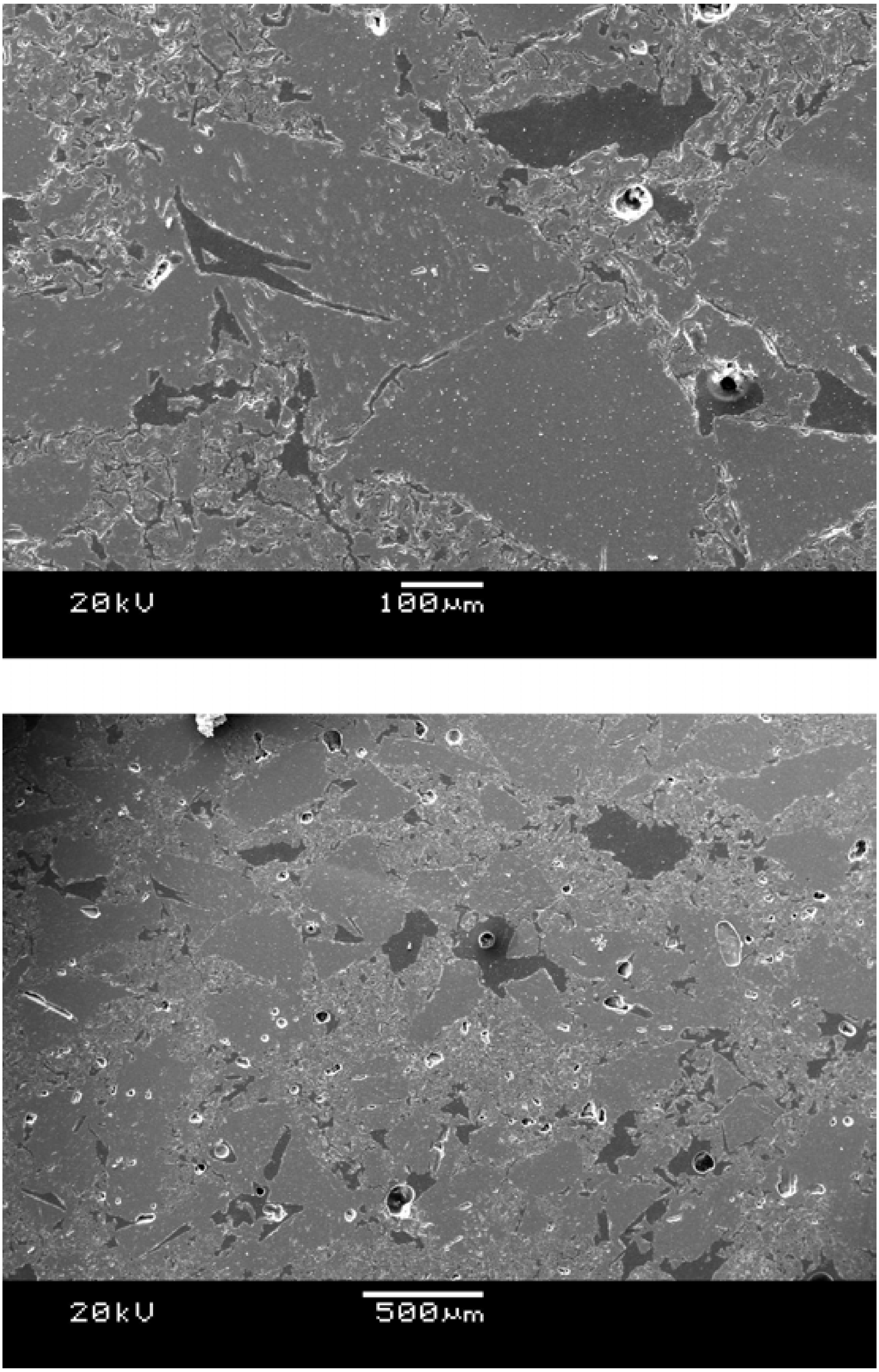

FIGURE 5.27: SEM micrographs showing the structure of Wexcoat bound, SiAl2080 shell material.

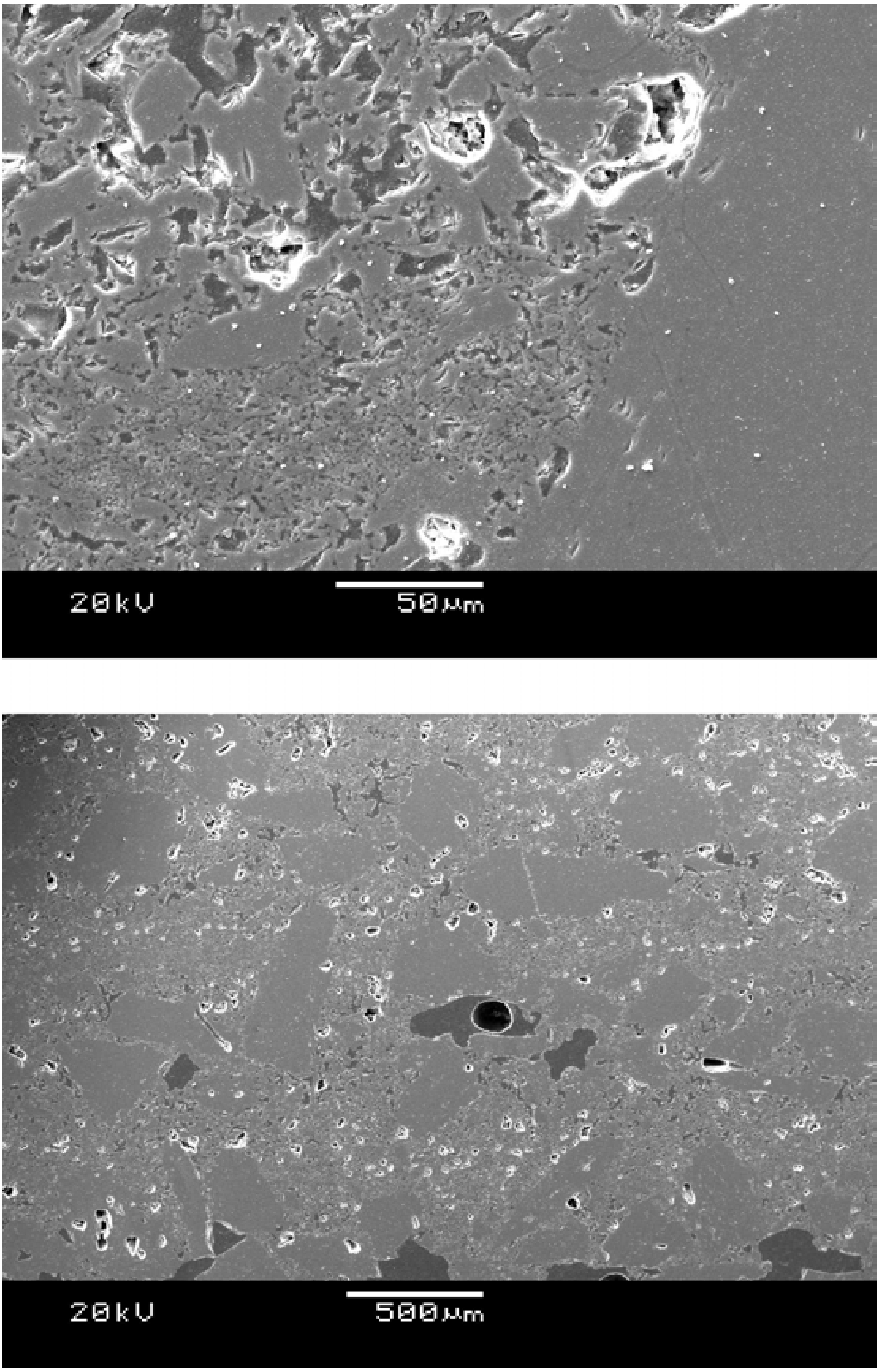

FIGURE 5.28: SEM micrographs showing the structure of S20 shell material, based on reduced silica content Ludox HSA. Silica-alumina ratio of the slurry matrix was stoichiometric mullite.

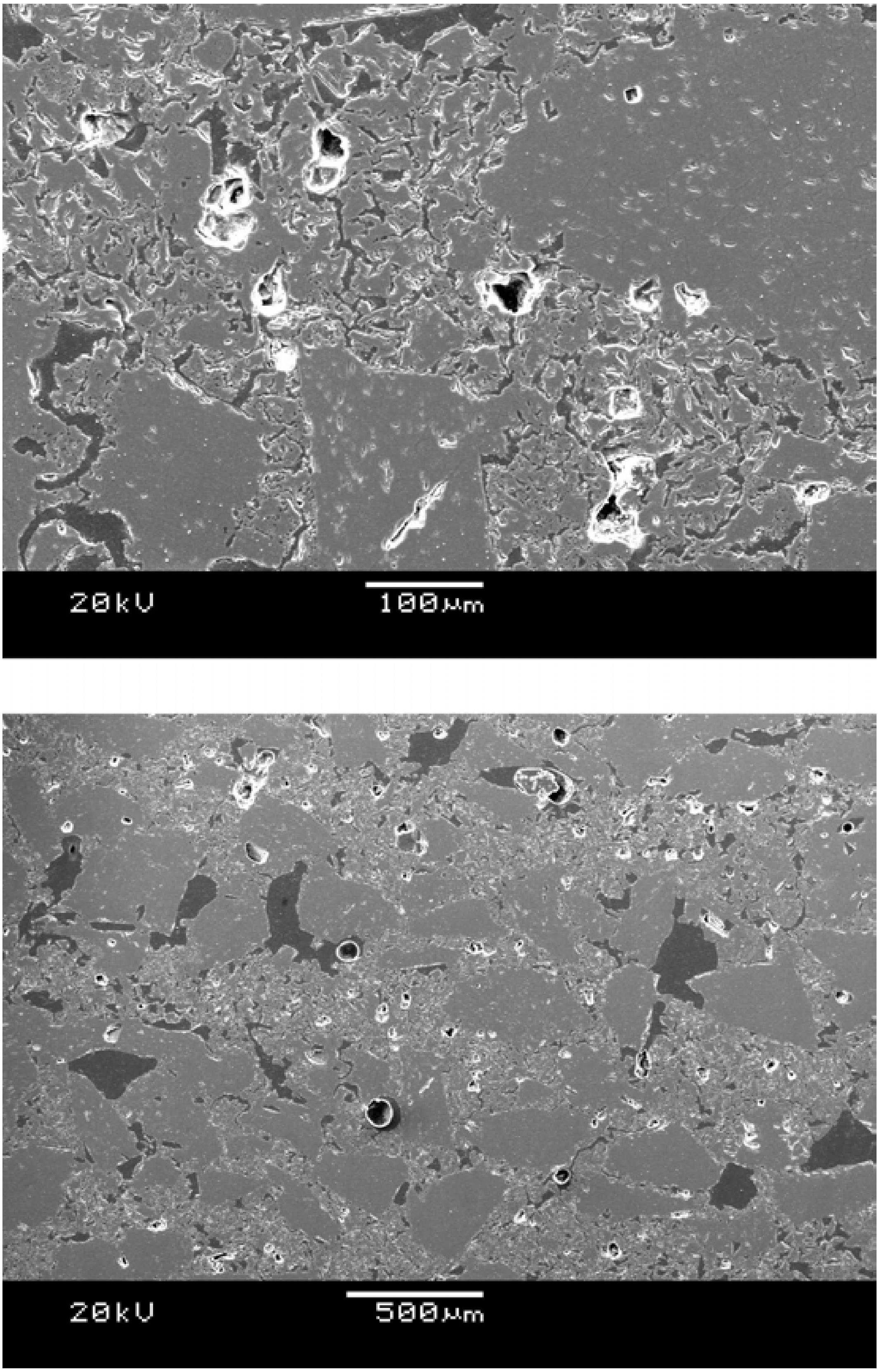

Figure 5.29: SEM micrographs showing the structure of F200 shell material, based on original SiAl2080 shell material but with a large quantity of the fine reactive alumina having been replaced by coarser fused alumina.

which featured the same basic formulation as the original. However unlike the Ludox-HSA bound version the microstructure of the sodium-stabilised specimens did not show the same level of cracking. It is likely that this was due to the effect of sodium during sintering. It was mentioned in section 5.2.3 that the presence of sodium can reduce the level of sintering of alumina during firing and in combination with silica promote the formation of glassy phase between grains. Both of these processes would serve to reduce the contraction between the shell matrix and stucco grains and hence reduce the level of voidage within the specimen; this was observed as an increase in the fired strength of Wex specimens.

The structure of S20 specimens, presented in Figure 5.28 was indistinguishable from that of the SiAl4060 system on which it was based. Inspection of the flexural strengths revealed that the 5 % reduction in silica content produced an approximate reduction of 25 % in strength measured in all states except green, where it was only reduced by 5 %. The causes of this could not be observed directly within micrographs of the specimens structure.

The structure of the F200 shell material showed significant differences to that of the original SiAl2080 system. As shown in Figure 5.29 the structure featured crack-like voids within it, however, the length and width of those cracks was reduced compared to those present in the original system. Since much of the fine alumina content had been replaced with larger, fused alumina it was expected that the shell samples would experience less sintering during firing. This was confirmed during thermal expansion measurement; Figure 5.30 shows derivative thermal expansion data for SiAl2080 and F200 systems. A large contraction was observed for the original system indicating the occurrence of sintering between approximately 1400 - 1500 °C; from examination of Figure 5.12 it is likely that the sintering ceased at this point due to the voids formed within the material reaching a critical size. In contrast the F200 system experienced no notable contraction in this temperature range. The reduced level of cracking within the shell structure was consistent with the increased fired strength exhibited by flexural test specimens.

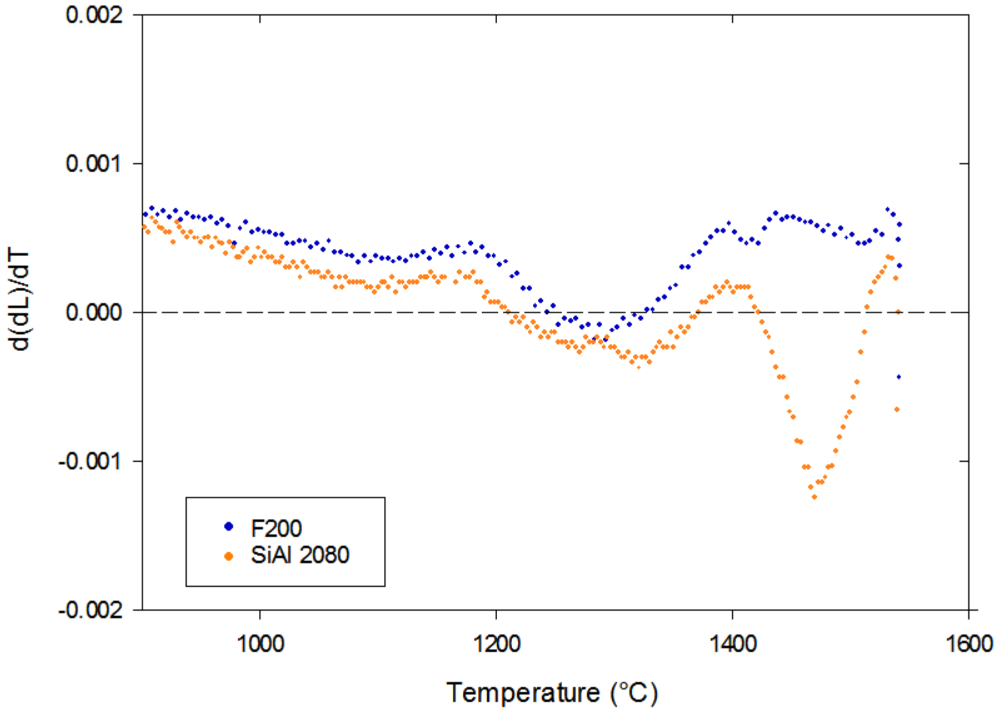

Figure 5.30: Derivative thermal expansion data for sintering of original SiAl2080 and replacement F200 systems.

Whilst the mechanical properties of all the replacement systems were similar it was also necessary to consider the slurry stability; whilst each system had showed stability during the trial period the long term implications of using the Wex system which retained the high proportion of fine alumina were not known. By this point it had also been observed during the original zirconia-stuccoed small-bore trial, (see section 4.4) that the SiAl4060 system suffered from a similar instability as that of the original SiAl2080 leading to reduced shell strength with increasing slurry age. Based on these observations the F200 system was selected for further evaluation using small-bore mould trials; this process is discussed in the following section.

5.5 F200 slurry stability

During small scale testing, it was necessary to retain ceramic slurries for several days, however, due to the logistics involved with supplying and transporting moulds it was necessary to maintain them for a much longer duration during larger scale trials. It would also be necessary to understand the stability of a system before it could be considered for industrial-scale production usage. It was observed with both of the original trial systems that slurries which had exhibited stability within the small-scale overhead stirrer tanks became unstable when scaled-up to larger, rotary tanks. In order to determine the long term behaviour and stability of the F200 slurry the slurry properties were observed over a period of several months; the results of testing are presented in Figures 5.31 to 5.34.

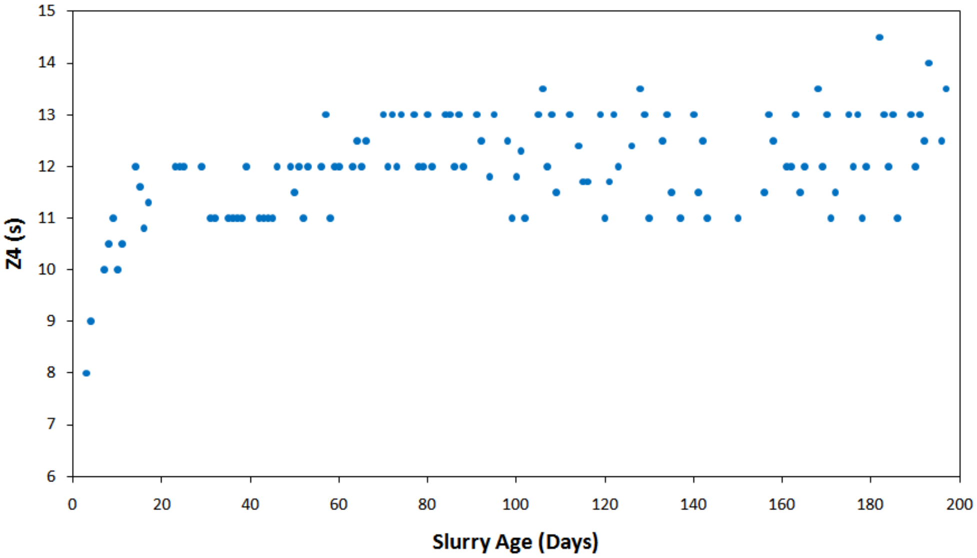

FIGURE 5.31: Zahn-4 flow cup measurements for F200 slurry recorded daily during slurry stability characterisation trial. Flow-cup was used as the control parameter during the trial.

In order to correct for water evaporation during the trial, de-mineralised water was added daily based on the observed increase in slurry viscosity (the control parameter) as measured by Zahn 4 flow-cup (see Figure 5.31). The target value

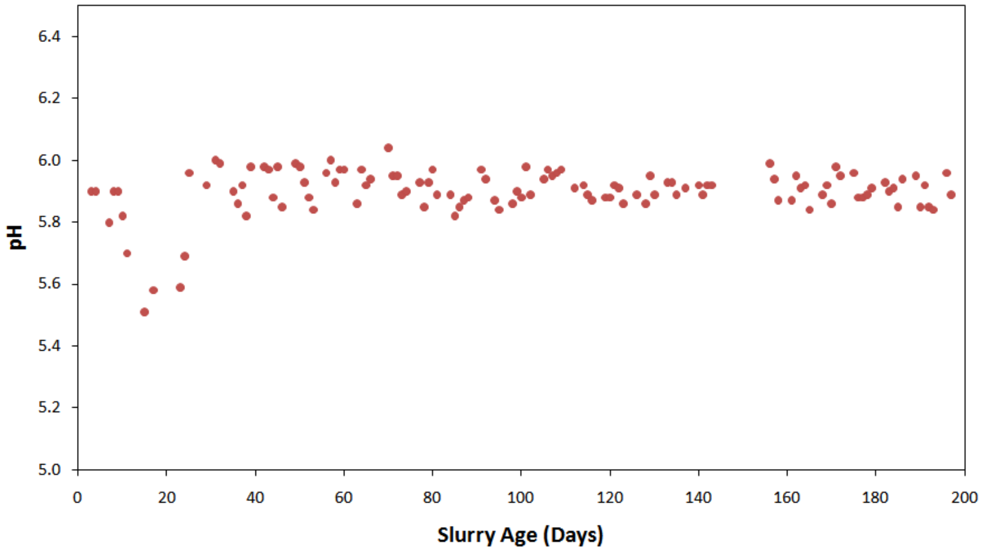

FIGURE 5.32: pH measurements for F200 slurry recorded daily during slurry stability characterisation trial.

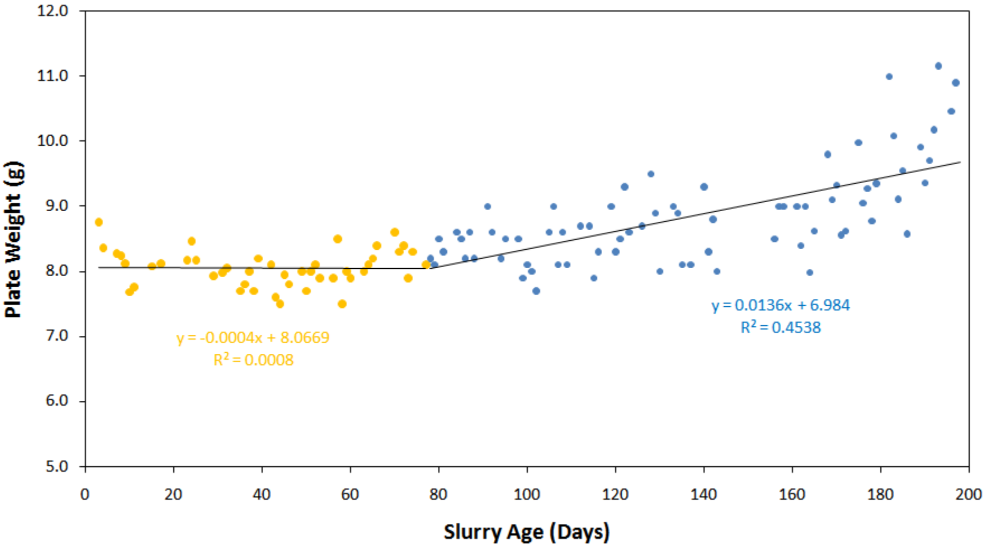

FIGURE 5.33: Plate-weight measurements for F200 slurry recorded daily during slurry stability characterisation trial.

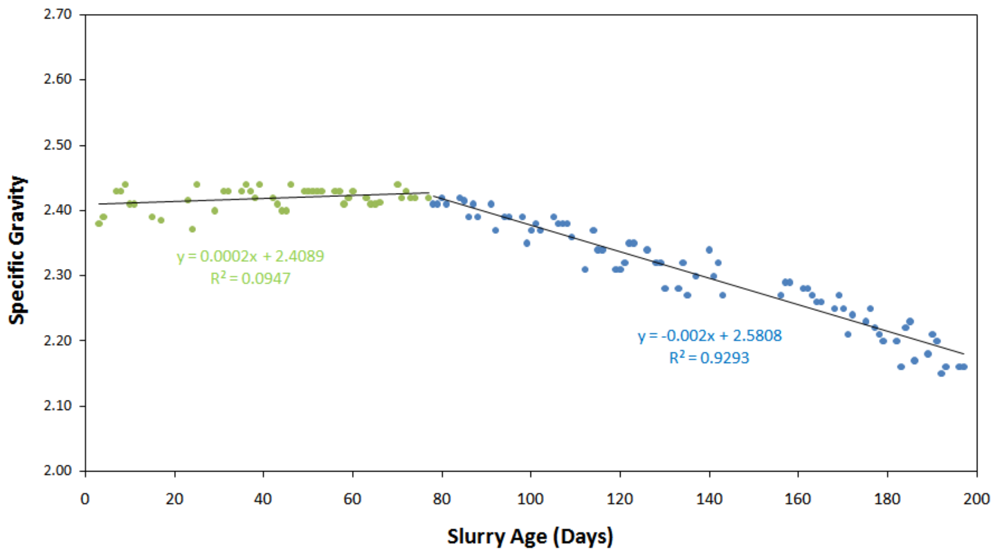

FIGURE 5.34: Specific gravity measurements for F200 slurry recorded daily during slurry stability characterisation trial.

for flow-time on the flow cup was 11-12 seconds; although the results showed variability, it was within the expected ± 11 % expected for a single operator using a the Zahn-type flow cup [80].

Plate-weight, specific gravity and slurry pH were also recorded, but no water-additions were made based on their results. It can be seen that during the first 10-12 weeks of the trial the slurry remained stable exhibiting no significant change in any of the measured parameters. However beyond this period a decrease in measured slurry density and an accompanying increase in plate weight was observed; it is likely that this is due to the formation of agglomerates within the slurry. These agglomerates cause an increase in the observed viscosity of the slurry, since this is the control parameter the increase triggers dilution. Following dilution the viscosity of the slurry appears correct however the agglomerates remain but are simply distributed in additional fluid. This process leads to an overall decrease in the slurry density; during plate weight testing some agglomerates remain adhered to the surface of the plate causing an increased measurement. It is possible that this was related to the instability of the silica alumina system at intermediate pH (see section 7.2).

It was also observed during the initial SiAl4060-Z trial that instability within the slurry led to a reduction in shell strength over a period of 3 weeks; in order to monitor this effect shell test bars were manufactured on a weekly basis during the slurry stability trials. Flexural strength results for test bars manufactured in this period are presented in Figure 5.35.

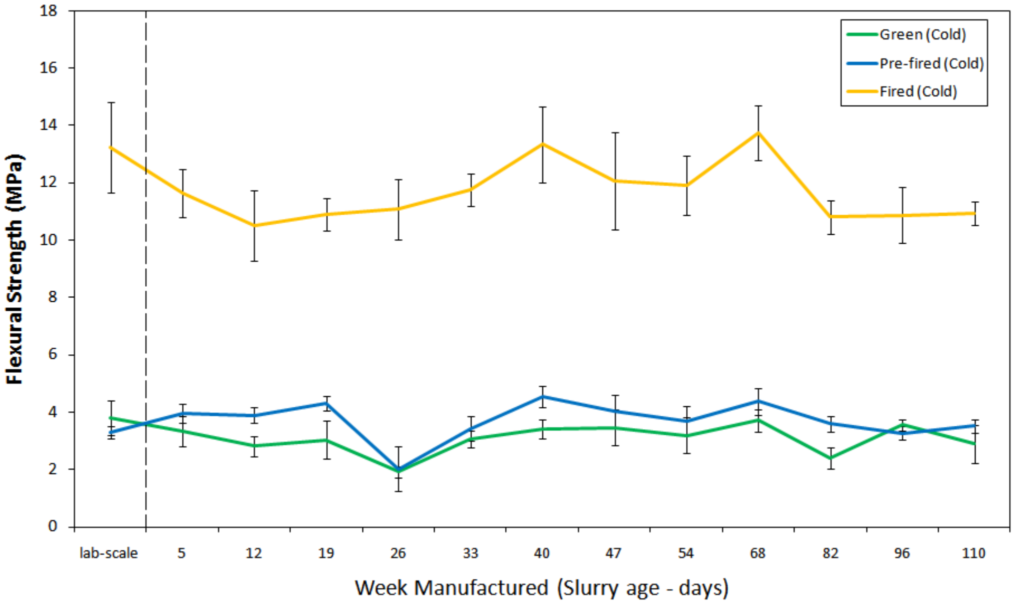

FIGURE 5.35: Flexural strength measurements for F200-M shell specimens manufactured weekly in order to monitor slurry stability.

During the original SiAl4060-Z trial a decrease in slurry density of 0.22 $\mathrm{kg\,m^{-3}}$ was observed over the 3 week slurry lifespan, this was accompanied by a significant reduction in the mechanical properties of the shell material in all conditions. As shown in Figure 5.35 the slurry density remained stable at approximately 2.40 $\mathrm{kg\,m^{-3}}$ for around 80 days before beginning to decrease. After 110 days the density was 2.36 $\mathrm{kg\,m^{-3}}$ and continued to drop to a value of 2.16 $\mathrm{kg\,m^{-3}}$ by day 196. Whilst the density reduction was similar for each system the manifestation in flexural test results was very different, it can be seen from Figure 5.35 that the flexural strength for samples in each condition remained stable for the duration of the trial. Average strength values are summarised in Table 5.9.

Table 5.9: Average flexural strength of F200-M batches manufactured during slurry stability trial.

	Flexural Strength (MPa)		
Condition	Mean	Std. Dev	Sample
Green	3.17	0.70	77
Pre-fired	3.73	0.73	78
Fired	11.49	1.35	76

Across all samples tested the spread of the flexural strengths was small; green and pre-fired exhibited standard deviations of around 20 % for sample sizes of 77 and 78 respectively compared to mean in-batch standard deviations of 15 and 11 % respectively. Fired specimens showed less spread at 12 % across 76 specimens compared to a mean in-batch standard deviation of 8 %; this was expected due to a certain amount of homogenisation and defect removal during the sintering process. Overall the variation in the data was acceptable compared to known levels for similar heterogeneous ceramic materials.

5.6 F200-M Mould Trials

As detailed for zirconia containing shell systems in section 4.4, trials using Rolls-Royce small bore moulds were performed to assess the overall performance of shell materials throughout the entire investment casting process. As mentioned in section 4.7 during scale-up of the original zirconia stuccoed shell system it was found that the SiAl4060 slurry exhibited instability over time leading to reduced slurry density and hence a progressive drop in material strength.

Before commencement of the mould trial, the stability of the slurry was monitored for approximately 7 weeks using both slurry checks and through the manufacture of test specimens. As discussed in section 5.5 the results of each measurement suggested stability within the slurry. Since the original zirconia shell system was not suitable for shelling due to its instability, an F200 slurry based zirconia shell system was formulated; variants were designated F200-M and F200-Z for the use of mullite and zirconia stucco respectively. The development and investigation of various zirconia stucco types using the F200-Z system are discussed in section 4.6 and the subsequent mould trials performed using the material are reported in section 4.7. The procedure for shelling small bore moulds was identical to that described for the zirconia stuccoed moulds; for the F200-M trial 8 Pegasus low-pressure turbine blade moulds (referred to by part number 522') were available to be shelled along with a mould containing suitable wax patterns to make shell test specimens.

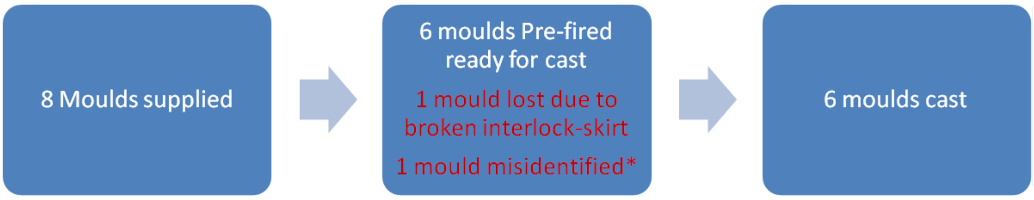

FIGURE 5.36: F200-Z mould progression and loss during processing. Breakage occurred at a bayonet fixture used to secure mould to furnace during casting. Mould lost due to identification has no reflection on shell mechanical properties.

Due to the mould losses detailed in Figure 5.36 only 6 of the 8 blade moulds were cast (test bar moulds were not intended to be cast) yielding 24 blades for inspection. As described in section 4.7 each blade passes through a number of inspection operations in order to determine its compliance with the specification. As was the case with blades manufactured using the F200-Z shell material, all blades were inspected at every operation even if they were classified as scrap during previous inspection operations.

Due again to the small number of blades manufactured the statistical significance of any reduction in the occurrence of re-crystallisation (RX) was too low to attribute to the change in shell properties. However for completeness the results are presented in Figure 5.37.

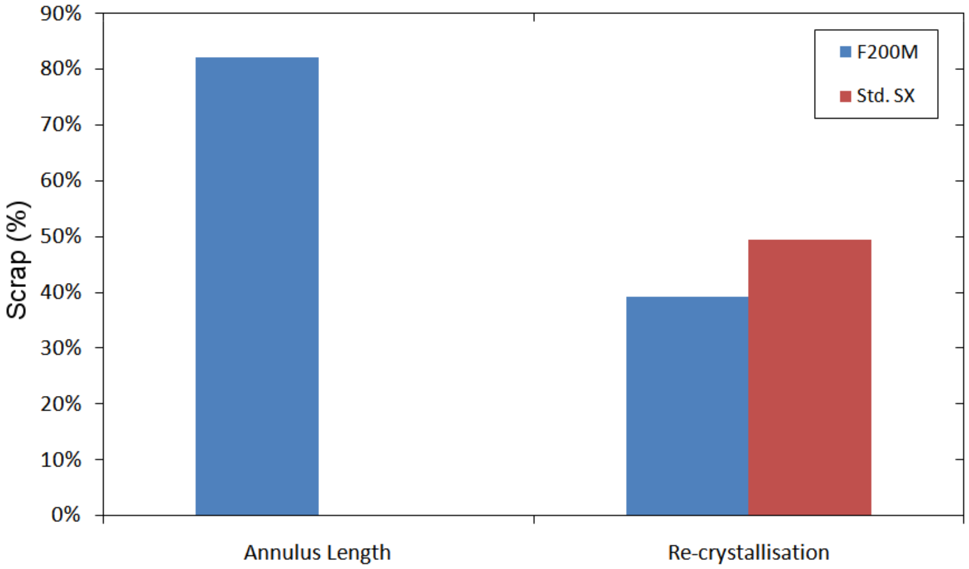

FIGURE 5.37: Results of casting trials for Pegasus LP Turbine blade manufactured using F200-Z mould material. Results based on inspection of 24 blades; observed reduction in RX is not statistically significant.

As with the previous trial it was observed that the F200-M material caused blades to exhibit longer aerofoil length, it is understood that this was due to the difference in sintering and thermal expansion coefficient of the mould material compared to the zircon-filled Std. SX shell material. Investment casting is not a true net-shape process and as such the standard wax formers used are tailored to account for the contraction rate of the Std. SX shell material. Scrap losses due to this defect were therefore expected. Moulds losses due to damage in the green and pre-fired states were still observed to be higher than those recorded for the Rolls-Royce Std SX shell material.

5.6.1 Wexcoat F200

It appeared to be the case that aluminium-modified binders such as Ludox HSA provided insufficient strength for backup shell materials in the green and pre-fired states. In an attempt to investigate this the F200 shell material was re-formulated replacing Ludox HSA with the sodium stabilised Wexcoat binder material. The reformulated system was designated as W200; like F200 the system was also used to investigate the effect of unstabilised zirconia stucco, the details of which are reported in section 4.8. This section reports the performance of the mullite stuccoed variant; due to the logistical limitations and costs associated with mould trials only test-bar and material analysis were performed on this shell material. Figure 5.38 summarises the shell strengths of various alumina-rich shell materials derived from the original SiAl2080 shell system; strengths are shown for binders featuring both Wexcoat and Ludox HSA binders. Along with the original formulation which contained high solids content of fine reactive alumina, the replacement system featuring fused alumina is also presented for each binder.

It had been observed during shell trials that sodium stabilised binders gave greater levels of green and pre-fired strengths than aluminium modified ones. The explanation for this is not well understood and is discussed in section 2.7.2. However it remains the case that the results presented in Figure 5.38 were consistent with this trend.

It was also observed that unlike for the original SiAl2080 formulation the fused alumina containing variants exhibited greater fired strengths when using sodium-stabilised binders.

It was also the case that samples bound by the sodium containing Wexcoat binder showed greater fired strength, with the original formulation showing an increase of approximately 20 % and the fused alumina variant giving approximately 30 %;

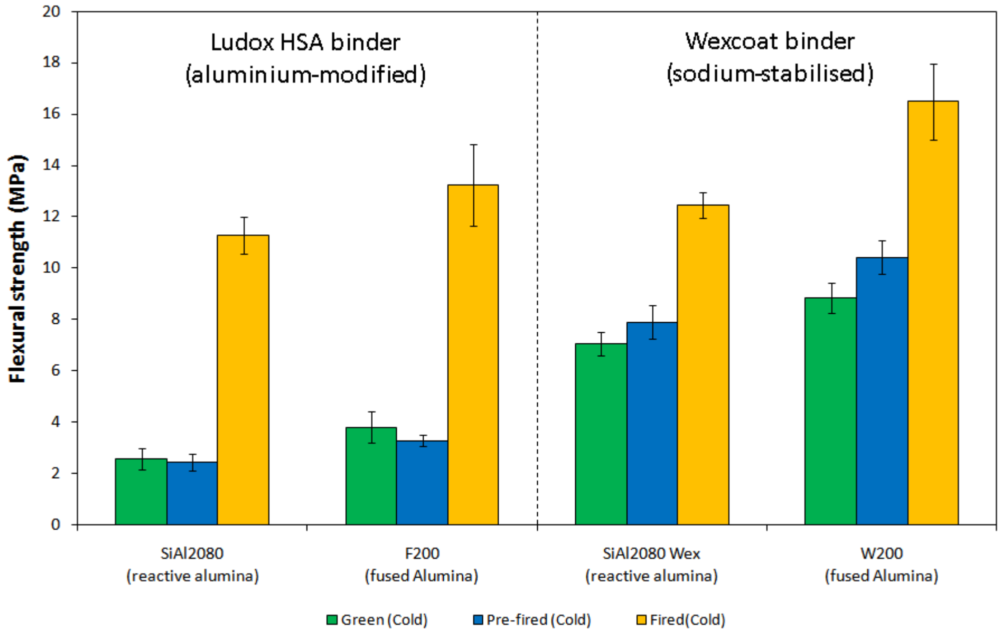

FIGURE 5.38: Flexural strengths for Wexcoat and Ludox HSA bound F200 shell specimens.

however within errors the difference between these strength increases was negligible. It is known from the chemical analysis provided by respective manufacturers that the reactive alumina PFR15 and fused alumina F200 contain sodium-oxide levels of approximately 600 ppm and 2500 ppm respectively. It is also known that the level of calcium-oxide within PFR15 was approximately 800 ppm however the level within the fused alumina was not reported. The effect of impurities on the sintering of alumina were discussed in section 2.9.2, and it is likely that the additional sodium present within the Wexcoat binder enabled greater sintering and the formation of glassy phase within the material allowing greater connectivity between stucco particles. To investigate this the structures were examined using SEM; the results are presented in Figure 5.39.

Samples were additionally characterised by thermal expansion measurements, the results of which are presented in Figures 5.40 and 5.41. It can be seen from the comparison with the F200 system that the sintering of the F200 shell material

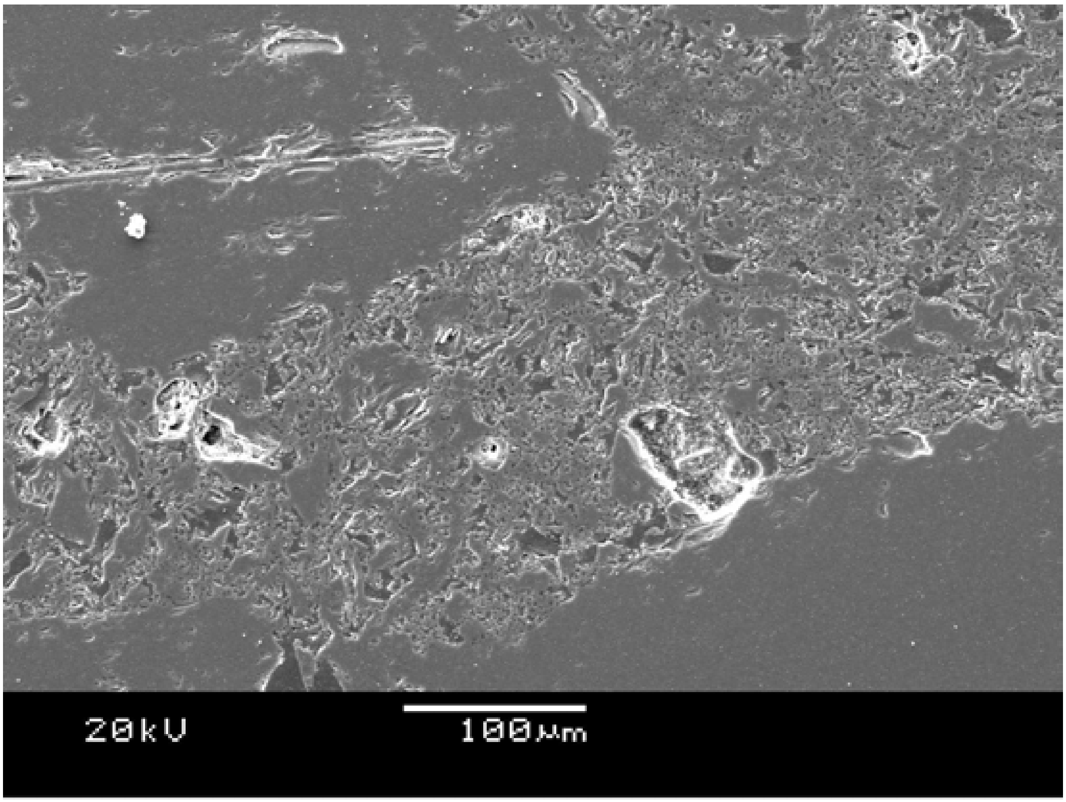

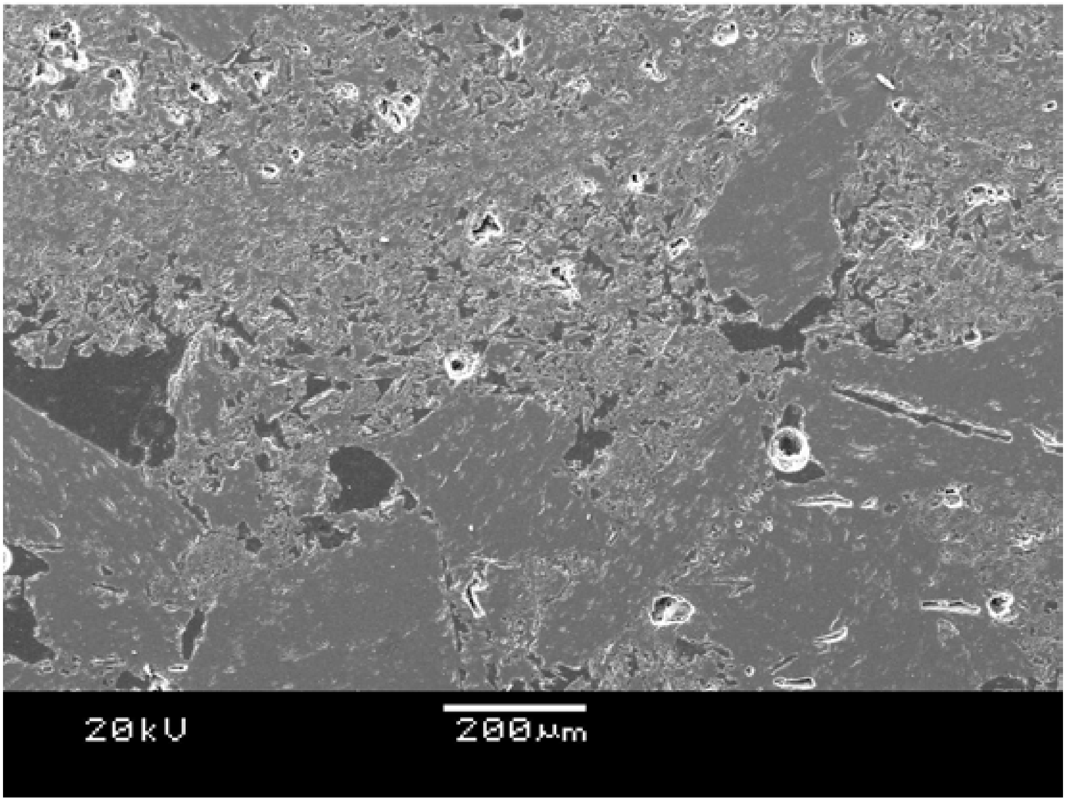

FIGURE 5.39: SEM micrographs showing the structure of Wexcoat bound, W200 shell material. Featuring same material composition as F200 shell.

in the temperature range 1200 - 1400 °C is greater than that of the W200 material. This behaviour was discussed in section 5.2 with regard to the relative silica alumina content within the material. It was observed that silica rich material exhibited reduced sintering in this temperature range compared to the alumina rich formulation: these observations were consistent with those reported in the literature. The mechanism to which this was attributed was the formation of silica layers surrounding the alumina particles which retarded the diffusion and sintering of alumina grains; the presence of sodium within the Wexcoat binder would have reduced the viscosity of the silica at high temperatures. The more mobile silica within the W200 shell specimens may have better enveloped the alumina grains during firing leading to reduced sintering compared to the sodium-free F200 variant. This was also observed in microstructural observations; the W200 material exhibited greater connectivity between the silica-alumina matrix and the mullite stucco particles. This also explained the increased flexural strength exhibited by Wexcoat bound specimens in the fired condition.

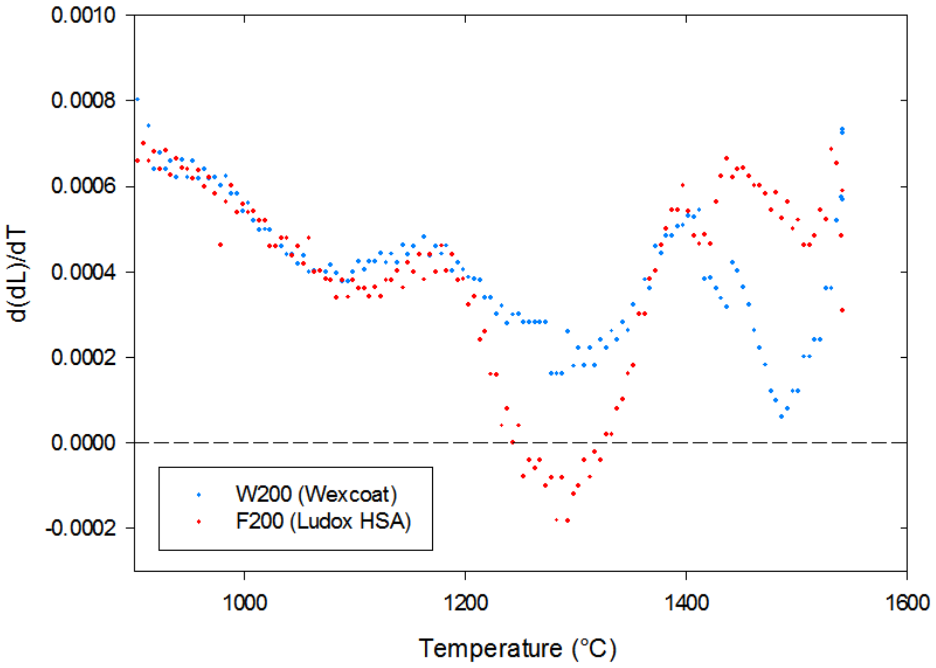

FIGURE 5.40: Derivative thermal expansion data for W200 and F200 shell materials during heating cycle.

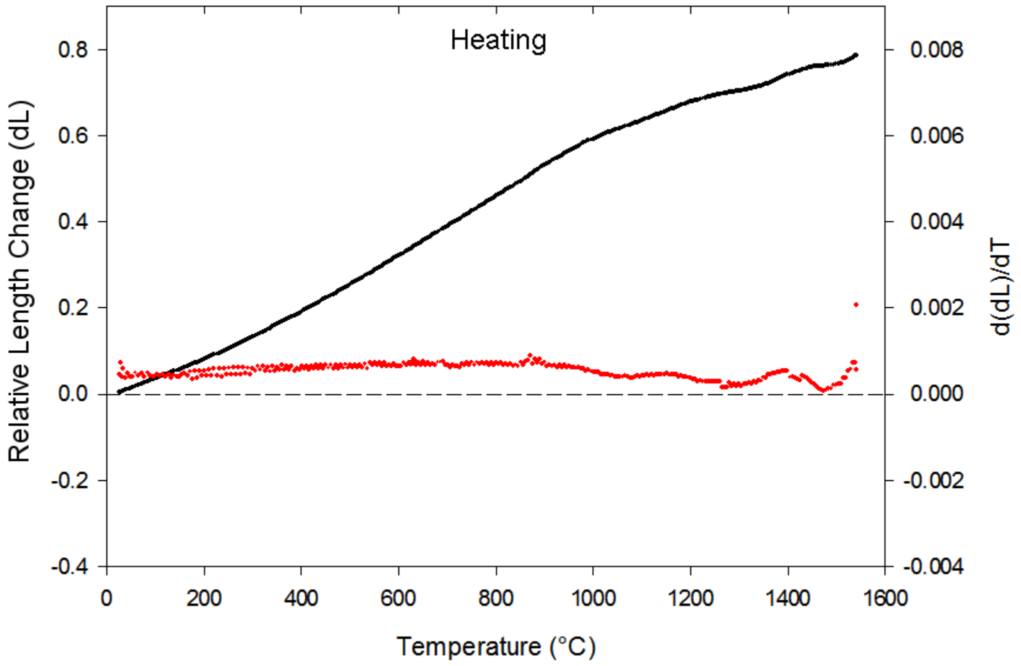

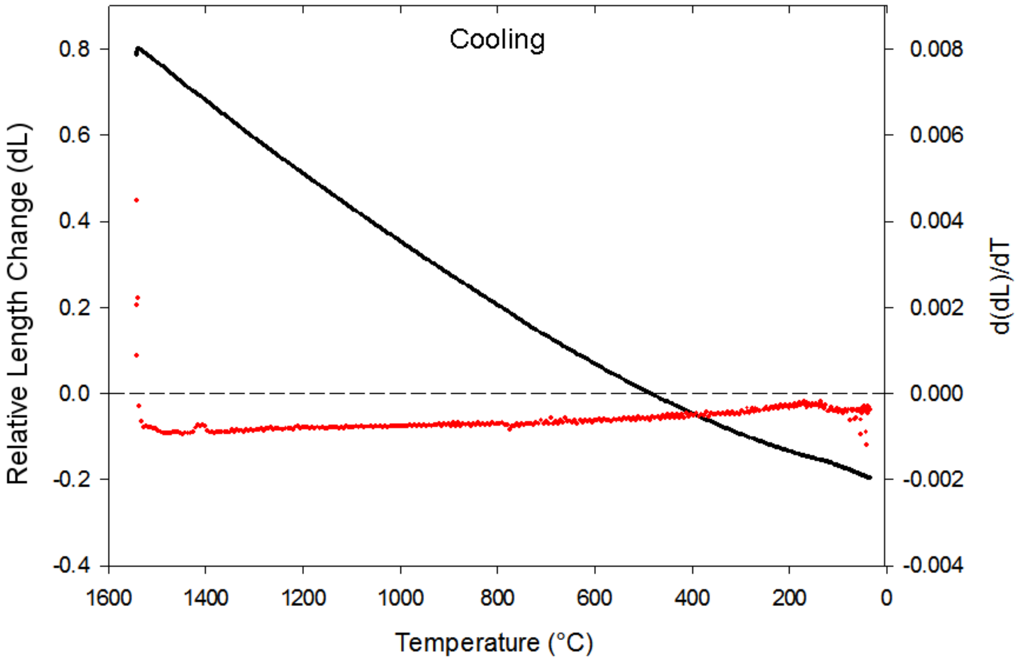

FIGURE 5.41: Thermal expansion of W200 system featuring Wexcoat binder. Relative change in length is shown in black, rate of length change is shown in red.

5.7 Conclusions

It has been observed that the properties of investment casting shell materials based on the silica alumina system are highly dependant on the relative proportions of each constituent material. As expected and consistent with similar systems reported in the literature, alumina rich shell materials exhibited significantly different sintering characteristics to those featuring silica rich formulations. Mullite forming materials similar in composition to the Rolls-Royce Hi-shell system were seen to give high-strength both at high temperature and in the fired condition. High-temperature creep resistance was observed to be most dependant on the silica content within the shell with both the silica-rich formulation and the Rolls-Royce Standard SX shell exhibiting the highest creep rates.

In terms of green and pre-fired strength, the most significant differences were seen for materials containing different types of binder. A number of green strength enhancers were included within formulations to attempt to increase the strength of the aluminium modified Ludox HSA binder. Flexural testing however revealed that none of the additives provided any significant increase in green strength, in contrast the conventional sodium-stabilised binders trialled showed significantly greater levels of both green and pre-fired strength both flexurally and in compression. Based on significant mould damage during Rolls-Royce small-bore mould trials it was necessary to reformulate the slurry to include Wexcoat; the subsequent observations of moulds (reported in section 4.8) showed that handling strength of moulds was consistent with the observations made using flexural testing.

Unfortunately, due to the high number of moulds required it was not possible to show a statistically significant reduction in recrystallisation resulting from changes in the behaviour of shell materials. The trials did however provide useful information regarding the influence of shell formulation on the thermal and mechanical properties of investment casting shells.

6

Fugitive Shell Systems

6.1 Introduction

One of the techniques by which the strength of ceramic materials can be intentionally reduced is through increasing the level of porosity within the material. This reduces the strength by both reducing the amount of material supporting an applied load and also since the pores act as stress concentration sites and in some cases failure initiation sites. It has been shown in the preceding chapters that all shell materials inherently contain porosity and defects; through the inclusion of a pore-forming agent (PFA) shell materials presented in this chapter develop additional porosity during firing. All shell systems described feature polyethylene (PE) powder in varying amounts as the PFA. Various PFA materials were discussed in section 2.5. It was possible to manufacture a range of shell materials to investigate the relationship between porosity and mechanical properties of the materials.

The following sections give the details of the trial shell formulations tested and present the results of both mechanical testing and other materials characterisation. Finally conclusions based on the use of these materials and future developments are discussed.

6.2 Trial formulations

The base formulation which was modified using the PFA was based on the silica alumina system and featured a formulation as shown in Table 6.1. Based on molar concentrations of silica and alumina included in the shell the overall ratio was 27 % silica and 73 % alumina; the designation SiAl2773 was given in keeping with other systems using varying silica alumina ratio.

TABLE 6.1: The formulation of the silica-alumina matrix which provided the basis for all fugitive shell systems.

Material		Concentration	
		Wt %	Mol %
Silica	(Ludox HSA)	8.9	27.3
Alumina	(PFR15)	58.5	72.7
Mullite	(Duralum 0.04)	11.7	
	(Duralum 0.07)	20.8	

The PFA was included in the shell as both a filler and stucco material, in the case of the former different concentrations of PE were included to observe the relationship between PFA amount and shell properties. For completeness the shell system was also characterised without inclusion of the PFA material. Shell formulations are given in Table 6.2.

Table 6.2: Polyethylene content for fugitive trial shell formulations. SiAl 2773 was used as the base formulation for all systems and was also tested without PFA addition. The system designated PES was included PE only as a stucco material.

Designation	PE Content (vol %)	Application
SiAl2773	none	n/a
PE025	2.5	Filler
PE050	5.0	Filler
PE100	10	Filler
PE200	20	Filler
PE300	30	Filler
PES	n/a	Stucco

To calculate the volume concentration of PFA to include it was necessary to estimate slurry volume; this was done by calculating the total slurry volume by relating theoretical density and mass added of each constituent. Clearly this approach neglects the effects of particle packing, however it provided a useful and repeatable approach to formulation. PE was added to the slurry during the mixing process as the final constituent.

Unlike other systems featuring PE as a slurry constituent the system designated PES featured the material as a stucco, the slurry was common to the base formulation of SiAl 2773.

6.3 Results

6.3.1 Manufacturing observations

During the initial mixing of the PE300 slurry it was apparent that at this PE concentration the rheology was unsuitable for dipping. The relatively large diameter of PE particles made the slurry coarse and at this concentration the viscosity was sufficiently high as to prevent flow-cup measurement. The rheological problems were sufficient that it was not possible to add the required dose of PE and the system was eliminated from trials.

The system featuring PE as a stucco material was also eliminated before dipping could be completed. Samples in this shell system were made using alternating layers of mullite and PE stucco with PE at backup coats 2 and 4. It was possible to apply PE as a stucco material, however subsequent dipping was not possible due to poor wetting of the PE stuccoed surface. Upon draining of the PE stuccoed test bars very little slurry remained on the surface preventing subsequent stucco application and the manufacture of a full shell. This led to the elimination of the material for this application. It was possible for all other formulations to both mix slurries and manufacture test pieces.

6.3.2 Porosity characterisation

In order to verify that the pore forming agent was working as intended the porosity of specimens of each fugitive shell material was measured using the Archimedes' technique discussed in section 3.1. Samples in the pre-fired condition, having been pre-fired to 800 ℃ exhibited the highest porosity as they had experienced sufficient thermal cycling to remove the PFA, but insufficient temperature to begin to sinter the ceramic matrix. The porosity of samples in the green state was not tested due to the wax residue from the dewax process. The results are shown in Figure 6.1.

6.3.3 The effect of porosity on mechanical strength

It is well known that ceramic materials exhibit greater strength in compression than in tension due to the presence of defects within their structure. Porosity

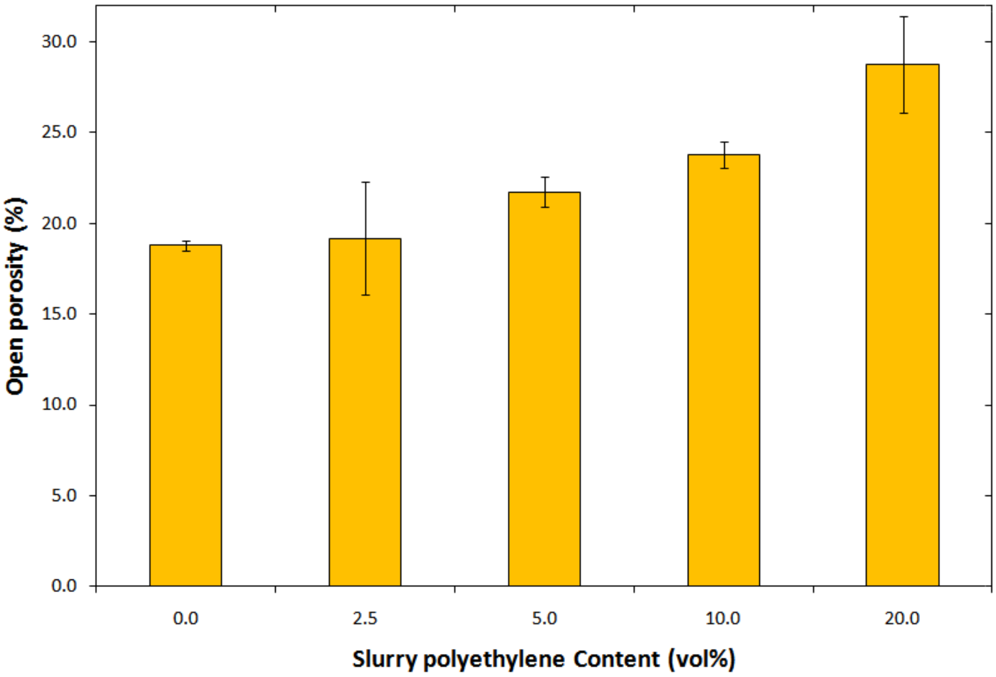

FIGURE 6.1: Measured values for open porosity for shell materials containing polyethylene powder measured by water immersion. All results are average of three measurements on different test pieces. All samples characterised in Fired state.

generated through the inclusion of pore forming agents, in this case PE, will affect the structure in the same way. Figures 6.2 and 6.3 show the results of flexural and compressive testing for fugitive shell materials. Edge strength is also presented in Figure 6.4.

It was observed that mechanical test results of all three types for systems containing 2.5 and 5 vol % PE exhibit little deviation from the system with zero PE content, also common to all testing is the significant decrease in measured strengths at 10 and 20 vol %. Edge specimens containing 20 vol % PE possessed insufficient strength to undergo testing following the pre-fire cycle. It is likely that this is due to the lack of shell material remaining at the shell edge following burn-out of PE particles.

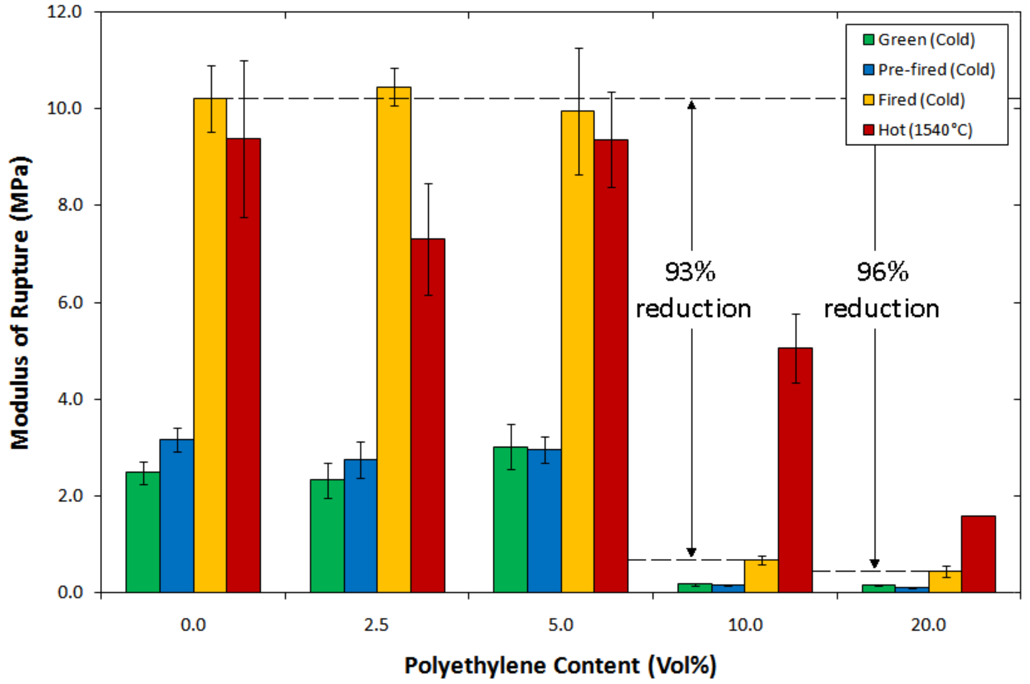

FIGURE 6.2: Flexural strengths for various fugitive shell materials, note the sharp reduction in properties above 5 vol % PE content.

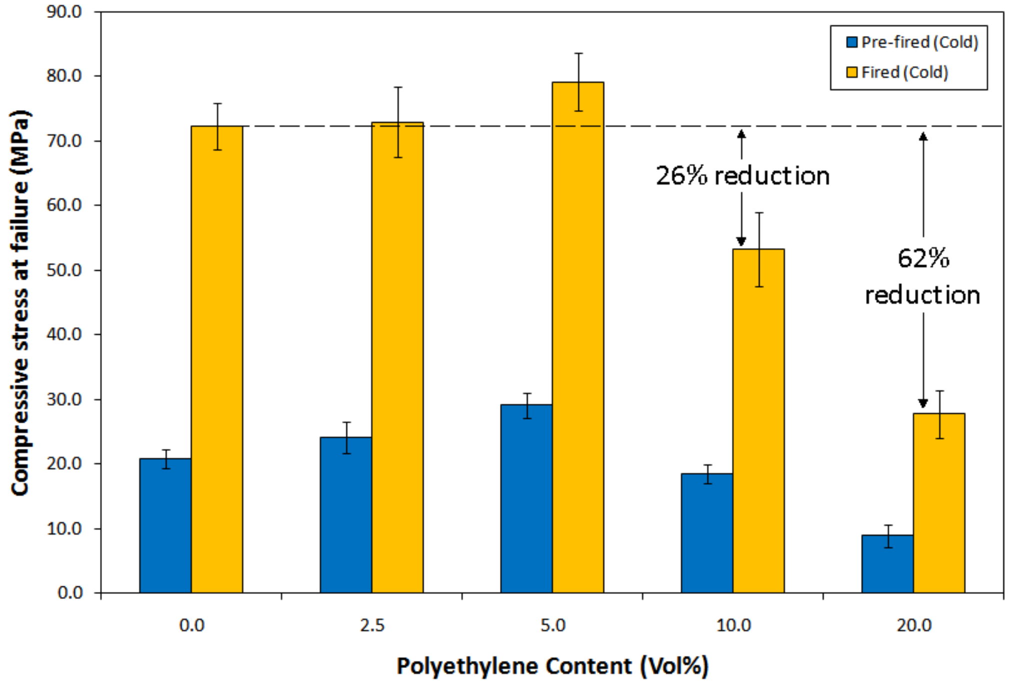

FIGURE 6.3: Compressive stress at failure for shell specimens containing various polyethylene contents.

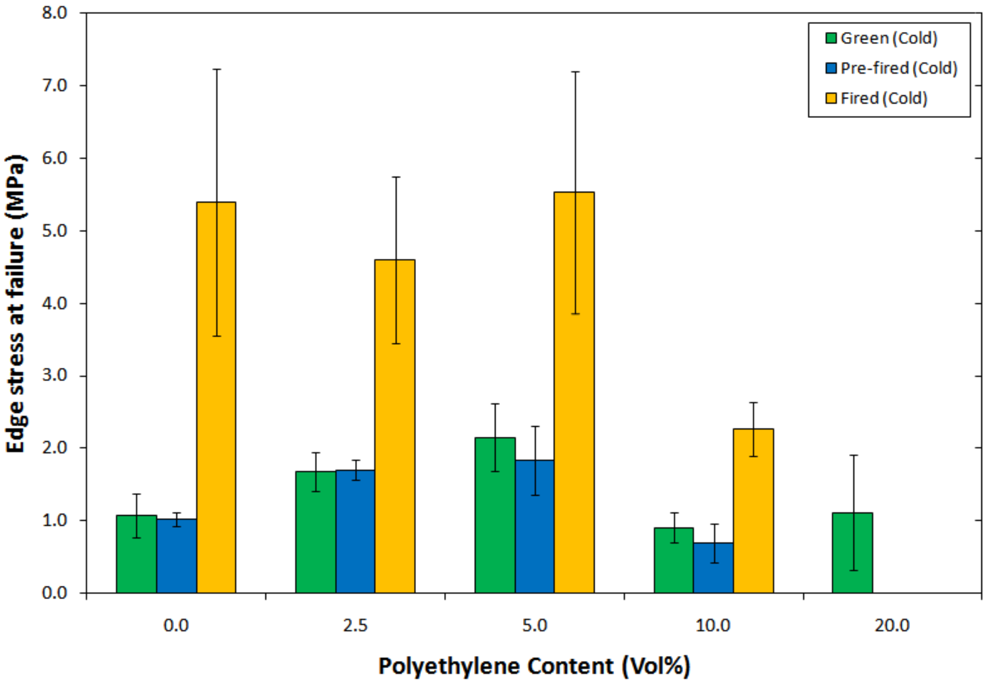

FIGURE 6.4: Stress at failure for edge test specimens of polyethylene containing shell systems.

6.4 Discussion

Compressive testing

The results of compressive testing are shown in Figure 6.3, however it is also pertinent to mention that the predominant failure mechanism exhibited by fugitive test pieces was a barrelling-type in which an annulus around the centre-line of the specimen parted outwards. Also apparent during failure were a number of cracks extending along the sample parallel to the principle stress axis. Unfortunately due to the nature of the test geometry and the shell materials attempts to record these observations photographically were unsuccessful, however they are shown schematically in Figure 6.10.

The observations are consistent with those reported by Sammis [109] that four different failure modes are possible for porous ceramics in compression. Figure

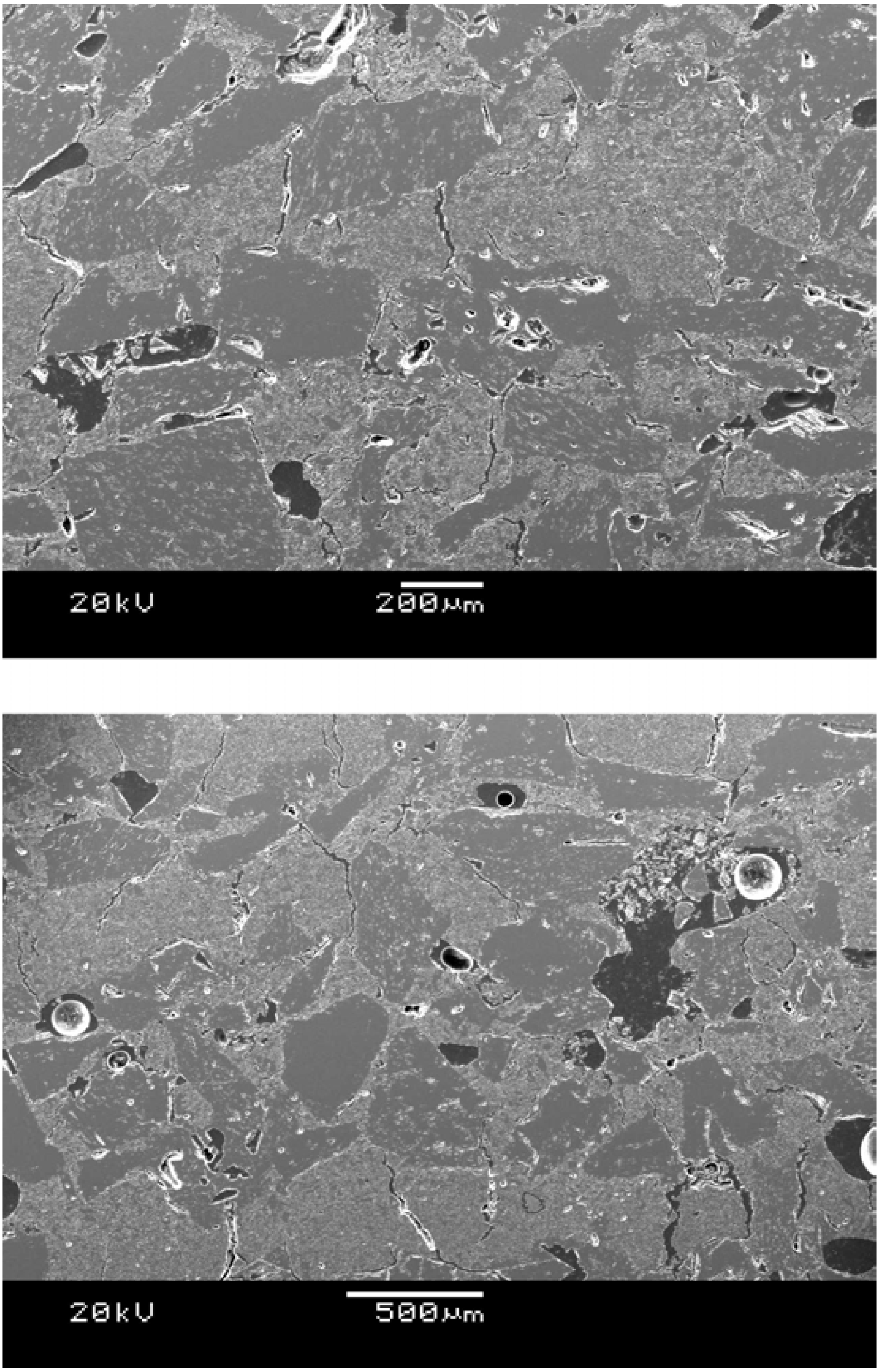

Figure 6.5: SEM micrographs of shell material containing no PFA content. Some porosity still visible in sample inherent to manufacturing technique.

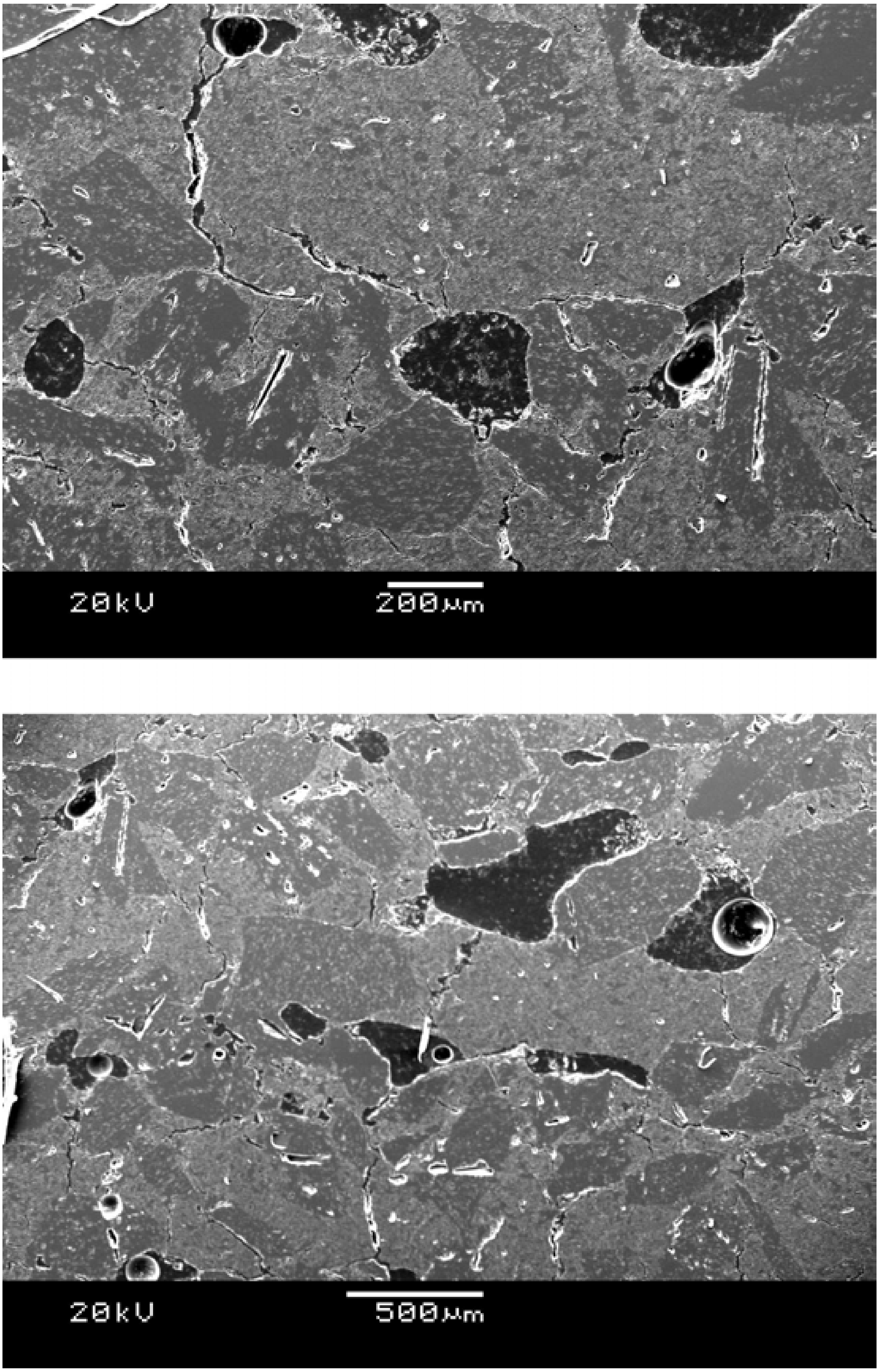

FIGURE 6.6: SEM micrographs of shell material manufactured using 2.5 vol % PFA content slurry. Porosity induced by PFA is not readily apparent at this concentration.

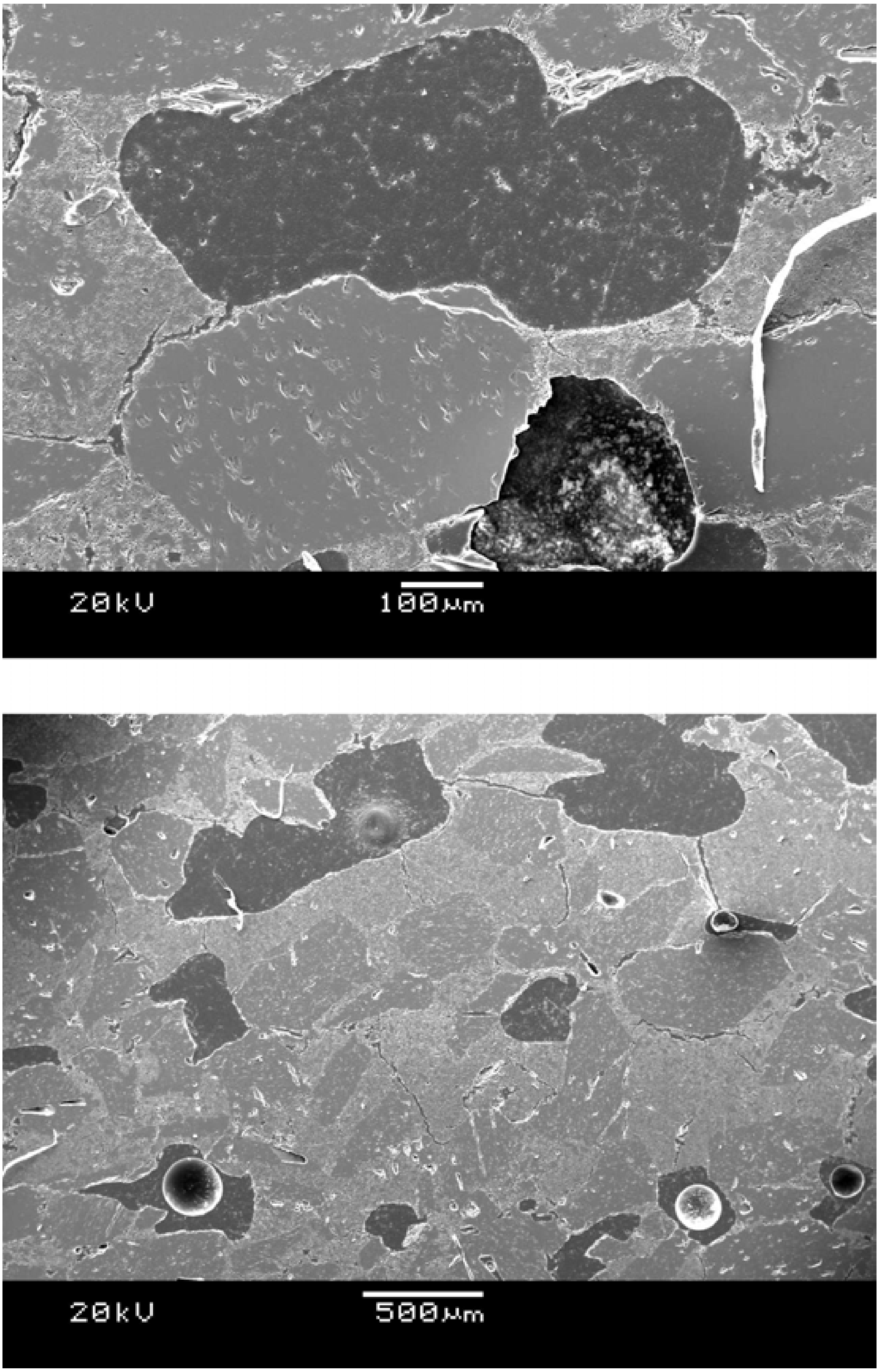

FIGURE 6.7: SEM micrographs of shell material manufactured using 5.0 vol % PFA content slurry. Larger pores were observed at this PFA concentration; cracks leading into pores were also widely observed.

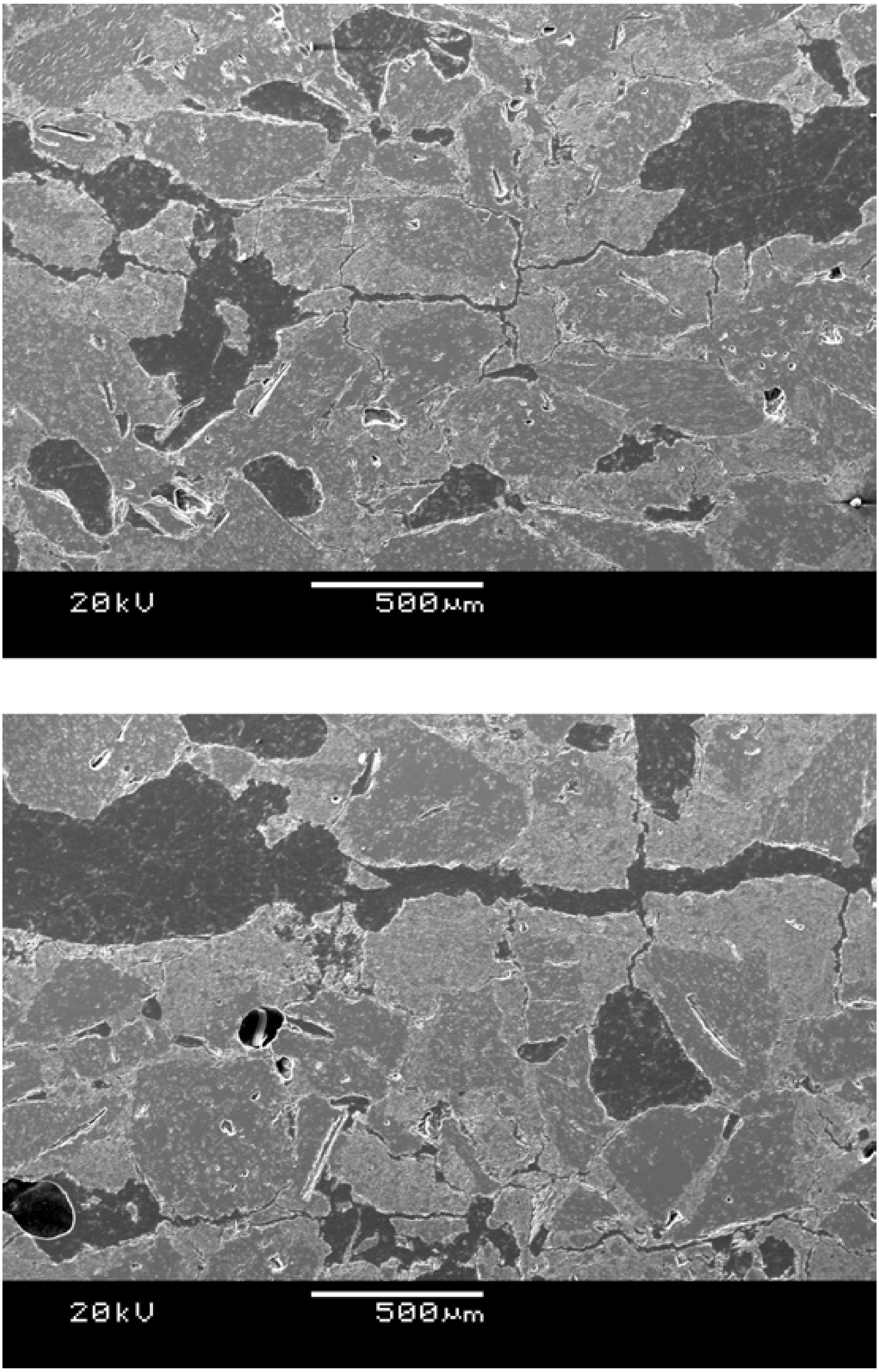

FIGURE 6.8: SEM micrographs of shell material manufactured using 10.0 vol % PFA content slurry. Large pores were observed at this PFA concentration with areas of connected porosity becoming apparent.

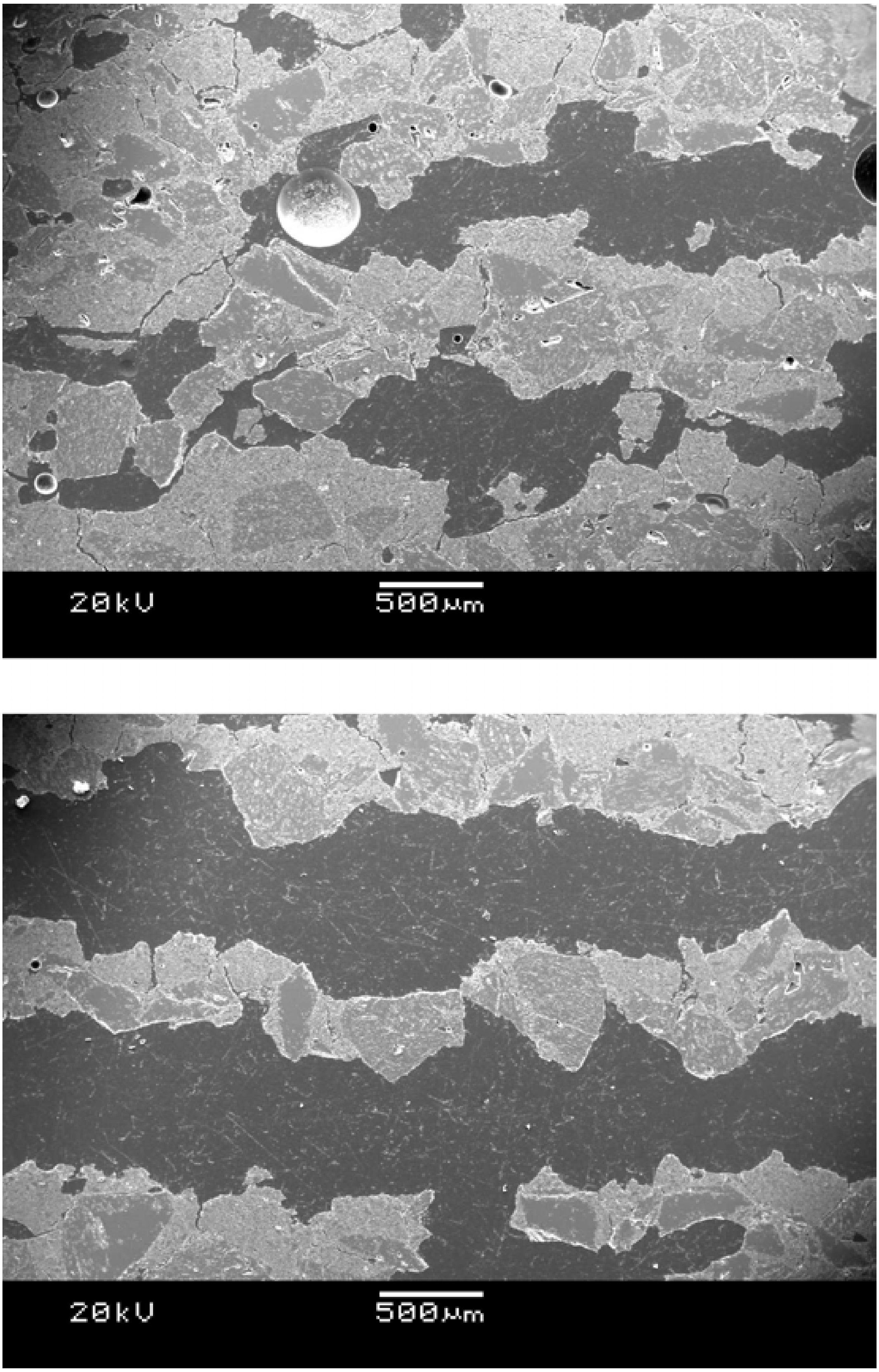

FIGURE 6.9: SEM micrographs of shell material manufactured using 20.0 vol % PFA content slurry. Extensive areas of connected porosity visible at this leve. It is likely that some sample material was lost during grinding and polishing due to low strength at this concentration.

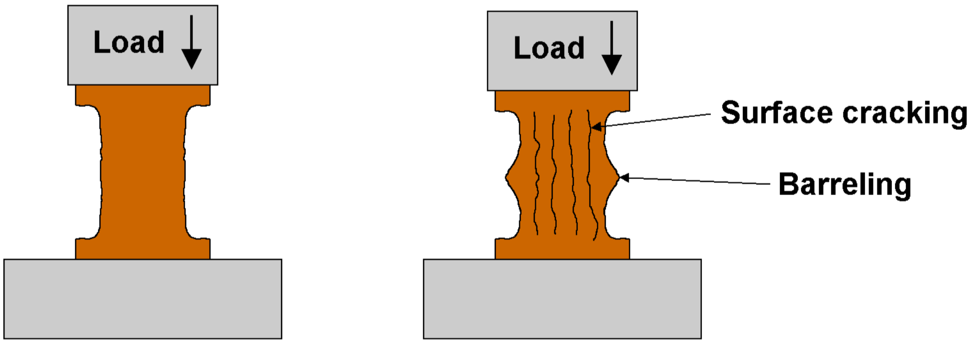

FIGURE 6.10: Schematic representation of observed failure mode for fugitive compression test-pieces.

6.11 shows two of the reported four failure modes which were observed during compressive testing of shell material; fugitive materials exhibited failure mode (a). Under this failure regime it is reported that failure occurs due to microcracks propagating through the length of the sample originating from pores or other defects. As was the case for fugitive shell materials the microcracks are parallel to the applied stress. Failure mode (b) was not observed for fugitive shell materials, but was observed for systems exhibiting greater tensile strengths such as Hi-shell and Std SX. It was proposed by Sammis that in order for failure mode (b) to occur the sample must be constrained from barreling. Although no constraint stress was applied to any sample during testing those materials with greater flexural strength would resist the bending of the surface associated with barreling more greatly than weaker systems. It is likely that this provides sufficient constraint that mode (b) is observed.

Flexural strength

Flexural and edge testing suggested that there was a critical level of porosity below which the measurable strength remains unaffected and above which the mechanical properties become sensitive to the level of PFA content. This is shown

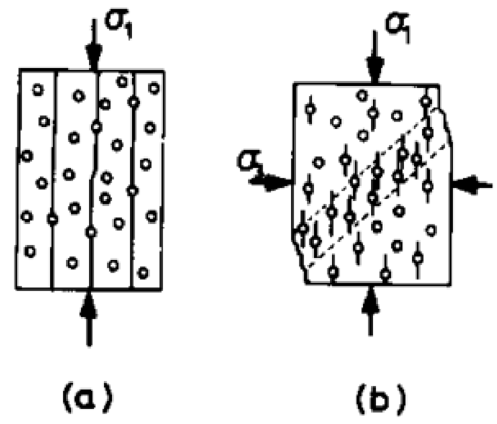

FIGURE 6.11: Possible failure modes for porous ceramics under axial compression and their microstructural origins. Adapted from [109].

in both Figures 6.2 and 6.4; systems containing 0.0, 2.5 and 5.0 vol % PE are indistinguishable from the results of both flexural and compressive testing. The decrease in mechanical properties for systems containing 10 and 20 vol % are however severe, the inclusion of 10 vol % reduces the fired strength by 93.3 % and 20 vol % reduces the strength to 95.6 % compared to the PFA-free system. The explanation for this sensitivity to PFA content can be explained by considering the manner in which stress concentrations are concentrated at pores. In order to simplify the mathematical treatment of the problem pores can be approximated as either spheres or 2-dimensionally as circular holes [110]. It is shown by Green that the stress field due to a circular hole decreases primarily as $\frac{1}{r}$ where r is the distance from a circular hole of radius r_0 such that at a distance three times the radius the stress field is unperturbed by the presence of the hole [110]. If the number of holes within the ceramic is increased the areas in which the applied stress field is concentrated will increase until a critical density is reached whereby the stress field never falls to the applied value, i.e. the distance between pores is less than $3r_0$. Whilst this treatment is somewhat idealised it offers some explanation as to the nature of the relationship between pore density and mechanical properties.

The discrepancy between the reduction in flexural and compressive strengths can be explained by considering the behaviour of ceramic materials. It is understood that strength of a material should be approximately 10 % of the Youngs' modulus, however even for homogeneous ceramics this is not experimentally achievable with actual values being only 1 % [111]. The discrepancy is due to the lack of fracture toughness exhibited by ceramic materials. As mentioned above, pores and other defects act as nucleation sites for the formation of microcracks and cause the material to fail under applied stresses below its predicted strength. In compression toughness is less significant since the propagation of cracks due to the applied stress is either eliminated or reduced to indirect means (through barreling). The observation that flexural strength is more significantly affected than compressive strength for shell materials including high defect populations is in agreement with the accepted theory.

6.5 Conclusions

Whilst the inclusion of PE as a PFA was shown to reduce the mechanical properties of shell materials both in flexure and in compression the effect on the former was far greater. This is unsurprising given the mechanisms at work during each type of testing. Another concern was the sensitivity of flexural strength to PFA concentration, especially as it was only possible to utilise the material as a filler constituent. It is known that the composition of investment casting slurries changes over time and use and the problem is especially germane for systems in which the relative density of constituent materials is so different. It would be undesirable in a production environment to have a shell material which could exhibit such a difference in strength based on the concentration of a constituent which is impractical to measure [112]. For these reasons it was decided that fugitive shell materials did not offer an industrially relevant solution to the reduction of mechanical strength for investment casting shell systems and were not evaluated further.

7

Slurry Stability

7.1 Introduction

Whilst the focus of the preceding chapters has been based on the performance of the shell material as a solid mould, this chapter focuses on the shell material in its liquid form as a slurry. The general role played by the slurry in the investment casting process was mentioned in Section 2.1, in the following sections the slurry is investigated in detail paying particular attention to particle interactions present with the system.

7.2 Instability in Silica-Alumina systems

The shell systems documented in the preceding chapters exclusively feature colloidal silica as the binder material, common also to many of the shell systems is the presence of alumina within the slurry. Understanding the silica - alumina system is therefore important if one is to understand the behaviour exhibited by shell materials based on it. The preceding chapters have focused on the effects of the silica alumina system on the performance of the shell mould, in this section the behaviour of the system is investigated with regards to the performance of the slurry systems from which the moulds are produced.

In section 5.2 the development of shell systems based on variation of the silica alumina content were discussed. The degree of mullitisation within the shell mould is controlled by altering the proportion of reactive alumina within the filler material. In the initial trial variants of these systems the only materials present within the slurry were aqueous colloidal silica binder, reactive alumina powder and mullite powder. The binder used for these trials was Ludox HSA, a commercially available low-sodium binder known for its long-term stability towards aggregation in ceramic slurries. As documented in Section 3.1 trials during stages 1 & 2 were performed in 3 litre slurry tanks with agitation supplied by overhead rotary mixers; in these trials slurries were only retained for a few days. Following the evaluation of a large number of trial systems two were selected to progress to large scale trials. This necessitated mixing slurries in 120 litre rotating tanks, with agitation provided by means of a stationary mixer within the tank.

The explanation for the selection of SiAl 2080 and ZF systems for large scale evaluation is discussed in Chapters 4 & 5. SiAl 2080 is an alumina biased system generated by enriching the slurry beyond the stoichiometric ratio required for mullite formation. The slurry system used for ZF moulds is identical to SiAl 4060, a stoichiometric blend of silica and alumina designed to entirely react both components to form mullite in situ. During the mixing stage of the larger slurries no rheological problems were observed with either formulation, however over a period of approximately 48 hours the rheology of the SiAl 2080 slurry began to behave irregularly developing floating gel-like structures on its surface which can be seen in Figure 7.1.

Figure 7.1: Images of the original Ludox HSA based SiAl2080 slurry, note the significant flocculation on the surface.

The subsequent reformulation of the SiAl 2080 system into what would become the F200 system is documented in Chapter 5.4, this section is concerned with the cause of the instability. In order to gain greater understanding of the mechanisms responsible for the instability three experimental techniques were employed. Zeta potential measurements were used in order to determine the stability of the constituent particles of the slurry in isolation; sedimentation rate and viscosity measurements were employed to determine the stability of various silica alumina systems in combination; the results are discussed further in the following sections.

7.3 Zeta Potential

Suspensions of particles remain stable to aggregation due to charges present on their surface, particles with similar charges of sufficiently high magnitude will repel each other and thus be stable against aggregation. Stability problems can arise when the charge on the particles is insufficiently high or, in systems containing more than one particle type, particles are stabilised by opposite charges. To determine the charge stabilisation characteristics of the various filler materials the zeta potential was measured using the technique described in section 3.1. The machine used in this work was incapable of measuring the zeta potential of multi-phase systems and therefore measurements were performed on the binder and reactive alumina filler powder separately. Ludox HSA binder was diluted to 25 wt % using de-ionised water and PFR15 was mixed into de-ionised water at the same concentration, pH values were altered through additions of hydrochloric acid and potassium hydroxide; Zeta-potential results are presented in Figure 7.2.

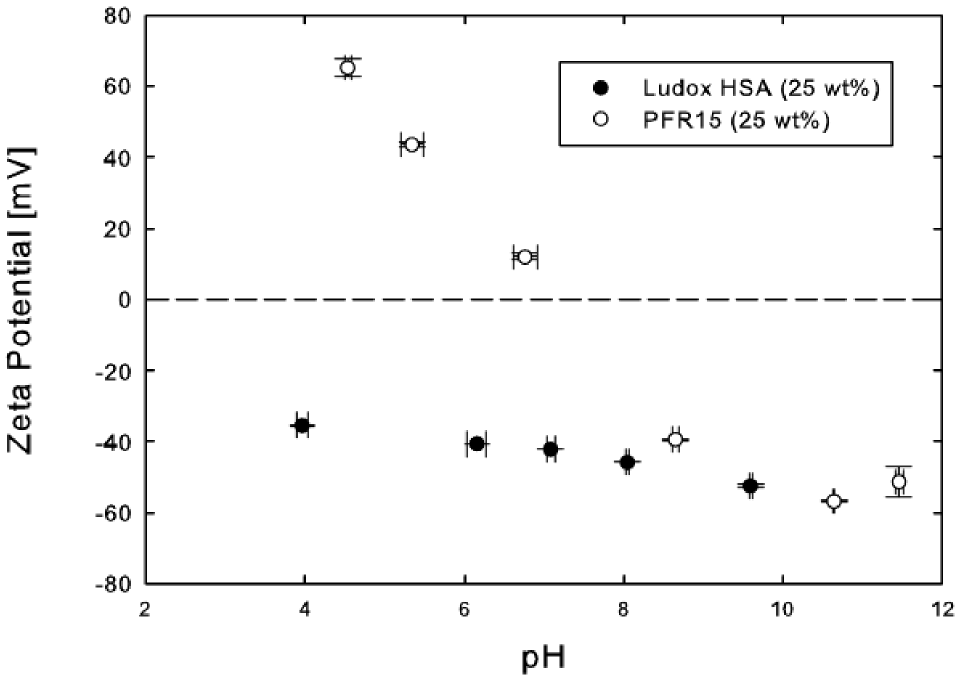

FIGURE 7.2: Zeta-potential values for 25 wt % suspensions of Ludox HSA colloidal silica (black) and PFR15 reactive alumina (white); error bars reflect standard deviation.

Inspection of the results clearly show that at alkaline pH both reactive alumina and HSA particles are stabilised by negative surface charge, this infers stability in a system composed of these particles under alkaline conditions. At acid pH however, alumina particles have gone through their iso-electric point and become stabilised by a positive surface charge. In isolation both systems would be stable at acid pH, however, in combination the resultant system would have reduced stability due to the inter-species attraction caused by opposite surface charges. This effect was observed by Fisher *et al.* whilst attempting to measure the attractive potential between alumina and silica at intermediate pH values [73]. Ludox HSA, unlike so-called sodium stabilised binders, does not rely on the presence of hydroxyl ions to impart a stabilising charge onto its surface. Instead aluminate ions embedded in the surface provide permanent, pH independent, charged sites.

One of the systems proposed to eliminate the instability, the Wex system, replaced the Ludox HSA binder with Wexcoat 0825. Wexcoat is a conventional sodium stabilised binder; in this formulation the filler constituents remained the same as the unstable SiAl 2080 system. The instability inherent in the original system was not observed during this trial; examination of Figure 7.3 offers some explanation for this. Although it is true that the zeta-potential for Wexcoat is lower than that of HSA across all pH values it is pertinent to note that when mixing slurries each component will contribute to the overall pH of the system. SiAl 2080 slurries bound by Ludox HSA operate at near-neutral pH whereas Wexcoat bound slurries operate at alkaline pH. Figures 7.2 and 7.3 clearly show that at pH values relevant to each slurry, particles of different types within HSA bound slurries exhibit opposite surface charge and Wexcoat bound slurries are stabilised by the same charge. Considering these results alone gives an indication as to the cause of the behaviour of each system.

Another system investigated, and ultimately selected, to treat the instability was based on the replacement of a proportion of the reactive alumina content with a larger fused alumina product called WRG IC-200, commonly referred to as F200. In order to preserve mullitisation within the shell material, only the alumina in excess of that needed to react with the silica present in the binder was replaced with F200. The static mixer within a conventional slurry tank provides low-shear

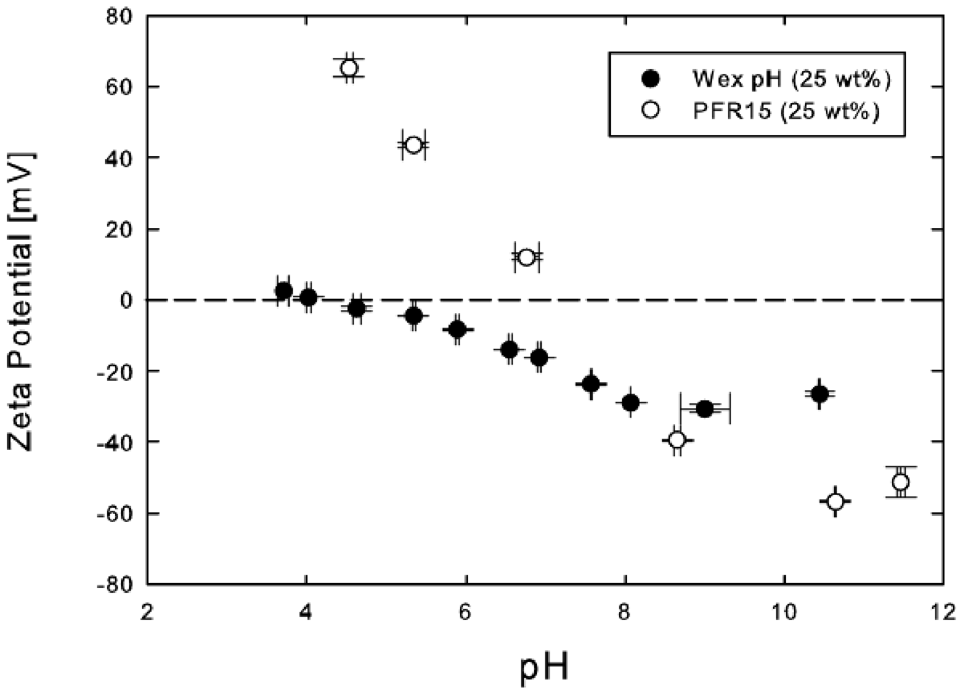

FIGURE 7.3: Zeta-potential values for 25 wt % suspensions of Wexcoat 0825 colloidal silica (black) and PFR15 reactive alumina (white); error bars reflect standard deviation.

mixing, it is likely that the agitation is insufficient to break-down the aggregates which form on the slurry surface. Considering the formation mechanism within the network, as two particles collide due to opposite surface charge they will contact at 3 separate points; this will be the case for all particles independent of their size. In order to form a continuous network it will be necessary for this process to happen many times without disrupting the bonds already present. The forces required to hold a larger particle in such a network will be greater than those for a smaller particle and as such the network will be less likely to form and persist.

Figures 7.4 and 7.5 compare the respective zeta potentials for Ludox HSA and Wexcoat with F200 alumina in deionised water as individual materials. As surface charge is a function of material rather than particle size the same trends are observed for this material as with the reactive alumina, however, since the surface area is reduced the magnitude of the charge was also slightly reduced. The resultant reduction in the attraction between alumina and silica particles at intermediate pH may also have contributed to the increased stability of the revised Ludox HSA bound F200 system.

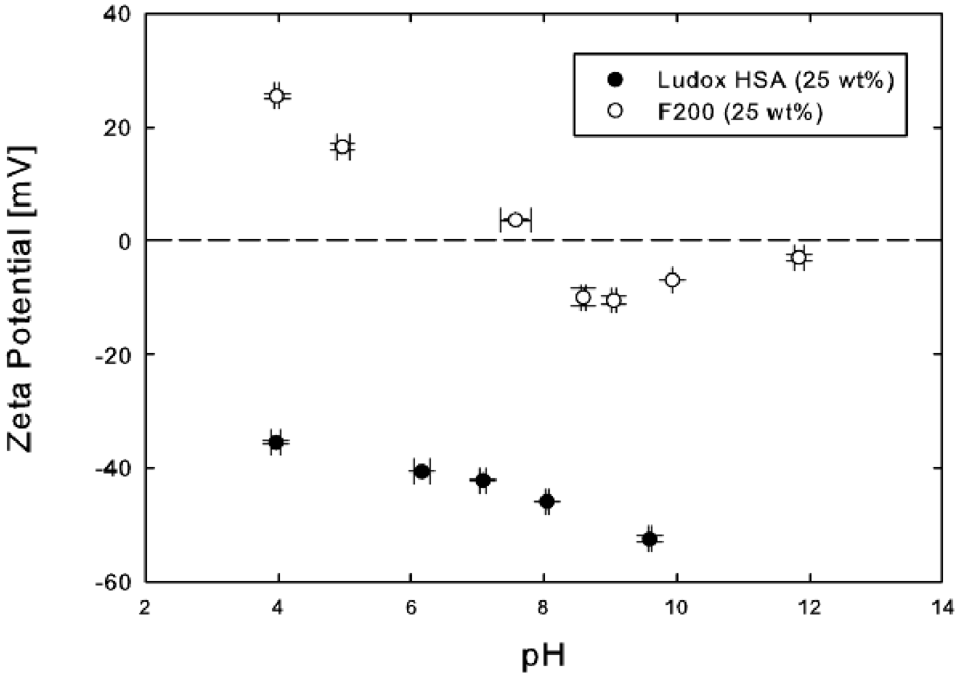

FIGURE 7.4: Zeta-potential values for 25 wt % suspensions of Ludox HSA colloidal silica (black) and F200 fused alumina (white); error bars reflect standard deviation.

Observations of slurry behaviour during the initial mixing and subsequent long-term mixing in the holding tank indicated that the revised, F200 modified SiAl2080 slurry exhibited greater stability than its predecessor. This was evident in the measurements of slurry properties shown in Figures 5.31 to 5.34. In contrast, the poor rheology of the original system prevented the acquisition of meaningful flow-time and plate weight measurements. The precise mechanisms responsible for the change in behaviour between the two systems are not fully understood but several mechanisms have been discussed. Another possible explanation for the increased stability associated with adding F200 is that of surface coating. When one species is much larger than another, as is the case for the F200 and colloidal silica particles, and have opposing surface charges the smaller particles coat the

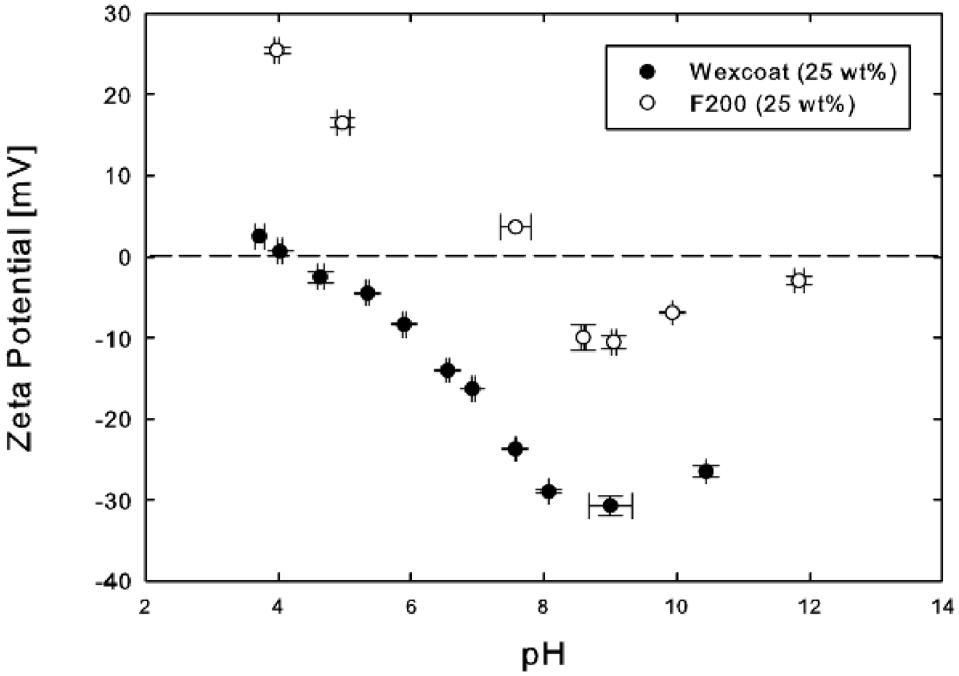

FIGURE 7.5: Zeta-potential values for 25 wt % suspensions of Wexcoat 0825 colloidal silica (black) and F200 fused alumina (white); error bars reflect standard deviation.

surface of the larger one. In the F200 modified SiAl 2080 system the Ludox HSA particles would coat the F200 alumina surface causing it to behave like a larger HSA particle. The effect was observed by Fisher *et al.* on a number of alumina silica systems.

7.4 Flocculation Experiments

Whilst zeta potential measurements provided an indication of the stability of particles in suspension they were unable to indicate the occurrence of flocculation. To do this a series of sedimentation experiments were performed across a range of pH values chosen to encompass relevant changes in surface charge. The systems evaluated reflected those tested in the previous section and are detailed in Table 7.1.

Table 7.1: Dilute slurry formulations used during flocculation experiments

Silica Content			Alumina Content		
Type	Mass (g)	(wt %)	Type	Mass (g)	(wt %)
Ludox HSA	25.0	21.0	PFR15	4.4	15.0
	25.0	21.0	F200	4.4	15.0
Wexcoat	25.0	21.0	PFR15	4.4	15.0
	25.0	21.0	F200	4.4	15.0

The experimental procedure used for the sedimentation experiments was described in section 3.1.9. Results of the sedimentation experiment are presented in Tables 7.2 to 7.5.

Table 7.2: Sedimentation testing results for dilute slurry of Ludox HSA and PFR15 reactive alumina. The symbol * denotes slurries which had gelled at the point of measurement.

Slurry pH		Sediment Height (mm)	
Target	Actual	Initial	48 hours
4.00	3.95	111.3	6.9
6.00	6.09	112.8	112.4*
7.00	7.04	110.3	8.2
8.00	8.06	111.5	12.3
10.00	10.01	112.5	7.2

Table 7.3: Sedimentation testing results for dilute slurry of Ludox HSA and F200 fused alumina.

Slurry pH		Sediment Height (mm)	
Target	Actual	Initial	48 hours
4.00	3.95	111.5	4.4
6.00	5.97	110.1	4.0
7.00	7.02	112.9	5.9
8.00	7.97	111.3	4.5
10.00	9.99	111.3	5.3

As expected, for slurries containing Ludox HSA and PFR15 alumina in combination it was observed that at approximately pH 6 the slurry gelled during the

Table 7.4: Sedimentation testing results for dilute slurry of Wexcoat 0825 and PFR15 reactive alumina. The symbol * denotes slurries which had gelled at the point of measurement.

Slurry pH		Sediment Height (mm)	
Target	Actual	Initial	48 hours
4.00	4.04	111.45	110.5*
6.00	6.09	113.3	109.5*
7.00	7.01	112.0	21.0*
8.00	8.02	112.6	18.3
10.00	10.05	110.9	8.0

Table 7.5: Sedimentation testing results for dilute slurry of Wexcoat 0825 and F200 fused alumina. The symbol * denotes slurries which had gelled at the point of measurement.

Slurry pH		Sediment Height (mm)	
Target	Actual	Initial	48 hours
4.00	4.03	113.4	5.8*
6.00	6.04	113.2	5.8*
7.00	7.00	112.4	5.9*
8.00	8.00	111.9	4.7*
10.00	9.95	112.7	4.7

flocculation trial. This result was consistent with observations of zeta potential (shown in Figure 7.2) that at this pH the silica and alumina particles feature strongly opposite surface charges. It is likely that the gellation of the slurry occurred at this pH due to the attraction between these particles. Considering that the height of the gelled slurry was similar to the original height of the slurry it is also likely that this was a relatively fast process. This behaviour was concurrent with the observation of rapid formation of flocs on the surface of the original SiAL2080 slurry.

Results of the experiment using Ludox HSA in combination with F200 alumina, showed reduced sediment heights across all pH values compared to the results using Ludox HSA in combination with PFR15. It was also noted that no gellation of the slurry occurred at any pH value. The greatest sediment height occurred at pH 7, however, zeta potential measurements of the system presented in Figure 7.4 suggested that the interspecies attraction due to surface charge should be similar at pH values of 6 and 7. The discrepancy in the sediment height cannot therefore be explained by this effect and may be due to natural variation or error in the measurement.

For sedimentation experiments using both PFR15 and F200 alumina powders in combination with the sodium stabilised Wexcoat binder, it was observed that below pH values of 8 & 10 and 10 respectively the slurries gelled. This could be due to the reduction in stability (due to depleted hydroxyl ion concentration) of the sodium stabilised binder at pH values below pH 10; the effect of charge stabilisation was discussed further in section 2.7.2. Inspection of the results shown in Tables 7.4 and 7.5 showed that the heights of the gelled slurries were greater for the PFR15 containing slurries than for those containing F200. As previously mentioned, this implied that the gellation process had occurred more rapidly in slurries containing PFR15.

7.5 Viscosity measurements

The final technique applied to the determination of the stability of various colloidal silica and alumina slurries was the measurement of viscosity using a conventional rotational rheometer. In the preceding sections it has been shown that at intermediate and acidic pH values the surface charge on silica and alumina particles facilitates heterocoagulation. It was also shown that this manifested as gellation of dilute slurries of colloidal silica and alumina powders. In order to determine the manifestation of these effects on the rheology of the slurries, the viscosity of each slurry was determined across the same pH range employed in section 7.4.

Figures 7.6 to 7.9 show the measured values of viscosity versus slurry pH for at three shear rates. It should be noted that due to the sampling frequency of the rheometer there was some variation in the shear rate at which these viscosity measurements were taken; the stated shear rate is the average across all pH values.

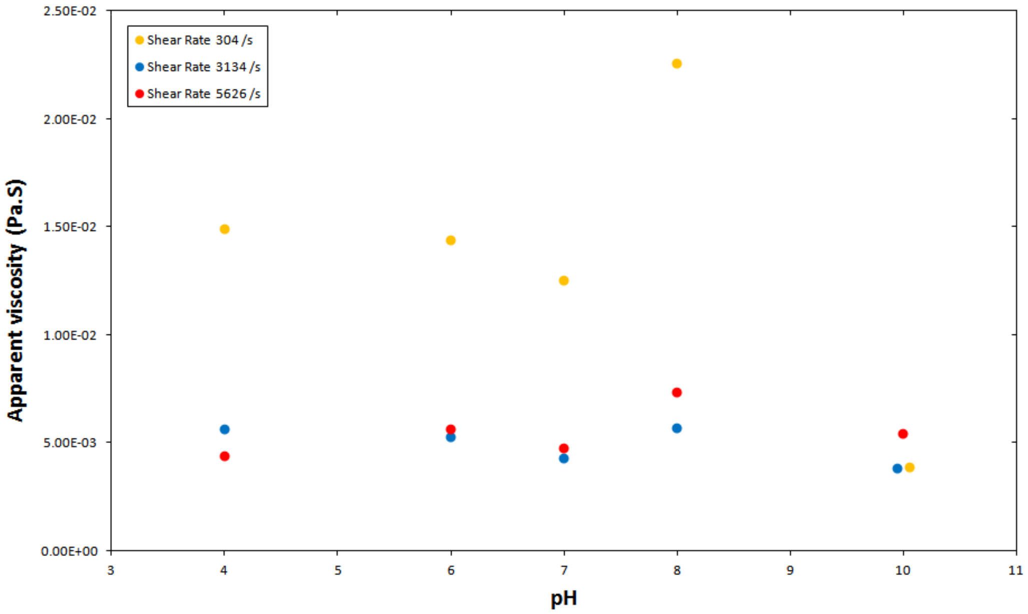

FIGURE 7.6: Viscosity measurements made using a flat plate rheometer for slurries of Ludox HSA and PFR15 at different pH values.

Figures 7.6 and 7.7 show the behaviour of slurries based on Ludox HSA and PFR15 and F200 aluminas respectively. It can be seen that at all shear rates the behaviour of the slurry was similar suggesting minimal shear dependent behaviour in the range tested. It was observed that, with the exception of the PFR15 system at pH 8, the viscosity of both slurries increased with increasing pH. Considering the zeta potential data presented in Figures 7.2 and 7.4 these results are somewhat counter-intuitive. It was expected that at acidic pH where alumina and silica particles exhibit opposite surface charge, the viscosity would be higher than at alkaline pH where both particles are stabilised by negative charge. The relatively low viscosity of the Ludox HSA bound PFR15 slurry at pH 8 was consistent with the stability suggested by observations of zeta potential, however the return to higher viscosity at pH 10 suggested that this result may have been anomalous rather than a genuine reflection of the behaviour of the system.

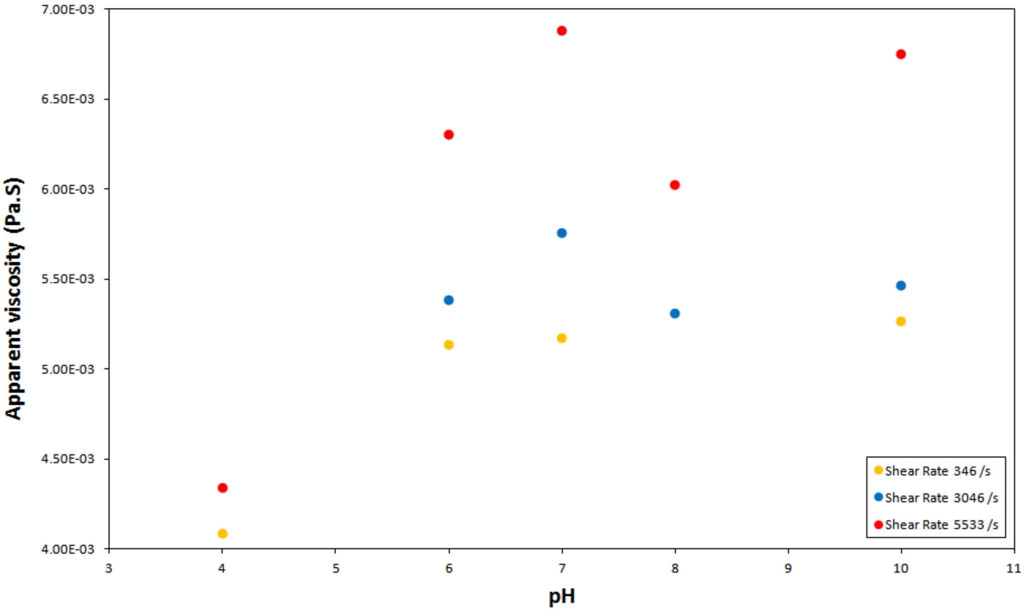

FIGURE 7.7: Viscosity measurements made using a flat plate rheometer for slurries of Ludox HSA and F200 at different pH values.

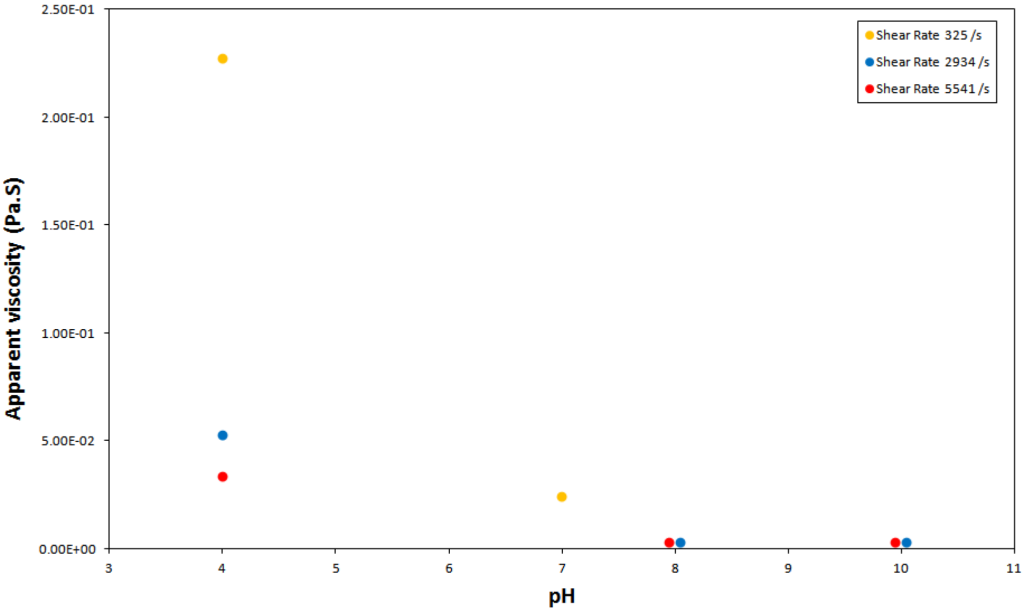

FIGURE 7.8: Viscosity measurements made using a flat plate rheometer for slurries of Wexcoat 0825 and PFR15 at different pH values.

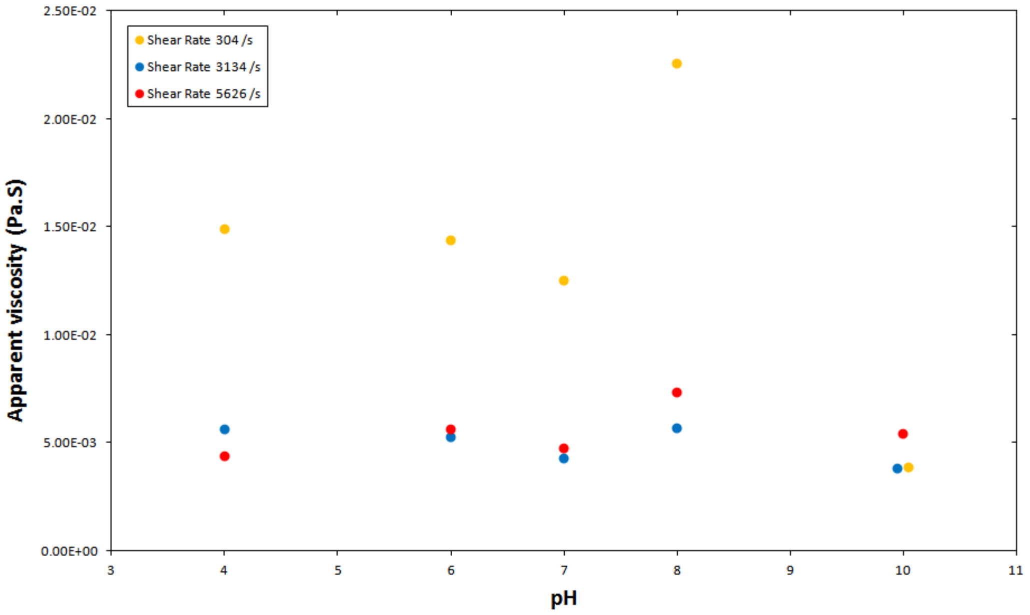

FIGURE 7.9: Viscosity measurements made using a flat plate rheometer for slurries of Wexcoat 0825 and F200 at different pH values.

7.6 Conclusions

The cause of the instability in the original Ludox HSA bound SiAl 2080 slurry was investigated using three experimental techniques. The results of both zeta potential and sedimentation suggested that the poor rheology was due to heterocoagulation between the colloidal silica particles and the PFR15 alumina filler particles. It was also observed that using the Wexcoat binder material the rheology was dramatically improved. It is likely that the instability arose due to the ability of the Ludox HSA slurry to operate across a much broader pH range than conventional sodium stabilised binders. It was possible to operate the slurry at a pH which caused the alumina particles to reverse their surface charge. With the conventional Wexcoat binder, both species were stabilised by the same charge, and subsequently no rheological problems were observed.

The results of the rheological testing disagreed with observations made using both other techniques and also those made on the ceramic slurries directly. It is possible that the settling nature of the slurries had an effect on the measurement, and that this effect either masked or altered the effect of the surface charge.

8

Conclusions and Future Work

8.1 Conclusions

An investigation into the performance of ceramic shell mould materials for the investment casting process was performed. The standard mould materials used by Rolls-Royce for single-crystal (SX) casting were characterised using a number of techniques in order to form a baseline against which candidate shell materials could be compared. An attempt was made to establish a link between these properties and the occurrence of recrystallisation during the investment casting process.

Based on casting observations and the mechanical properties of shell materials (as determined by flexural and compressive testing) it was believed that the RX performance was linked to a combination of high-temperature strength and the strength of shell materials following the casting cycle. It was also believed that the high-temperature creep behaviour had an effect on the formation of RX. Unfortunately due to equipment limitations it was not possible to determine the high-temperature creep behaviour of shell specimens in compression; it is likely that such measurements would have provided the most accurate basis for the prediction of RX. The results of casting trials suggested that from the data available, results of fired and high temperature strength provided the most reliable indication of the propensity to cause RX.

It was shown in Chapter 4 that the inclusion of unstabilised zirconia within the shell in the form of stucco particles was able to reduce the strength of shell specimens tested both flexurally and in compression. It was proven that there is a correlation between the concentration of stucco particles within the shell and the reduction in fired strength. The fact that the strengths of specimens tested in other states, namely green and in the pre-fired condition were similar to materials made with the same matrix but featuring mullite stucco, further supported the conclusion that it was the occurrence of the volumetric transition which led to the reduction in strength. The dimensional changes observed during thermal cycling proved the occurrence of the phase transition within the shell specimens. Cracking observed in the structures of the specimens in the Fired states further supported the conclusion that the volumetrically induced cracking was responsible for the reduction in strength. High-temperature strength measurements showed that the difference between mullite and zirconia stuccoed specimens was not significant. This suggested that the damage induced in the specimens during the contraction associated with the forward phase transition was either inherently less damaging or that during sintering at high temperature it was possible for the specimens to recover from the damage.

The mechanical strengths of shell materials based on the silica and alumina matrix were shown to be highly dependent on the relative proportions of silica and alumina within the formulation. This was particularly evident for flexural strength testing in 3-point bend, but was also supported through observations made on compressive test specimens. As with unstabilised zirconia stuccoed shell materials, thermal expansion measurements were made on the samples in order to investigate the behaviour of the microstructure during thermal cycling. As with mechanical strength, there was a clear relationship between the relative amounts of silica and alumina within the formulation and the sintering behaviour of the resultant ceramic. As expected, and consistent with observation within the literature on similar ceramics, those formulations high in silica exhibited severe contraction during high-temperature sintering. Formulations containing fine alumina powder also exhibited unusual sintering behaviour compared to their counterparts. It was shown that alteration of the amount of fine alumina could change the sintering behaviour during the high temperature sintering phase. Whilst these results were similar to those reported in the literature for conventional ceramics, no reference to such materials within the investment casting industry could be found. It can be concluded that shell materials rich in silica exhibited significantly reduced high temperature strength and creep resistance. It can also be concluded that formulations rich in fine alumina powder exhibited reduced Fired strength due to the presence of sintering cracks within the structure.

The incorporation of polyethylene (PE) particles as a Pore Forming Agent (PFA) within the shell matrix was shown to be an effective method of reducing both the flexural and compressive strength of shell specimens. Inspection of the results showed the presence of a threshold concentration corresponding to approximately 5 to 10 vol% PE content within the slurry. Below this the strength of both compressive and flexural specimens appeared unchanged from the PE free material;

at 10 and 20 vol% however the flexural strength was shown to decrease rapidly by 93.3 % and 95.6 % respectively. The occurrence of this reduction was linked to the presence of pores within the matrix acting as sites for stress concentration within the matrix; it was also noted that the strength reduction effect on compressive strength was markedly lower than for flexural strength with average values of 26 % and 62 % for 10 and 20 vol% PE respectively. It is likely that the different failure mechanisms associated with each test method are responsible for the discrepancy.

The experiments performed during the course of this work provide a useful basis for continued research into the performance of investment casting shell materials and also present a number of usable shell materials with very different material properties.

8.2 Future work

The conclusions of this thesis are restricted to the performance of the shell materials themselves; whilst these are of scientific interest the overall aim of the project was to develop a reduced RX system and one which was capable on Large-Chill furnace architecture. Future work on this project should be focussed on investigating the link between shell properties and RX behaviour through the performance of extensive casting trials. The samples sizes should be chosen to be of sufficient size to produce statistically significant results. Casting trials were also performed only using small bore furnace technology; in order to fulfil the initial project aim future work should be centred around the use of large chill furnaces for casting trials.

Another area in which further work could be performed is in the development of a method for testing the compressive strength and creep characteristics at high temperature. It is likely that the results of this testing would provide a closer representation to the behaviour of the shell material during the casting cycle.

The future work can be broken down into two categories, the first being the work necessary for development of a commercially viable shell materials. The work is summarised as follows:

- Investigation of the relationship between shell properties and RX behaviour.
- All casting trials performed on large chill furnaces
- Development of a test method capable of detemining compressive strength at 1540 °C
- Development of a test method capable of measuring compressive creep at 1540 °C
- Sufficiently large sample sizes to ensure statistical significance of casting trial results

From a more broadly scientific basis, future work could be focused on the following aspects:

It was observed that in all cases sodium stabilised binders produce shell materials with significantly higher levels of green and fired strength, the mechanisms responsible for this are not understood and no explanation was found in the literature nor during surveys of commercial intelligence. One of the main aspects of future work should be focused on understanding these mechanisms.

The possible mechanisms responsible for the destabilisation of the silica alumina slurry systems were discussed in chapter 7. In order to more conclusively determine the effect further work should be performed to understand the difference in behaviour (within the slurry environment) of reactive and fused aluminas when in used in conjunction with various colloidal silicas.

References

[1] P. Taylor, "An illustrated history of lost wax casting," in *Proc. Seventeenth Annual BICTA Conference*, 1983.

[2] E. Kotzin, *Metalcasting & Molding Processes.* American Foundrymen's Society Des Plaines, Ill, 1981.

[3] S. Jones, *Improved sol based ceramic moulds for use in investment casting.* PhD thesis, The University of Birmingham, 1993.

[4] S. Jones, M. Jolly, S. Blackburn, J. Gebelin, A. Cendrowicz, and K. Lewis, "Measurement of autoclave thermal profiles during high pressure steam dewaxing of investment shells Part 2-Wax body profiles," *Materials Science and Technology*, vol. 20, pp. 617–622, 2004.

[5] G. Arruebarrena, I. Hurtado, J. Vainola, C. Cingi, S. Devenyi, J. Townsend, S. Mahmood, A. Wendt, K. Weiss, and A. Ben-Dov, "Development of Investment-Casting Process of Mg-Alloys for Aerospace Applications," *Advanced Engineering Materials*, vol. 9, p. 751, 2007.

[6] F. VerSnyder and M. Shank, "The Development of Columnar Grain and Single Crystal High Temperature Materials Through Directional Solidification," *Materials Science and Engineering*, vol. 6, pp. 213–247, 1970.

[7] G. Fuchs, "Solution heat treatment response of a third generation single crystal ni-base superalloy," *Materials Science and Engineering: A*, vol. 300, no. 1, pp. 52–60, 2001.

[8] R. Reed, *The Superalloys: Fundamentals and Applications.* Cambridge, 2006.

[9] D. Cox, B. Roebuck, C. Rae, and R. Reed, "Recrystallisation of single crystal superalloy CMSX-4," *Materials Science and Technology*, vol. 19, pp. 440–446, 2003.

[10] S. Welch, 2010. (private communication).

[11] H. Schneider, J. Schreuer, and B. Hildmann, "Structure and properties of mullite – a review," *Journal of the European Ceramic Society*, vol. 28, no. 2, pp. 329–344, 2008.

[12] R. Torrecillas, J. Calderon, J. Moya, M. Reece, C. Davies, C. Olagnon, and G. Fantozzi, "Suitability of mullite for high temperature applications," *Journal of the European Ceramic Society*, vol. 19, no. 13-14, pp. 2519–2527, 1999.

[13] R. Penty and D. Hasselman, "Creep kinetics of high-purity, ultra-fine grain polycrystalline mullite," *Materials Research Bulletin*, vol. 7, pp. 1117–1123, 1972.

[14] P. A. Creasey, 2010. Private Communication.

[15] J. Bailey, "The monoclinic-tetragonal transformation and associated twinning in thin films of zirconia," *Proceedings of the Royal Society of London. Series A, Mathematical and Physical Sciences*, vol. 279, pp. 395–412, 1964.

[16] L. Lenz and A. Heuer, "Stress induced transformation during subcritical crack growth in partially stabilized zirconia," *Journal of the American Ceramic Society*, vol. 65, pp. C–192 – C–194, 1982.

[17] R. Stevens, *An Introduction to Zirconia.* Magnesium Elektron Ltd., 1986.

[18] R. Patil and E. Subbarao, “Monoclinic-tetragonal phase transition in zirconia: Mechanism, pretransformation and coexistence,” *Acta Crystallographica Section A: Crystal Physics, Diffraction, Theoretical and General Crystallography*, vol. 26, pp. 535–542, 1970.

[19] E. Subbarao, H. Maiti, and K. Srivastava, “Martensitic transformation in zirconia,” *Physica Status Solidi (a)*, vol. 21, pp. 9–40, 1974.

[20] A. Dietzel and H. Tober, “Ber. deut. keram,” *Ges*, vol. 30, p. 71, 1953.

[21] C. Curtis, L. Doney, and J. Johnson, “Some properties of hafnium oxide, hafnium silicate, calcium hafnate, and hafnium carbide,” *Journal of the American Ceramic Society*, vol. 37, pp. 458–465, 1954.

[22] F. Mumpton and R. Roy, “Low-Temperature Equilibria Among ZrO_2, ThO_2, and UO_2,” *Journal of the American Ceramic Society*, vol. 43, pp. 234–240, 1960.

[23] I. Hinz and A. Dietzel, “The Phase Inversion of Various ZrO_2 Samples,” *Ber. Deut. Keram. Ges.*, vol. 39, 1962.

[24] W. Baun, “Phase transformation at high temperatures in hafnia and zirconia,” *Science*, vol. 140, p. 1330, 1963.

[25] G. Wolten, “Diffusionless phase transformations in zirconia and hafnia,” *Journal of the American Ceramic Society*, vol. 46, pp. 418–422, 1963.

[26] L. Fehrenbacher and L. Jacobsen, “Metallographic observation of the monoclinic- tetragonal phase transformation in ZrO_2 (Monoclinic-tetragonal phase transformation of zirconium dioxide examined by vacuum hot stage microscope fulfills criteria of diffusionless martensitic reaction),” *J. Am. Ceram. Soc*, vol. 48, pp. 157–161, 1965.

[27] R. Vest and N. Tallan, “Electrical properties and defect structure of zirconia: II, tetragonal phase and inversion,” *Journal of the American Ceramic Society*, vol. 48, pp. 472–475, 1965.

[28] V. Glushkova and E. Koehler, “X-ray and spectrographic investigations of phase transitions in refractory oxides (ZrO_2 and rare-earth oxides),” *Materials Research Bulletin*, vol. 2, pp. 503–513, 1967.

[29] R. Ruh, H. Garrett, R. Domagala, and N. Tallan, “The System Zirconia-Hafnia,” *Journal of the American Ceramic Society*, vol. 51, pp. 23–28, 1968.

[30] R. Patil and E. Subbarao, “Axial thermal expansion of ZrO_2 and HfO_2 in the range room temperature to 1400 Celsius,” *Journal of Applied Crystallography*, vol. 2, no. 6, pp. 281–288, 1969.

[31] H. Maiti, K. Gokhale, and E. Subbarao, “Kinetics and burst phenomenon in ZrO_2 transformation,” *Journal of the American Ceramic Society*, vol. 55, pp. 317–322, 1972.

[32] S. Park, B. Saruhan, and H. Schneider, “Mullite/zirconia laminate composites for high temperature application,” *Journal of the European Ceramic Society*, vol. 20, pp. 2463–2468, 2000.

[33] J. Hart and A. Chaklader, “Superplasticity in pure ZrO_2,” *Materials Research Bulletin*, vol. 2, pp. 521–526, 1967.

[34] F. J. Parker and R. W. Rice, “Correlation between grain size and thermal expansion for aluminium titanate materials,” *Journal of the American ceramic society*, vol. 72, pp. 2364–2366, 1989.

[35] Y. Ohya, Z. E. Nakagawa, and K. Hamano, “Crack healing and bending strength of aluminium titanate ceramics at high temperature,” *Journal of the American Ceramic Society*, vol. 71, pp. C232 – C233, 1988.

[36] X. Cao, R. Vassen, and D. Stoever, "Ceramic materials for thermal barrier coatings," *Journal of the European Ceramic Society*, vol. 24, no. 1, pp. 1–10, 2004.

[37] R. Garvie, "Zirconium Dioxide and some of its binary systems.," tech. rep., Corning Glass Works, NY, 1970.

[38] K. Lee, R. Miller, and N. Jacobson, "New Generation of Plasma-Sprayed Mullite Coatings on Silicon Carbide," *Journal of the American Ceramic Society*, vol. 78, pp. 705–710, 1995.

[39] T. Liu and D. Perera, "Long-term thermal stability and mechanical properties of aluminium titanate at 1000–1200 C," *Journal of Materials Science*, vol. 33, pp. 995–1001, 1998.

[40] C. Yuan, "Private Communication," 2011.

[41] M. Springgate, D. Nikolas, D. Sturgis, and M. Yaserbi, "Investment casting brittle, reactive materials," 2000. US Patent 6,024,163.

[42] J. Snow, R. Frost, and D. Sturgis, "Fused silica as a high temperature shell material," 1982.

[43] C. Chen, K. Takita, S. Honda, and H. Awaji, "Fracture behavior of cylindrical porous alumina with pore gradient," *Journal of the European Ceramic Society*, vol. 25, no. 4, pp. 385–391, 2005.

[44] S. Ding, S. Zhu, Y. Zeng, and D. Jiang, "Fabrication of mullite-bonded porous silicon carbide ceramics by in situ reaction bonding," *Journal of the European Ceramic Society*, vol. 27, no. 4, pp. 2095–2102, 2007.

[45] E. Gregorová and W. Pabst, "Porous ceramics prepared using poppy seed as a pore-forming agent," *Ceramics International*, vol. 33, pp. 1385–1388, 2007.

[46] E. Gregorová, W. Pabst, and I. Bohačenko, "Characterization of different starch types for their application in ceramic processing," *Journal of the European Ceramic Society*, vol. 26, pp. 1301–1309, 2006.

[47] Z. Živcová, E. Gregorová, and W. Pabst, "Porous alumina ceramics produced with lycopodium spores as pore-forming agents," *Journal of Materials Science*, vol. 42, no. 20, pp. 8760–8764, 2007.

[48] E. Gregorová and W. Pabst, "Porosity and pore size control in starch consolidation casting of oxide ceramics," *Journal of the European Ceramic Society*, pp. 669–672, 2007.

[49] M. T. Kush, 2008. (private communication).

[50] W. Kaminsky and C. Eger, "Pyrolysis of filled PMMA for monomer recovery," *Journal of Analytical and Applied Pyrolysis*, vol. 58, pp. 781–787, 2001.

[51] K. Voorhees, S. Baugh, and D. Stevenson, "The thermal degradation of poly (ethylene glycol)/poly (vinyl alcohol) binder in alumina ceramics," *Thermochimica Acta*, vol. 274, pp. 187–207, 1996.

[52] P. Bhandare, B. Lee, and K. Krishnan, "Study of pyrolysis and incineration of disposable plastics using combined TG/FT-IR technique," *Journal of Thermal Analysis and Calorimetry*, vol. 49, pp. 361–366, 1997.

[53] I. McNeill and L. Memetea, "Pyrolysis products of poly (vinyl chloride), dioctyl phthalate and their mixture," *Polymer Degradation and Stability(UK)*, vol. 43, no. 1, pp. 9–25, 1994.

[54] I. McNeill, L. Memetea, and W. Cole, "A study of the products of PVC thermal degradation," *Polymer degradation and stability*, vol. 49, no. 1, pp. 181–191, 1995.

[55] H. Arito and R. Soda, "Pyrolysis products of polytetrafluoroethylene and polyfluoroethylenepropylene with reference to inhalation toxicity," *Annals of Occupational Hygiene*, vol. 20, no. 3, pp. 247–255, 1977.

[56] P. Aimone, B. Kilinski, and K. Ramthun, "Complaint investment casting mold and method," 1994. US Patent 5,297,615.

[57] C. Watts, "Investment casting method and stucco therefore," 1987. US Patent 4,689,081.

[58] X. Yang and B. Mueller, "Reinforced Shell Mold and Method," 2003. US Patent App. 20,040/134,634.

[59] P. Johnson and E. Lassow, "Ceramic shell mold for investment casting and method of making the same," 1990. US Patent 4,966,225.

[60] S. Leyland and I. Smith, "Implementation of a water based shell mould investment casting process," in *9th World Conference on Investment Casting*, 1996.

[61] F. Ullmann, *Ullmann's Encyclopedia of Industrial Chemistry*, ch. Silica, pp. 36–51. Wiley-VCH, 2003.

[62] P. Bird, "Colloidal solutions of inorganic oxides," 1941. US Patent 2,244,325.

[63] H. Bergna and W. Roberts, *Colloidal Silica Fundamentals and Applications.* CRC Press, 2005.

[64] G. Alexander and R. Iler, "Process for modifying the properties of a silica sol and product thereof," 1959. US Patent 2,892,797.

[65] R. Iler, *The chemistry of silica.* Wiley New York, 1979.

[66] P. Withey, 2011. (private communication).

[67] S. Irwin, "Prime coat binder rationalisation - the introduction of Ludox HSA," 2009. (private communication).

[68] M. Elimelech, *Particle Deposition & Aggregation: Measurement, Modelling and Simulation.* Butterworth-Heineman, 1998.

[69] D. Everett, *Basic Principles of Colloid Science.* The Royal Society of Chemistry, 1988.

[70] P. Debye, "A method for the determination of the mass of electrolytic ions," *Journal of Chemical Physics*, vol. 1, pp. 13–16, 1933.

[71] R. Greenwood, "Review of the measurement of zeta potentials in concentrated aqueous suspensions using electroacoustics," *Advances in Colloid and Interface Science*, vol. 106, no. 1-3, pp. 55–81, 2003.

[72] R. O'Brien, "Electro-acoustic effects in a dilute suspension of spherical particles," *Journal of Fluid Mechanics*, vol. 190, pp. 71–86, 1988.

[73] M. Fisher, M. Colic, M. Rao, and F. Lange, "Effect of silica nanoparticle size on the stability of alumina/silica suspensions," *Journal of the American Ceramic Society*, vol. 84, no. 4, pp. 713–718, 2001.

[74] I. Larson, C. Drummond, D. Chan, and F. Grieser, "Direct Force Measurements between Silica and Alumina," vol. 13, pp. 2109–2112, 1997.

[75] P. Yates, G. Franks, S. Biggs, and G. Jameson, "Heteroaggregation with nanoparticles: effect of particle size ratio on optimum particle dose," *Colloids and Surfaces A: Physicochemical and Engineering Aspects*, vol. 255, no. 1-3, pp. 85–90, 2005.

[76] P. Bruinsma, Y. Wang, X. Li, J. Liu, P. Smith, and B. Bunker, "Rheological and solid-liquid separation properties of bimodal suspensions of colloidal

gibbsite and boehmite," *Journal of Colloid and Interface Science*, vol. 192, no. 1, pp. 16–25, 1997.

[77] L. Aksay and J. Pask, "Stable and metastable phase equilibria in the system Al_2O_3 - SiO_2," *Journal American Ceramic Society*, vol. 58, pp. 507–512, 1975.

[78] N. Louet, M. Gonon, and G. Fantozzi, "Influence of the amount of Na_2O and SiO_2 on the sintering behavior and on the microstructural evolution of a Bayer alumina powder," *Ceramics International*, vol. 31, no. 7, pp. 981–987, 2005.

[79] Rolls-Royce, "pcf technical instruction - preparation of slurry," tech. rep.

[80] J. Lavelle, "NAPIM studies show Zahn is least accurate efflux cup," *Flexo*, June 1988.

[81] "Paints and varnishes. determination of flow time by use of flow cups."

[82] R. Krechetnikov and G. Homsy, "Experimental study of substrate roughness and surfactant effects on the Landau-Levich law," *Physics of Fluids*, vol. 17, pp. 102–108, 2005.

[83] N. Dowling, *Mechanical Behaviour of Materials*. Prentice Hall, second ed., 1999.

[84] *Particle Size Measurements: Fundamentals, Practice, Quality*, ch. 8: Sieves and Sieving. Springer, 2009.

[85] R. Lewis, *Hawleys condensed chemical dictionary 15th edn.* 2007.

[86] G. Samsonov, "The oxide handbook," *New York*, 1973.

[87] G. Brunauer, F. Frey, H. Boysen, and H. Schneider, "High temperature thermal expansion of mullite: an in situ neutron diffraction study up to

1600 Celsius," *Journal of the European Ceramic Society*, vol. 21, no. 14, pp. 2563–2567, 2001.

[88] N. Mesrati, H. Ajhrourh, N. Du, and D. Treheux, "Thermal spraying and adhesion of oxides onto graphite," *Journal of Thermal Spray Technology*, vol. 9, pp. 95–99, 2000.

[89] D. Ford, 2009. (private communication).

[90] J. Adams, H. Nakamura, R. Ingel, and R. Rice, "Thermal expansion behavior of single-crystal zirconia," *Journal of the American Ceramic Society*, vol. 68, no. 9, pp. C–228, 1985.

[91] M. Pontin, M. Rao, A. Sánchez-Herencia, and F. Lange, "Laminar ceramics utilizing the zirconia tetragonal-to-monoclinic phase transformation to obtain a threshold strength," *Journal of the American Ceramic Society*, vol. 85, no. 12, pp. 3041–3048, 2002.

[92] C. Aita, M. Wiggins, R. Whig, C. Scanlan, and M. Gajdardziska-Josifovska, "Thermodynamics of tetragonal zirconia formation in a nanolaminate film," *Journal of Applied Physics*, vol. 79, no. 2, pp. 1176–1178, 1996.

[93] J. Chevalier, L. Gremillard, A. Virkar, and D. Clarke, "The tetragonal-monoclinic transformation in zirconia: Lessons learned and future trends," *Journal of the American Ceramic Society*, vol. 92, no. 9, pp. 1901–1920, 2009.

[94] J. Eichler, J. Rodel, U. Eisele, and M. Hoffman, "Effect of Grain Size on Mechanical Properties of Submicrometer 3Y-TZP: Fracture Strength and Hydrothermal Degradation," *Journal of the American Ceramic Society*, vol. 90, no. 9, pp. 2830–2836, 2007.

[95] N. Claussen, "Fracture Toughness of Al_2O_3 with an Unstabilized ZrO_2 Dispersed Phase," *Journal of the American Ceramic Society*, vol. 59, no. 1-2, pp. 49–51, 1976.

[96] D. Green, "Critical Microstructures for Microcracking in Al_2O_3-ZrO_2 Composites," *Journal of the American Ceramic Society*, vol. 65, no. 12, pp. 610–614, 1982.

[97] S. Prochazaka, J. Wallace, and N. Claussen, "Microstructure of sintered mullite-zirconia composites," *Journal of the American Ceramic Society*, vol. 66, no. 8, pp. C–125, 1983.

[98] J. Gebelin, 2011. (private communication).

[99] R. Worthington, "The use of slip-coats in investment casting shell moulds," 2011. (private communication).

[100] W. Kingrey, H. Bowen, and D. Uhlmann, *Introduction to ceramics.* John Wiley and Sons, New York, 1976.

[101] T. Carneim and D. Green, "Mechanical properties of dry-pressed alumina green bodies," *Journal of the American Ceramic Society*, vol. 84, no. 7, pp. 1405–1410, 2001.

[102] T. Takei, Y. Kameshima, A. Yasumori, and K. Okada, "Crystallization kinetics of mullite in alumina–silica glass fibers," *Journal of the American Ceramic Society*, vol. 82, no. 10, pp. 2876–2880, 1999.

[103] I. Low and R. McPherson, "The origins of mullite formation," *Journal of Materials Science*, vol. 24, no. 3, pp. 926–936, 1989.

[104] E. Tkalcec, H. Ivankovic, R. Nass, and H. Schmidt, "Crystallization kinetics of mullite formation in diphasic gels containing different alumina components," *Journal of the European Ceramic Society*, vol. 23, no. 9, pp. 1465–1475, 2003.

[105] N. Louet, H. Reveron, and G. Fantozzi, “Sintering behaviour and microstructural evolution of ultrapure α-alumina containing low amounts of SiO_2,” *Journal of the European Ceramic Society*, vol. 28, no. 1, pp. 205–215, 2008.

[106] E. Liniger and R. Raj, “Packing and sintering of two-dimensional structures made fro bimodal particle size distributions,” *Journal of the American Ceramic Society*, vol. 70, no. 11, pp. 843–849, 1987.

[107] “Remasol Ultra! Control manual,” 2001. (private communication).

[108] A. Tsetsekou, C. Agrafiotis, and A. Milias, “Optimization of the rheological properties of alumina slurries for ceramic processing applications part i: Slip-casting,” *Journal of the European Ceramic Society*, vol. 21, no. 3, pp. 363–373, 2001.

[109] C. Sammis and M. Ashby, “The failure of brittle porous solids under compressive stress states,” *Acta Metallurgica*, vol. 34, no. 3, pp. 511–526, 1986.

[110] D. Green, *An introduction to the mechanical properties of ceramics*. Cambridge University Press, 1998.

[111] J. Birchall, “High strength ceramics: Problems and possibilities,” *Journal of Physics and Chemistry of Solids*, vol. 49, no. 8, pp. 859–862, 1988.

[112] J. Knight, “Measuring nylon fibre content in Hi-shell,” 2011. (private communication).